

**Visible-Light-Driven Photocatalytic Organic  
Synthesis with Surface Modified  
TiO<sub>2</sub>-Composites**

Von der Naturwissenschaftlichen Fakultät der  
Gottfried Wilhelm Leibniz Universität Hannover

zur Erlangung des Grades

**Doktorin der Naturwissenschaften  
(Dr. rer. nat.)**

genehmigte Dissertation

von

**Narmina Oktay Balayeva, Magistr Diploma  
(Aserbaidshan)**

2020

Referent: Apl. Prof. Dr. rer. nat. habil. Detlef Bahnemann

Korreferent: Prof. Dr. rer. nat. Jürgen Caro

Tag der Promotion: 24.06.2020

*Dedicated to My Family*



# Acknowledgements

At this point, I would like to thank all those who supported me during my Ph.D. and contributed to the success of this thesis.

First and foremost, I would like to express my sincere gratitude to my supervisor, Prof. Dr. Detlef W. Bahnemann, for accepting me as a Ph.D. student in his group. I would like to thank him for his stimulating discussions, excellent academic guidance, the opportunity to take part in various projects, and the freedom to develop my ideas.

I also would like to acknowledge Prof. Dr. Jürgen Caro for kindly agreeing to be a co-referee of my thesis and Prof. Dr. Ursula Rinas for kindly agreeing to be Chair of the Examining Committee.

I am deeply grateful to Dr. Ralf Dillert for his continuous support, numerous valuable discussions, and constructive comments throughout this work. I wish to thank him for his critical reading of this thesis and his important statement of opinion.

I am very thankful for the efficient, friendly, and open cooperation of Prof. Dr. Nan Zhang from the University of Arkansas. Indeed, visiting his group in 2018 was a significant step towards completing this project. In his group, I learned a lot about organic synthesis, and I would like to thank Enoch and Elvis for their kind help.

Special thanks go to Dr. Manuel Fleisch for his academic guidance and the productive discussions during the first half of my Ph.D.

I wish to express my warm thanks to Graduiertenakademie Leibniz Universität Hannover for the Exposé, Research Stay Abroad, and Completion scholarships.

Experimental research is almost impossible without the close interaction of a lot of people. I am deeply indebted to all those involved in the research that I present in this thesis for their help,

guidance and friendship.

I would also like to thank Barbara Nunes and Luis Granone for TEM and XRD measurements at the Laboratorium für Nano- und Quantenengineering and Institut für Physikalische Chemie und Elektrochemie, respectively. Dr. Jörg Fohrer at the Institut für Organische Chemie is also gratefully acknowledged for giving me access to NMR devices. I thank Malte Schäfer from Prof. P. Behrens group at the Institut für Anorganische Chemie for the BET (physisorption isotherms) measurements and Zamin Mamiyev from Prof. H. Pfnür group at the Institut für Festkörperphysik for XPS measurements.

I thank all the members in the group of Prof. Dr. Detlef W. Bahnemann. It has been a great pleasure to be a part of this amazing group. The helpful and lighthearted spirit made the efforts a lot less strenuous.

I wish to extend my warmest thanks to my friends, including Saher, Soukaina, Didem, Samia, Faryal, Barbara, and Bianca at the University of Hannover and Yoshie Sakamaki from the University of Arkansas, for making Ph.D. life more enjoyable and entertaining.

Last but not least, I thank my parents and family members for their great support during the time of my study and for their unconditional love and prayers, which indeed I feel at the bottom of my heart. Finally, I offer my sincere appreciation and love to my husband, Zamin Mamiyev, for his consistent support in every moment of life.

## Kurzzusammenfassung

Die Verwendung von sichtbarem Licht in der organischen Synthese erregte in den letzten Jahren aufgrund seines Anteils im Sonnenspektrum (~45%) erhebliche Aufmerksamkeit. Die niedrige Energie des sichtbaren Lichts ermöglicht selektive und saubere chemische Reaktionen. Normalerweise ist jedoch ein Photokatalysator erforderlich, um die gewünschte lichtinduzierte Reaktion auszulösen. Die Verwendung von halbleitenden Metalloxiden wie  $\text{TiO}_2$  als Photokatalysatoren ist aus verfahrenstechnischen Gründen von besonderem Interesse. Obwohl  $\text{TiO}_2$  in vielen photokatalytischen, für die Umwelt relevanten chemischen Reaktionen eingesetzt wurde, wurde nur eine begrenzte Anzahl von Arbeiten über selektive organische Synthesen an  $\text{TiO}_2$  veröffentlicht. Die vorliegende Arbeit konzentriert sich auf selektive akzeptorunterstützte (aerobe) und akzeptorlose (anaerobe) Dehydrierungsreaktionen von Tetrahydrochinolinen, Tetrahydroisochinolinen, Indolinen und andere N-Heterocyclen in Gegenwart von oberflächenmodifizierten  $\text{TiO}_2$ -Photokatalysatoren bei Umgebungstemperatur unter Belichtung mit sichtbarem Licht. Lewis-Säure-Base-Wechselwirkungen zwischen den eingesetzten N-Heterocyclen und dem  $\text{TiO}_2$  führen zu Oberflächenkomplexen, die sichtbares Licht absorbieren. Ein einzelner Elektronentransfer vom N-Heterocyclen zum Leitungsband des  $\text{TiO}_2$  erzeugt ein Aminokationradikal. Das eingefangene Elektron wird über Cokatalysator-Nanopartikel, die an der  $\text{TiO}_2$ -Oberfläche gebunden sind, auf oberflächenadsorbierten Sauerstoff oder auf ein Proton übertragen. Bei diesem Syntheseverfahren wird die Bildung von Löchern im Valenzband des Halbleiters vermieden. Dadurch wird die Selektivität der Gesamtreaktion erhöht. Als Photokatalysator wurden hauptsächlich handelsübliche Hombikat UV100  $\text{TiO}_2$ -Nanopartikel verwendet. Übergangsmetalle oder Metallionen wurden als Cokatalysatoren auf die Oberfläche des  $\text{TiO}_2$  aufgebracht, um die Reaktionsausbeute und die Selektivität zu erhöhen. Die Reaktionsbedingungen wurden unter Verwendung von 1,2,3,4-Tetrahydrochinolin als Edukt optimiert. Der Einfluss des Lösungsmittels, des Cokatalysators und der Katalysatormenge auf die Ausbeute und Selektivität wurden untersucht. In Gegenwart von molekularem Sauerstoff als Elektron- und Wasserstoff-Akzeptor erhöhten zusätzlich zugefügte TEMPO-Derivate die Selektivität der Reaktion signifikant. Abschliessend wurden fünfundzwanzig verschiedene N-heterocyclische Verbindungen unter optimierten Reaktionsbedingungen dehydriert. Die gewünschten aromatischen Produkte wurden in guten bis ausgezeichneten Ausbeuten (49%-99%) erhalten. Plausible Reaktionsmechanismen werden vorgeschlagen.

**Stichwörter:**  $\text{TiO}_2$  Photokatalysator, Oberflächenmodifikation, N-Heterocyclen, sichtbares Licht, Dehydrierungsreaktionen





## Abstract

In recent years, the use of visible light in organic synthesis has received considerable attention due to its particular abundance in the solar spectrum (~45%). Its low energy enables selective and clean chemical reactions. However, a photocatalyst is usually required to initiate the desired light-induced reaction. The use of semiconducting metal oxides such as TiO<sub>2</sub> as photocatalyst is of particular interest due to process engineering reasons. Although TiO<sub>2</sub> has been employed in many photocatalytic reactions for environmental remediation, only limited work regarding selective organic synthesis over TiO<sub>2</sub> has been reported. The present work focus on selective acceptor-assisted (aerobic) and acceptorless (anaerobic) dehydrogenation reactions of tetrahydroquinolines, tetrahydroisoquinolines, indolines, and others N-heterocycles in the presence of surface grafted and noble-metal photodeposited TiO<sub>2</sub> photocatalysts upon visible light irradiation at room temperature. It was observed that TiO<sub>2</sub> and N-heterocycles form surface complexes due to the Lewis acid-base interaction. The resulting complexes act as the visible-light-absorbing centers. A single electron transfer from the N-heterocycle to the conduction band of TiO<sub>2</sub> generates a radical amine cation, and a trapped electron inside the TiO<sub>2</sub>. The trapped electron is transferred to surface adsorbed oxygen or to a proton via cocatalyst nanoparticles being attached on the TiO<sub>2</sub> surface. This synthetic procedure avoids hole formation in the semiconductor valence band, thus increasing the chemoselectivity of the overall reaction. Commercially available Hombikat UV100 TiO<sub>2</sub> nanoparticles were mainly used as photocatalysts. Transition metals or metal ions were loaded on the surface of TiO<sub>2</sub> to increase the reaction yield and selectivity. The reaction condition were optimized employing 1,2,3,4-tetrahydroquinoline as the probe reactant on bare and surface modified TiO<sub>2</sub> in oxygen and in an inert atmosphere. It revealed that the combination of a TiO<sub>2</sub> photocatalyst with TEMPO derivatives significantly enhanced the chemoselectivity of the overall reaction in oxygen atmosphere. The impact of different noble metal cocatalysts, solvents, catalyst amounts, and cocatalyst loading amounts with respect to TiO<sub>2</sub> was investigated. Finally, the optimized reaction conditions were applied in each particular system to 25 N-heterocyclic compounds bearing electron-deficient or electron-rich functional groups. The desired dehydrogenated products were obtained in good to excellent yields (49%-99%). Plausible reaction mechanisms are proposed.

**Keywords:** TiO<sub>2</sub> photocatalyst, surface modification, N-heterocycles, visible light, dehydrogenation reactions



# Contents

<b>Abstract</b>	<b>v</b>
<b>1. Introduction</b>	<b>1</b>
1.1. Historical background . . . . .	1
1.2. Titania as a photocatalyst . . . . .	3
1.3. Band gap engineering . . . . .	9
1.3.1. Metal and non-metal doping of TiO <sub>2</sub> . . . . .	9
1.3.2. Noble metal nanoparticles photodeposited on TiO <sub>2</sub> . . . . .	10
1.3.3. Surface grafting of TiO <sub>2</sub> with transition metal ions . . . . .	12
1.3.4. Dye sensitized TiO <sub>2</sub> . . . . .	13
1.4. Heterogeneous photocatalytic organic synthesis . . . . .	14
1.4.1. TiO <sub>2</sub> as a heterogeneous photocatalyst in organic synthesis . . . . .	15
1.4.2. Visible-light-mediated organic synthesis with sensitized TiO <sub>2</sub> . . . . .	18
1.4.3. Surface complexation of amines with semiconducting photocatalysts . . . . .	20
1.5. Dehydrogenation of N-heterocyclic amines . . . . .	22
1.5.1. Oxidative dehydrogenation of N-heterocyclic amines . . . . .	22
1.5.2. Acceptorless dehydrogenation of N-heterocyclic amines . . . . .	23
1.6. Objectives . . . . .	25
<b>2. Materials and experimental methods</b>	<b>29</b>
2.1. Materials and Chemicals . . . . .	29

2.2.	Modification of the surface of TiO <sub>2</sub> . . . . .	30
2.2.1.	Impregnation method . . . . .	30
2.2.2.	Photodeposition method . . . . .	30
2.3.	Characterization techniques of the prepared materials . . . . .	30
2.3.1.	X-ray powder diffraction analysis (XRD) . . . . .	30
2.3.2.	ICP-OES measurement . . . . .	31
2.3.3.	Transmission electron microscopy (TEM) . . . . .	31
2.3.4.	Specific surface area measurements . . . . .	31
2.3.5.	UV–visible spectroscopy . . . . .	32
2.3.6.	EPR spectroscopy . . . . .	32
2.3.7.	ATR-FTIR spectroscopy . . . . .	33
2.3.8.	X-ray photoelectron spectroscopy (XPS) . . . . .	33
2.4.	Synthetic procedures . . . . .	33
2.4.1.	Photocatalytic reaction procedure under aerobic condition . . . . .	33
2.4.2.	Photocatalytic reaction procedure in anaerobic condition . . . . .	34
2.5.	Synthesis of substrates . . . . .	35
2.5.1.	Protection of hydroxyl group with tert-butyldimethylsilyl chloride . . . . .	35
2.5.2.	Synthesis of 4-methylthio-2-phenyl-1,2,3,4-tetrahydroquinoline . . . . .	35
2.6.	Analysis of the reaction mixture . . . . .	36
2.6.1.	Gas chromatography with flame ionization detector measurements . . . . .	36
2.6.2.	Gas chromatography with thermal conductivity detector . . . . .	38
2.6.3.	Nuclear magnetic resonance (NMR) . . . . .	39
2.6.4.	Column chromatography . . . . .	40
2.6.5.	Detection of hydrogen peroxide (H <sub>2</sub> O <sub>2</sub> ) . . . . .	40
2.6.6.	Photonic efficiency . . . . .	41
<b>3.</b>	<b>Results</b>	<b>43</b>
3.1.	Materials characterization of the prepared photocatalysts . . . . .	43
3.2.	Formation of surface complexes . . . . .	50
3.3.	Dehydrogenation in the presence of molecular oxygen . . . . .	54
3.3.1.	Effect of different TEMPO derivatives . . . . .	56

---

3.3.2.	Effect of grafting metal ions on THQ dehydrogenation . . . . .	57
3.3.3.	Kinetics of the oxidative THQ dehydrogenation . . . . .	59
3.3.4.	Superoxide radical anion generation studies by EPR . . . . .	60
3.3.5.	Detection of H <sub>2</sub> O <sub>2</sub> after THQ dehydrogenation . . . . .	64
3.3.6.	Recycling of the photocatalysts . . . . .	65
3.3.7.	ATR-FTIR measurements before and after THQ dehydrogenation . . . . .	68
3.3.8.	N-heterocyclic amines in aerobic dehydrogenation . . . . .	69
3.4.	ADH of N-heterocyclic amines on surface modified TiO <sub>2</sub> . . . . .	73
3.4.1.	Surface complexation between Rh/TiO <sub>2</sub> and N-heterocycles . . . . .	73
3.4.2.	Effect of different co-catalysts . . . . .	73
3.4.3.	Solvent effect and control experiments . . . . .	74
3.4.4.	Effect of the photocatalyst loading . . . . .	76
3.4.5.	Recycling of the 1 wt% Rh/TiO <sub>2</sub> in ADH reactions . . . . .	77
3.4.6.	Acceptorless dehydrogenation of tetrahydroquinolines . . . . .	79
3.4.7.	Acceptorless dehydrogenation of tetrahydroisoquinolines . . . . .	81
3.4.8.	Acceptorless dehydrogenation of indolines . . . . .	83
3.4.9.	Acceptorless dehydrogenation of other N-heterocycles . . . . .	84
<b>4.</b>	<b>Discussion</b>	<b>87</b>
4.1.	Overview . . . . .	87
4.2.	Formation of surface complexes . . . . .	89
4.3.	Dehydrogenation in the presence of molecular oxygen . . . . .	96
4.3.1.	Formation of radicals during oxidative dehydrogenation . . . . .	100
4.3.2.	The role of 4-amino-TEMPO . . . . .	101
4.3.3.	Effect of grafting metal ions in photocatalytic performance . . . . .	107
4.3.4.	<i>In-situ</i> EPR spectroscopy studies of Ni(II)/TiO <sub>2</sub> . . . . .	109
4.3.5.	Proposed reaction mechanism . . . . .	111
4.3.6.	Oxidative dehydrogenation of N-heterocycles . . . . .	112
4.4.	ADH of THQ - effect of different reaction parameters . . . . .	115
4.4.1.	Effect of noble metals on the reaction yield . . . . .	117
4.4.2.	General overview of ADH of N-heterocycles . . . . .	120

4.4.3. Proposed mechanism of the ADH reaction . . . . .	124
<b>5. Conclusions and outlook</b>	<b>127</b>
<b>Appendix</b>	<b>133</b>
<b>A. List of chemicals</b>	<b>135</b>
<b>B. NMR characterization of the products from aerobic dehydrogenation</b>	<b>139</b>
<b>Bibliography</b>	<b>145</b>
<b>List of Publications</b>	<b>171</b>
<b>Curriculum Vitae</b>	<b>173</b>

# List of Figures

1.1.	Crystal structures of TiO <sub>2</sub> : anatase, rutile, and brookite . . . . .	4
1.2.	Schematic electron energy levels near the surface of a clean semiconductor . . . . .	5
1.3.	Schematic illustration for energetics and primary reaction mechanism of TiO <sub>2</sub> photocatalysis . . . . .	7
1.4.	Schematic illustration of surface grafted TiO <sub>2</sub> photocatalysis . . . . .	12
1.5.	Schematic illustration of dye-sensitized TiO <sub>2</sub> photocatalysis . . . . .	14
1.6.	Schematic illustration of dye sensitized TiO <sub>2</sub> and TEMPO in alcohol oxidation reaction . . . . .	18
1.7.	Schematic illustration of visible-light-mediated LMCT . . . . .	19
2.1.	Calibration curve of the for the reactant (R) THQ obtained from the GC device . . . . .	36
2.2.	Calibration curve of the for the product (P) quinoline obtained from the GC device . . . . .	37
2.3.	Calibration curves for the molecular hydrogen obtained from the GC-TCD . . . . .	39
3.1.	X-ray diffraction patterns of the photocatalysts . . . . .	44
3.2.	Diffuse reflectance spectra of the employed powder samples . . . . .	46
3.3.	TEM micrographs of powder samples . . . . .	47
3.4.	Set of XPS spectra . . . . .	48
3.5.	EPR spectra of TiO <sub>2</sub> UV100 and Ni(II)/TiO <sub>2</sub> . . . . .	50
3.6.	Normalized extinction spectra of amine and TiO <sub>2</sub> . . . . .	51

3.7.	Absorption spectra of the surface grafted TiO <sub>2</sub> and normalized extinction spectra for the surface grafted TiO <sub>2</sub> /THQ . . . . .	52
3.8.	FTIR spectra of amine (THQ) and TiO <sub>2</sub> UV100 complex . . . . .	54
3.9.	The photocatalytic dehydrogenation of THQ . . . . .	56
3.10.	The photocatalytic dehydrogenation of THQ . . . . .	60
3.11.	DMPO spin-trapping EPR spectra in acetonitrile in the dark and under visible light illumination . . . . .	63
3.12.	Detection of H <sub>2</sub> O <sub>2</sub> after oxidative dehydrogenation of THQ . . . . .	64
3.13.	Recycling of the Ni(II)/TiO <sub>2</sub> photocatalyst in aerobic dehydrogenation . . . . .	66
3.14.	Nitrogen physisorption isotherms for the employed catalysts before and after experiments . . . . .	67
3.15.	XRD pattern of the bare and 0.1 wt% Ni grafted TiO <sub>2</sub> UV-100 before and after experiments . . . . .	68
3.16.	EPR spectra of 4-amino-TEMPO . . . . .	69
3.17.	Normalized extinction spectra of 1 wt.% Rh/TiO <sub>2</sub> (UV100) suspension . . . . .	73
3.18.	Effect of different co-catalysts photodeposited on TiO <sub>2</sub> on the ADH . . . . .	74
3.19.	Influence of the photocatalyst amount on the kinetics of the ADH . . . . .	76
3.20.	The influence of the loading amount of Rh on TiO <sub>2</sub> on ADH . . . . .	77
3.21.	The influence of the loading amount of Rh on TiO <sub>2</sub> on ADH . . . . .	78
4.1.	UV-vis absorption spectra of bare TiO <sub>2</sub> and THQ spectrum subtracted from TiO <sub>2</sub> /THQ, Ni(II)-TiO <sub>2</sub> /THQ, Rh-TiO <sub>2</sub> /THQ . . . . .	90
4.2.	Scheme of proposed electrostatic Lewis acid-base interaction . . . . .	94
4.3.	DFT calculation of the trimethylamine interaction with anatase TiO <sub>2</sub> . . . . .	95
4.5.	Proposed mechanism for the aerobic oxidation of THQ on TiO <sub>2</sub> . . . . .	99
4.6.	EPR spectra of 4-amino TEMPO . . . . .	105
4.7.	UV-vis absorption spectrum of TiO <sub>2</sub> , 4-amino-TEMPO, and TiO <sub>2</sub> -H <sub>2</sub> O <sub>2</sub> . . . . .	106
4.8.	TiO <sub>2</sub> -H <sub>2</sub> O <sub>2</sub> surface complex and a possible hydroxyl radical generation mechanism upon visible light illumination . . . . .	107
4.9.	EPR spectra of bare TiO <sub>2</sub> and 0.1 wt% Ni/TiO <sub>2</sub> UV100 . . . . .	110



4.10. Proposed mechanism of anaerobic amine dehydrogenation over Au/TiO <sub>2</sub> nanoparticles . . . . .	117
4.11. ADH reactions depend on the work function of employed noble metals . . . . .	119
4.12. Absorption spectra of 8-Acetyl-5,6,7,8-THQ and 8-Acetyl-5,6,7,8-THQ/ 1 wt% Rh/TiO <sub>2</sub> . . . . .	122
4.13. Proposed ADH mechanism of N-heretocycles over 1 wt% Rh/TiO <sub>2</sub> . . . . .	124



# List of Tables

1.1. Examples of photocatalytic organic reactions in the presence of UV-active TiO <sub>2</sub> . . .	17
3.1. Specific surface area (BET) of pure and surface modified TiO <sub>2</sub> powders. . . . .	45
3.2. Dehydrogenation of THQ over TiO <sub>2</sub> <sup>a</sup> . . . . .	55
3.3. The photocatalytic dehydrogenation of THQ in the presence of different redox mediators <sup>a</sup> . . . . .	57
3.4. Effect of grafted transition metals on the aerobic oxidative dehydrogenation of THQ <sup>a</sup> . . . . .	58
3.5. Oxidative dehydrogenation of tetrahydroquinolines. <sup>a</sup> . . . . .	71
3.6. Oxidative dehydrogenation of tetrahydroisoquinolines, indolines, 2-phenyl-2-imidazoline, and quinoxaline. <sup>a</sup> . . . . .	72
3.7. Control reactions for the ADH of THQ in an inert atmosphere. <sup>a</sup> . . . . .	75
3.8. Acceptorless dehydrogenation of tetrahydroquinolines over 1 wt% Rh photodeposited TiO <sub>2</sub> <sup>a</sup> . . . . .	80
3.9. Acceptorless dehydrogenation of tetrahydroisoquinolines over 1 wt% Rh photodeposited TiO <sub>2</sub> <sup>a</sup> . . . . .	81
3.10. Acceptorless dehydrogenation of indolines over 1 wt% Rh photodeposited TiO <sub>2</sub> <sup>a</sup> . . . . .	83
4.1. Peak frequencies and assignments of the FTIR bands (cm <sup>-1</sup> ) obtained from acetonitrile suspension of TiO <sub>2</sub> UV100 mixed with THQ and measured in the dark. . . . .	92
* . . . . .	92
4.2. Dehydrogenation of THQ over TiO <sub>2</sub> <sup>a</sup> . . . . .	96

4.3. Photocatalytic dehydrogenation of THQ in the presence of different redox mediators <sup>a</sup>	.102
4.4. Effect of the employed transition metals modified on TiO <sub>2</sub> UV100 surface in aerobic oxidative dehydrogenation of THQ compared with the photonic efficiency. <sup>a</sup>	. . . . .108
4.5. EPR parameters of the detected signals on 0.1 wt% Ni/UV100 upon UV-vis illumination and their assignment. . . . .	.109
4.6. Dehydrogenation of the tetrahydroquinolines in oxygen <sup>a</sup> . . . . .	.113
4.7. Dehydrogenation of the tetrahydroisoquinolines in oxygen <sup>a</sup> . . . . .	.115
4.8. Correlation between dielectric constant of solvents and photonic efficiencies in ADH reactions of THQ <sup>a</sup> . . . . .	.116
A.1. List of compounds name, chemicals structure, and symbols that employed in this study . . . . .	.136

# List of Schemes

1.1. Proposed mechanism for the formation of imines by the oxidation of amines on a TiO <sub>2</sub> . . . . .	21
1.2. Synthesis of imines by the oxidation of amines on a TiO <sub>2</sub> or Nb <sub>2</sub> O <sub>5</sub> . . . . .	21
1.3. Aerobic dehydrogenation of 1,2,3,4-tetrahydroisoquinoline over TiO <sub>2</sub> and Nb <sub>2</sub> O <sub>5</sub> photocatalysts . . . . .	22
1.4. Different derivatives of TEMPO employed in this study . . . . .	26
3.1. Schematic illustration of dehydrogenation of THQ . . . . .	51
3.2. Scheme of the ADH of other N-heterocycles . . . . .	85
4.1. Dehydrogenation reaction conditions of N-heterocycles in O <sub>2</sub> atmosphere . . . . .	88
4.2. ADH reaction conditions of N-heterocycles . . . . .	89
4.3. ADH reaction conditions of N-heterocycles . . . . .	101
4.4. Proposed ongoing reactions pathway with 4-amino-TEMPO . . . . .	104
4.5. The possible coordination structure of H <sub>2</sub> O <sub>2</sub> -adsorbed on the TiO <sub>2</sub> surface . . . . .	106
4.6. Proposed reaction mechanism for the aerobic dehydrogenation of N-heterocycles . . . . .	111
4.7. Acceptorless decarboxylation and dehydrogenation mechanism of 2-carboxyl-indoline upon visible-light illumination. . . . .	121
4.8. The ongoing reaction mechanism of photocatalytic acceptorless dehydrogenation of 8-Acetyl-5,6,7,8-THQ over 1 wt% Rh/UV100 . . . . .	124

5.1. The general ongoing reaction mechanism of photocatalytic dehydrogenation of THQ in aerobic and anaerobic atmosphere . . . . . 129

# Abbreviations, variables, and constants

## Abbreviations

XPS	X-ray photoelectron spectroscopy
RT	Room temperature ( $\approx 25\text{ }^{\circ}\text{C}$ )
EHP	Electron-hole pairs
XRD	X-ray diffraction
EPR	Electron paramagnetic resonance
FTIR	Fourier-transform infrared spectroscopy
TEM	Transmission electron microscopy
ATR	Attenuated total reflection
LED	Light-emitting diode
GC-FID	Gas chromatography - flame ionized detector
ADH	Acceptorless dehydrogenation
BET	Brunauer–Emmett–Teller
VB	Valence band
CB	Conduction band
eV	Electron volt
NHE	Normal Hydrogen Electrode
SPR	Surface Plasmon Resonance
BJH	Barrett-Joyner-Halenda

NMR	Nuclear magnetic resonance
ICP-OES	Inductively coupled plasma atomic emission spectroscopy
GC-TCD	Gas chromatography - thermal conductivity detector
UV	Ultraviolet

## Used variables

$E_g$	Bandgap energy
$E_F$	Fermi level
$\epsilon$	Relative permittivity of the surrounding medium, to be multiplied with $\epsilon_0$
$I$	Intensity
$\lambda$	Wavelength
$\alpha$	Absorption Coefficient
$A$	Area
$\rho$	Density
$\zeta$	Photonic efficiency

## Constants<sup>1</sup>

$c$	Speed of light	$= 299\,792\,458\text{ m s}^{-1}$
$\epsilon_0$	Electric constant	$= 8.854\,187\,817 \times 10^{-12}\text{ F/m} = 1/(\mu_0 c^2)$
$h$	Planck constant	$= 6.626\,070\,040(81) \times 10^{-34}\text{ Js}$
$\hbar$	Reduced Planck constant	$= h/2\pi$
$m_e$	Electron mass	$= 9.109\,383\,56(11) \times 10^{-31}\text{ kg}$
$\mu_0$	Magnetic constant	$= 4\pi \times 10^{-7}\text{ N A}^{-2}$

---

<sup>1</sup>The listed constants have been taken from the wikipedia, [https://en.wikipedia.org/wiki/Physical\\_constant](https://en.wikipedia.org/wiki/Physical_constant)







# Chapter 1

## Introduction

This chapter presents the historical and theoretical background of titanium oxide ( $\text{TiO}_2$ ), which was used as a semiconducting photocatalyst in this study. Subsequently, relevant literature about the modification of  $\text{TiO}_2$  to increase its physical and photocatalytic properties will be reviewed. Consequently, reported researches about the possible organic synthesis over  $\text{TiO}_2$  photocatalyst upon visible light illumination will be summarized. The chapter will be concluded with the presentation of the scope of this thesis.

### 1.1. Historical background

Starting early in the 20<sup>th</sup> century,  $\text{TiO}_2$  powders have been commonly used as white pigments in the areas of a coating such as lacquers and paints, as well as plastic coloring and laminate papers applications. In 1921, the earliest work was reported by Renz about the photocatalytic activity of  $\text{TiO}_2$ , which was found to be partially reduced upon solar light illumination in the presence of glycerol. The color of powder titania was found to turn from white to grey, blue, or even black due to the formation of  $\text{Ti}^{3+}$  species. A similar phenomenon was observed with  $\text{CeO}_2$ ,  $\text{Nb}_2\text{O}_5$ , and  $\text{Ta}_2\text{O}_5$ . [1] Thus,  $\text{TiO}_2$  holds its stability in the darkness, whereas upon UV absorption, surface adsorbed oxygen molecules on titania are activated, causing the photobleach-

ing of dyes in an ambient atmosphere. This was discovered by Doodeve and Kitchener in 1938, who called  $\text{TiO}_2$  as a “photosensitizer” and not a “photocatalyst”. [2] The first researchers who used the term “photocatalyst” relating to  $\text{TiO}_2$  might be Kato and Mashio in their several reports from 1956. They studied the photocatalytic oxidation of various organic solvents such as alcohols and hydrocarbons over  $\text{TiO}_2$  powder and simultaneous  $\text{H}_2\text{O}_2$  formation upon the UV irradiation with a Hg lamp. [3] Similarly, in 1964 Kato and Mashio reported the photocatalytic oxidation of tetralin (1,2,3,4-tetrahydronaphthalene) by a titania suspension. [4] In 1965, the first solid-gas phase photocatalytic oxidation of ethylene and propylene in the presence of adsorbed oxygen on titania was reported by McLintock and Ritchie. [5] However, limited exciting breakthroughs relating to the photocatalytic performance of  $\text{TiO}_2$  were made until Fujishima and Honda’s discovery in the 1970s. They reported on the photo-oxidation of pure water yielding  $\text{O}_2$  and  $\text{H}_2$  through an electrochemical method via photoirradiation of a  $\text{TiO}_2$  single-crystal anode immersed in an aqueous electrolyte. A Pt wire was used as the counter electrode. This finding has opened up a new aspect to consider the photocatalytic process as an alternative way of dealing with the energy problem. [6] In 1977, Frank and Bard reported the first photocatalytic degradation of cyanide,  $\text{CN}^-$ , in water using titanium dioxide and different semiconductors aiming wastewater treatment and environmental pollutant remediation. [7, 8] Additionally, the photocatalytic decomposition of organic acids such as acetic acid, accompanied by hydrocarbon formation, was reported by Bard et al., who observed an unstable intermediate methyl radical during the photocatalytic reaction of acetic acid. [9, 10] In 1977, Wang et al. reported on the super hydrophilic properties of photoexcited  $\text{TiO}_2$  for excellent anti-fogging and self-cleaning applications. [11] In 1991, Graetzel and O’Regan discovered an efficient activity of nano titanium dioxide for dye-sensitized solar cells (DSSC). [12] The noteworthy development of environmentally friendly and energy sustainable organic transformations over  $\text{TiO}_2$  was made during the last decades. One of the first reports on photocatalytic organic synthesis by Reiche and Bard in 1979 reported the production of highly valuable amino acids from methane-ammonia-water over Pt/ $\text{TiO}_2$ . [13] Another important finding was reported by Masamichi Fujihira et al. in 1981 who investigated the photocatalytic oxidation of various aromatic hydrocarbons with simultaneous photoelectrochemical hydrogen-peroxide production at  $\text{TiO}_2$  semiconductor electrodes. [14] In 1981 Fox et al. reported on mechanistic features of some semiconductors ( $\text{TiO}_2$ ,  $\text{ZnO}$ ,  $\text{CdS}$ ) in selective olefin-to-carbonyl

oxidation. [15]

During the past decades, photocatalytic reactions over  $\text{TiO}_2$  have been investigated extensively, with applications focusing on solar energy conversion and storage, air and water purification, organic synthesis, reduction of carbon dioxide or mineralization and/or detoxification of organic compounds. Thousands of research and review papers have been published in these areas based on particulate and single-site  $\text{TiO}_2$  photocatalysts (some of them are cited in this thesis). Concerns about photocatalytic performance, stability, underlying reaction mechanisms, and so on of photocatalysis have been addressed. However, many topics are rather underexplored. For instance, in comparison to energy, environmental, and water applications, there are limited reports on the application of  $\text{TiO}_2$  as a photocatalyst for green organic synthesis.

## 1.2. Titania as a photocatalyst

It is well known that  $\text{TiO}_2$  has three major crystal structures: rutile, anatase, and brookite (see Figure 1.1). [16] Rutile and anatase have both a tetragonal crystal structure with 6 and 12 atoms per unit cell, respectively. In rutile and anatase, every Ti atom is coordinated to six O atoms where each O atom is also coordinated to three Ti atoms. Brookite has a more complicated structure with an orthorhombic unit cell. In all three crystal structures, existing  $\text{TiO}_6$  octahedra are slightly distorted. While rutile and anatase have two Ti-O bonds that are somewhat different from the other four bonds, brookite has six different Ti-O bonds. Therefore, rutile is considered the most stable phase among these polymorphs due to less distortion of the bonds. Anatase and brookite are metastable and are irreversibly converted to rutile at above  $600^\circ\text{C}$ . [17] Rutile has three main crystal faces (110, 001, and 100), which are quite low in energy and are thus regarded to be significant for the practical application of polycrystalline powder materials. [18] However, (110) is the most thermally stable face, and for that reason, it has been studied extensively. It has bridging oxygens rows, which are linked to two Ti atoms. The corresponding Ti atoms are 6-fold coordinated. [19] Moreover, 5-fold coordinated Ti atom rows are in parallel to the bridging oxygens rows with low electron density. They act as Lewis acid sites. [20] Anatase has two low energy surfaces (101 and 001), which commonly occur in natural crystals. Unlike rutile, the most ubiquitous face for anatase nanocrystals is the (101) surface, which is corrugated with 5-fold coordinated Ti atom rows and bridging oxygen atoms at the edges of the distortions. [21] In

contrary, brookite has three different crystal faces with low energy:  $(010) < (110) < (100)$ . Since preparing brookite is more difficult than other crystal phases, it has been studied less extensively as a photocatalyst. [17] Apart from the crystal faces, the nanoparticle sizes of these structures are also affecting the stability of the semiconducting material. Thus, rutile with a particle size above 35 nm, anatase nanoparticles below 11 nm, and brookite nanoparticles in the 11-35 nm range have been found to be the most stable phases at ambient temperature. [22, 23]

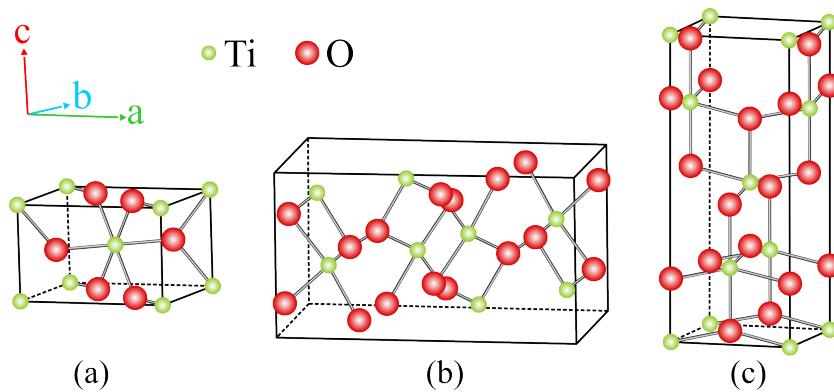


Figure 1.1.: Crystal structures of TiO<sub>2</sub>: anatase (a), rutile (b), and brookite (c).

Being a semiconductor, TiO<sub>2</sub> has two characteristic bands, the highest occupied energy band, i.e., the valence band (VB) and the lowest empty energy band, i.e., the conduction band (CB), which are separated by an energy bandgap ( $E_g$ ). The bandgap energies based on optical absorption spectra of the three different polymorphs were determined to be 3.0 eV for rutile [24, 25], 3.2 eV for anatase [26], and 3.4 eV for brookite [27].

Semiconductors are typically classified into three types: intrinsic or undoped semiconductors, n-type semiconductors where the majority of charge carriers are electrons, and p-type semiconductors wherein contrary the majority charge carriers are holes. In a practical matter, the Fermi energy  $E_f$  represents the highest energy electrons in an equilibrium solid notwithstanding the Fermi tail. [28] In intrinsic semiconductors, the Fermi level lies in the middle of the bandgap. In n-type semiconductors, the Fermi level lies below the conduction band, and in p-type semiconductors, the Fermi level is above the valence band edge. Typically, the surface state exists on a clean semiconductor due to the crystal lattice periodicity's termination at the surface. Unpaired electrons in the dangling bonds at the surface atoms interact with each other and create narrow bandgap energy at the surface of a semiconductor. Therefore, depending on the type of semi-

conductors, the Fermi level of a surface state differs from the Fermi level of the bulk state. The bulk and surface state interfaces for intrinsic, n-type, and p-type semiconductors are illustrated in Figure 1.2 in disequilibrium and equilibrium conditions before and during illumination. When a semiconductor is undoped, which is called an intrinsic semiconductor, the Fermi level of the semiconductor in the bulk state ( $E_{F(bulk)}$ ) is located at the midgap and is equal to the Fermi level of the surface state of the semiconductor ( $E_{F(surface)}$ ). Therefore no charge transfer occurs in the intrinsic semiconductor, and the valence and conduction bands stay flat. However, a band bending is induced by the surface state in n-doped and p-doped semiconductors. In an n-type semiconductor, the Fermi level of the bulk  $E_{F(bulk)}$  is higher than its surface state Fermi level  $E_{F(surface)}$  under disequilibrium condition. Electrons will then migrate from the bulk to the surface, and while  $E_{F(bulk)}$  drops,  $E_{F(surface)}$  will rise until equilibrium is acquired, which results in an upward bending of the energy bands. On the contrary, in p-type semiconductor,  $E_{F(bulk)}$  is lower than  $E_{F(surface)}$  under disequilibrium condition. Therefore to achieve equilibrium, the electron from the surface will migrate to the bulk, and the energy bands will bend downward. [29]

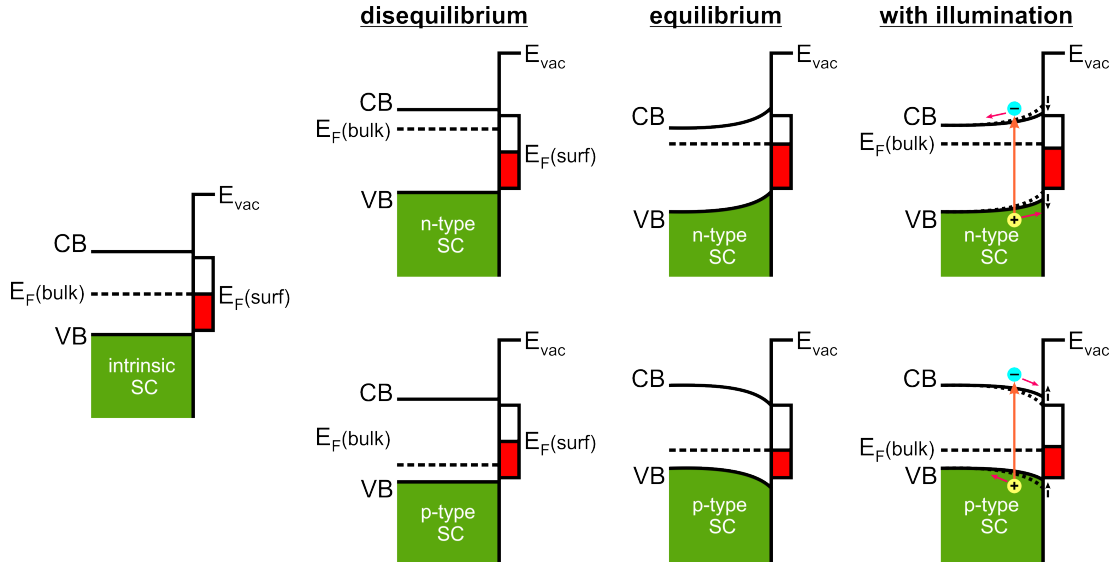


Figure 1.2.: Schematic electron energy levels near the surface of a clean semiconductor: (left middle) undoped (intrinsic) semiconductor; (top left) disequilibrium and (top middle) equilibrium between n-type bulk and its surface; (top right) with illumination n-type bulk and its surface (bottom left) disequilibrium and (bottom middle) equilibrium between p-type bulk and its surface (bottom right) with illumination p-type bulk and its surface. Adapted from Ref. [29].

TiO<sub>2</sub> is reported to be an n-type semiconductor due to the presence of oxygen vacancies. Increasing partial pressure of O<sub>2</sub> decreases the conductivity at temperatures above 600 °C. [30] This behavior was explained with the assumption that O<sub>2</sub> is released from the lattice when the specimen reaches thermal equilibrium, which corresponds with the formation of Ti<sup>3+</sup> sites.

Upon excitation TiO<sub>2</sub> nanoparticles with photon energy equal to or greater than its bandgap energy, electron-hole pairs are generated via band-to-band transition. These free electrons and holes will move in different directions due to the electric field in the band-bend region at the surface-bulk interface. Generally, in n-type semiconductors i.e. TiO<sub>2</sub>, photogenerated electrons will move to the bulk, and holes will transfer to the surface, which results in partial band flattening (see Figure 1.2 top right). Opposite charge migration occurs in p-type semiconductors where the surface will be more negatively charged, and the degree of downward band bending will decrease (see Figure 1.2 bottom right).

When molecules are adsorbed at the surface of TiO<sub>2</sub>, the fate and lifetime of the photogenerated charge carriers change, as illustrated in Figure 1.3. The electron-hole pair is photogenerated within a femtosecond time scale (Figure 1.3, path 1). Subsequently, the charge carriers are trapped in shallow traps within 50-260 fs and deep traps within 50 ns. The recombination of charges could occur on the surface of TiO<sub>2</sub> within 1-10 ps (Figure 1.3, path 2) and in bulk in the range of nanoseconds (Figure 1.3, path 3). Photocatalytic reactions are facilitated when the trapping rate of separated electron-hole pairs by active sites is higher than the recombination rate. While surface adsorbed reactive species undergo reduction reactions by the photogenerated electrons at the bottom of the conduction band (Figure 1.3, path 5), oxidation reactions by the photogenerated holes occur at the top of the valence band (Figure 1.3, path 4), according to thermodynamic and kinetic constraints. Therefore, the conduction band of the semiconductor must have more negative potential than the reduction potential of the chemical species, and the valence band of the semiconductor must have more positive than the oxidation potential of the chemical species to allow photo-reduction and photo-oxidation processes, respectively. Knowing the band positions and the flat band position of the semiconductors is of utmost importance for better understanding the thermodynamic restrictions for the surface-initiated photocatalytic reactions.



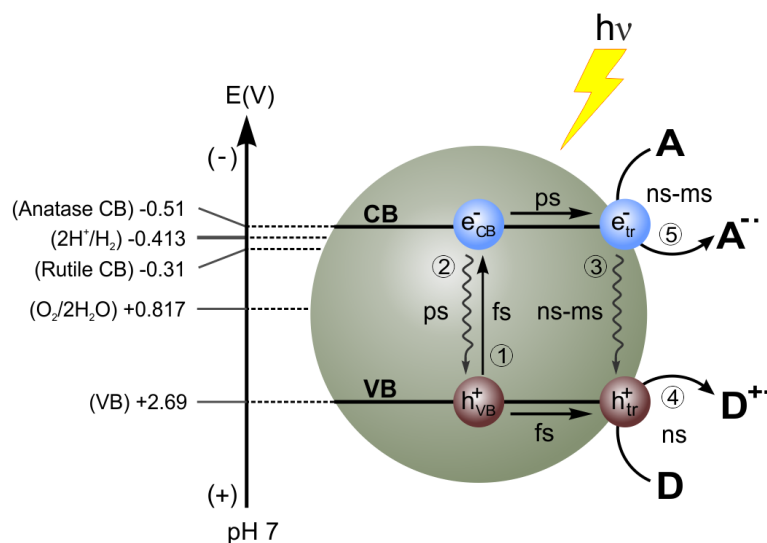
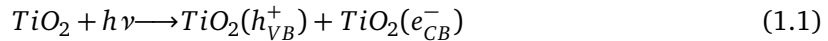


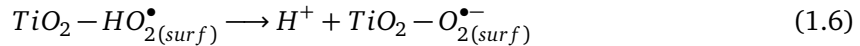
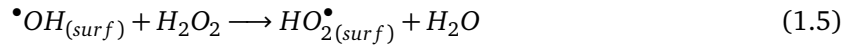
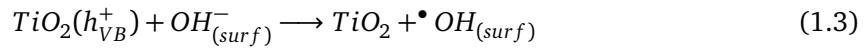
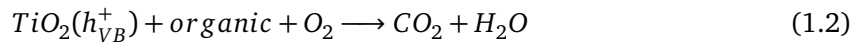
Figure 1.3.: Schematic illustration for energetics and primary reaction mechanism of TiO<sub>2</sub> photocatalysis upon UV light illumination. 1: excitation and electron-hole pair generation, 2 and 3: recombination, 4: electron transfer to electron acceptor, 5: hole transfer to electron donor.

The conduction band position of anatase TiO<sub>2</sub> is reported to be  $-0.51$  V at pH 7 which lies slightly above the reduction potential of molecular oxygen ( $E^0(\text{O}_2/\text{O}_2^{\bullet-}) = -0.33$  V vs NHE) and the hydroperoxyl radical ( $E^0(\text{O}_2/\text{HO}_2^{\bullet}) = -0.45$  V vs NHE). [31] Therefore, anatase TiO<sub>2</sub> is considered an efficient photocatalyst since its conduction band energy is suitable for the reduction of O<sub>2</sub>, which is an abundant and green oxidant in the environmental atmosphere, by a trapped electron. Nevertheless, rutile is reported to be less active due to its lower conduction band energy and Fermi level, which are supposed to be ca.  $-0.31$  V and  $-0.2$  V at pH 7 with respect to NHE. [32] Karakitsou et al. investigated the photogeneration of H<sub>2</sub> molecules in a mixture of anatase-rutile composites and reported that the yield was decreasing while increasing the ratio of rutile [33] Due to the positive oxidation potential of TiO<sub>2</sub> ( $E^0 = +2.69$  V vs NHE), most reactive oxygen species such as hydrogen peroxide ( $\text{HOO}^{\bullet}/\text{H}_2\text{O}_2 = +1.007$  V) and hydroxyl radical (surface-bonded or free) ( $E^0(\text{OH}^-/\text{OH}^{\bullet}) = +1.9$  V vs NHE at pH7) are easily generated on the surface. [31] Moreover, in principle, most organic compounds have less positive oxidation potentials than the positive potential of the TiO<sub>2</sub> VB, which allows them to be oxidized upon UV light illumination. Eqs. 1.1 - 1.10 show the possible occurring reaction pathways on the surface of a

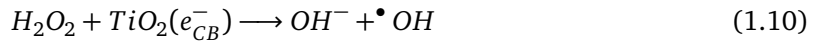
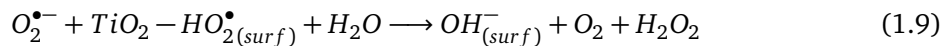
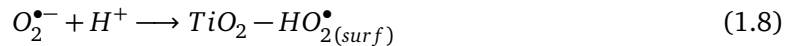
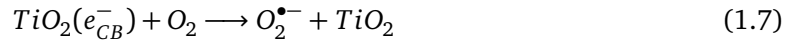
TiO<sub>2</sub> photocatalyst upon illumination with light of suitable energy. As mentioned above, upon illumination with light of suitable energy electrons ( $e_{CB}^-$ ) and holes ( $h_{VB}^+$ ) are generated in particulate TiO<sub>2</sub> (Eq 1.1). Trapped holes could directly participate in the oxidation process of surface adsorbed organic molecules (Eq. 1.2). Since the surface of TiO<sub>2</sub> is populated with hydroxyl anions (OH<sup>-</sup>), the trapping of photogenerated holes at this sites result in the formation of surface-bound hydroxyl radicals ( $\bullet$ OH) (Eq. 1.3).



Oxidation reactions:



Reduction reactions:



Hydroxyl radicals could either recombine with each other to yield hydrogen peroxide or oxidize surface adsorbed organic molecules (Eq. 1.4). Another recombination of a hydroxyl radical with hydrogen peroxide leads to the formation of a TiO<sub>2</sub>-HO<sub>2</sub><sup>•</sup> surface complex (Eq. 1.5). Dissociation of this complex yields a proton and surface-bound superoxide radical (Eq. 1.6). In parallel to the oxidation processes, reduction reactions occur on the surface of TiO<sub>2</sub>. Initially, in the presence of molecular oxygen, fast trapping of electrons by surface-adsorbed oxygen molecules results in the formation of superoxide radicals (Eq. 1.7). These superoxide radicals could react with free protons yielding a TiO<sub>2</sub>-HO<sub>2</sub><sup>•</sup> surface complex (Eq. 1.8). Moreover, it can further react with a

TiO<sub>2</sub>-HO<sub>2</sub><sup>•</sup> surface complex to form surface hydroxyl radicals (Eq. 1.9). Surface trapped electrons possibly reduce hydrogen peroxide yielding a hydroxyl anion and a hydroxyl radical (Eq. 1.10).

### 1.3. Band gap engineering

Pristine TiO<sub>2</sub> photocatalysts with anatase or rutile crystal phase, typically absorb UV-A light due to their large band gap energy. However, when considering the solar spectrum, only a small range of the electromagnetic spectrum emitted by the sun contains ultraviolet light (less than 5%). On the other hand, fast recombination of charge carriers upon UV illumination restricts TiO<sub>2</sub> to act as an efficient photocatalyst. Therefore, through the past years, different approaches have been applied. Many important findings have been reported to improve the lifetime of the photogenerated charge carriers and to facilitate the photocatalytic response of TiO<sub>2</sub> to the broad range of the solar spectrum, i.e., visible region. As mentioned above, TiO<sub>2</sub> shows only poor photocatalytic activity when used alone due to the fast recombination of the electron-hole pairs. Significant efforts have been made to modify TiO<sub>2</sub>, including impurity doping with metals (cation doping) [34–37] and non-metals (anion doping) [38, 39], surface modification [31, 40, 41], sensitization with dyes, combination with narrow band-gap semiconductors [42], etc.

#### 1.3.1. Metal and non-metal doping of TiO<sub>2</sub>

Metal doping was the earliest effort to shift the photoresponse of TiO<sub>2</sub> into the visible region. Different transition metal cations, either 3d or 4d elements, were incorporated into the TiO<sub>2</sub> crystal lattice resulting in the formation of new sub-levels between the VB and the CB, which serve the narrowing of the bandgap energy and shifting the absorption towards the visible region. [43] However, it has also been observed that transition metals initiate the thermal instability of the anatase TiO<sub>2</sub> phase. [44] Additionally, there are several other potential drawbacks, such as an increase of the photocorrosion rate or charge recombination at metal sites due to the creation of significant lattice defects. For instance, Fe(III) and V(IV) metal dopants increase the lifetime of e<sup>-</sup>/h<sup>+</sup> pairs. At the same time, Cr(III) is reported to act as recombination centers, thus decreasing the photocatalytic efficiency of the doped TiO<sub>2</sub> under both UV and visible light irradiation [45]. Nevertheless, due to the substantial drawbacks mentioned above, there is no remarkable improvement in photocatalytic activity by metal doping, which might be due to a poor interaction of metal

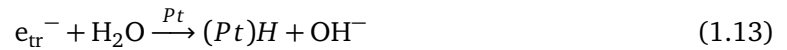
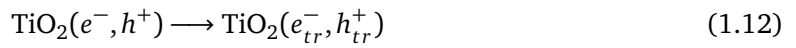
ions with the  $\text{TiO}_2$  crystal lattice. [16]

Due to its similar atomic size to oxygen, small ionization energy, and high stability, nitrogen atoms are reported being easily coordinated into the  $\text{TiO}_2$  lattice. In 1986, Sato et al. reported for the first time that the calcination of a  $\text{TiO}_2$  sol with ammonium hydroxide ( $\text{NH}_4\text{OH}$ ) resulted in the synthesis of a visible light-sensitive material. [46] 15 years after this work, Asahi and co-workers discovered the first N-doped  $\text{TiO}_2$  photocatalysts which absorbed light at 500 nm and showed activity under visible light illumination for the decomposition of acetaldehyde and decoloration of methylene blue solution. This photocatalyst was synthesized by sputtering of  $\text{TiO}_2$  in  $\text{N}_2/\text{Ar}$  gas mixture as well as by calcination of a  $\text{TiO}_2$  powder in a  $\text{NH}_3/\text{Ar}$  atmosphere. [47,48] Umebayashi et al. theoretically calculated the densities of states of substitutional doping of  $\text{TiO}_2$  by fluorine, carbon and phosphorous, thus explaining the source of the visible light response. [49,50] There have been essential endeavors after these achievements and deep electronic, optical, structural, and mechanistic investigations were performed to understand the underlying mechanisms. [37, 51, 52] Thus, it has been reported that incorporating non-metal atoms into the  $\text{TiO}_2$  lattice as substitution of some oxygen atoms in a crystal cell results in narrowing the bandgap and generation of localized midgap states above the valence band. Although fluorine doping is not influencing the shrinking of bandgap energy, it improves the surface acidity of  $\text{TiO}_2$ , which facilitates the reduction of  $\text{Ti}^{4+}$  and eventually the photooxidation of organic compounds.

### **1.3.2. Noble metal nanoparticles photodeposited on $\text{TiO}_2$**

Although  $\text{TiO}_2$  already possesses a suitable band position for proton reduction, photogenerated electrons cannot reduce proton to the hydrogen molecule due to insufficient active sites on the  $\text{TiO}_2$  surface which results in fast recombination of trapped electrons. However, a suitable cocatalyst, which also provides a better electron-hole separation, could assist in proton reduction. For this purpose, different noble metal or metal oxide nanoparticles such as Pt, Pd,  $\text{RuO}_2$ , Rh, Ag, and Au loaded on  $\text{TiO}_2$  surface has been reported. The most applied method is the photodeposition technique, where aqueous-alcoholic suspensions of  $\text{TiO}_2$  are mixed with the appropriate amount of the metal precursor and illuminated with UV-A light in an inert atmosphere. Generally, organic alcohol (methanol, ethanol, 2-propanol, etc.) is used as the hole scavenger to re-

duce metal ions with trapped electrons to the metallic nanoparticles. The surface photodeposited noble metal nanoparticles act as strong electron acceptors and enable hydrogen evolution and concomitant photooxidation of organic molecules in an inert atmosphere. The advantage of the photodeposition method is that the crystal structure of the semiconductor remains unchanged since photodeposition is performed at ambient temperature without the requirement of thermal treatment [53, 54]. Different from doping methods, the noble metals do not substitute Ti atoms in the crystal lattice. Therefore, sublevels below the conduction band are considered to act as the main recombination centers are not formed. Depending on the type of the noble metals, the size of the loaded particles, and the loading amount, the photocatalytic efficiency can be changed. Furthermore, the work function value of noble metals, which is defined as the energy required to promote an electron from the Fermi energy level into a vacuum, affects the photocatalytic performance. Thus, it has been reported that the photodeposited noble metals should have a higher work function value than the semiconductor ( $\Phi_M > \Phi_{SC}$ ) to achieve better charge separation. [55, 56] Having a high work function, Pt is considered to be a better electron acceptor than Ag and Au which are widely used as co-catalysts in photocatalytic reactions. [57] The possible ongoing water oxidation pathways over Pt photodeposited TiO<sub>2</sub> are given in Eq (1.11 -1.17)



Moreover, the plasmonic effect of some noble metal nanoparticles has also been reported to be beneficial for absorbing light at lower energy, increasing the population of charge carriers. While Pt photodeposited TiO<sub>2</sub> does not show any optical absorption in a visible region, Ag modified TiO<sub>2</sub> demonstrates visible light respond via electron transfer from Ti<sup>3+</sup> to the silver nanoparticles or visa-versa upon illumination (>450 nm). [58, 59] This phenomenon is called surface plasmon

resonance of silver nanoparticles, which later was also observed with gold nanoparticles. [60]

### 1.3.3. Surface grafting of TiO<sub>2</sub> with transition metal ions

Surface grafting of vanadia species on TiO<sub>2</sub> and other metal oxides surfaces was first reported by Wokaun et al. [61]. Lately, breakthroughs on surface grafted TiO<sub>2</sub> have been reported by Irie et al., who impregnated Cu(II) nanoclusters on the semiconductor surface at low temperature. The synthesized photocatalyst was tested in visible-light-mediated 2-propanol oxidation in the gas phase. [62,63] The same group applied the impregnation method for the grafting of the TiO<sub>2</sub> surface by other transition metal ions such as Cr(III), Fe(III), and Ce(III). The prepared surface grafted TiO<sub>2</sub> samples were employed in the oxidative degradation of 2-propanol upon visible light illumination. The reaction mechanism of visible-light responsive Cu(II)-grafted TiO<sub>2</sub> [62] and Fe(III)-grafted TiO<sub>2</sub> [64] photocatalysts was analyzed using electron spin resonance (ESR) spectroscopy by detecting trapped holes and electrons.

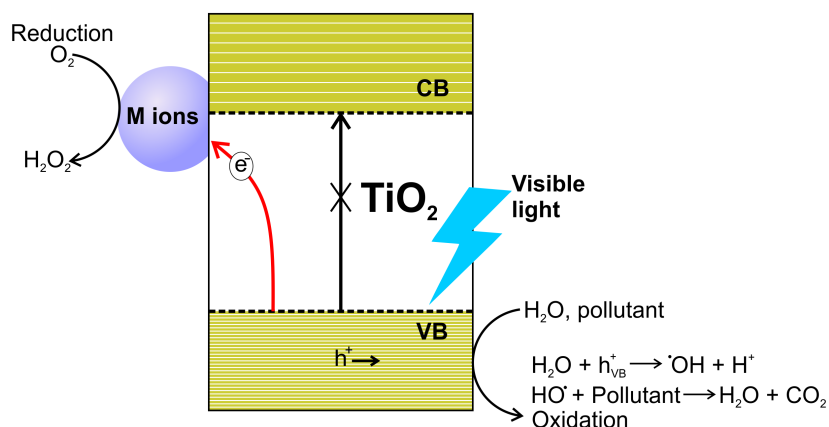


Figure 1.4.: Schematic illustration of surface grafted TiO<sub>2</sub> photocatalysis with transition metal ions.

It was revealed that Cu(II) grafted ions on the TiO<sub>2</sub> surface shows a distorted amorphous CuO-like structure and Fe(III) grafted ions on the TiO<sub>2</sub> surface is distorted amorphous FeO(OH)-like clusters. The visible light activation was attributed to the interfacial charge transfer (IFCT) process without exhibiting additional impurity levels in the bandgap of the TiO<sub>2</sub>. In electron transfer processes, grafted transition metal nanoclusters can expeditiously launch the rapid photoinduced charge separation while lowering the charge carrier recombination rate due to their remarkable

action as electron acceptors. However, the activity of nanocluster grafted photocatalytic systems for visible light absorption is restricted because IFCT only occurs at the  $\text{TiO}_2$  particle/nanocluster interfaces (Figure 1.4). Thus, in an inert atmosphere, the reduction of protons can not be realized with this method upon visible light illumination. As a promising technique, the photocatalytic performance of  $\text{TiO}_2$  in the photodegradation of gaseous 2-propanol under visible light irradiation was improved doping by Nb ions and surface grafting of Cu(II) clusters. [65] Merging doping and grafting significantly increased the separation and mobility of photogenerated charge carriers. Similarly,  $\text{Ti}^{3+}$  self-doped and Cu(II) grafted  $\text{TiO}_2$  nanoclusters demonstrated a higher quantum efficiency (10.8%) than only grafted Cu(II)/ $\text{TiO}_2$  under visible light irradiation in the photodegradation of gaseous 2-propanol. [66] Hashimoto et al. reported that Fe(III) ions grafted at the surface and doped in the bulk of  $\text{TiO}_2$  shows high efficiency for 2-propanol oxidation under visible-light irradiation due to energy-level matching of dopant and grafting ions. [67] However, it is well-known that bulk doping by metal ions originates impurity levels located in the forbidden band of  $\text{TiO}_2$ , which also act as recombination centers for the charge carriers. Coupling  $\text{TiO}_2$  with  $\text{WO}_3$ , which has smaller bandgap energy and grafting with Fe(III) ions result in better charge separation without introducing interband energy levels between the CB and the VB of the semiconductors. This composite has successfully degraded acetaldehyde and  $\text{NO}_x$  under visible light illumination. It has been reported that the  $\text{TiO}_2/\text{WO}_3$  heterojunction has increased the population of photogenerated charge carriers due to synergistic interaction, while the surface grafted Fe(III) ions participated in the multi-electron reduction process and suppressed the recombination of electron and hole pairs. [68]

#### 1.3.4. Dye sensitized $\text{TiO}_2$

Another effective method to activate  $\text{TiO}_2$  for visible light response is dye photosensitization. [69, 70] Many groups have extensively investigated dye-sensitized reactions following pioneer work of O'Regan and Grätzel in 1991 [12]. They have used dye-sensitized colloidal  $\text{TiO}_2$  semiconductor films as a solar cell material. This discovery opened a new perspective for photodegradation of water and air pollutants, energy application, and organic synthesis upon visible light illumination. It employs wide bandgap semiconductors such as  $\text{TiO}_2$  with high surface area and stability. [69] Dyes with appropriate spectral characteristics that emerged with  $\text{TiO}_2$  may

harvest incident solar energy flux up to 46%. Thus, upon illumination with visible light, a photogenerated electron from the highest occupied molecular orbital (HOMO) leaps to the lowest unoccupied molecular orbital (LUMO) of the engaged dye and ultimately migrates into the conduction band of the semiconductor. Therefore, the energetic position of the LUMO of the dye has to be higher (more negative) than that of the conduction band of the semiconductor. The CB of  $\text{TiO}_2$  acts as an electron mediator for transferring electrons from the dye sensitizer to the adsorbed substrates (active sites) on the  $\text{TiO}_2$  surface. Here the valence band of  $\text{TiO}_2$  does not participate in photocatalytic reactions and stays unchanged. In aerobic system, the photoinjected electrons are transferred from the CB to the surface of the  $\text{TiO}_2$  where they interact with surface adsorbed oxygen molecules resulting in the generation of superoxide radical anions ( $\text{O}_2^{\bullet-}$ ) and hydrogen peroxide radicals ( $\bullet\text{OOH}$ ) (Figure 1.5). [71] The reactive species could further be transformed into the hydroxyl radical and hydroxyl anion. [72]

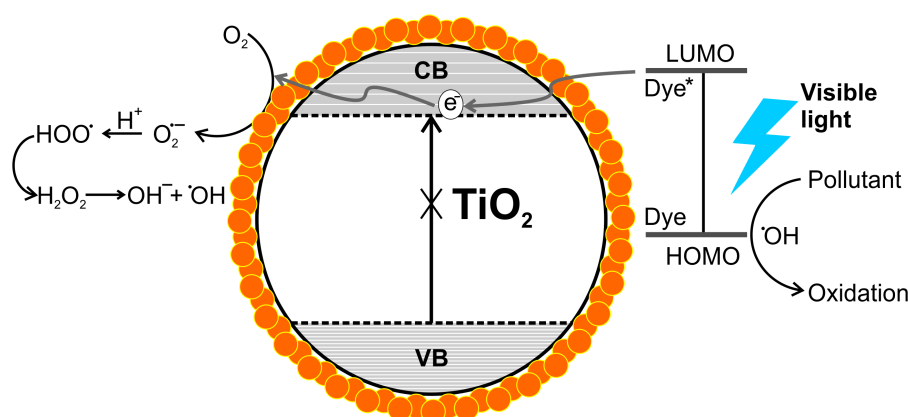


Figure 1.5.: Schematic illustration of dye-sensitized  $\text{TiO}_2$  photocatalysis.

Subsequent radical reactions might initiate the dye's degradation unless reductive species being present in the system regenerate the dye to the ground state. The nature of the dye sensitizer, the semiconductor, and its interface essentially affect the lifetime of the injected electrons. [73, 74]

## 1.4. Heterogeneous photocatalytic organic synthesis

Organic compounds that are consumed in our daily life cover the most substantial chemical manufacturing processes. Traditional synthesis methods usually exploit thermal energy, toxic solvents,



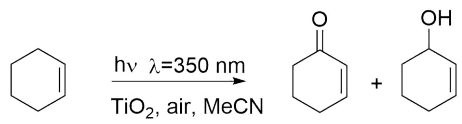
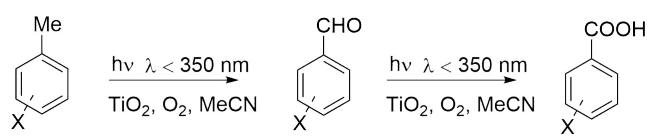
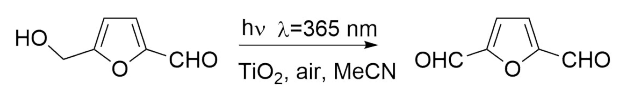
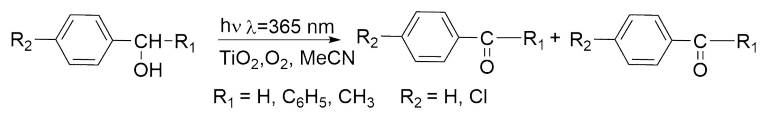
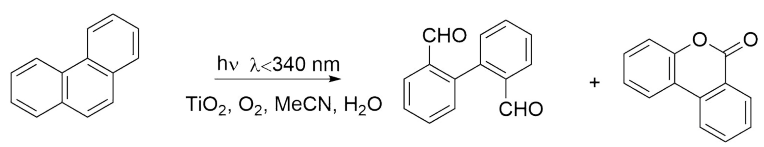
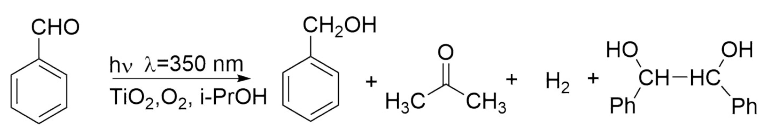
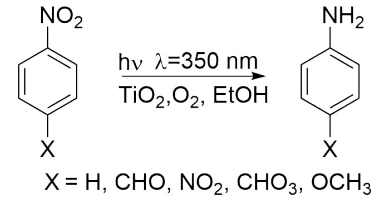
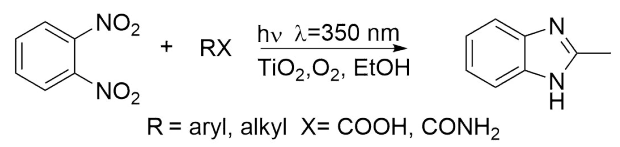
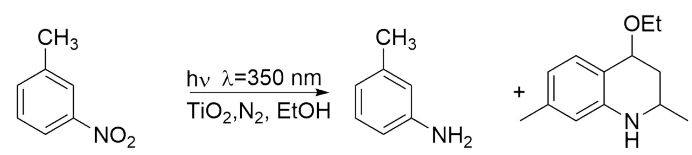
and corrosive additives. Also, the emergence of harmful by-products in thermal organic synthesis has created serious health and environmental problems. Therefore, designing and developing sustainable chemical processes to produce organic products that could replace conventional thermal synthesis procedures are highly desired. [75] Green synthesis procedures avoid the introduction of hazardous materials and go beyond, including atom-economy, recycling, and the use of renewable feed-stocks. From this perspective, the use of solar energy in chemical transformations of organic compounds could be an alternative approach for organic synthesis. [76, 77] The sun is one of the most potent and abundant sources of clean energy. Therefore, the direct use of light photons would shift the evident thermodynamic barrier in redox reactions at room temperature by preventing side effects that are thermally caused. Besides, light-mediated reactions provide access to structures that are difficult or unavailable to obtain in thermally induced organic synthesis. Organic photochemistry ideas were invigorated by the Italian chemist Giacomo Ciamician who started in 1886 to use solar light to perform organic reactions. [78] Extensive work on light-mediated organic transformations and new pathways to organic reactions have been developed, employing photosensitizers and photocatalysts. [79] The use of photosensitizers drives the photochemistry indirectly, where the photosensitizers absorb the light energy and transfer part of this energy to the reagent. Although photosensitizers mediate the desired photochemical process, they can also serve as a photoinitiator of undesired radical chain reactions. Similarly, in a photocatalytic reaction, a reagent is activated indirectly by electron transfer from or to the excited photocatalyst. Two types of photocatalysts are used in organic synthesis: homogeneous and heterogeneous.

### 1.4.1. $\text{TiO}_2$ as a heterogeneous photocatalyst in organic synthesis

Heterogeneous photocatalysis is particularly important because it facilitates the isolation of the catalyst after organic transformation. Because of their suitable electronic structure, semiconductors were extensively investigated in organic synthesis after 1974 with pioneer research performed by Teichner, Fox, Bard, and Reiche. [13, 80, 81]  $\text{TiO}_2$  is one of the most investigated metal oxide photocatalysts for this purpose. Due to its exceptional chemical and biological stability, non-toxicity, and abundance,  $\text{TiO}_2$  was used in energy, environmental, and sustainable synthetic applications. [82] Although UV-active  $\text{TiO}_2$  has been widely used for organic synthesis, i.e. ox-

oxidation reactions of alcohols [83], amines [84], cycloalkanes [85] and alkanes [80], reduction of nitrobenzenes [86–88] selectivity still remains the main issue of the overall system. [89, 90] Some examples of organic synthetic reactions over  $\text{TiO}_2$  photocatalyst upon UV light irradiation are summarized in Table 1.1. Restrictions, such as only ultraviolet (UV) light excitation and the formation of highly oxidizing holes during excitation, often prevent  $\text{TiO}_2$  from being widely used in selective organic synthesis. [19] Thus, the photogenerated holes in the valence band hole ( $h_{\nu b}$ ) induce radical reactions due to the formation of highly oxidizing reactive oxygen species in the presence of  $\text{O}_2$ . [91] Compared to UV light, visible light provides high chemoselectivity of organic reactions due to its lower energy. Additionally, it also facilitates the valuable photoreaction of organic compounds with weak UV-sensitive bonds. Since the solar energy reaching the surface of the earth contain only  $\sim 4.5\%$  ultraviolet light but  $\sim 45\%$  visible light, it allows photoreactions to be carried out effectively using daylight, thus avoiding the need for specialized UV photoreactors. [92] Nonetheless, most organic molecules only absorb UV light and cannot be activated by visible light. Therefore, visible-light-responsive photocatalysts are often required to initiate organic transformations. On visible light photocatalysis, the reactivity of the intermediates could be predicted due to the tolerance of the functional groups to the reaction conditions compared to those required for direct UV photo-excitation. Thus, the application of these reactions to the synthesis of a wide range of complex target molecules can be facilitated. In recent years, there has been an increasing interest in the design of photoredox systems in synthetic photochemistry, which are also capable of converting visible light energy into synthetically available chemical energy. Nearly all the latest research was devoted to developing visible light active photoredox catalysts that activate a variety of organic compounds through single-electron oxidation or reduction. This feature has increased photochemical reactions' accessibility by using visible-light-sensitive organometallic complexes or organic dyes in a significant workhorse. The advancement is driven primarily by the development of many sophisticated tools and a deep understanding of how ligands can be designed to adapt the properties of metals to specific organic reactions. [92] Nevertheless, some of these catalysts are difficult to synthesize or contain complex, expensive ligands and metals. In addition, the commonly observed drawbacks of these catalysts are difficult separation and limited recyclability.

Table 1.1.: Examples of photocatalytic organic reactions in the presence of UV-active TiO<sub>2</sub>

	<b>References</b>
<b><u>Oxidation reactions</u></b>	
 <p style="text-align: center;"> <chem>C1=CCCCC1</chem> <math>\xrightarrow[\text{TiO}_2, \text{air, MeCN}]{h\nu \lambda=350 \text{ nm}}</math> <chem>O=C1C=CCCC1</chem> + <chem>OC1=CCCCC1</chem> </p>	Fox, 1983 [81]
 <p style="text-align: center;"> <chem>Cc1ccc(X)cc1C=O</chem> <math>\xrightarrow[\text{TiO}_2, \text{O}_2, \text{MeCN}]{h\nu \lambda &lt; 350 \text{ nm}}</math> <chem>Cc1ccc(X)cc1C=O</chem> <math>\xrightarrow[\text{TiO}_2, \text{O}_2, \text{MeCN}]{h\nu \lambda &lt; 350 \text{ nm}}</math> <chem>Cc1ccc(X)cc1C(=O)O</chem> </p>	Worsley, 1995 [93]
 <p style="text-align: center;"> <chem>OCC1=CC(=O)C=C1C=O</chem> <math>\xrightarrow[\text{TiO}_2, \text{air, MeCN}]{h\nu \lambda=365 \text{ nm}}</math> <chem>OCC1=CC(=O)C=C1C=O</chem> </p>	Yurdakal, 2013 [94]
 <p style="text-align: center;"> <chem>R2-C6H4-CH(OH)-R1</chem> <math>\xrightarrow[\text{TiO}_2, \text{O}_2, \text{MeCN}]{h\nu \lambda=365 \text{ nm}}</math> <chem>R2-C6H4-C(=O)-R1</chem> + <chem>R2-C6H4-C(=O)-R1</chem> </p> <p style="text-align: center;">R<sub>1</sub> = H, C<sub>6</sub>H<sub>5</sub>, CH<sub>3</sub>    R<sub>2</sub> = H, Cl</p>	Abdel-Wahab, 2001 [95]
 <p style="text-align: center;"> <chem>C1=CC=C2C=CC=CC2=C1</chem> <math>\xrightarrow[\text{TiO}_2, \text{O}_2, \text{MeCN, H}_2\text{O}]{h\nu \lambda &lt; 340 \text{ nm}}</math> <chem>O=C1C=CC2=CC=CC2=C1</chem> + <chem>O=C1C=CC2=CC=CC2=C1</chem> </p>	Michio, 2006 [96]
<b><u>Reduction reactions</u></b>	
 <p style="text-align: center;"> <chem>c1ccccc1C=O</chem> <math>\xrightarrow[\text{TiO}_2, \text{O}_2, \text{i-PrOH}]{h\nu \lambda=350 \text{ nm}}</math> <chem>c1ccccc1CO</chem> + <chem>CC(=O)C</chem> + H<sub>2</sub> + <chem>OC(Ph)C(Ph)O</chem> </p>	Li, 1992 [97]
 <p style="text-align: center;"> <chem>O=C1C=CC(=CC=C1)[N+](=O)[O-]</chem> <math>\xrightarrow[\text{TiO}_2, \text{O}_2, \text{EtOH}]{h\nu \lambda=350 \text{ nm}}</math> <chem>O=C1C=CC(=CC=C1)N</chem> </p> <p style="text-align: center;">X = H, CHO, NO<sub>2</sub>, CHO<sub>3</sub>, OCH<sub>3</sub></p>	Li, 1993 [86]
 <p style="text-align: center;"> <chem>O=C1C=CC(=CC=C1)[N+](=O)[O-]</chem> + RX       <math>\xrightarrow[\text{TiO}_2, \text{O}_2, \text{EtOH}]{h\nu \lambda=350 \text{ nm}}</math> <chem>C1=CC=C2N=C(N1)C=C2</chem> </p> <p style="text-align: center;">R = aryl, alkyl    X = COOH, CONH<sub>2</sub></p>	Li, 1997 [98]
 <p style="text-align: center;"> <chem>Cc1ccc([N+](=O)[O-])cc1C=O</chem> <math>\xrightarrow[\text{TiO}_2, \text{N}_2, \text{EtOH}]{h\nu \lambda=350 \text{ nm}}</math> <chem>Cc1ccc(N)cc1C=O</chem> + <chem>CCOC1=CC=CC=C1NCC1</chem> </p>	Park, 1995 [99]

### 1.4.2. Visible-light-mediated organic synthesis with sensitized TiO<sub>2</sub>

The inherent drawbacks of UV-light active heterogeneous photocatalysts could be surmounted by coordinating them with several organic catalysts (dyes). For example, the addition of an enantioselective organocatalyst can facilitate inaccessible enantioselective reactions. [100] Zhao et al. have proposed selective aerobic alcohol oxidation under visible-light illumination in a system containing dye-sensitized TiO<sub>2</sub> and TEMPO. [101] The proposed ongoing reaction mechanism is shown in Figure 1.6, where the anthraquinone dye Alizarin Red is used as a sensitizer and TEMPO as a cocatalyst. Due to the electron-transfer cycle of TEMPO (TEMPO → TEMPO<sup>+</sup> → TEMPOH → TEMPO), the dye is regenerated after excitation and electron injection into the conduction band of TiO<sub>2</sub>.

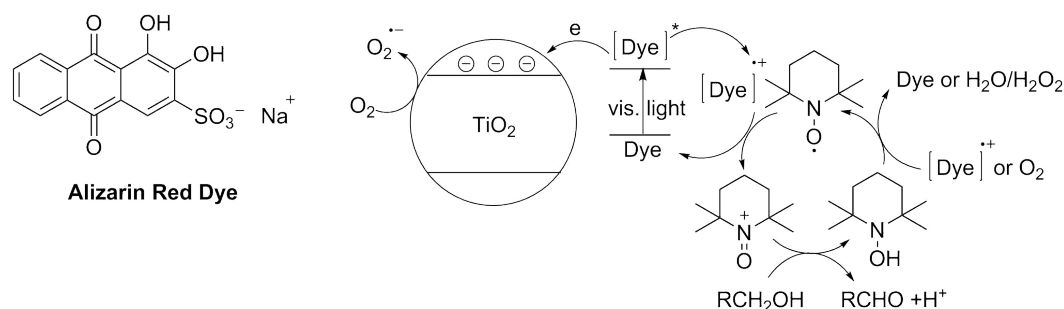


Figure 1.6.: The proposed mechanism of visible-light-induced photocatalytic alcohol oxidation system in the presence of dye/TiO<sub>2</sub> /TEMPO. [101]

Several research groups have extensively studied dye-sensitized TiO<sub>2</sub> for organic synthesis, hydrogen generation, and environmental applications. Grätzel and Houding accounted for the visible light sensitization of TiO<sub>2</sub> particles by surface complexation with 8-hydroxyquinoline for hydrogen generation. [102] However, it should be noted that, for dye sensitization, the dye should possess a broad range of absorption in the visible region. The LUMO (lowest unoccupied molecular orbital) energy potential of dye must be more negative than the CB of the semiconductor, and the HOMO (highest occupied molecular orbital level) positioning energy level must be more positive than the redox potential of sacrificial electron donor. Contrary to the dye sensitization, a simplified yet more practical approach was found to be a ligand-to-metal charge transfer (LMCT), which has been less investigated than the dye sensitization technique. With this sensitization technique, electron-rich organic compounds (sometimes inorganic compounds as well) adsorbed on

a semiconductor surface form visible-light-responsive surface complexes (Figure 1.7). Unlike the dye molecule, these adsorbates do not absorb visible light alone, and the excited state (LUMO) is not involved in the chemical reaction. Upon visible light excitation of this complex, electrons are injected from the ground (HOMO) level of the adsorbed molecule directly into the CB of the semiconductor. A suitable electron acceptor on the semiconductor's surface is required for better charge separation and, eventually, photocatalytic conversion of the adsorbate. This method has been used in many applications, such as the degradation of several pollutants and the production of molecular hydrogen in the presence of suitable redox mediators to regenerate the surface adsorbed molecule to maintain visible light activity. When a redox mediator is not provided, self-conversion or self-degradation of the adsorbate occurs upon visible light illumination until the surface complex has vanished.

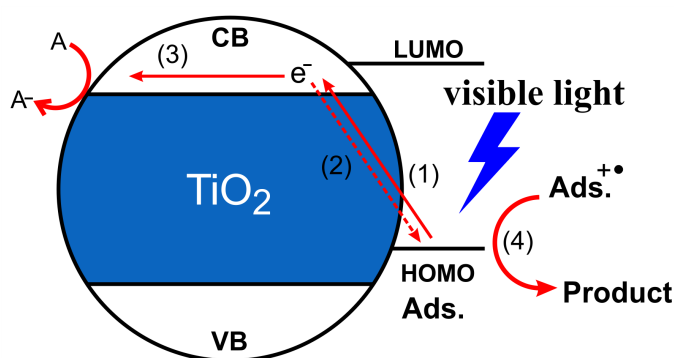


Figure 1.7.: Schematic illustration of visible-light-mediated LMCT mechanism. Adsorbate-TiO<sub>2</sub> surface complex. (1) visible light-induced LMCT, (2) recombination, (3) electron transfer to the acceptor, (4) adsorbate oxidation in the absence of donor.

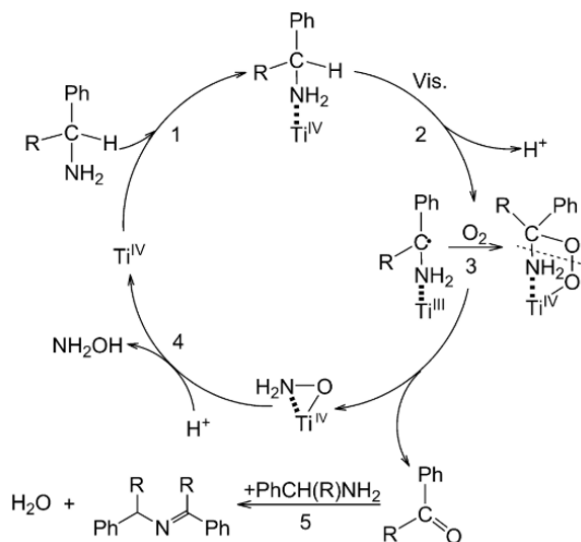
Choi et al. have investigated this technique, where TiO<sub>2</sub> interacted with colorless molecules such as methanol, formic acid, acetic acid, triethanolamine, and ethylenediaminetetraacetic acid (EDTA). [103] They observed that EDTA and TiO<sub>2</sub> form a visible-light-responsive complex through an LMCT mechanism. Ohtani et al. also developed a new methodology to oxidize triethanolamine under visible-light irradiation by a binaphthol-titanium (IV) oxide surface complex in aqueous media. [104] The oxidation of trans-ferulic acid (C<sub>10</sub>H<sub>10</sub>O<sub>4</sub>) was reported to occur in TiO<sub>2</sub> suspension in water due to the formation a charge-transfer complex on the TiO<sub>2</sub> surface that was able to absorb visible light ( $\lambda \geq 400$  nm). [105] Moreover, visible-light mediated oxidation of primary and secondary amines into the corresponding imines employing visible-light absorb-

ing surface complexes of different organic molecules such as phenol [106], catechol [107], N-hydroxyphthalimide [108], and salicylic acid [109] on TiO<sub>2</sub> in the presence of TEMPO derivatives was reported by Lang and his group. Selective oxidation of sulfides by assembling polydopamine on TiO<sub>2</sub> surface was achieved due to an amine-TiO<sub>2</sub> surface complexation. [110] Zhao and Chen applied this approach to develop several photocatalytic aerobic oxidation methods such as oxidation of amines to imines and sulfides to sulfoxides using visible light [111, 112] Certainly, visible-light-sensitization of TiO<sub>2</sub> propose suitable access to the reactivity of organic compounds in electronically excited states by using photons of much lower energy than those required for direct photoexcitation. [92]

### 1.4.3. Surface complexation of amines with semiconducting photocatalysts

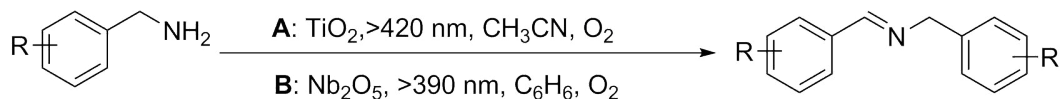
Typically, separate components in the reaction system, such as semiconductor metal oxide and nitrogen-containing substrates, are unable to directly absorb visible light. However, surface adsorbed organic substrates containing heteroatoms (X = S, N, or O) being adsorbed onto the surface of metal oxides such as TiO<sub>2</sub>, Nb<sub>2</sub>O<sub>5</sub>, and ZnO generate weak surface complexation. Visible-light mediated tertiary amine oxidation was reported by Lang et al. on bare TiO<sub>2</sub> under visible light illumination due to Lewis acid-base interaction. [100, 113] Upon visible light illumination, the electron-rich nitrogen atom quickly injects its lone pair electron into the semiconductor's conduction band. Subsequently, this electron is transferred to a surface adsorbed oxygen molecule or another electron acceptor. The positive charge (h<sup>+</sup>) localized at the nitrogen atom can induce the activation of the adjacent C-H bond and its subsequent functionalization by O<sub>2</sub> or nucleophiles. [114] This organic transformation is significantly crucial since amines are essential components for the synthesis of bioactive compounds. The use of O<sub>2</sub> as the terminal oxidant in visible-light-induced reactions does not deteriorate the reaction's selectivity compared to UV-light-induced reactions. Zhao et al. reported the selective oxidation of a series of benzylic amines into their corresponding imines by molecular oxygen on a surface of anatase TiO<sub>2</sub> under visible-light irradiation in CH<sub>3</sub>CN ( $\lambda > 420$  nm) (Scheme 1.1). It was observed that upon adsorption of tertiary amines on the surface of TiO<sub>2</sub>, a visible-light-harvesting surface complex is formed, resulting in a red-shift of the absorption spectrum by about 10 nm. The same reaction was carried out in the water, and it was found that water is a more selective solvent than acetonitrile. [115]

A high surface area of the semiconductor was reported to be beneficial while it presents more coordination sites for amines.



Scheme 1.1: Proposed mechanism for the formation of imines by the oxidation of amines on a  $\text{TiO}_2$  surface under visible-light irradiation. Adapted from Ref. [115]

Selective amine oxidation over various metal oxides ( $\text{TiO}_2$ ,  $\text{ZnO}$ ,  $\text{Nb}_2\text{O}_5$ ,  $\text{MoO}_3$ ,  $\text{CeO}_2$ ,  $\text{Ta}_2\text{O}_5$ ,  $\text{ZrO}_2$ ,  $\text{WO}_3$ ,  $\text{V}_2\text{O}_5$ ) upon UV light illumination was also reported by Tanaka et al., who showed that higher selectivity and yield of oxidation of benzylidene benzylamine was obtained on a  $\text{Nb}_2\text{O}_5$  surface. [116] A 390 nm cutoff filter was employed to test the visible light performance of  $\text{Nb}_2\text{O}_5$  in aerobic amine oxidation. Even though the obtained yield was relatively low, the selectivity was significantly higher than using  $\text{TiO}_2$  (Scheme 1.2). [114]



A:  $\text{R}=\text{H}$ ,  $p\text{CH}_3$ ,  $p\text{-tBu}$ ,  $p\text{CH}_3\text{O}$ ,  $p\text{F}$ ,  $p\text{Cl}$ , conv.=78-95%, select.= 88-94%

B:  $\text{R}=\text{H}$ ,  $p\text{CH}_3$ ,  $p\text{-tBu}$ ,  $p\text{CH}_3\text{O}$ ,  $p\text{CF}_3$ ,  $m\text{CH}_3\text{O}$ ,  $o\text{CH}_3\text{O}$ , conv.=12-30%, select.= 94-97%

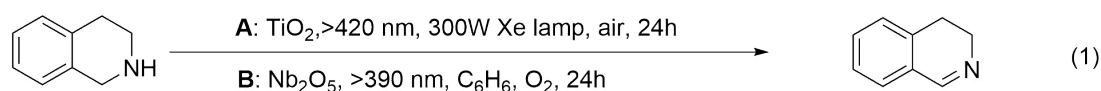
Scheme 1.2: Proposed mechanism for the formation of imines by the oxidation of amines on a  $\text{TiO}_2$  surface under visible-light irradiation.

## 1.5. Dehydrogenation of N-heterocyclic amines

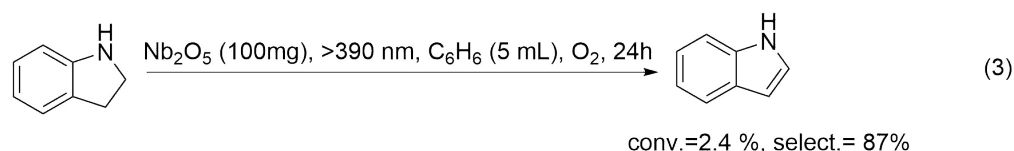
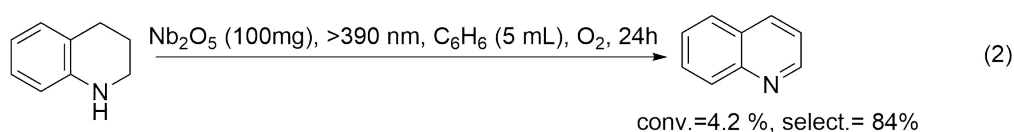
Depending on whether a hydrogen acceptor is used in the dehydrogenation, it can be grouped into two subclasses: acceptor-assisted or oxidative and acceptorless or anaerobic dehydrogenation.

### 1.5.1. Oxidative dehydrogenation of N-heterocyclic amines

For the acceptor-assisted dehydrogenation, various classical oxidants such as 2,3-dichloro-5,6-dicyano-1,4-benzoquinone (DDQ) [117], chloranil [118], sulfur, and selenium [119] have been used in stoichiometric amounts as the hydrogen acceptor. Thermal catalysts have also reported in acceptor-assisted dehydrogenation reactions of N-heterocycles mostly using air or oxygen as the stoichiometric oxidant. Copper-based [120,121] and oxyvanadium-based systems [122] have recently been reported to catalyze the acceptor dehydrogenation. The heterogeneous counterpart has also been considerably developed, and quite diverse catalysts such as Co@N-doped graphene shells [123],  $\text{Co}_3\text{O}_4$ -NGr/C [124],  $\text{FeO}_x$ @NGr-C [125], nanoparticles (Pd, Pt, Rh) stabilized by  $\text{G}_4\text{OH}$  PAMAM dendrimers in SBA-15 [126], AuNPs/C [127], Au nanoclusters [128],  $\text{Ru}(\text{bpy})_3$  adsorbed on  $\text{Al}_2\text{O}_3$  [129], Rh nanoparticles on carbon nanotube [130] and polymaleimide [131] have been reported.



A: amine (0.1 mmol), 100 mg  $\text{TiO}_2$ , 5 mL  $\text{CH}_3\text{CN}$  conv.=100%, select.= 68%  
 B: amine (5 mmol), 100 mg  $\text{Nb}_2\text{O}_5$ , 5 mL  $\text{C}_6\text{H}_6$ , conv.=47%, select.= 85%



Scheme 1.3: Aerobic dehydrogenation of 1,2,3,4-tetrahydroisoquinoline (1), 1,2,3,4-tetrahydroquinoline (2), and indoline (3) over  $\text{TiO}_2$  and  $\text{Nb}_2\text{O}_5$  photocatalysts under visible light illumination. [113, 116]



Unlike the approaches mentioned above, visible-light-harvesting photocatalytic aerobic dehydrogenation reactions have been successfully performed under milder reaction conditions. Visible light-mediated oxidative dehydrogenation of N-heterocycles at ambient temperature was reported using  $\text{Ru}(\text{bpy})_3\text{Cl}_2 \cdot 6\text{H}_2\text{O}$  metal-organic complex. [132] Moreover, dual catalyst systems employing the Fukuzumi acridinium salt with  $\text{Pd}(\text{BF}_4)_2$  photocatalysts have recently been reported by Kanai et al. [133] Later, rose Bengal has been used to replace organometallic complexes for the dehydrogenation of N-heteroarenes. [134]

Oxidative dehydrogenation of N-heterocyclic amines was also investigated employing  $\text{TiO}_2$  [113] and  $\text{Nb}_2\text{O}_5$  [116] upon visible light illumination. Two different groups reported the partial dehydrogenation of 1,2,3,4-tetrahydroisoquinoline yielding 3,4-dihydroisoquinoline on  $\text{TiO}_2$  and  $\text{Nb}_2\text{O}_5$ . Similar to benzylic amine oxidation, high selectivity, but less yield was obtained while using  $\text{Nb}_2\text{O}_5$  instead of  $\text{TiO}_2$  (Scheme 1.3). However,  $\text{Nb}_2\text{O}_5$  was reported to be almost inactive for the oxidative dehydrogenation of 1,2,3,4-tetrahydroquinoline (Scheme 1.3, (2)) and indoline (Scheme 1.3, (3)). These substrates are chemically important due to their flexibility in merging new C–C bonds with suitable nucleophiles.

### 1.5.2. Acceptorless dehydrogenation of N-heterocyclic amines

Although molecular oxygen is a much greener acceptor than the traditionally used stoichiometric oxidants such as DDQ and sulfur, highly reactive oxygen species such as the superoxide radical ( $\text{O}_2^{\cdot-}$ ), hydroxyl radical ( $\cdot\text{OH}$ ), and hydrogen peroxide are usually produced in the former method. These species often result in over-oxidation of the product, causing poor selectivity and low yield. Therefore, these catalytic systems show less functional group tolerance attached to the heterocyclic amine. In contrast, an anaerobic or acceptorless dehydrogenation (ADH) method provides a more compelling and environmentally friendly alternative for N-heterocyclic amine synthesis. Although the presence of the nitrogen atom reduces the endothermicity, the release of hydrogen molecules provides a large positive entropic change and thus further reduces the endothermicity. [135] Moreover since the liberation of hydrogen molecules as the sole byproduct enables saturated N-heterocycles to function as potential hydrogen-storage materials, this aspect enhances the appeal of developing the acceptorless dehydrogenation of saturated N-heterocycles. The first homogeneous catalyst system developed by Fujita et al. for the ADH of saturated N-

heterocycles was an iridium complex containing a pyridonate ligand. [136] Subsequently, several homogeneous catalysts such as ruthenium-hydride complexes [137], osmium [138], iridium [139–143], cobalt [144], iron [135], and nickel [145, 146] organo-complexes were reported for the acceptorless dehydrogenation of N-heterocycles by several research groups. The transition metal complex could be substituted by a base, K<sup>+</sup>OtBu [147], or a strong Lewis acid such as B(C<sub>6</sub>F<sub>5</sub>)<sub>3</sub> [148] that formed a frustrated Lewis pair with saturated N-heterocycles. Regardless of the important progress made, most of the reported ADH reactions in homogeneous catalytic processes required high temperature (above 110 °C), base/acid, or a toxic solvent such as trifluoroethanol. TEMPO-mediated electrolysis enabled the acceptorless dehydrogenation to be performed at ambient temperature in an undivided electrochemical cell where dehydrogenation of N-heterocycles occurred at the anode with the release of H<sub>2</sub> at the cathode. [149]

However, the complexities in recyclability of the homogenous catalysts remain as the main concern. Therefore, heterogeneous catalysts were developed to improve the recyclability of the catalyst. Diverse types of catalysts, which were typically composed of transition metals on solid supports, were reported. Some notable and recent examples include Pd-doped hydrotalcites [150], single cobalt atoms on an ordered porous nitrogen-doped carbon matrix [151], cobalt phenanthroline complex on exfoliated graphene oxide [152] and core-shell iron on exfoliated graphitic oxide. [153] Like the homogenous alternatives, the reactions employing these heterogeneous catalysts are usually performed at 110 °C or above.

Using visible-light enables both homogeneous and heterogeneous catalytic ADH of N-heterocycles at room temperature in an economical and environmentally friendly way. A homogeneous photocatalytic ADH process is usually realized with dual catalysis merging photoredox catalysis with transition metal catalysis. Y. Li et al. reported the first ADH of cyclic amines at ambient temperature by using a homogeneous ruthenium complex (Ru(bpy)<sub>3</sub>Cl<sub>2</sub>·6H<sub>2</sub>O) and Co(dmgh)<sub>2</sub>PyCl photocatalysts in ethanol (EtOH). [154] Furthermore, the same dual catalysis system was adopted for the acceptorless dehydrogenative coupling reaction of saturated N-heterocycles. [155] Modification of the Co complex allowed the ADH of N-heterocycles to be performed in water. [156] Kanai et al. developed a different dual catalyst system composed of an acridinium photoredox catalyst and a palladium catalyst to catalyze the ADH of N-heterocycles. [157] Most recently, a single catalyst system such as a binuclear platinum(II) diphosphite complex [158] and a supramolecu-

lar assembly consisting of a carbazolyl dicyanobenzene fluorophore with four cobaloximes was reported for the ADH of N-heterocycles. [159] Although these reported methods were performed at ambient temperature with the assistance of blue LED light, the recyclability of these photocatalysts is still challenging. Recently, ADH of tetrahydroquinolines has been reported using visible-light-responsive hexagonal boron carbon nitride as a recyclable heterogeneous photocatalyst. [160] A MoS<sub>2</sub>/ZnIn<sub>2</sub>S<sub>4</sub> nanocomposite has also been tested for the acceptorless semidehydrogenation of 1,2,3,4-tetrahydroisoquinoline. [161] However, the latter system was demonstrated to be effective only for partial dehydrogenation of 1,2,3,4-tetrahydroisoquinoline to 3,4-dihydroisoquinoline.

## 1.6. Objectives

N-heteroarenes are considered as a privileged structure in medicinal chemistry and materials science. [162,163] Therefore, the development of innovative methods and improvement of existing ones for N-heteroarene synthesis have become an essential topic in contemporary organic synthesis. [164,165] Compared to the commonly used cross-coupling strategy that relies on the availability of the pre-functionalized heteroarene precursors, dehydrogenation of N-heterocycles has provided a complementary approach that can introduce substituents to the saturated N-heterocycle core. This feature overcomes the precursor's constraint in the former procedure and thus permits the synthesis of substituted N-heteroarenes that are not accessible by the cross-coupling reaction. The primary objective of this study is to promote the development of surface properties of TiO<sub>2</sub> based on semiconductor materials for synthetic applications of N-heterocyclic imines instead of using organometallic complexes.

It was known:

(1) Amines interact with TiO<sub>2</sub> resulting in a shift of the absorbance to the visible region of the solar spectrum (Section 1.4.3)

(2) The excitation of this surface complex results in an electron injection into the CB of the TiO<sub>2</sub> (Section 1.4.3)

(3) These CB electrons are capable of reducing the O<sub>2</sub> yielding O<sub>2</sub><sup>•-</sup> which is known to be involved in the dehydrogenation of N-heterocyclic amines (section 1.5.1)

(4) The aerobic oxidation of amines is accelerated by the presence of TEMPO (section 1.4.2)

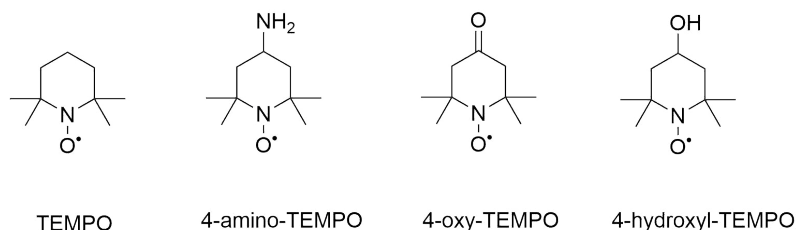
(5) Conduction band electrons can reduce  $H^+$  when suitable cocatalysts are present on the  $TiO_2$  surface (section 1.3.2)

Based on these known facts, the task of the present work was to develop a selective dehydrogenation of N-heterocyclic amines such as tetrahydroquinolines, tetrahydroisoquinolines, indolines, and other N-heterocyclic amines.

Although, visible-light mediated oxidative dehydrogenation of aliphatic or benzylic amines was studied intensively over  $TiO_2$  photocatalyst, dehydrogenation of N-heterocyclic amines over  $TiO_2$  in aerobic condition was not studied in-depth apart from only one example shown in Scheme 1.3 (Section 1.5.1). Furthermore, for the first time in this work, the acceptorless or oxidant-free dehydrogenation of N-heterocycles over noble metal photodeposited  $TiO_2$  nanoparticles under visible light illumination was studied.

The first part of this project comprises the development of selective oxidative dehydrogenation (ODH) method for N-heterocycles over  $TiO_2$  photocatalysts under visible light illumination. For this purpose, commercially available  $TiO_2$  Hombikat UV100 from Venator with large surface area ( $320\text{ m}^2/\text{g}$ , 100% anatase) was employed as a photocatalyst.

Transition metals ions were grafted on the  $TiO_2$  surface to improve the photocatalytic activity of  $TiO_2$  in ODH of N-heterocycles. Additionally, different derivatives of TEMPO (2,2,6,6-tetramethylpiperidinyloxy) (Scheme 1.4) have been employed to improve chemoselectivity. Thus, in the first part of the project, three important components are combined, i.e., an N-heterocycle- $TiO_2$  surface complex as the visible light-absorbing species, Ni(II) ion-grafted  $TiO_2$ , and TEMPO as a redox mediator to perform selective visible-light-mediated dehydrogenation of N-heterocycles.



Scheme 1.4: Different derivatives of TEMPO (2,2,6,6-tetramethylpiperidinyloxy) employed in this study.

The main objectives of the first part of the project are as follows:

- (1) Oxidative dehydrogenation of the broad range cyclic amines such as tetrahydroquinolines,

tetrahydroisoquinolines, and indolines other N-heterocycles in the presence of surface-grafted TiO<sub>2</sub> upon visible light illumination at ambient temperature.

(2) Optimization of the reaction condition by investigating additional parameters such as the solvent effect, TEMPO's role, and the effect of the various co-catalysts.

(3) Understanding the effect of the changed reaction parameters on the reaction mechanism.

The second part of this project dealt with the development of a selective acceptorless dehydrogenation (ADH) method for N-heterocycles over TiO<sub>2</sub> photocatalysts under visible light illumination. The possibility of oxidant-free or ADH of tetrahydroquinolines, tetrahydroisoquinolines, indolines, and several other N-heterocycles using noble metal nanoparticles photodeposited TiO<sub>2</sub> was envisaged inspired by the developed visible-light-mediated oxidative dehydrogenation method in the first part of the project.

Since in an inert atmosphere the transfer of an electron to H<sup>+</sup> (releasing from amine cation radical) could be realized only in the presence of a co-catalyst such as a noble metal the surface of TiO<sub>2</sub> was modified with Pt, Pd, Rh, RuO<sub>2</sub> and Au nanoparticles. Thus, two separate strategies have been combined for achieving ADH of N-heterocycles, by employing noble metal nanoparticles photo-deposited on TiO<sub>2</sub> to retard the charge carrier recombination while facilitating H<sub>2</sub> generation and an N-heterocyclic amine-TiO<sub>2</sub> surface complex for visible-light activation. With this methodology, the high chemoselectivity of the overall system could be achieved using a single photocatalyst in an inert atmosphere due to avoiding the formation of reactive oxygen species. Moreover, since TiO<sub>2</sub> not responding to visible light, no strongly oxidizing holes are created in the valence band, which are the main species that react with intermediate products. The main objectives of the second part of the project are as follows:

(1) Development of an acceptorless dehydrogenation methodology for the range of tetrahydroquinolines, tetrahydroisoquinolines, and indolines imidazolines on the surface-photodeposited TiO<sub>2</sub> upon visible light illumination at ambient temperature.

(2) Optimization of the reaction condition by changing different parameters, such as solvents, co-catalysts, and loading content, and the amount of catalyst in the reaction system.

(3) Understanding the ongoing reaction mechanisms influenced by different reactants.



# Chapter 2

## Materials and experimental methods

### 2.1. Materials and Chemicals

Commercial Evonik Aeroxide TiO<sub>2</sub> P25 powder with 20% rutile and 80% anatase crystal phase and 50 m<sup>2</sup>/g specific surface area and TiO<sub>2</sub> Hombikat UV 100 with 100% anatase crystal phase and ~ 320 m<sup>2</sup>/g specific surface areas were kindly provided by Evonik and Venator, respectively. All other reagents for the organic synthesis were purchased from Combi-Blocks and Sigma-Aldrich (the list of compounds are given in Appendix, Table A.1). All chemicals had a purity ≥96%. The other employed metal-oxide powders namely ZnO, WO<sub>3</sub>, SiO<sub>2</sub>, Al<sub>2</sub>O<sub>3</sub> were purchased from Sigma-Aldrich. The employed solvents, i.e., methanol, ethanol, 2-propanol, acetonitrile, hexanes, ethyl acetate, all with a purity >99.9%, were purchased from Carl-Roth. Metal salts, i.e., nickel(II) nitrate hexahydrate Ni(NO<sub>3</sub>)<sub>2</sub>·6H<sub>2</sub>O, copper(II) chloride dihydrate CuCl<sub>2</sub>·2H<sub>2</sub>O, iron(III) chloride hexahydrate FeCl<sub>3</sub>·6H<sub>2</sub>O, cobalt(II) chloride hexahydrate CoCl<sub>2</sub>·6H<sub>2</sub>O, niobium(V) chloride NbCl<sub>5</sub>, chloroplatinic acid H<sub>2</sub>PtCl<sub>6</sub>·6H<sub>2</sub>O, palladium (II) acetate Pd(OAc)<sub>2</sub>, and rhodium-acetate dimer Rh<sub>2</sub>(OAc)<sub>4</sub> were purchased from Sigma-Aldrich and used without further purification. The deionized water (18.2 MΩ cm) was obtained from a Sartorius Arium 611 apparatus.

## 2.2. Modification of the surface of TiO<sub>2</sub>

### 2.2.1. Impregnation method

The grafting of Fe(III), Cu(II), Ni(II), Co(II), or Nb(V) nanoclusters on the surface of TiO<sub>2</sub> UV100 was performed by following a simple impregnation method that has been reported before. [166] In brief, salts with the appropriate ratio (0.1 wt %) relative to titania were added into an aqueous TiO<sub>2</sub> suspension and stirred at 90 °C for one h to attain metal ion nanoclusters on the surface of TiO<sub>2</sub>. Subsequently, the suspension was rinsed and centrifuged three times with copious amounts of distilled water. Afterward, the solid was dried at 110 °C for 24 h and ground into a fine powder using agate mortar and pestle.

### 2.2.2. Photodeposition method

The salts of noble metals with the appropriate amount (0.1-5 wt.%) of metals with respect to the amount of TiO<sub>2</sub> were dissolved in 30 mL of a mixture of 30 vol.% methanol and deionized water. Additionally, 3 g of the commercially available Hombikat TiO<sub>2</sub> UV100 (Venator) with 100% anatase crystal phase and ~320 m<sup>2</sup>/g specific surface area was added to the solution inside the photoreactor. Subsequently, the photoreactor (50 mL) was tightly closed, purged with Ar for 20 min, and irradiated by UV-A light with the intensity of 1 mW/cm<sup>2</sup> with vigorously stirring for 24 h. In the next step, the obtained suspension was rinsed three times with deionized water in conical bottom plastic vials and centrifuged each time to eliminate irrelevant ions from the surface. Finally, the obtained residue was dried in a muffle oven at 110°C and ground to a fine powder properly.

## 2.3. Characterization techniques of the prepared materials

### 2.3.1. X-ray powder diffraction analysis (XRD)

The X-ray powder diffractograms of powder catalysts were obtained by the Burker D8-advance X-ray diffractometer (Operating current: 40 mA, Operating Voltage: 40 kV) with Cu-K $\alpha$  radiation ( $\lambda_{max}$  = 0.15406 nm) at room temperature in a scanning  $2\theta$  over the angular range of 10° –



80° with a step size of 0.05°. The diffraction data were analyzed using TOPAS 4.2 (Bruker-AXS) software by comparison with reference patterns in the database.

### **2.3.2. ICP-OES measurement**

The content of metal ions grafted or photodeposited onto the TiO<sub>2</sub> surface before and after photocatalytic reactions was determined by using a Varian 715-ES from VARIAN optical emission spectrometer equipped with a radial inductively coupled plasma as the excitation source and a VistaChip CCD simultaneous detector with echelle grating. The samples were digested in aqua regia (1 : 3 v/v nitric and hydrochloric acid) at 150 °C for three hours before measurement. Elemental analysis was carried out in 3% HNO<sub>3</sub> aqueous solutions as well as by coupling to a femtosecond laser.

### **2.3.3. Transmission electron microscopy (TEM)**

The photocatalysts' morphology was measured using transmission electron microscopy (TEM), employing a Tecnai G2 F20 TMP from FEI at 200 kV field-effect FEG. The samples were sonicated in ethanol for 15 min before the TEM analysis. The alcoholic solution was dropped on a 300 mesh carbon-coated copper TEM grid, purchased from Quantifoil, and the images were taken in a bright field mode.

### **2.3.4. Specific surface area measurements**

A single-point FlowSorb II 2300 instrument (Micromeritics AutoMate 23, USA) has been employed to determine the BET (Brunauer-Emmett-Teller) surface area of the catalysts. A gas mixture consisting of 30% N<sub>2</sub> and 70% He was employed for the adsorption - desorption measurement. Before all measurements, powders were degassed for 40 min by heating at 150 °C in order to remove the surface adsorbed water molecules. The measurement was carried out at liquid nitrogen temperature (77 K). The mesoporosity of the samples before and after the photocatalytic experiments has been determined employing a Quantachrome Autosorb-3 instrument at liquid nitrogen temperature (77 K). The samples were degassed under vacuum at 80 °C for 24 h prior to measurement. The specific surface area was obtained by applying the Brunauer-Emmett-Teller (BET) method. Barrett-Joyner-Halenda (BJH) equation was used for the calculation of the pore

size distribution. The total pore volume was estimated using the single point method at  $p/p_0 = 0.99$ .

### 2.3.5. UV–visible spectroscopy

The diffuse reflectance spectra of the powder samples were measured using a UV - vis photospectrometer (Varian Spectrophotometer Cary-100 Bio from Agilent) in the wavelength range from 200 - 800 nm. The employed powders were pressed in a Teflon holder before measurement. Anhydrous barium sulfate was used as the white standard for the background. The Kubelka-Munk function of powders was calculated by applying  $F(R)=(1-R)^2/2R$ . Employing a UV - vis photospectrometer (Agilent Technologies, Cary 100), the absorption spectra of the suspensions were also measured. For this purpose, the same concentration of the suspensions as for the following photocatalytic reactions was employed (Section 2.4.1). By simultaneous measurement of absorbance and scattering of the suspension, the extinction spectra were obtained.

### 2.3.6. EPR spectroscopy

Bare  $\text{TiO}_2$  UV100 and 0.1 wt% Ni(II) grafted UV100 powder were analyzed to detect paramagnetic sites existing in darkness and generated under illumination. A MiniScope MS 400 X-band electron paramagnetic resonance (EPR) spectrometer was employed. All measurements were carried out at 77 K liquid nitrogen temperature. During the measurement, the input parameters were as follows: microwave frequency = 9.54 GHz, microwave power = 5 mW, modulation frequency = 100 kHz, modulation amplitude 0.15 mT. Measurements under irradiation were performed with UV-vis light (Xe lamp from Hamamatsu, LC 8) with the wavelength of  $\lambda_{max}=300-450$  nm and 200 W power. The  $g$  values were calculated with the Equation:  $g = h\nu/\beta B_0$  ( $B_0$  – external magnetic field,  $\beta$  – Bohr magneton,  $g$  – Lande  $g$ -factor). The EPR spectra are obtained from liquid measurement using a capillary tube at room temperature. During the measurement the input parameters were as following: the microwave frequency = 9.42 GHz, microwave power = 5 mW, modulation frequency = 100 kHz, modulation amplitude = 0.15 mT. LED blue light with a wavelength  $\lambda_{max} = 453$  nm has been used as the light source (A H150W tuna blue Kessil lamp (P/N: H150-blue, S/N: L4C3DG0006, 24 VDC, 1.5 A, 34 W)).

### 2.3.7. ATR-FTIR spectroscopy

Attenuated total reflection (ATR)-Fourier transform infrared (FTIR) spectra of the suspension samples were recorded using the ATR-FTIR spectrometer IFS 66 BRUKER equipped with an internal reflection element ( $45^\circ$  ZnSe crystal) and a deuterated triglycine sulfate (DTGS) detector. The spectra were recorded from all photocatalysts and reactants mixtures with 300 scans at four  $\text{cm}^{-1}$  resolutions. The OPUS version 6.5 software was used for data analysis. The background was subtracted with a baseline correction spectrum to reduce the slight shift as a result of device unsteadiness. An FT-IR spectroscopy device, Tensor 27 from Bruker, which has a Pike Miracle single-bounce attenuated total reflectance (ATR) cell equipped with a ZnSe single crystal, was used for the powder measurement of the samples before and after the photocatalytic experiment. The device was equipped with a room temperature DTGS detector, a KBr beam-splitter, and a mid-IR source ( $4000$  to  $650 \text{ cm}^{-1}$ ) with a resolution of  $1 \text{ cm}^{-1}$ . The OPUS 5.0 program (Optical User Software) from Bruker was employed for data collection and analysis.

### 2.3.8. X-ray photoelectron spectroscopy (XPS)

X-ray photoelectron spectroscopy (XPS) experiments were performed to study the oxidation states of the metal islands. A Leybold Heraeus XPS device, equipped with X-ray Al  $K\alpha$  beam as an excitation source was used. The binding energy corresponding to the metals was determined with a calibrated 1s Carbon peak. XPS 4.1 software was used to fit the curves of raw data by the Gaussian/Lorentzian fitting equation.

## 2.4. Synthetic procedures

### 2.4.1. Photocatalytic reaction procedure under aerobic condition

10 mg  $\text{TiO}_2$  or surface-modified  $\text{TiO}_2$  ( $2.5 \text{ g}\cdot\text{L}^{-1}$ ) dispersed in 4 mL of an appropriate solvent was filled in an oven-dried 20 mL vial employed as the photoreactor. 4-amino-TEMPO or TEMPO derivatives (0.08 mmol, 20 mol% respective to the reactant), the organic reactant (0.4 mmol), or other substrates, were added to the suspension. The reaction mixture was sonicated for 5 min until the  $\text{TiO}_2$  catalyst was dispersed entirely. After tightly sealing the photoreactor, the

suspension was purged with molecular oxygen for about 20 min to displace any air present in the reactor. The reaction was carried out for 24 h under visible light illumination (LED blue light,  $\lambda_{max}=453$  nm (A H150W tuna blue Kessil lamp (P/N: H150-blue, S/N: L4C3DG0006, 24 VDC, 1.5A, 34W)) with continuous stirring. Afterward, the catalyst was separated from the reaction mixture by centrifugation. The reaction product was isolated employing column chromatography using 230-400 mesh silica gel ( $\text{SiO}_2$ ) as the stationary phase and (a 3:1 hexane/ethylacetate mixture) as an eluent and concentrated. In the case of optimization reactions, shown in Appendix, Table 6.1, benzyl alcohol (20.6  $\mu\text{L}$ , 0.2 mmol, 50 mol %) was added to the solution as an internal standard. 1, 2, 3, 4-tetrahydroquinoline was chosen as the representative substrate to optimize the reaction conditions. The corresponding calibration curves of the starting material (reactant) and the product were obtained by GC-FID (gas chromatography - flame ionized detector). The yield and the rest of the reactant were calculated using calibration curves obtained by GC-FID. Details of the GC-FID parameter will be given in Section 2.6.1.

#### **2.4.2. Photocatalytic reaction procedure in anaerobic condition**

An oven-dried 10 mL reaction vial was used as the photoreactor. 5 mg photocatalyst was dispersed in 2 mL appropriate solvent, and then 0.2 mmol reactants (various N-heterocyclic amines) was added. After sealing the reactor tightly, the reaction mixture was sonicated for 10 min to disperse the powder particles properly. Then, the suspension was purged for 15 min with argon gas to exchange all air inside the reactor. The presence of an inert atmosphere (without  $\text{N}_2$  and  $\text{O}_2$ ) was established by analyzing the headspace of the reactor by gas chromatography (Shimadzu 8A, TCD detector). Depending on the substrates, the photocatalytic experiments were carried out for 24 h or longer under visible-light illumination with continuous shaking (LED blue light,  $\lambda_{max}=453$  nm A H150W tuna blue Kessil lamp (P/N: H150-blue, S/N: L4C3DG0006, 24 VDC, 1.5A, 34W)). Afterward, the evolved hydrogen gas was analyzed by gas chromatography with a thermal conductivity detector (GC-TCD) (Details of the GC-TCD parameter are given in Section 2.6.1). Later on, the catalyst was separated from the reaction mixture by centrifuging. The product was isolated by column chromatography using 230-400 mesh silica gel ( $\text{SiO}_2$ ) as the stationary phase and (a 3:1 hexane/ethylacetate mixture) as the eluent. The purity of the isolated compound was confirmed by both  $^1\text{H}$  NMR and  $^{13}\text{C}$  NMR measurements recorded in  $\text{CDCl}_3$ . In the case of op-

timization of the reaction condition, benzyl alcohol (10.3  $\mu$ L, 0.1 mmol, 50 mol % with respect to the substrate) was added to the solution as an internal standard. 1,2,3,4-tetrahydroquinoline was chosen as the representative substrate to optimize the reaction conditions.

## 2.5. Synthesis of substrates

### 2.5.1. Protection of hydroxyl group with tert-butyldimethylsilyl chloride

To an oven-dried 10 mL round bottom flask with a magnetic stirring bar was added 7-hydroxy-1,2,3,4-tetrahydroquinoline (298 mg, 2 mmol), triethylamine (0.82 mL, 5.9 mmole) and 0.5 mL of anhydrous dichloromethane ( $\text{CH}_2\text{Cl}_2$ ) as the solvent. [167] After cooling to 0 °C in an ice bath, tert-butyldimethylsilyl chloride TBDMSCl (543 mg, 3.6 mmol) was added. The reaction mixture was purged with molecular nitrogen and kept at the inert condition during the reaction for 12 h. Afterwards, the organic mixture was separated with brine (saturated aqueous sodium chloride). The brine layer was extracted with  $\text{CH}_2\text{Cl}_2$  three times. The organic layers were combined, dried over  $\text{MgSO}_4$ , and filtered. After concentrating by a rotary evaporator, the residue was purified by column chromatography using 230-400 mesh silica gel ( $\text{SiO}_2$ ) as the stationary phase and (a 5:1 hexane/ethylacetate ) as the eluent. 368 mg (70%) of TBSO-THQ (**1e**) was isolated. The purity of the synthesized compound was verified by NMR.

### 2.5.2. Synthesis of 4-methylthio-2-phenyl-1,2,3,4-tetrahydroquinoline

4-methylthio-2-phenyl-1,2,3,4-tetrahydroquinoline (**1j**) was synthesized according to a published procedure. [168] 2-chloro-1,2,3,4-quinoline (163.60 mg, 1 mmol), 4-methylthio-phenylboronic acid (252.03 mg, 1.5 mmol), potassium phosphate  $\text{K}_3\text{PO}_4$  (424.56 mg, 2 mmol),  $\text{Pd}_2(\text{dba})_3$  (9.1572 mg, 0.01 mmol), x-Phos (19.052 mg, 0.04 mmol), and 2 mL dichloromethane ( $\text{CH}_2\text{Cl}_2$ ) as the solvent were added to a oven-dried, 10 mL round bottom flask equipped with a magnetic stirring bar. Afterward, the mixture was degassed by freeze pumping cycles. The reaction was carried out for 12 h at 100 °C. The organic mixture was filtered with celite, and the synthesized 4-methyl-2-phenylquinoline was purified by column chromatography using 230-400 mesh silica gel ( $\text{SiO}_2$ ) as the stationary phase and ((a 10:1 hexane/ethylacetate )) as the eluent. 154.7 mg, 0.616 mmol 4-methylthio-2-phenylquinoline were obtained. Reduction of 4-methylthio-2-

phenylquinoline to 4-methylthio-2-phenyl-1,2,3,4-tetrahydroquinoline (1i) was performed out by using two equivalent of sodium cyanoborohydride  $\text{NaBH}_4\text{CN}$  (77.4 mg, 1.2 mmol) in 4.1 mL acetic acid. After the reaction, acetic acid was neutralized with 15 mL KOH (5 M) solution. The aqueous solution was extracted with  $\text{CH}_2\text{Cl}_2$ . The organic layers were combined, dried over  $\text{MgSO}_4$ , and filtered. After concentrating by a rotary evaporator, the residue was purified by column chromatography using 230-400 mesh silica gel ( $\text{SiO}_2$ ) as the stationary phase and (Hex-EtOAc 10:1) as the eluent. The purity of the synthesized compound was verified by NMR.

## 2.6. Analysis of the reaction mixture

### 2.6.1. Gas chromatography with flame ionization detector measurements

A Gas chromatography (A Shimadzu GC 2010) equipped with a flame ionization detector (GC-FID) and an Rtx-5 ( $d = 0.25$  mm) capillary column were used to analyze the reaction mixtures after the photocatalytic reactions. The operating temperature was as following: injection temperature = 250 °C, column temperature = 100 °C (hold 2 min), with an increase from 100 °C to 300 °C at a rate of 10 °C/min, in splitless mode. The injection volume was 1.0  $\mu\text{l}$  with nitrogen as the carrier gas.

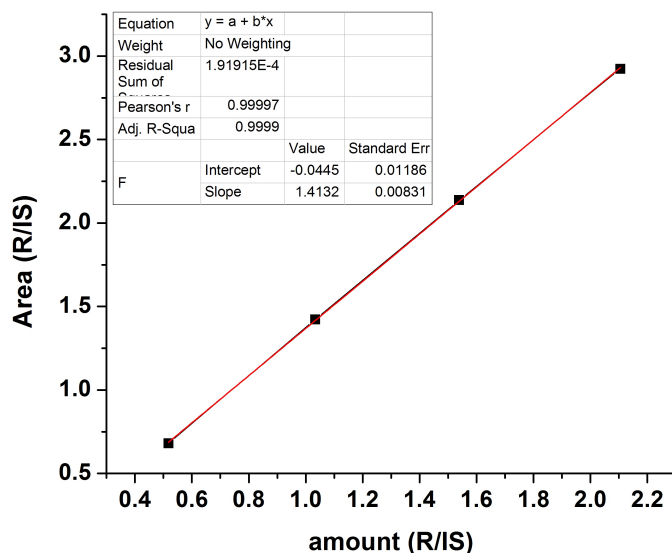


Figure 2.1.: Calibration curves for the reactant (R) 1,2,3,4-tetrahydroquinoline (THQ) obtained from the GC device with the presence of 50 mol% benzyl alcohol as the internal standard (IS).

The concentrations of the substrate and the products were determined derived from linear calibration curves prepared with a commercial organic reactant and product purchased from Sigma-Aldrich (95-99.8% purity). Acetonitrile was used as the solvent, and 50 mol% benzyl alcohol (purchased from Sigma-Aldrich with the highest (99.9%) purity) with respect to the substrate was used as the internal standard (IS). Calibration curves for the reactant (1,2,3,4-tetrahydroquinoline (THQ)) and product (quinoline) are obtained from the GC device ( $R^2 = 0.999$ ) by measuring four different concentration of THQ and quinoline in the range between 25, 50, 75, and 100 mmol/L. The reactant ((Figure 2.1) and the product (Figure 2.2) formation of quinoline were quantified by using the linear fitting equations from the corresponding calibration curves.

According to this calibration curve (Figure 2.1) the molar amount (mmol) of the unreacted reactant was calculated with the following Equation 2.1:

$$n_R = \left( \frac{A_R}{A_{IS}} - \text{intercept} \right) \times \frac{n_{IS}}{\text{slope}} \quad (2.1)$$

The internal standard (IS) was introduced into the reaction system 50 mol% (molar amount) with respect to the initial amount of the reactant  $n_{R_0}$ .

where  $n_R$  is the remaining amount of the reactant, and  $n_{IS}$  is the constant amount of the internal standard, which was 0.2 mmol.  $A_R$  and  $A_{IS}$  are the areas of the peaks of the reactant (R) and the internal standard (IS), respectively.

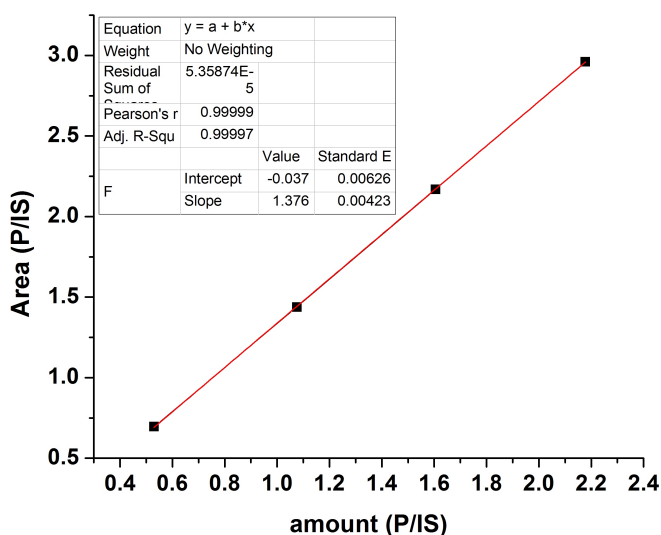


Figure 2.2.: Calibration curves for the product (P) quinoline (Q) obtained from the GC device with the presence of 50 mol% benzyl alcohol as the internal standard (IS).

According to this calibration curve (Figure 2.2) the amount (mmol) of the product was calculated with the following Equation 2.2:

$$n_P = \left( \frac{A_P}{A_{IS}} - \text{intercept} \right) \times \frac{n_{IS}}{\text{slope}} \quad (2.2)$$

where  $n_P$  is the amount of the product (P), and  $n_{IS}$  is the amount of the internal standard, which was 0.2 mmol.  $A_P$  and  $A_{IS}$  are the peaks areas of the product (P) and the internal standard (IS), respectively.

Moreover, the yield of the product (Y), the conversion of the reactant (C), and the selectivity of the reaction (S) have been calculated by the Equations 2.3-2.5:

$$Y(\%) = \frac{n_P}{n_{R_0}} \times 100 = \frac{A_P \times f_R}{n_{R_0}} \times 100 \quad (2.3)$$

$$C(\%) = \frac{n_{R_0} - n_R}{n_{R_0}} \times 100 = \frac{n_{R_0} - A_R \times f_R}{n_{R_0}} \times 100 \quad (2.4)$$

$$S(\%) = \frac{Y}{C} \times 100 \quad (2.5)$$

where  $n_P$  is the amount of the product,  $n_R$  is the remaining amount of the reactant, and  $n_{R_0}$  is the starting amount of the reactant.  $A_P$  and  $A_R$  are the peaks areas of the product and the reactant, respectively,  $f_P$  and  $f_R$  are the conversion factor as determined from the calibration curves of the product and the reactant.

### 2.6.2. Gas chromatography with thermal conductivity detector

The evolved molecular hydrogen ( $H_2$ ) gas during the reaction in the headspace of the photoreactor, above the reaction mixture was analyzed using a gas chromatograph (Shimadzu 8A) equipped with a molecular sieve 5A column, a TCD detector, and Ar as the carrier gas. The column temperature was adjusted to be 80 °C, and the detector temperature was 120 °C. The current was 80 A. The quantitative analysis of evolved hydrogen during the reaction has been calculated according to the equation obtained from the linear calibration curve of hydrogen (Figure 2.3). A calibration curve ( $R^2 = 0.997$ ) of gaseous hydrogen was obtained by measuring five different volumes of hydrogen in the range between 0.1 and 0.5 mL. The plot of concentration of molecules of hydrogen



vs. time is presented in Figure 2.3, and the linear fitting equation was derived. By applying linear fitting equation, the total volume of the photogenerated  $H_2$  could be calculated as follows: the volume of the headspace of the reactor was 6.4 mL, and the injector volume was 0.5 mL:

$$V_{H_2} = \frac{6.5 \times slope}{(A_{H_2} - intercept) \times 0.5} \quad (2.6)$$

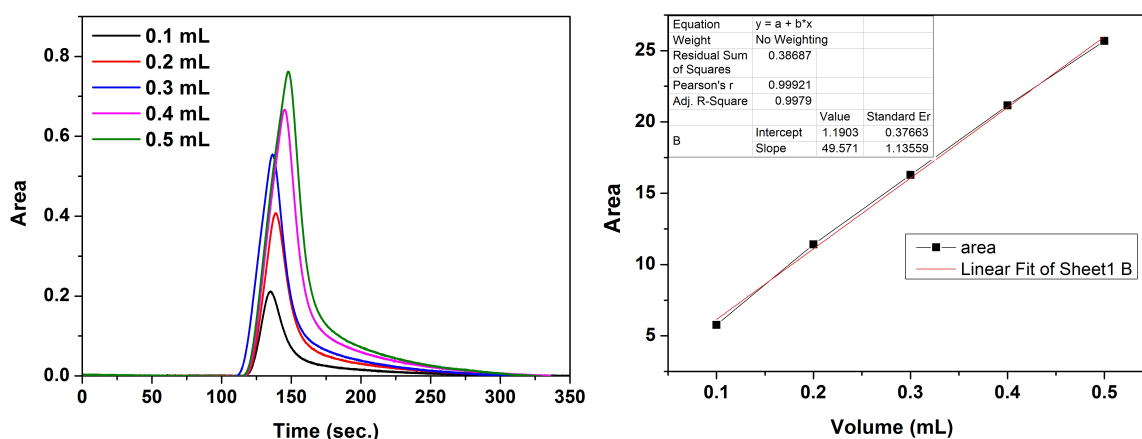


Figure 2.3.: The molecular hydrogen peaks obtained from the GC-TCD device detected at various injection volumes (left). Calibration curve and linear fit for the molecular hydrogen obtained from the GC-TCD (right).

Using ideal gas law the total volume of the photogenerated  $H_2$  could be converted into the moles as follow:

$$n = \frac{P \times V_{H_2}}{R \times T} \quad (2.7)$$

where  $P = 1$  atm is pressure,  $V_{H_2}$  is the total volume of the generated  $H_2$ ,  $R = 8.314 \text{ J mol}^{-1} \text{ K}^{-1}$  is a molar gas constant.

### 2.6.3. Nuclear magnetic resonance (NMR)

NMR characterization of all the isolated compounds was done with a Bruker Avance DPX-400 spectrometer.  $^1H$  NMR and  $^{13}C$  NMR measurements were recorded in chemical shifts ( $\delta$  in parts per million) relative to residual signals of deuterated chloroform  $CDCl_3$  (7.26 ppm for  $^1H$ ; 77.00 ppm for  $^{13}C$ ) at room temperature. Abbreviations used in the NMR experiments are: br, broad; s, singlet; d, doublet; t, triplet; q, quartet; sep, septet; m, multiplet.

#### 2.6.4. Column chromatography

Thin-layer chromatography (TLC) was carried out to optimize the appropriate eluent before doing column chromatography on a commercial glass covered with a 0.25 mm layer of Merck Silica gel 60F254 Aluminum oxide 60F254 (EMD, Inc.). The separation of the reaction mixture was visualized under fluorescence UV light with a 254 nm wavelength. Column chromatography was performed to isolate the products from the reaction mixtures. The separation of substances was carried out in a 150 ml chromatographic column with a reservoir, frit, and PTFE stopcock from Duran. Column chromatography was done using either gravity to move the solvent or, if needed, compressed N<sub>2</sub> gas to push the solvent through the column. 230-400 mesh silica gel (SiO<sub>2</sub>) or Alumina Neutral flash grade was used as stationary phases. A mobile phase eluent was determined for each substrate separately using solvent mixtures of hexanes and ethyl acetate or dichloromethane (CH<sub>2</sub>Cl<sub>2</sub>) and acetone. Finally, the products were collected, and the eluent was evaporated with Rotavapor (R-300, Buchi Rotary Evaporators). The amount of the collected product was obtained by weighting in a semi-micro balance (Mettler Toledo - MS105).

#### 2.6.5. Detection of hydrogen peroxide (H<sub>2</sub>O<sub>2</sub>)

Detection of hydrogen peroxide (H<sub>2</sub>O<sub>2</sub>) was performed after the dehydrogenation reactions of 1,2,3,4-tetrahydroquinoline in the presence and the absence of 4-amino-TEMPO. The formation of H<sub>2</sub>O<sub>2</sub> in the reaction mixture was detected with KI by slightly changing a reported method. [134] H<sub>2</sub>O<sub>2</sub> oxidizes iodide ions to iodine in the presence of an acid and molybdate catalyst. The liberation of iodine could be detected using a starch solution as the indicator. This method is suitable for low concentrations of H<sub>2</sub>O<sub>2</sub> (0.1-5%) with minimal interference from organic compounds.



All reagents were analytical reagent grade, and deionized water (Milli-Q, 18.2 mΩ · cm) was used. Initially, 10 g of KI was dissolved in 100 mL of water (0.6 M). Subsequently, 0.018 g ammonium molybdate, (NH<sub>4</sub>)<sub>6</sub> Mo<sub>7</sub>O<sub>24</sub> · 4H<sub>2</sub>O, was dissolved in 75 mL water (2 · 10<sup>-3</sup> M). While stirring, 30 mL concentrated H<sub>2</sub>SO<sub>4</sub> (98%) was slowly added. 0.357 g of potassium iodate KIO<sub>3</sub> was weighed and transferred to a 100 mL volumetric flask, and 40 mL of deionized water, 0.2 g

of sodium hydroxide, and 2 g of potassium iodide were added.

The mixture was agitated until complete dissolution and diluted to the volume to make a 1.7 M solution. 10 g of soluble starch was added into a 150 mL beaker. While stirring, about 5 mL of water was gradually added until a paste was formed. The paste was then added to 100 mL of boiling water, and the resulting solution was cooled to room temperature. 5 g of KI was added to the solution and stirred until complete dissolution. The obtained solution was used in order to detect H<sub>2</sub>O<sub>2</sub> in the reaction mixture after the dehydrogenation reaction, according to Eq 2.8.

After 24 h photocatalytic dehydrogenation of 1,2,3,4-THQ to quinoline, the reaction mixture was collected by separation of the catalyst with centrifugation. The results are presented in the following Chapter 3.

### 2.6.6. Photonic efficiency

Indeed, by calculating photonic efficiency ( $\zeta$ ) the performance of heterogeneous photocatalysis could be compared. Photonic efficiency ( $\zeta$ ) describes the number of molecules of the transformed or photogenerated reaction product over the absorbed photon flux at a given wavelength, an incident light inside the reactor's front window [169]. The photocatalytic activity of all reactions was evaluated by calculating photonic efficiency with the following Equation 2.9

$$\zeta = \frac{N_{molecules}(mol \cdot s^{-1})transformed/produced}{N_{photonflux}(einstein \cdot s^{-1})incident \ inside \ reactor \ cell} \times 100 \quad (2.9)$$

It should not be neglected that the incident light is not completely absorbed in the heterogeneous system and is scattered or reflected by the surfaces of dispersed powder particles. Therefore, it differs from the conventional way of the measurement of homogeneous systems where product molecules are related to the total number of incident flux on the reactor walls, for unknown reactor geometry, and polychromatic radiation than the number of absorbed quanta at a given wavelength. In order to take into consideration the wavelength and the illuminated area in heterogeneous systems, the photon flux could be determined by the Equation 2.10

$$N_{photonflux} = \frac{I \cdot A \cdot \lambda}{N_A \cdot h \cdot c} \quad (2.10)$$

where I is the irradiance, equal to 4 mW/cm<sup>2</sup>, A is the irradiated area, equal to 4 cm<sup>2</sup>, and the  $\lambda$  is a maximum wavelength of monochromatic light which is 453 nm, N<sub>A</sub>, h, and c are the

Avogadro constant, Planck number, and speed of light, respectively. Photon flux ( $N_{\text{photonflux}}$ ) was found to be  $6.05 \times 10^{-8} \text{ mol s}^{-1}$ . The maximum photonic efficiency ( $\zeta$ ) would be 7.65% if all the reactant molecules transformed into the desired product.

# Chapter 3

## Results

In this chapter, the obtained experimental results will be presented. Firstly, the detailed characterization data of the employed materials will be presented. This will be followed by an overview of the photocatalytic performance of titanium dioxides in dehydrogenation reactions of N-heterocycles in aerobic and anaerobic conditions. In the next section, the effect of surface grafted  $\text{TiO}_2$  and the effect of the different TEMPO derivatives in selective dehydrogenation reactions of N-heterocycles in the oxygen atmosphere will be given in detail. Furthermore, the acceptorless photocatalytic dehydrogenation of N-heterocycles employing noble metal nanoparticles deposited  $\text{TiO}_2$  will be presented. Effect of different solvents, various noble metals, co-catalysts content respect to  $\text{TiO}_2$ , and loading amount of photocatalyst in photocatalytic reactions will be presented.

### 3.1. Materials characterization of the prepared photocatalysts

The main catalysts used for this study were commercial anatase  $\text{TiO}_2$  UV100. The employed photocatalyst for the oxidative dehydrogenation of N-heterocyclic amines was 0.1 wt% Ni(II) nanoclusters surface grafted  $\text{TiO}_2$  UV100. The employed photocatalyst for the acceptorless dehydrogenation (ADH) of N-heterocyclic amines was 1 wt%  $\text{Rh}^0$  nanoparticles photodeposited  $\text{TiO}_2$

UV100. Different noble metals such as  $\text{RuO}_2$ ,  $\text{Au}^0$ ,  $\text{Pd}^0$ ,  $\text{Pt}^0$  were also photodeposited on the surface of  $\text{TiO}_2$  UV100 for comparison with rhodium nanoparticles. X-ray diffractograms were taken to determine their crystal phase. The XRD pattern of  $\text{TiO}_2$  UV100 is given as the reference. XRD pattern of all powders is shown in Figure 3.1. All diffractograms were analyzed with the DIFFRAC Plus Eva software and compared to the ICDD database.

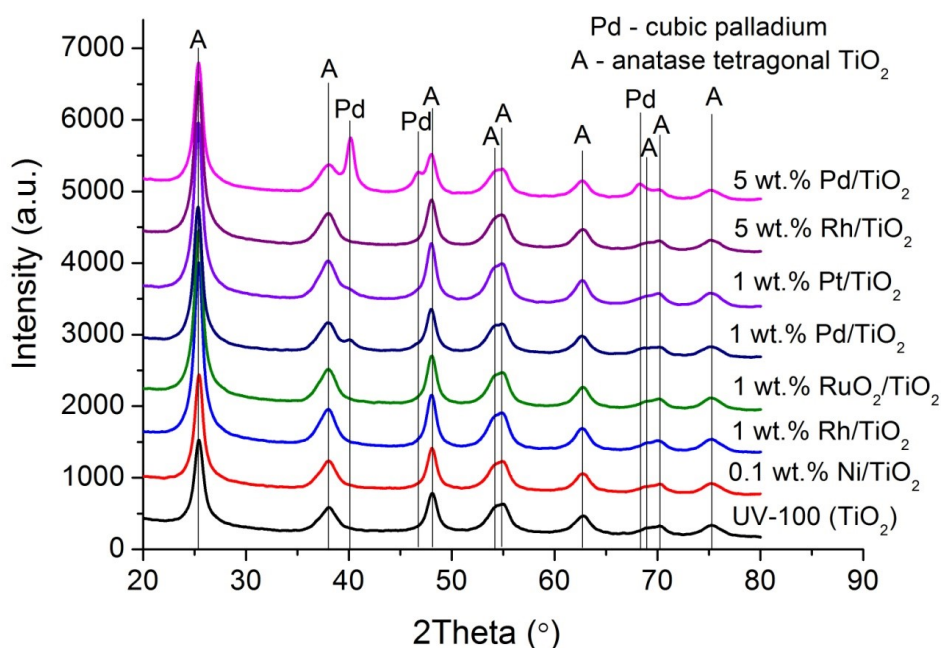


Figure 3.1.: X-ray diffraction patterns of the photocatalysts  $\text{TiO}_2$  UV100 (black), 0.1 wt% Ni(II)/ $\text{TiO}_2$  (red), 1 wt% Rh/ $\text{TiO}_2$  (blue), 1 wt%  $\text{RuO}_2$ / $\text{TiO}_2$  (green), 1 wt% Pd/ $\text{TiO}_2$  (navy), 1 wt% Pt/ $\text{TiO}_2$  (violet), 5 wt% Rh/ $\text{TiO}_2$  (purple), and 5 wt% Pd/ $\text{TiO}_2$  (magenta)

It was observed that all peaks are assigned to the pure anatase crystal phase. No shift of the original  $\text{TiO}_2$  peaks and usually no peak belonging to the surface modifying transition metals are observed. Low loading of the transition metals on the  $\text{TiO}_2$  surface ( $\leq 5\%$ ) is undoubtedly below the detection limit of the XRD diffractometer. Only the diffractograms of  $\text{Pd}^0$ / $\text{TiO}_2$  materials show peaks belonging to cubic phase palladium nanocrystals. These peaks intensities were found to be low for the material having only 1 wt%  $\text{Pd}^0$  and increased while 5 wt%  $\text{Pd}^0$  nanoparticles was photodeposited on  $\text{TiO}_2$ . Any peak belonging to  $\text{Rh}^0$  nanoparticles was not detected even at a

high amount of photodeposition (5 wt% Rh<sup>0</sup> with respect to TiO<sub>2</sub>). The specific surface area of the commercial TiO<sub>2</sub> UV100 and the surface-modified TiO<sub>2</sub> photocatalysts were determined by BET measurements. Commercial TiO<sub>2</sub> UV100 is described in the literature as a mesoporous material consisting of 3-5 nm spherical particles with  $\sim 300$  m<sup>2</sup>/g surface area, which is consistent with the results that were obtained here (Table 3.1). The surface-modified TiO<sub>2</sub> nanoparticles exhibit similar surface area than the pure anatase TiO<sub>2</sub> with small differences (Table 3.1). It should also be noted that every BET measurement of single-point BET is provided with  $\pm 5$  m<sup>2</sup>/g experimental error. The surface area of commercial TiO<sub>2</sub> P25 from Evonik-Degussa Aeroxide, Germany, with 20% rutile and 80% anatase phase, is provided as a reference photocatalyst which will be compared with TiO<sub>2</sub> UV100 in photocatalytic activity measurements in the following results section. The obtained specific surface area of the employed photocatalysts are summarized in Table 3.1.

Table 3.1.: Specific surface area (BET) of pure and surface modified TiO<sub>2</sub> powders.

Catalysts(Powders)	Specific surface area* BET [m <sup>2</sup> /g]
P25	50
UV100	320
0.1 wt% Ni(II)/TiO <sub>2</sub>	318
1 wt% Au/TiO <sub>2</sub>	312
1 wt% Ru/TiO <sub>2</sub>	315
1 wt% Pd/TiO <sub>2</sub>	321
1 wt% Pt/TiO <sub>2</sub>	319
1 wt% Rh/TiO <sub>2</sub>	316

\* The relative errors are about  $\pm 5$  m<sup>2</sup>/g as evaluated from 3 times repeated measurements

The results in Figure 3.2 illustrate the results of diffuse reflectance spectroscopy measurements. As expected, pure TiO<sub>2</sub> UV100 and TiO<sub>2</sub> P25 are only absorbing in the UV range. All surface-modified TiO<sub>2</sub> exhibit lower reflectance of visible light when compared with the bare TiO<sub>2</sub>. The Ni(II) ions grafted TiO<sub>2</sub> UV100 sample showed slightly lower reflectance compared to UV100 TiO<sub>2</sub>. However, each noble metal nanoparticles on the TiO<sub>2</sub> UV100 surface influence differently to the overall reflectance spectra despite their small content in TiO<sub>2</sub>. It becomes obvious from the results that Pd/TiO<sub>2</sub> and Pt/TiO<sub>2</sub> powders have less reflectance in comparison with other

samples due to their dark grey color. Additionally, little absorption in the range from 600 nm to 800 nm is observed for Pd/TiO<sub>2</sub> and Pt/TiO<sub>2</sub> powders. Although Rh photodeposited TiO<sub>2</sub> has less reflectance in comparison with pure UV100 TiO<sub>2</sub>, the absorption spectrum shows that it can only be excited by UV light (< 390 nm). RuO<sub>2</sub> nanoparticles photodeposited TiO<sub>2</sub> powders show plasmonic peaks at a wavelength of 450 and 600 nm. Similarly, a plasmonic absorption peak was observed in the Au /TiO<sub>2</sub> sample at a wavelength of 523 nm.

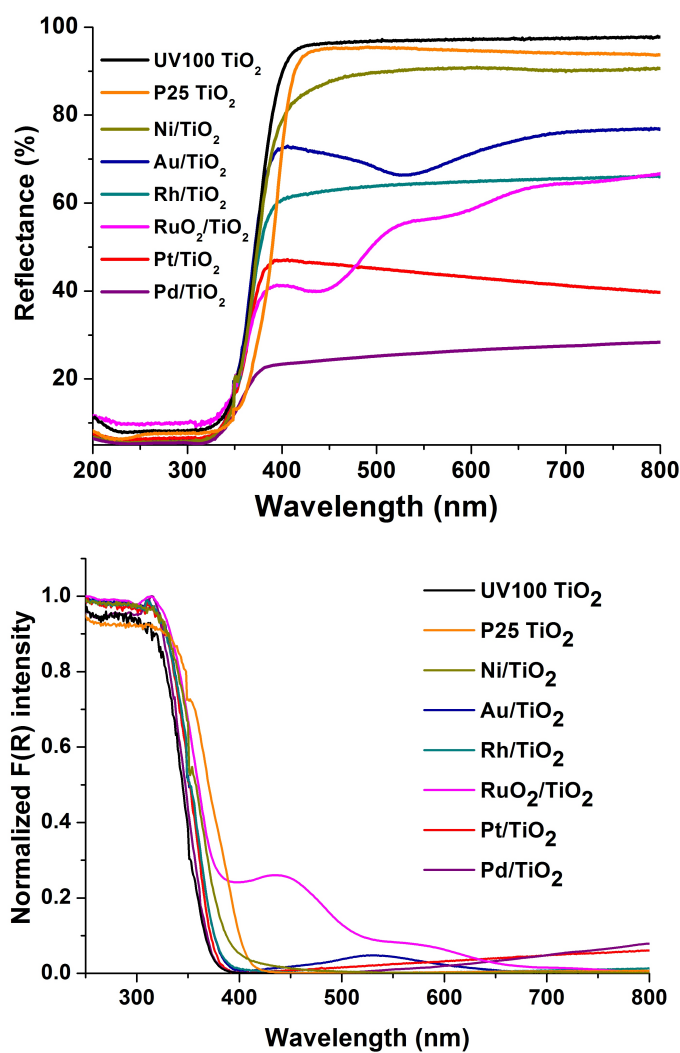


Figure 3.2.: Diffuse reflectance spectra of the employed powder samples (top), F(R) spectra calculated according to the Kubelka-Munk function of pure UV100 TiO<sub>2</sub>, P25 TiO<sub>2</sub> and surface modified TiO<sub>2</sub> UV100 with transition metal nanoparticles (bottom).

The morphology of the surface-modified TiO<sub>2</sub> UV100 particles with transition metals were ex-



### 3.1. MATERIALS CHARACTERIZATION OF THE PREPARED PHOTOCATALYSTS

---

amined by TEM in nanoscale. Figure 3.3 shows the micrograms of the employed photocatalysts, i.e., surface grafted 0.1 wt% Ni(II)/TiO<sub>2</sub> UV100, surface photodeposited TiO<sub>2</sub> UV100 with 1 wt% Rh, 1 wt% Pd, 1 wt% RuO<sub>2</sub>, 1 wt% Pt, and 1 wt% Au nanoparticles.

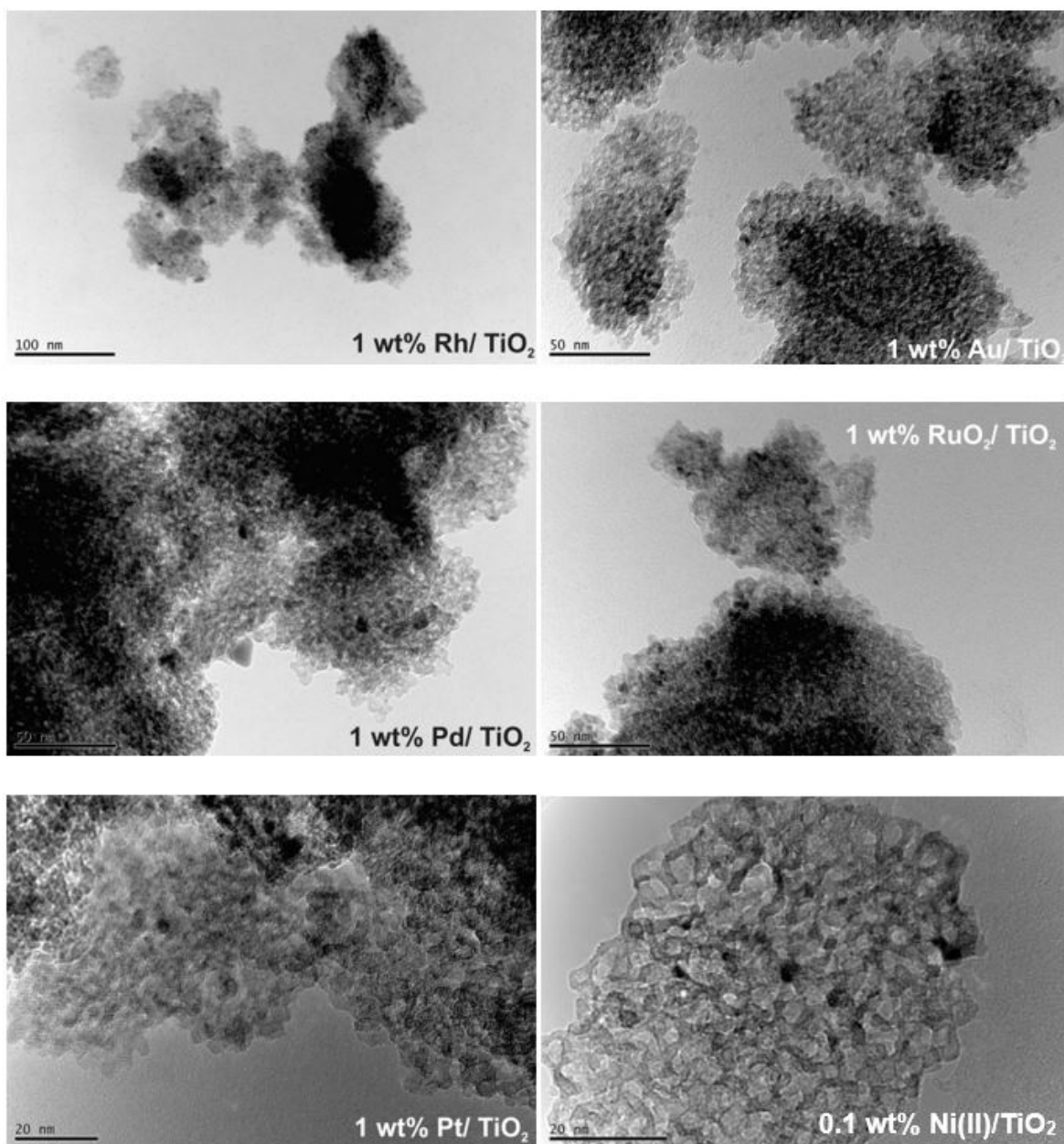


Figure 3.3.: TEM micrographs of a powder sample of TiO<sub>2</sub> UV100 with 1 wt% Rh, Au, Pd, Pt, RuO<sub>2</sub> nanoparticles and 0.1 wt% Ni(II) nanoclusters.

As can be seen in the pictures, the particles are mostly spherical with mesoporous morphology.

The particles sizes are quite homogeneous in the range of 3 to 5 nm. In the images, the darker spots are assigned to transition metal nanoparticles, which are homogeneously distributed on the photocatalyst's surface. According to the TEM images (Figure 3.3) no significant change is observed, thus indicating that the particles' morphology and size were not affected by the modification with the various transition metals. X-ray photoelectron spectroscopy (XPS) experiments were performed for all metal photodeposited TiO<sub>2</sub> samples to study the oxidation states of the metal islands. The resulting XPS spectra for photodeposited metals (namely Rh, Pd, Au, and Pt) with corresponding hybridization states are given in the Figure 3.4.

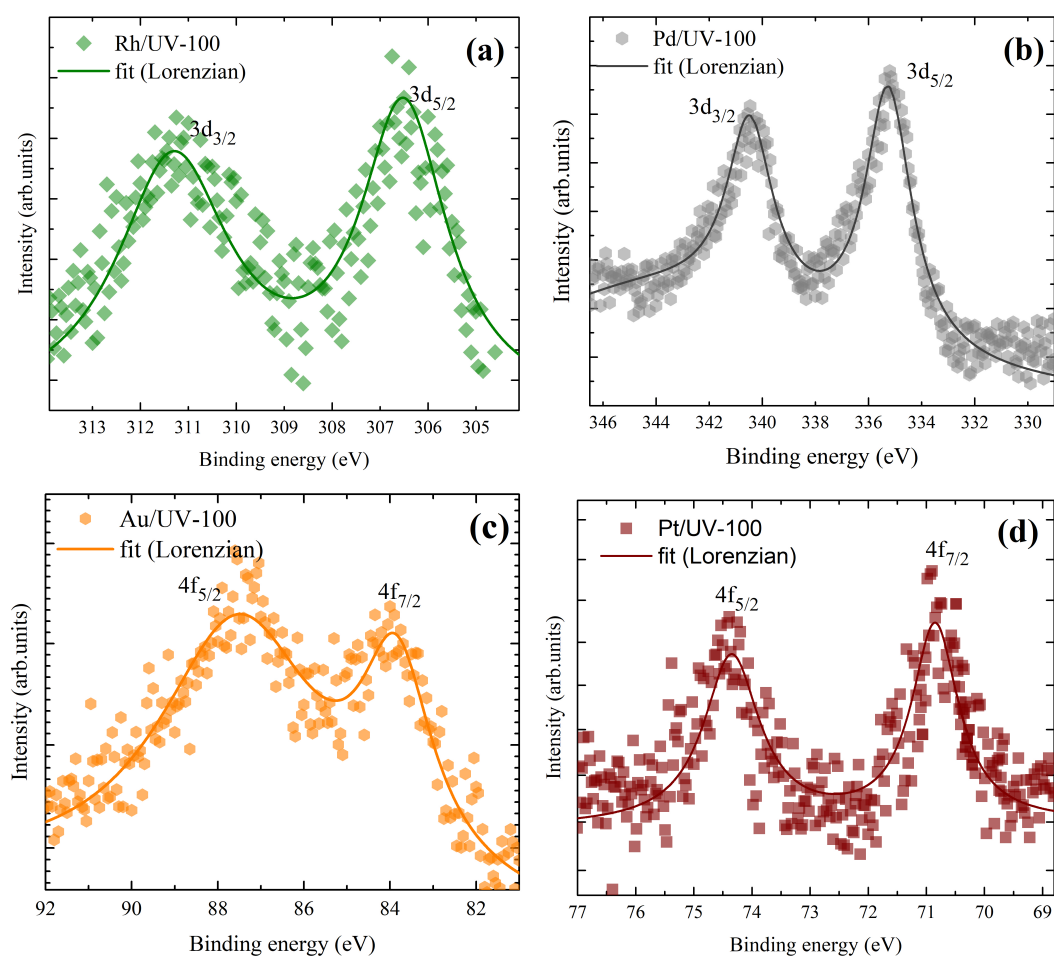


Figure 3.4.: The set of XPS spectra obtained from the corresponding metal nanoparticles photodeposited TiO<sub>2</sub>. The solid lines are corresponding to the fits to extract the exact position of the XPS maxima.

According to the results presented in Figure 3.4 photodeposited metals are present in the metal-

lic state. Rh/UV100 powder exhibits two peaks at 311.5 eV and 306.5 eV related to  $3d_{3/2}$  and  $3d_{5/2}$  states, respectively. This is in accordance with the literature value of 311.45 ( $3d_{3/2}$ ) and 306.7 ( $3d_{5/2}$ ) for metallic Rh, thus proving the state of photodeposited Rh nanoparticles on the UV100 surface. [170] The XPS spectrum for Pd/UV100 (Figure 13(b)) exhibits doublet peaks at 340.2 eV and 334.9 eV which are related to  $3d_{3/2}$  and  $3d_{5/2}$  Pd metallic states as reported in the literature. [171] The XPS spectrum of Au/UV100 also shows doublet energy peaks at 87.5 eV and 83.9 eV. These values are related to  $4f_{5/2}$  and  $4f_{7/2}$  Au states which proves the existence of metallic Au nanoparticles on the  $TiO_2$  surface. [172] Similarly, Pt/UV100 also shows the metallic state of Pt nanoparticles. The corresponding binding energies for Pt  $4f_{5/2}$  and  $4f_{7/2}$  states were observed at 74.3 eV and 70.9 eV, respectively, being in accordance with literature values. [173] Only photodeposition of  $TiO_2$  nanoparticles with Ru precursor appeared in oxide state  $RuO_2$ , however the peaks are overlapped with standard C peaks, which are not represented here.

*In-situ* EPR spectroscopy measurements were performed with powders of 0.1 wt% Ni(II)/UV100 and bare  $TiO_2$  (UV100) at 77 K in an argon atmosphere to examine the impact of the grafted Ni(II) ion on the electron shuttle process (Figure 3.5). In the dark, both samples showed characteristic peaks with g values of  $g_1 = 2.027$ ,  $g_2 = 2.009$  and  $g_3 = 2.005$  (Signals D) which has been assigned to  $Ti^{4+}-O_2^{\bullet-}$  species. [174] Upon UV-vis illumination, peaks at  $g_1 = 2.018$ ,  $g_2 = 2.014$  and  $g_3 = 2.005$  (Signals A) were generated which have been proposed to correspond to the trapped holes, i.e.,  $Ti^{4+}-O^{\bullet-}$ - $Ti^{4+}-OH^-$  radicals at the surface sites of  $TiO_2$ . [175, 176] A signal at  $g = 2.004$  in both catalysts arises, which most likely indicates the presence of electrons trapped at  $TiO_2$  oxygen vacancies. Additionally, signals  $g_{||} = 1.96$  and  $g_{\perp} = 1.990$  (Signals B) are formed during irradiation. These signals indicate the presence of  $Ti^{3+}$ , which are formed by trapping of photogenerated electrons. [177]

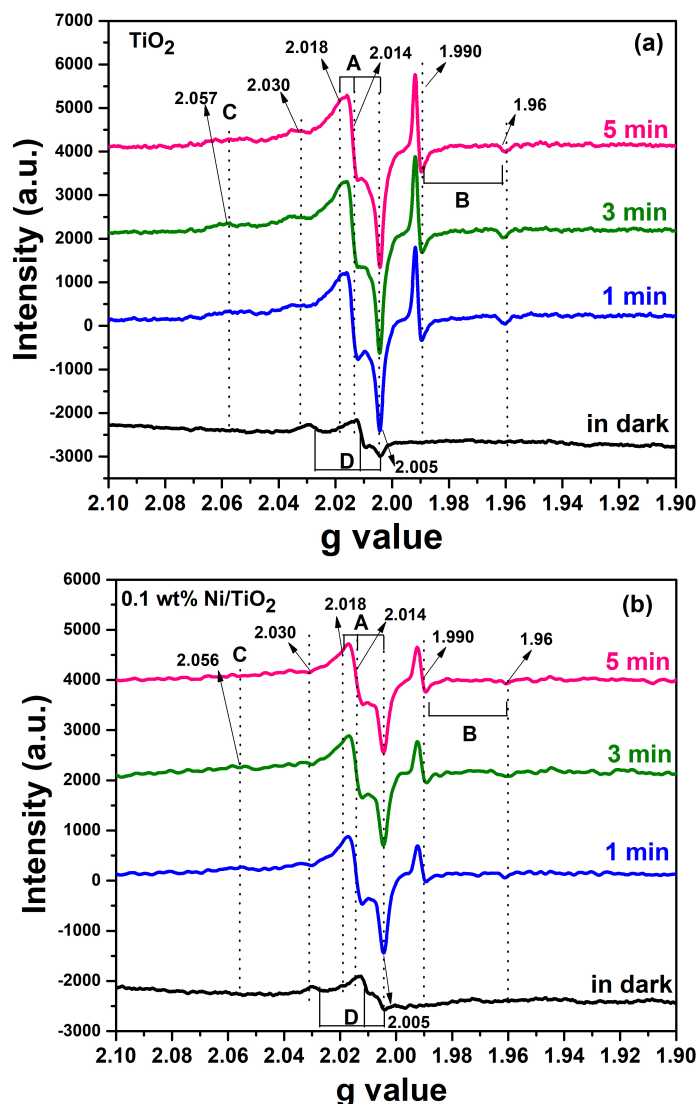
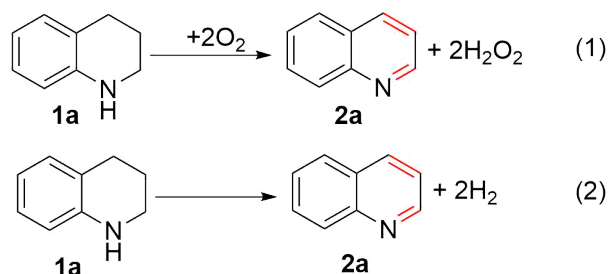


Figure 3.5.: *In-situ* EPR spectra at 77 K of TiO<sub>2</sub> (a) and 0.1 wt% Ni(II)/TiO<sub>2</sub> (b) in the dark and under 1, 2, 3, and 5 min of UV–vis light irradiation (Xe lamp,  $\lambda_{max} = 300\text{--}450$  nm). The spectra under light irradiation are obtained by subtracting the spectrum in the dark.

### 3.2. Formation of surface complexes

1,2,3,4-tetrahydroquinoline (THQ) **1a** was chosen as a model substrate for the investigation of the photocatalytic dehydrogenation. Principally, the dehydrogenation product of THQ in an oxygen atmosphere in alcoholic media is theoretically expected to be the quinoline as the main product

and hydrogen peroxide as the byproduct. However, in an inert Ar atmosphere, besides the corresponding quinoline, the release of two hydrogen molecules is expected to be the second product. The reaction pathways of THQ in the aerobic and anaerobic atmosphere are shown in Scheme 3.1.



Scheme 3.1: Schematic illustration of dehydrogenation of THQ in oxygen (1) and argon (2) atmosphere.

The absorption spectra of the probe reactant (THQ) with and without UV100 was measured by UV-vis spectroscopy in order to study the effect of N-heterocyclic amines on the absorption spectrum of  $\text{TiO}_2$  and to determine the suitable wavelength of the light source for the dehydrogenation reaction (Figure 3.6). It is well known that bare  $\text{TiO}_2$  can only be excited upon UV light irradiation.

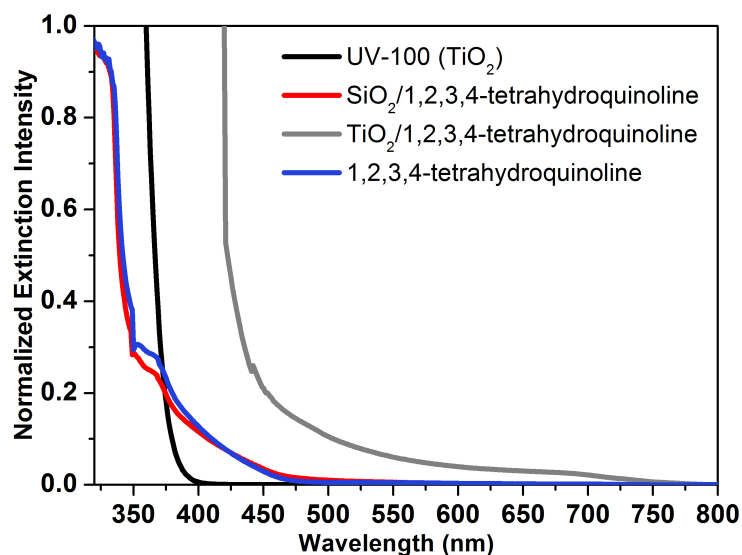


Figure 3.6.: Normalized extinction spectra for the bare  $\text{TiO}_2$  (UV100),  $\text{TiO}_2/\text{THQ}$ ,  $\text{SiO}_2/\text{THQ}$ , and THQ in acetonitrile ( $\text{CH}_3\text{CN}$ ). Absorption spectroscopy measurements were performed at the same concentration of the catalyst and substrate as appropriate to the organic reaction conditions in a  $\text{CH}_3\text{CN}$  solvent.

Similarly, THQ molecules in  $\text{CH}_3\text{CN}$  show the main absorption edge at a wavelength of about 350 nm. Interestingly, a significant red-shift of about 60 nm in the mixture of commercial  $\text{TiO}_2$  UV100 with THQ was observed. This could be attributed to a surface-complex formation in the amine- $\text{TiO}_2$  mixture responsible for the visible light absorption.

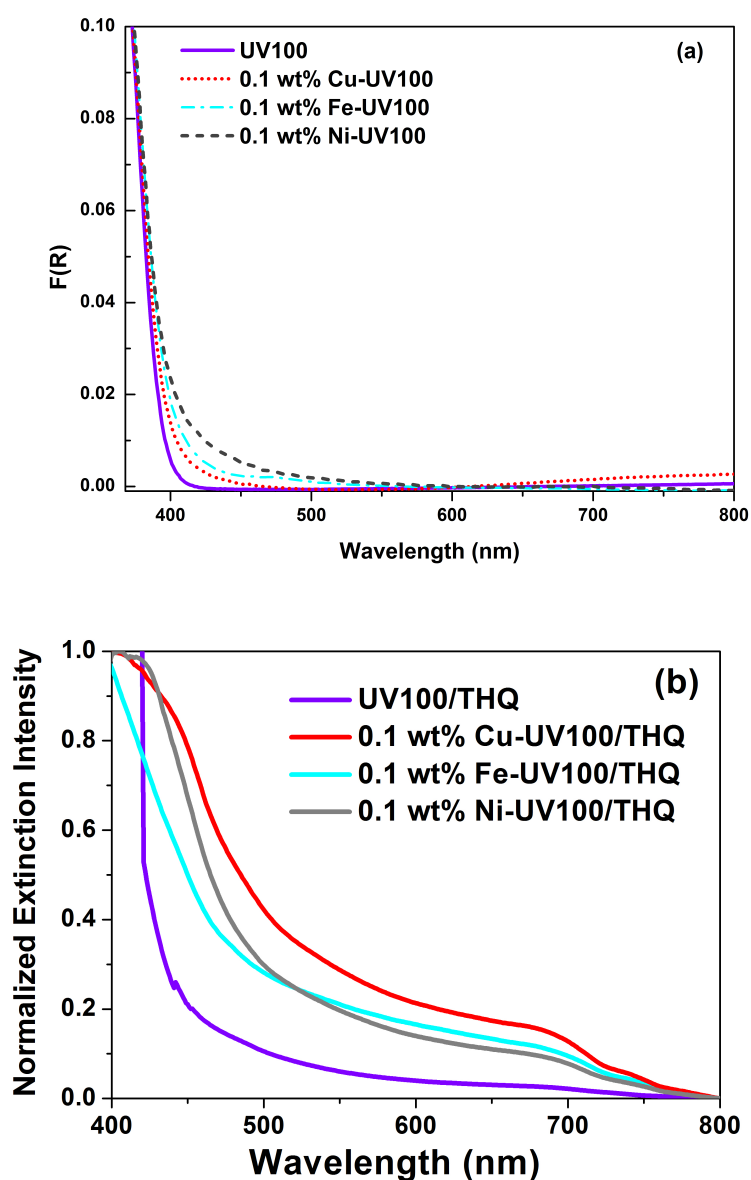


Figure 3.7.: Absorption spectra of the surface grafted  $\text{TiO}_2$  (a) and normalized extinction spectra for the bare  $\text{TiO}_2/\text{THQ}$ , and THQ with 0.1 wt% surface grafted metal ions with respect to  $\text{TiO}_2$  in acetonitrile ( $\text{CH}_3\text{CN}$ ) solvent (b). Absorption spectroscopy measurements were performed at the same concentration of the catalyst and substrate as appropriate to the organic reaction conditions in a  $\text{CH}_3\text{CN}$  solvent.

Since the suspension of the mixture of THQ and TiO<sub>2</sub> in acetonitrile absorbs in the visible region at 460 nm, the dehydrogenation of this compound was examined upon visible light illumination. It is worth mentioning that the use of other solvents, such as methanol, ethanol and 2-propanol, does not affect the surface complex (spectra are not presented here). In order to confirm the importance of semiconductor TiO<sub>2</sub>, further exploration of a non-semiconducting SiO<sub>2</sub> with a high surface area was employed (Figure 3.6). No red-shift is observed in the presence of silica, and the observed absorption edge corresponds to THQ (Figure 3.6).

Also, surface modified TiO<sub>2</sub> samples are used to observe their effect in absorption spectra when combined with THQ. The results of the UV-vis absorption spectroscopy presented in Figure 3.7 show that although the amount of grafted metal ions on TiO<sub>2</sub> was low, the absorption wavelengths of surface grafted TiO<sub>2</sub> and the THQ mixture showed increased absorption in the range of visible region in comparison with bare TiO<sub>2</sub> UV100.

To better understand the occurring surface chemical bond interaction between an amine and TiO<sub>2</sub>, ATR-FTIR spectroscopy measurements of CH<sub>3</sub>CN solvent, CH<sub>3</sub>CN /THQ, CH<sub>3</sub>CN/TiO<sub>2</sub>, and TiO<sub>2</sub>/THQ were performed. The results are shown in Figure 3.8. The same concentration of THQ was employed under optimized reaction conditions. The absorption bands at 1585 cm<sup>-1</sup>, 1500 cm<sup>-1</sup>, 1309 cm<sup>-1</sup>, 1268 cm<sup>-1</sup> are all ascribed to heteroatom-containing stretching vibration modes in THQ. The predominant peak at 1500 cm<sup>-1</sup> is associated with an aromatic ring stretch (Ar C-C<sub>(m)</sub>) of THQ. Additionally, the other two distinct absorption bands at 1606 cm<sup>-1</sup> and 3409 cm<sup>-1</sup> are attributed to the N-H stretching vibrations. When TiO<sub>2</sub> and THQ were dispersed in solution, the bands corresponding to the N-H bending vanished.

The bands at 1300 cm<sup>-1</sup> and 1268 cm<sup>-1</sup> are attributed to aromatic C-H in-plane bends. These bands in the THQ spectrum vanish when TiO<sub>2</sub> is added into the amine solution. The signals at 1606 cm<sup>-1</sup> and 1585 cm<sup>-1</sup> could also be attributed to the aromatic C-C stretches. Moreover, the band intensity at 1300 cm<sup>-1</sup> associated with a heterocyclic C-N stretching decreases in the presence of TiO<sub>2</sub>. This ATR-FTIR (Figure 3.8) data was, therefore, another proof for the surface-complex formation. This phenomenon is also expected to occur in the presence of other N-heterocyclic amines.

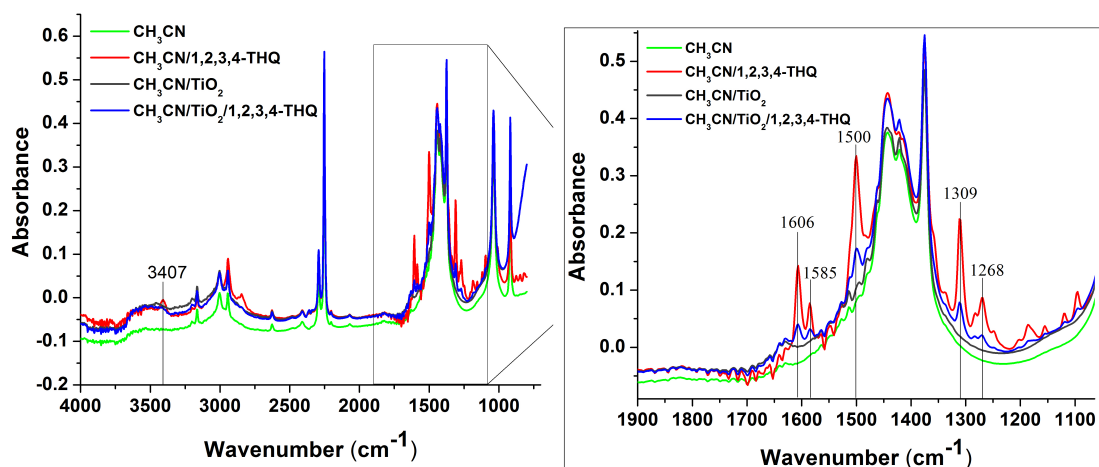


Figure 3.8.: FTIR spectra of CH<sub>3</sub>CN, CH<sub>3</sub>CN/THQ, CH<sub>3</sub>CN/TiO<sub>2</sub>, and TiO<sub>2</sub>/THQ. The right figure shows magnification of the selected area in the left figure. All measurements were performed at the same concentration of the catalyst and substrate as appropriate to the organic reaction condition.

### 3.3. Dehydrogenation in the presence of molecular oxygen

Visible-light-mediated dehydrogenation of N-heterocycles in the presence of molecular oxygen was performed at room temperature with bare TiO<sub>2</sub> or surface modified TiO<sub>2</sub> photocatalyst. In this regard, 1,2,3,4-tetrahydroquinoline (THQ) was used as a probe molecule and commercial TiO<sub>2</sub> UV100 or TiO<sub>2</sub> P25 were employed as a photocatalyst. Since it has been observed from UV-vis spectroscopy results that the mixture of TiO<sub>2</sub>-THQ has an absorption edge up to 460 nm (Figure 3.6), the feasible dehydrogenation of THQ was carried upon LED visible light ( $\lambda_{max}$ =453 nm) illumination. The experiment was performed in 20 mL glass vials in the presence of 0.4 mmol THQ, 10 mg of the photocatalyst in 4 mL acetonitrile CH<sub>3</sub>CN after purging the reaction mixture with molecular oxygen gas. Furthermore, by purging the same reaction mixture with argon gas, the viability of this process was analyzed in an inert atmosphere. The quinoline formation as the desired product was analyzed by GC-FID using the linear equations obtained from the calibration curves (see Section 2.6.1). The obtained results are summarized in Table 3.2. As it can be seen from Table 3.2, entries 1 and 2, the dehydrogenation of the THQ over TiO<sub>2</sub> UV100 and TiO<sub>2</sub> P25 photocatalysts was practical. During 24 h photocatalytic dehydrogenation reaction of THQ in the presence of TiO<sub>2</sub> UV100 photocatalysts, 324  $\mu$ mol of THQ was converted, and only 140  $\mu$ mol



quinoline was produced as the desired product. These results showed that although the visible-light-mediated dehydrogenation reaction was feasible in TiO<sub>2</sub> suspension, the reaction selectivity was still poor (Table 3.2, entry 1).

Table 3.2.: Dehydrogenation of THQ over TiO<sub>2</sub><sup>a</sup>.

Entry	Catalysts	Converted amount (μmol) <sup>b</sup>	Quinoline amount (μmol) <sup>b</sup>
1	TiO <sub>2</sub> UV100	324	140
2	P25 TiO <sub>2</sub>	96	40
3 <sup>c</sup>	TiO <sub>2</sub> UV100	-	-
4 <sup>d</sup>	No catalyst	12	8
5 <sup>e</sup>	No light	-	-
6	Ni(II)/UV100	372	228

<sup>a</sup> Reaction conditions: 10 mg photocatalyst TiO<sub>2</sub> (UV100 or P25) or Ni(II)/UV100, 24 h visible light illumination (LED lamp,  $\lambda_{max}$ =453 nm, 4 mW/cm<sup>2</sup>), 1 atm O<sub>2</sub>, 400 μmol THQ, 4 mL CH<sub>3</sub>CN. <sup>b</sup> converted amount and quinoline amount are calculated according to the GC-FID calibration using benzyl alcohol as an internal standard. <sup>c</sup> Argon atmosphere. <sup>d</sup> no TiO<sub>2</sub>, <sup>e</sup> in dark.

Over TiO<sub>2</sub> P25 photocatalysts, the conversion of the THQ and the formation of quinoline were three times less than the results when TiO<sub>2</sub> UV100 was used as a photocatalyst (Table 3.2, entry 2). Nevertheless, the conversion of the THQ was completely hindered (Table 3.2, entry 3) when the reaction was carried out the absence of O<sub>2</sub>. It was essential to carry out control experiments to evaluate the significance of photocatalyst and visible light for the oxidative dehydrogenation of THQ (Table 3.2, entries 4 and 5). The insignificant amount of THQ conversion and quinoline formation during the photolysis experiment showed the importance of the TiO<sub>2</sub> (Table 3.2, entry 4). Moreover, the dark reaction further validated the importance of visible light in the dehydrogenation reaction, as there was no catalytic reaction in the absence of light (Table 3.2, entry 5). After an initial evaluation of the appropriate conditions of the dehydrogenation reaction, experiments were conducted with the presence of different solvents, such as methanol, ethanol, and 2-propanol, and the results were compared with acetonitrile. The obtained results are presented in Figure 3.9. Generally, the dehydrogenation of THQ in all solvents resulted in a conversion of up

to 350  $\mu\text{mol}$ . However, when methanol and ethanol were used as a solvent, the amount of quinoline formation was significantly lower compared to 2-propanol and acetonitrile. 2-propanol and acetonitrile performance was almost similar in the photocatalytic formation of quinoline, while 2-propanol showed slightly higher product formation. Thus the highest formation of quinoline was 172  $\mu\text{mol}$  with 2-propanol solvent and 140  $\mu\text{mol}$  with acetonitrile. It should also be noted that all these experiments were carried out three times in order to derive an experimental error ( $\pm 6\%$ ).

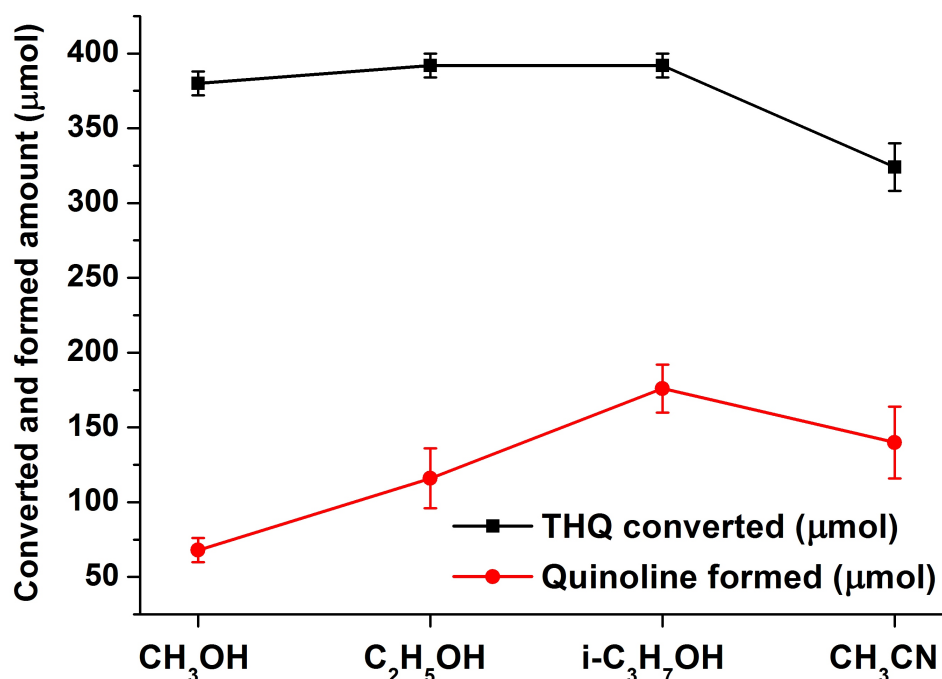


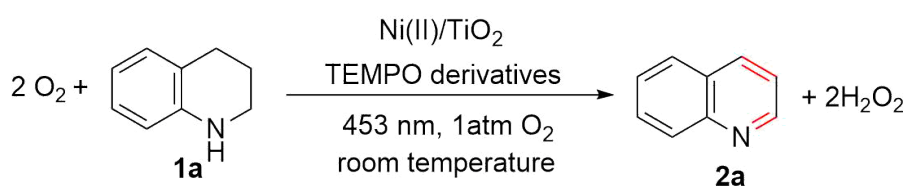
Figure 3.9.: The photocatalytic dehydrogenation of THQ in the presence of different solvents. Reaction conditions: 10 mg photocatalyst  $\text{TiO}_2$  (UV100), 24 h visible light illumination (LED lamp,  $\lambda_{\text{max}}=453$  nm,  $4$  mW/cm<sup>2</sup>), 1 atm  $\text{O}_2$ , 400  $\mu\text{mol}$  THQ ( $50.2\mu\text{L}$ ), 4 mL of solvent. Conversion and yield are calculated according to the GC calibration using benzyl alcohol as an internal standard.

### 3.3.1. Effect of different TEMPO derivatives

In order to increase the yield and the selectivity, different derivatives of TEMPO were employed in an amount of 20 mol% with respect to the reactant. The obtained data are shown in Table 3.3. Using the improved photocatalyst, 0.1 wt% Ni(II) ion-grafted  $\text{TiO}_2$ , TEMPO, and three other TEMPO derivatives were compared in the dehydrogenation reaction, establishing 4-amino-TEMPO as the

optimal redox mediator for improving the selectivity of the dehydrogenation reaction (Table 3.3). Inadequate to the reactions carried out without TEMPO derivatives, the reactions employing 4-amino-TEMPO and Ni(II)/UV100 shows better yield and selectivity in comparison with the reaction employing UV100 and 4-amino-TEMPO (Table 3.3, entry 6).

Table 3.3.: The photocatalytic dehydrogenation of THQ in the presence of different redox mediators <sup>a</sup>.



Entry	Catalysts	Redox mediator	Converted amount ( $\mu\text{mol}$ ) <sup>b</sup>	Quinoline amount ( $\mu\text{mol}$ ) <sup>b</sup>
1	UV100	TEMPO	344	284
2	UV100	4-amino-TEMPO	392	316
3	Ni(II)/UV100	TEMPO	320	232
4	Ni(II)/UV100	4-hydroxy-TEMPO	276	232
5	Ni(II)/UV100	4-oxo-TEMPO	372	308
6	Ni(II)/UV100	4-amino-TEMPO	400	368 (364 <sup>c</sup> )

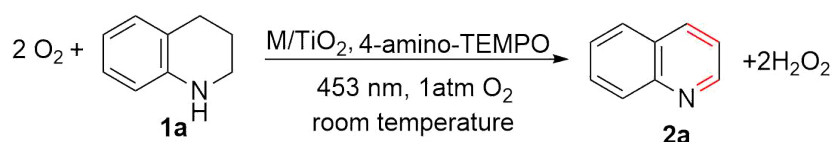
<sup>a</sup> Reaction conditions: 10 mg photocatalyst Ni(II)/TiO<sub>2</sub> (UV100), 24 h visible light illumination (LED lamp,  $\lambda_{max}$ =453 nm, 4 mW/cm<sup>2</sup>), 1 atm O<sub>2</sub>, 400  $\mu\text{mol}$  THQ (50.2  $\mu\text{L}$ ), 4 mL i-PrOH, 20 mol% redox mediators with respect to the reactant. <sup>b</sup> converted and quinoline amount are calculated according to the GC calibration using benzyl alcohol as an internal standard. <sup>c</sup> isolated yield.

### 3.3.2. Effect of grafting metal ions on THQ dehydrogenation

To further improve selectivity and yield, the surface of the TiO<sub>2</sub> UV100 nanoparticles was grafted with metal ions or photodeposited with a noble metal. Surface modification of TiO<sub>2</sub> with different transition metal nanoparticles or metal ions has been reported in the literature to enhance the photocatalytic performance where the co-catalyst act as an electron shuttle between the conduc-

tion band of TiO<sub>2</sub> and surface adsorbed molecular oxygen. Obviously, after 24 h photocatalytic reactions, all metal ions grafted UV100 samples (Cu<sup>2+</sup>, Ni<sup>2+</sup>, Co<sup>2+</sup>, Fe<sup>3+</sup>, Nb<sup>5+</sup>) consistently show improved yield and selectivity when compared with bare UV100 (Table 3.4). On the other hand, UV100 samples with 0.1 wt% photodeposited noble metal (Pd, RuO<sub>2</sub>, and Rh) show the significantly lower conversion of the probe compound (60%, 49%, and 30%, respectively) than UV100 even though the selectivity remained high (97%, 100%, and 88%) (Table 3.4). In the next step, the photocatalytic reactions were performed in the presence of different metal-oxides in an aerobic system using 2-propanol as an optimal solvent. However, it has been observed that when employing ZnO, WO<sub>3</sub>, and Al<sub>2</sub>O<sub>3</sub> as a photocatalyst only drastically low yields (3%, 5%, and 2%, respectively) were achieved. Moreover, silica has not shown any photocatalytic performance.

Table 3.4.: Effect of grafted transition metals on the aerobic oxidative dehydrogenation of THQ<sup>a</sup>.

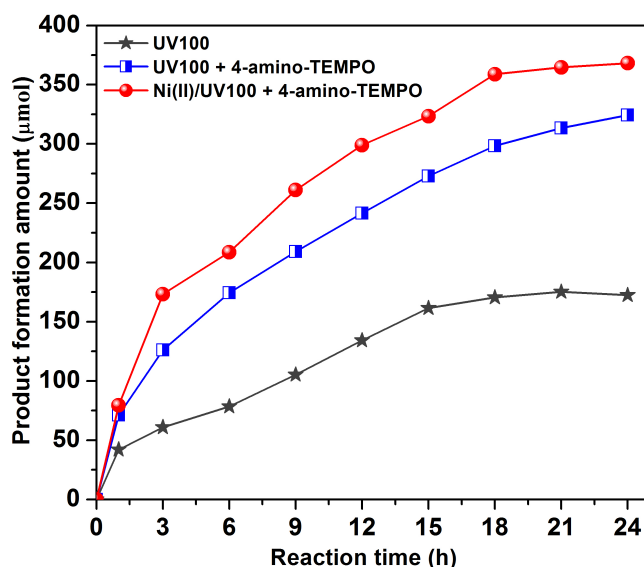


Entry	Catalysts	Converted amount ( $\mu\text{mol}$ )	Quinoline amount ( $\mu\text{mol}$ ) <sup>b</sup>
1	UV100	392	316
2	Cu(II)/UV100	400	364
3	Ni(II)/UV100	400	364
4	Nb(V)/UV100	380	360
5	Fe(III)/UV100	400	360
6	Co(II)/UV100	400	372
7	Pd(0)/UV100	248	240
8	RuO <sub>2</sub> /UV100	196	196
9	Rh(0)/UV100	136	120

<sup>a</sup> Reaction conditions: 10 mg photocatalyst, 24 h visible light illumination (LED lamp,  $\lambda_{max}=453 \text{ nm}$ ,  $4 \text{ mW/cm}^2$ ), 1 atm O<sub>2</sub>, 0.4 mmol THQ (50.2  $\mu\text{L}$ ), 4 mL CH<sub>3</sub>CN, 20 mol% 4-amino-TEMPO (0.08 mmol) as a redox mediator with respect to the reactant. <sup>b</sup> calculated according to the GC calibration using benzyl alcohol as an internal standard. <sup>c</sup> ratio of yield over conversion.

### 3.3.3. Kinetics of the oxidative THQ dehydrogenation

The kinetic experiments were performed employing the optimized reaction conditions in the presence and the absence of 0.08 mmol 4-amino-TEMPO using bare and 0.1 wt% Ni(II) grafted UV100 as photocatalysts. During 24 h of illumination with visible light, the starting material was gradually converted to completion in the presence of all three photocatalysts. The increase of the yield and the selectivity of the dehydrogenation reaction of THQ in the presence of the three different photocatalysts during 24 hours (measured in 3 hours time intervals) have been calculated from GC-FID data (Eqs (2.3-2.5)) and are shown in Figure 3.10. As becomes obvious from Figure 3.10 (top), large amounts of quinoline are produced in the presence of Ni (II)-grafted UV100 and 4-amino-TEMPO. Significantly lower amounts of product were obtained with ungrafted TiO<sub>2</sub> in the presence and the absence of 4-amino-TEMPO. Accordingly, the yields at a point in time during illumination calculated from the data given in Figure 3.10 (a) were found to decrease in the order Ni(II)/UV100 + 4-amino-TEMPO > UV100 + 4-amino-TEMPO > UV100 (Figure 3.10 (bottom)). The results reveal that 4-amino-TEMPO significantly improves the reaction selectivity. Concomitantly, the selectivity was observed to be ~10% higher when Ni(II)-grafted UV100 is used instead of bare UV100.



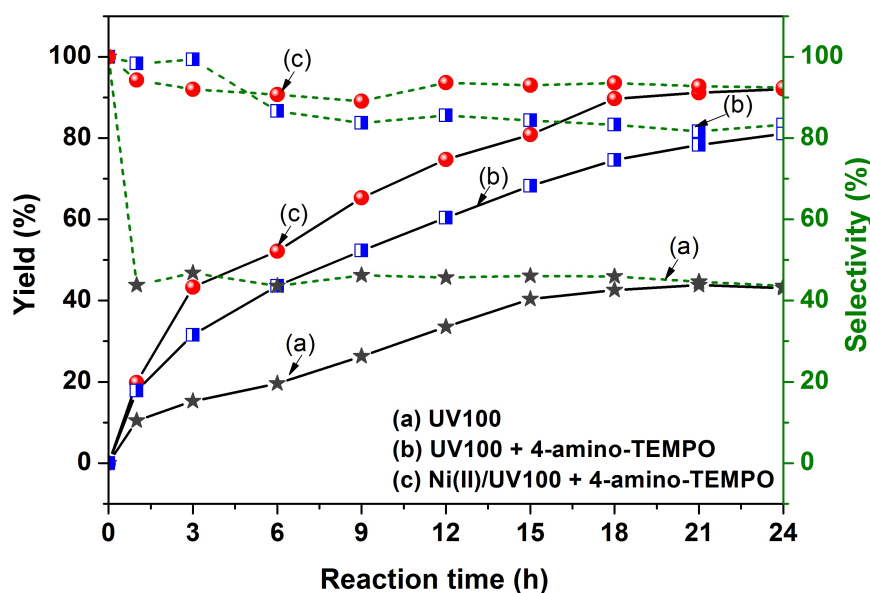
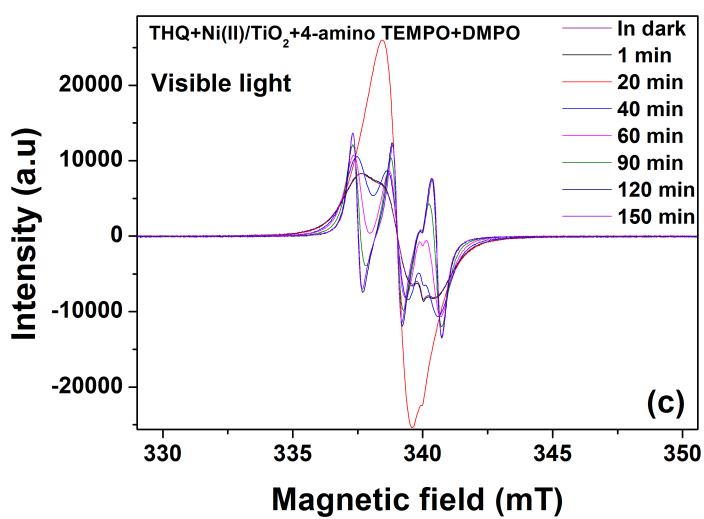
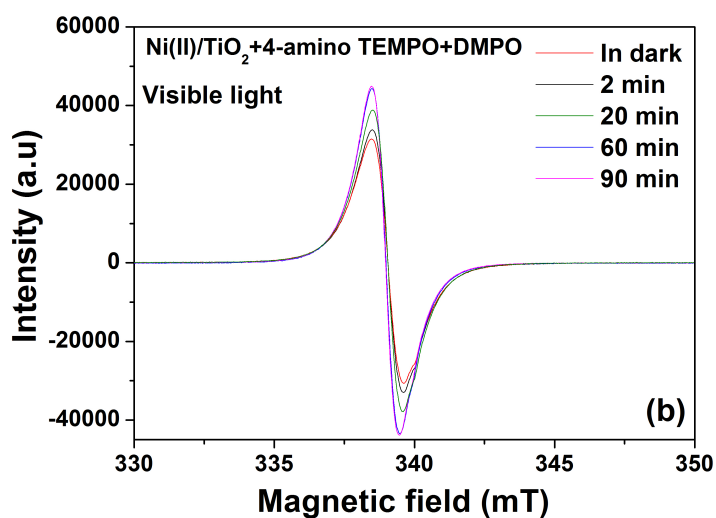
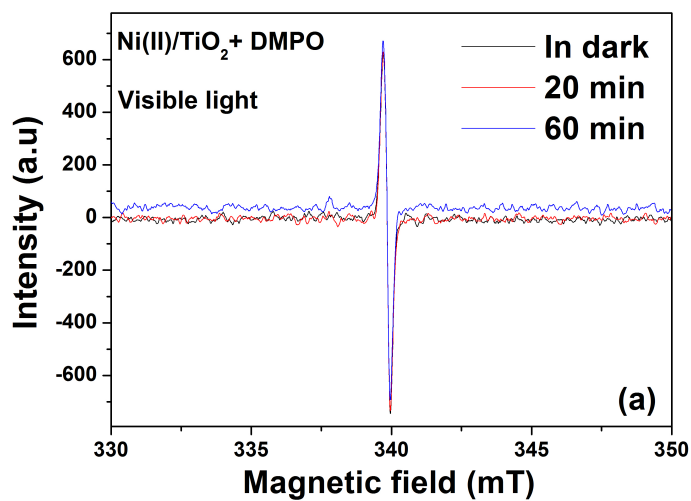


Figure 3.10.: Amounts of quinoline formation during 24 h of illumination (top) and time-dependent change in the yield (black solid lines) and selectivity (short dashed green lines) (bottom) in the presence of UV100 (gray star), UV100+ 4-amino-TEMPO (blue square), and N(II)/UV100+ 4-amino-TEMPO (red sphere). Reaction conditions: 10 mg photocatalysts (UV100 or Ni (II)-grafted UV100), LED lamp,  $\lambda_{max}=453$  nm,  $4$  mW/cm<sup>2</sup>, 1 atm O<sub>2</sub>, 400  $\mu$ mol THQ, 0.08 mmol 4-amino-TEMPO, 4 mL i-PrOH. Yield and selectivity are calculated according to the GC calibration using benzyl alcohol as an internal standard.

### 3.3.4. Superoxide radical anion generation studies by EPR

In-situ EPR spectroscopy was performed to test the formation of the light-induced superoxide radical anion (O<sub>2</sub><sup>-•</sup>) during visible light illumination. The EPR spectra were recorded at room temperature. In the first step, the suspensions were prepared under the same reaction conditions applied to the oxidative dehydrogenation process. Thus, before the test, the appropriate ratio of photocatalyst, THQ, 4-amino TEMPO was added into the glass vial containing 4 mL of acetonitrile and sonicated at approximately 5 min in order to obtain a homogeneous suspension. 1 mL of this suspension was transferred to the Eppendorf tube, and 20  $\mu$ L of 20 mM of DMPO was immediately added to the mixture as a spin trapping agent. For the control experiments, Ni(II)/TiO<sub>2</sub> photocatalyst in acetonitrile in the absence of THQ and 4-amino-TEMPO, Ni(II)/TiO<sub>2</sub> photocatalyst in acetonitrile and 4-amino-TEMPO in the absence of THQ, and only acetonitrile in the

absence of Ni(II)/TiO<sub>2</sub> photocatalyst and 4-amino-TEMPO suspensions were prepared. DMPO was used in all experimental conditions. Subsequently, the mixture was shaken by hand and purged with oxygen. The measurements were carried out in an EPR capillary tube. For the purpose of comparison, the experiments were carried out upon visible light (Figure 3.11 (a)-(c), and (e)) and UV-vis light (Figure 3.11 (d)) illumination. Figure 3.11 (a) demonstrates the EPR spectra of Ni(II)/TiO<sub>2</sub> photocatalyst in acetonitrile in the presence of DMPO in the dark and upon visible light illumination. As seen from these results, the formation of the reactive oxygen species was not realized due to the inherent limitation of the photoexcitation of titania upon visible light illumination. When 4-amino-TEMPO introduced to the system, a signal at 338.5 mT emerged, demonstrating the trapped electrons on the oxygen vacancies of TiO<sub>2</sub>. Upon illumination, the signal intensity slightly increased. However, usually the formation of O<sub>2</sub><sup>-•</sup> upon illumination and trapped by DMPO exhibit three hyperfine signals which were not observed in this system ((Figure 3.11 (b)). Moreover, no EPR signal was observed when pure DMPO was irradiated in acetonitrile or when the experiment was performed in the dark (Figure 3.11 (e)). Figure 3.11 (c) and (d) present the EPR results after the addition of THQ to the TiO<sub>2</sub> suspension in acetonitrile in the presence of DMPO and 4-amino-TEMPO. Thus as observed by UV-vis spectroscopy, THQ forms a surface complex with TiO<sub>2</sub>, which absorbs visible light. In the presence of molecular oxygen and DMPO, photogenerated O<sub>2</sub><sup>-•</sup> produces a DMPO-O<sub>2</sub><sup>-•</sup> radical that could be detected by EPR spectroscopy (Figure 3.11 (c)). As expected, the three hyperfine signals emerged upon UV-vis and visible light illumination. These signals correspond to the DMPO-O<sub>2</sub><sup>-•</sup> adduct. It could be seen from Figure 3.11 (d) the DMPO-O<sub>2</sub><sup>-•</sup> adduct formation rate upon UV-vis irradiation was significantly faster than the illumination under visible light. When the sample was irradiated longer time under UV light, the signal intensity decreased, and new peaks emerged. (Figure 3.11 (d)) This indicates the decomposition of DMPO-O<sub>2</sub><sup>-•</sup> and the generation of a nitroxide-like radical. In contrary, under visible light illumination it was observed that more stable DMPO-O<sub>2</sub><sup>-•</sup> adducts are generated ((Figure 3.11 (c)).





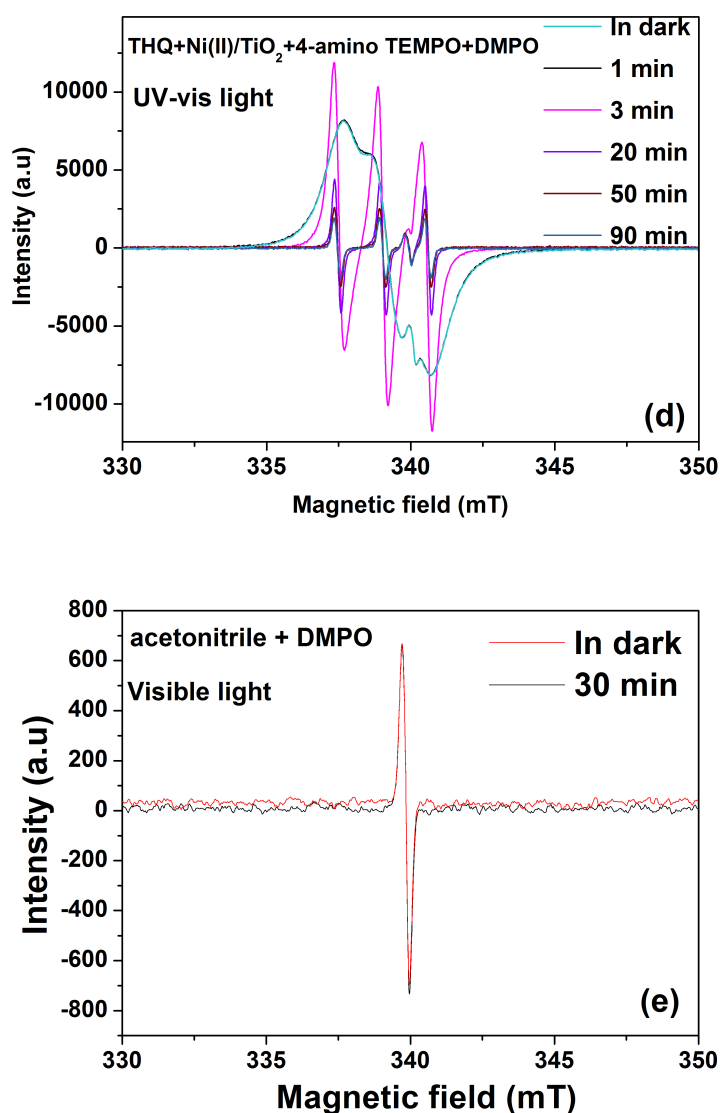


Figure 3.11.: EPR spectra of (a) Ni(II)/TiO<sub>2</sub> photocatalyst in acetonitrile in the presence of DMPO in the dark and under visible light illumination (b) Ni(II)/TiO<sub>2</sub> photocatalyst in acetonitrile in the presence of DMPO and 4-amino-TEMPO in the dark and under visible light illumination (c) Ni(II)/TiO<sub>2</sub> photocatalyst in acetonitrile in the presence of THQ, DMPO and 4-amino-TEMPO in the dark and upon visible light illumination (d) Ni(II)/TiO<sub>2</sub> photocatalyst in acetonitrile in the presence of THQ, DMPO and 4-amino-TEMPO in dark and upon UV-vis light illumination (e) acetonitrile in the presence of DMPO in the dark and upon visible light illumination. The ratio of the experimental components were kept as same as the optimized reaction condition. LED lamp was used as a visible light source,  $\lambda_{max} = 453 \text{ nm}$ ,  $4 \text{ mW/cm}^2$ . Xe lamp was employed for the UV-vis light irradiation,  $\lambda_{max} = 300\text{--}450 \text{ nm}$

### 3.3.5. Detection of H<sub>2</sub>O<sub>2</sub> after THQ dehydrogenation

For complete dehydrogenation of THQ, the reaction requires the removal of two equivalent molecules of H<sub>2</sub>O<sub>2</sub>. The reaction mixture containing the appropriate amount of TiO<sub>2</sub> UV100 and substrate (THQ) in 2-propanol solvent was found to be yellowish-white prior to photocatalytic reactions. However, in the oxygen atmosphere, the color of the reaction mixture turned dark brown after 24 h of photocatalytic reaction under visible light illumination (Figure 3.12 A1).

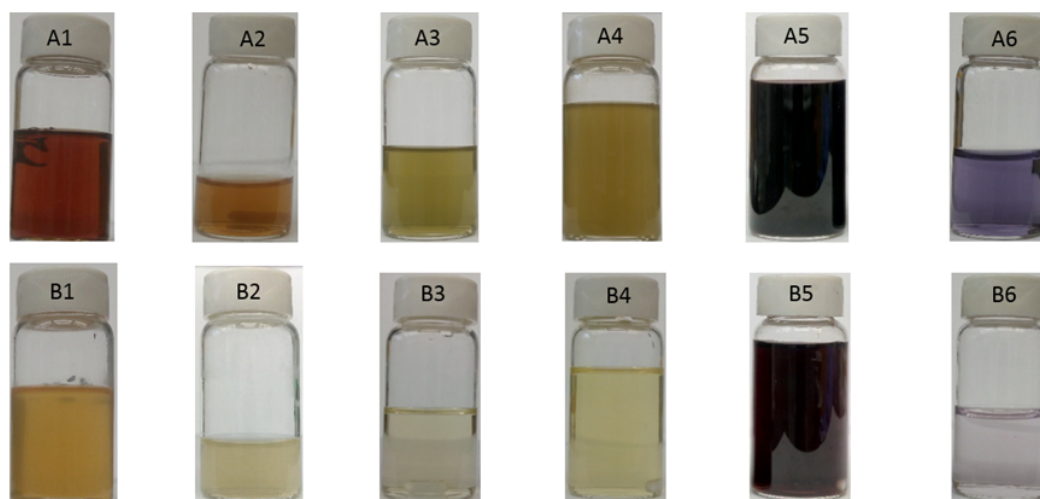


Figure 3.12.: Detection of H<sub>2</sub>O<sub>2</sub> after oxidative dehydrogenation of THQ. Experimental conditions: The solution obtained after dehydrogenation reaction of 1,2,3,4-tetrahydroquinoline using UV-100 as a photocatalyst (A1). The solution obtained after dehydrogenation reaction of 1,2,3,4-tetrahydroquinoline using UV-100 as a photocatalyst and 4-amino-TEMPO (B1).

Interestingly, when 20 mol% 4-amino-TEMPO was introduced to the reaction mixture and was illuminated in the oxygen atmosphere for 24 h, the reaction color remained yellowish-white. In fact, it was found that the selectivity and product formation amount of the former reaction was drastically low compared to the latter reaction (see Table 3.2 entries 1). Since the interaction of H<sub>2</sub>O<sub>2</sub> with TiO<sub>2</sub> UV100 forms a visible-light-responsive complex that affect its color change, it was thought that this dark color might indicate the surface complexation between H<sub>2</sub>O<sub>2</sub> and TiO<sub>2</sub> UV100. It was assumed that 4-amino-TEMPO could degrade the generated H<sub>2</sub>O<sub>2</sub> and thus clean the surface of TiO<sub>2</sub> UV100. Therefore the amount of photogenerated H<sub>2</sub>O<sub>2</sub> was analytically studied. The formation of H<sub>2</sub>O<sub>2</sub> in the reaction mixture was detected with KI by slightly

changing the previously reported method. [134] Thus, after the dehydrogenation reactions of 1,2,3,4-tetrahydroquinoline in the presence and in the absence of 4-amino-TEMPO, the reaction mixture was separated from the catalyst by centrifugation in order to detect the hydrogen peroxide content by titration. The clear reaction solution was diluted with DI water to 15 mL (Figure 3.12, A1 and B1). To a 20 mL scintillation vial, 2 mL from the diluted reaction mixture (Figure 3.12, A1 and B1) was added and additionally diluted with 5 mL of Milli-Q water with stirring in order to get a lighter-colored solution (Figure 3.12, A2 and B2). 3 mL of Ammonium molybdate and H<sub>2</sub>SO<sub>4</sub> solution was added which turned the color of the solution to the pale yellow (Figure 3.12, A3 and B3). To these solution 6 mL 10% KI solution was added. The color of the solution changed to darker yellow (Figure 3.12, A4 and B4) due to the formation of molecular iodine. As becomes obvious from the pictures, the color was more yellowish at A3. In the last step, 2 mL of freshly prepared starch solution was added to the solution and the color changes to dark blue-black (Figure 3.12, A5 and B5). The color of the B5 solution was lighter in comparison with the A5 solution. This observation supports the assumption that 4-amino-TEMPO is reducing hydrogen peroxide. When 2 mL of the dark blue solution was diluted with 10 mL of DI water, a more visible difference is observed (Figure 3.12, A6 and B6). The lighter color confirmed the presence of a lower amount of H<sub>2</sub>O<sub>2</sub> in the reaction mixture with 4-amino-TEMPO.

### 3.3.6. Recycling of the photocatalysts

Since the leaching of the impregnated active metal ion sites during the reaction, phase transformation, and agglomeration of nanoparticles is ubiquitous in heterogeneous photocatalysis, the reusability of 0.1 wt% Ni(II)/TiO<sub>2</sub> was examined by performing four consecutive experimental runs. Conversion of the probe compound, as well as the yield of the product and the selectivity of product formation, was found to be stable even after 4 experimental cycles (Figure 3.13). The surface area of the photocatalyst decreased from 318 m<sup>2</sup>/g to 217 m<sup>2</sup>/g after the 2<sup>nd</sup> cycle of the reaction but remained relatively constant after the 3<sup>rd</sup> and 4<sup>th</sup> cycles (210 and 206 m<sup>2</sup>/g, respectively). However, the surface area was restored from 206 m<sup>2</sup>/g after the 4<sup>th</sup> cycle to 313 m<sup>2</sup>/g by dispersing the used photocatalyst in 20 mL deionized water and illumination with a 500 W solar simulator lamp for 2 hours at ambient temperature (Figure 3.14). The photocatalyst's color also turned from pale yellow to pure white during illumination, and the surface-cleaned catalyst dis-

played high reactivity (91% yield) and selectivity (93%) in the 5<sup>th</sup> cycle. N<sub>2</sub> adsorption-desorption isotherm studies show that although the catalyst's mesoporosity decreases after the 4<sup>th</sup> cycle, the selectivity does not decrease drastically.

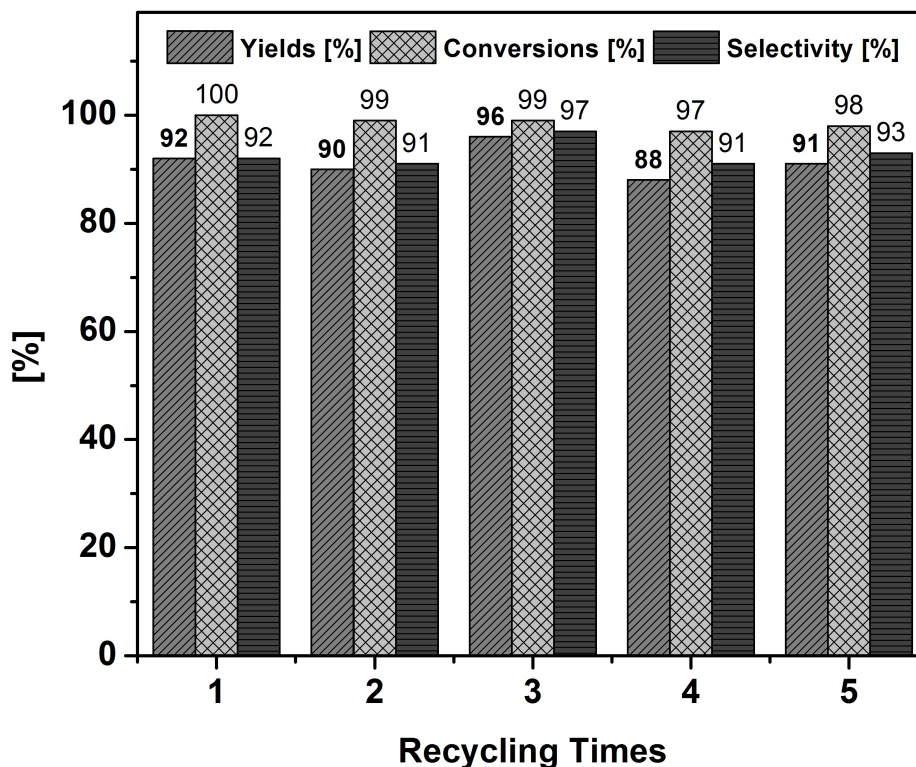


Figure 3.13.: 5 times consequence recycling of the Ni(II)/TiO<sub>2</sub> photocatalyst in aerobic dehydrogenation of THQ. The 5<sup>th</sup> run of the experiment was performed after recovering the surface of 0.1 wt% Ni grafted TiO<sub>2</sub> via illumination with 500W solar simulator light. The reaction conditions were kept as same as presented in the procedure.

Additionally, cleaning the catalyst's surface by illumination led to recovering the pore size as evinced by adsorption-desorption isotherms. The pore size of the used photocatalyst was found to be only 3 m<sup>2</sup>/g lower than the pore size of the non-used 0.1 wt% Ni(II)/TiO<sub>2</sub> photocatalyst. (Figure 3.14). XRD and ICP-OES measurements did not reveal poisoning and leaching of the photocatalyst, respectively (Section 2.3.2 for sample preparation for the ICP-OES measurement). XRD patterns for bare TiO<sub>2</sub>, 0.1 wt% Ni(II)/UV100 before the 1<sup>st</sup> cycle, and after the 4<sup>th</sup> cycle displayed the typical crystal structure of the anatase phase without showing the peaks corresponding to the nickel ion (Figure 3.15). Moreover, the ICP-OES measurement showed that the content of nickel ions before and after the reaction did not change drastically (before and after the 4<sup>th</sup> cycle

of reaction the content of nickel was 0.08 wt% with respect to  $\text{TiO}_2$ .

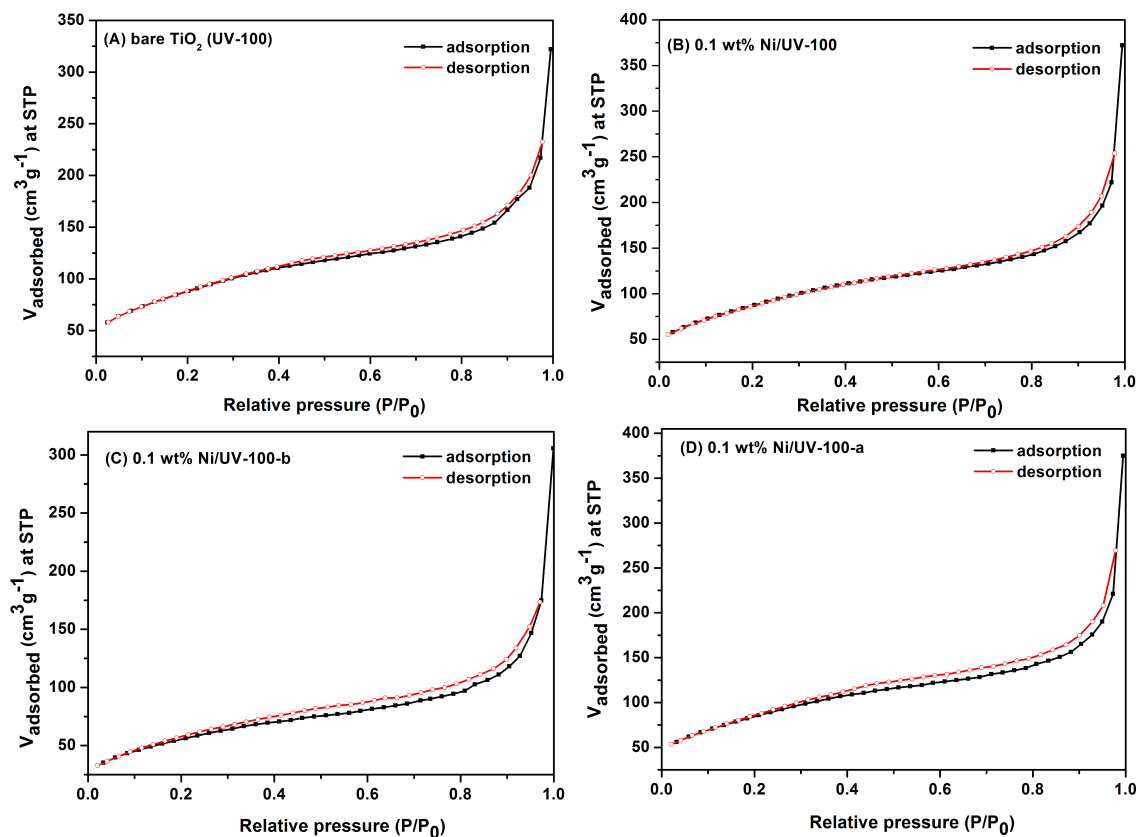


Figure 3.14.: Oxidative dehydrogenation of 1,2,3,4-tetrahydroquinoline: recycling of 0.1 wt% Ni(II)/ $\text{TiO}_2$ . Reaction conditions: 10 mg photocatalyst, 24 hours visible light illumination (Nitrogen physisorption isotherms for (A) bare  $\text{TiO}_2$  (UV-100); (B) surface grafted 0.1 wt% Ni(II)/UV-100 before reaction, (C) surface grafted 0.1 wt% Ni(II)/UV-100 after 4<sup>th</sup> cycle reaction cleaned by washing 3 times with acetone, (D) surface grafted 0.1 wt% Ni(II)/UV-100 after 4<sup>th</sup> cycle reaction cleaned by illumination with solar simulator (500 W) for 2 hours.

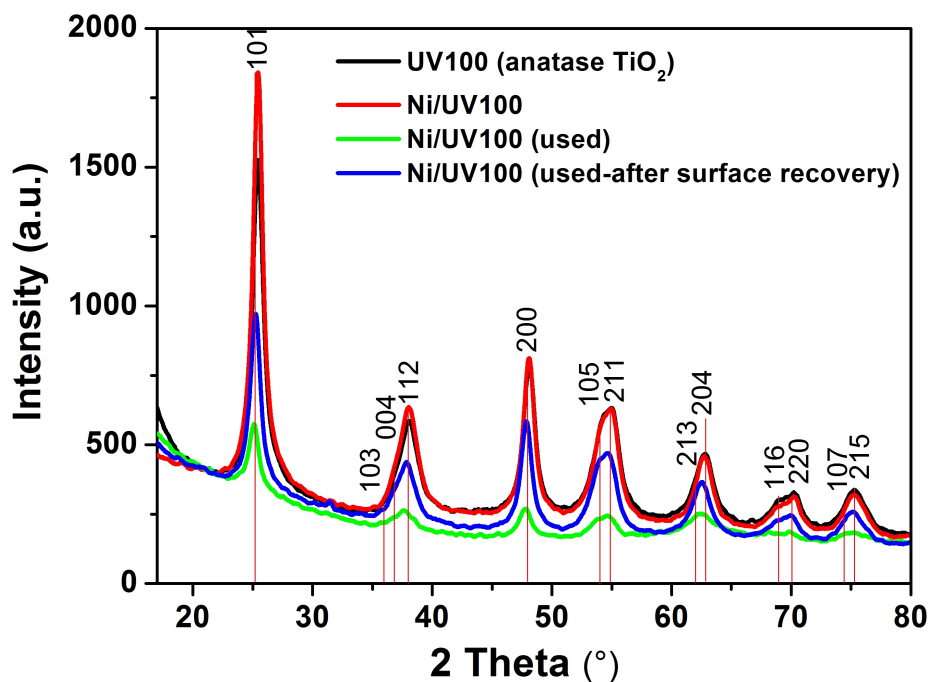


Figure 3.15.: XRD pattern of the bare  $\text{TiO}_2$  (UV-100) (black line), 0.1 wt% Ni grafted  $\text{TiO}_2$  before reaction (red line), used 0.1 wt% Ni grafted  $\text{TiO}_2$  after 3 cycles of the reaction (blue line), and used 0.1 wt% Ni grafted  $\text{TiO}_2$  after cleaning with 500W solar simulator light (green line).

### 3.3.7. ATR-FTIR measurements before and after THQ dehydrogenation

ATR-FTIR spectroscopy measurements were conducted to detect functional groups of organic compounds adsorbed on the catalyst's surface after the dehydrogenation reaction. Characteristic bands at  $2950\text{ cm}^{-1}$ ,  $2370\text{ cm}^{-1}$ , and  $1640\text{ cm}^{-1}$ , assigned to the stretching of C-H, C-O, and O-H groups in *i*-PrOH, respectively, and the broadband at  $3400\text{ cm}^{-1}$ , which corresponds to the OH stretching of surface-adsorbed water molecules, were observed in all spectra (Figure 3.16). The intensity of this broadband at  $3400\text{ cm}^{-1}$  was found to decrease after the 3<sup>rd</sup> cycle. The decline of the OH stretching band's intensity was rationalized by a gradual accumulation of organic compounds at the catalyst's surface that resulted in a displacement of the surface-adsorbed water by organic compounds. On the other hand, the band at  $1681\text{ cm}^{-1}$ , which was attributed to the C=N stretching, was observed only after the 3<sup>rd</sup> cycle and disappeared after the catalyst was subjected to surface cleaning by simulating solar light illumination. Characteristic peaks of aromatic rings in the range of  $1561\text{ cm}^{-1}$  (C=C),  $1429\text{ cm}^{-1}$  (C-C), and  $1276\text{ cm}^{-1}$  (Ar-N), were

detected only in the used 0.1 wt% Ni(II)/TiO<sub>2</sub>. This observation was expected as those peaks were assigned to the imine products that were bound to the Lewis acidic TiO<sub>2</sub> surface. [178]

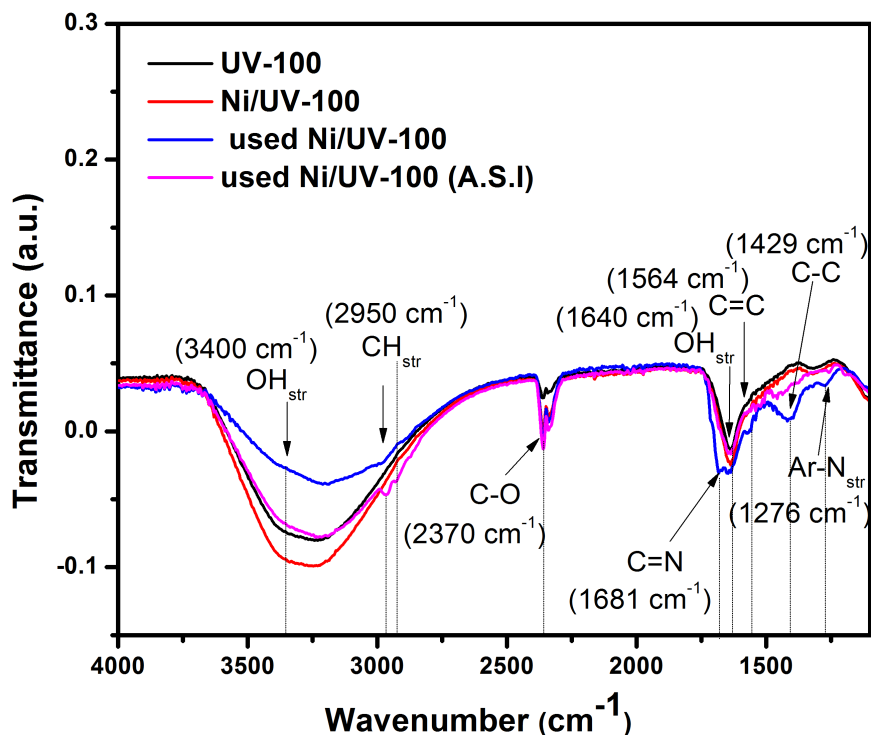


Figure 3.16.: ATR-FTIR spectra of the bare TiO<sub>2</sub> (UV-100) (black line), 0.1 wt% Ni(II) grafted TiO<sub>2</sub> before reaction (red line), used 0.1 wt% Ni(II) grafted TiO<sub>2</sub> after 3 cycles of the reaction (blue line), and used 0.1 wt% Ni(II) grafted TiO<sub>2</sub> after cleaning with 500W solar simulator light (magenta line).

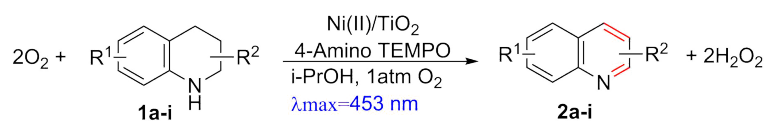
### 3.3.8. N-heterocyclic amines in aerobic dehydrogenation

The oxidative dehydrogenation results of the broad substrate scope of the N-heterocycles will be presented in this section. The yield of the products is measured quantitatively by an isolated compound with column chromatography. The purity of the compounds was confirmed by <sup>1</sup>H and <sup>13</sup>C NMR spectroscopy. The NMR characterization data of the product are provided in the Appendix. The aerobic dehydrogenation of tetrahydroquinolines (THQs), tetrahydroquinolines (THisoQs), indolines, quinoxaline, and imidazoline were investigated under the optimized reaction conditions inspired by the high photocatalyst activity of 0.1 wt% Ni(II)/UV100 and 20 mol% 4-amino-TEMPO in *i*-PrOH and an O<sub>2</sub> atmosphere (1 atm) at room temperature (Table 3.5 and Table 3.6). THQs bearing a methoxy (**1b**), methyl (**1c** and **1h**), chloride (**1g**), or both a methyl

and carboxyl group (**1i**) gave good to excellent yields of quinolines (74-94%). However, THQs having a nitro (**1f**) or a hydroxy group (**2d**) at C-7 failed to dehydrogenate. When the OH group was protected as a TBDMS (tert-butyldimethylsilyl) ether and then subjected to the standard conditions, the desired quinoline (**2e**) was isolated in 83% yield.

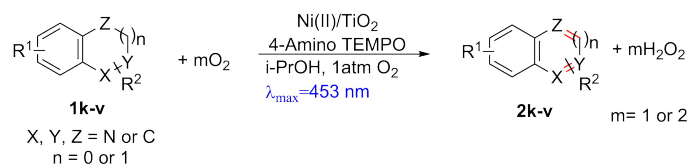
1,2,3,4-THisoQs reacted quite differently from the THQs as they easily afford the partial dehydrogenation product under the reaction conditions optimized for the dehydrogenation of THQs. The unsubstituted tetrahydroisoquinoline gave a mixture of the utterly dehydrogenated product (**2k**) and the partially dehydrogenated product (**2k\***) in 42% yield and 52% yield, respectively. Raising the reaction temperature to 47 °C improved the conversion to the completely dehydrogenated product, and the fully aromatized product **2m** was obtained in 75% yield. However, when the methyl substituent of 1-methyl-1,2,3,4-THisoQ is replaced by a larger group such as phenyl, the partially dehydrogenated product (**2n\***) was found to be the primary product with 54% yield with only 33% of the completely dehydrogenated product (**2n**) even when the temperature was raised to 47 °C. Interestingly, 6,7-dimethoxy-1,2,3,4-THisoQ only yields the completely dehydrogenated product (**2l**) in 81% yield at room temperature. The developed method was also applied to the dehydrogenation of indoline and 2-methylindoline under the optimized reaction conditions with slight changes (Table 3.6). Thus, the O<sub>2</sub> amount in the air was found to be sufficient to mediate the dehydrogenation of unsubstituted indoline to indole (**2o**) in 84% yield. The reactant's significant decomposition was observed when the reaction was performed in an O<sub>2</sub> atmosphere (1 atm), revealing that indoline is more reactive than the THQs. On the other hand, 2-methyl-substituted indoline was shown to be less reactive and more tolerant towards O<sub>2</sub> than unsubstituted indoline. An O<sub>2</sub> pressure of 1 atm was required to produce 2-methylindole (**2p**) in good yield (76%). 1,2,3,4-tetrahydroquinoxaline, which also exhibited good reactivity, yielded quinoxaline (**2v**) in 83% yield using 1 atm O<sub>2</sub> at room temperature. Similar to indolines and quinolines, dehydrogenation of 2-phenyl-2-imidazoline to 2-phenylimidazole (**2u**) was achieved with an excellent yield (93%) under optimized reaction condition.



Table 3.5.: Oxidative dehydrogenation of tetrahydroquinolines.<sup>a</sup>

Entry	Substrates	Products	Yield (%) <sup>b</sup>
1			91
2			94
3			91
4			n.d.
5			83
6			n.d.
7			92
8			74
9			93

<sup>a</sup> Reaction conditions: 10 mg photocatalyst, 24 h visible light illumination (LED lamp,  $\lambda_{\text{max}}=453 \text{ nm}$ ,  $4 \text{ mW/cm}^2$ ), 1 atm  $\text{O}_2$ , 0.4 mmol organic substrate, 0.08 mmol 4-amino-TEMPO, 4 mL i-PrOH, room temperature. <sup>b</sup> The yields are those of the isolated products.

Table 3.6.: Oxidative dehydrogenation of tetrahydroisoquinolines, indolines, 2-phenyl-2-imidazoline, and quinoxaline.<sup>a</sup>

Entry	Substrates	Products	Yield (%) <sup>b</sup>
1		 	42; 52*
3 <sup>c</sup>			81
2 <sup>d</sup>			75
4 <sup>d</sup>		 	33; 54*
5			84
6 <sup>e</sup>			76
7			93
8			83

<sup>a</sup> Reaction conditions: 10 mg photocatalyst, 24 h visible light illumination (LED lamp,  $\lambda_{\text{max}}=453 \text{ nm}$ ,  $4 \text{ mW/cm}^2$ ), 1 atm  $\text{O}_2$ , 0.4 mmol organic substrate, 0.08 mmol 4-amino-TEMPO, 4 mL i-PrOH, room temperature. <sup>b</sup> The yields are those of the isolated products. <sup>c</sup> 1:1  $\text{CH}_2\text{Cl}_2$  : i- $\text{C}_3\text{H}_7\text{OH}$ . <sup>d</sup> 47 °C.: i-PrOH was used as the solvent. <sup>e</sup> Air was used.

\*Partial dehydrogenation yield.

### 3.4. ADH of N-heterocyclic amines on surface modified TiO<sub>2</sub>

#### 3.4.1. Surface complexation between Rh/TiO<sub>2</sub> and N-heterocycles

As mentioned in Chapter 3.2, a prerequisite for the desired acceptorless dehydrogenation (ADH) reaction of N-heterocyclic amines is the adsorption of the reactant at the photocatalyst surface, yielding a visible-light-absorbing surface complex. UV-Vis absorption spectra of alcoholic suspensions containing substrate (THQ, THisoQ, indoline) and the metal-loaded photocatalyst 1 wt.% Rh/UV100 were measured (Figure 3.17). A significant redshift became obvious from Figure 3.17, indicating the formation of the desired surface complex. As expected, bare TiO<sub>2</sub> was found to be inactive in the dehydrogenation reaction of THQ (Table 4.2, entry 3) due to the hindered electron transfer from the conduction band of TiO<sub>2</sub> to H<sup>+</sup>.

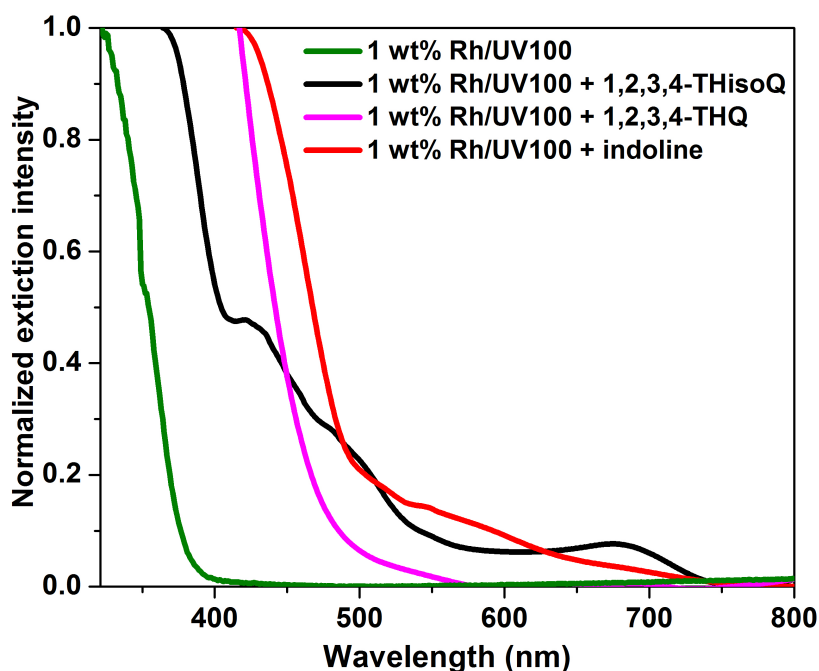


Figure 3.17.: Normalized extinction spectra of 1 wt.% Rh/TiO<sub>2</sub> (UV100) suspension containing THQ, 1,2,3,4-THisoQ, indoline and 8-Acetyl-5,6,7,8-THQ in 2 mL i-C<sub>3</sub>H<sub>7</sub>OH.

#### 3.4.2. Effect of different co-catalysts

TiO<sub>2</sub> loaded with Cu<sup>2+</sup>, Au<sup>0</sup>, RuO<sub>2</sub>, Pd<sup>0</sup>, Pt<sup>0</sup>, and Rh<sup>0</sup> nanoparticles have been employed as photocatalysts to enhance the necessary reduction of protons. The results are presented in Figure 3.18.

It becomes evident from these data that the highest yields are obtained with Pd<sup>0</sup>, Pt<sup>0</sup>, and Rh<sup>0</sup>. The order of activity of the metals was found to be Rh>Pt >Pd (Figure 3.18). RuO<sub>2</sub> and Au photodeposited TiO<sub>2</sub> showed dramatically low photocatalytic activity for the ADH reaction of THQ.

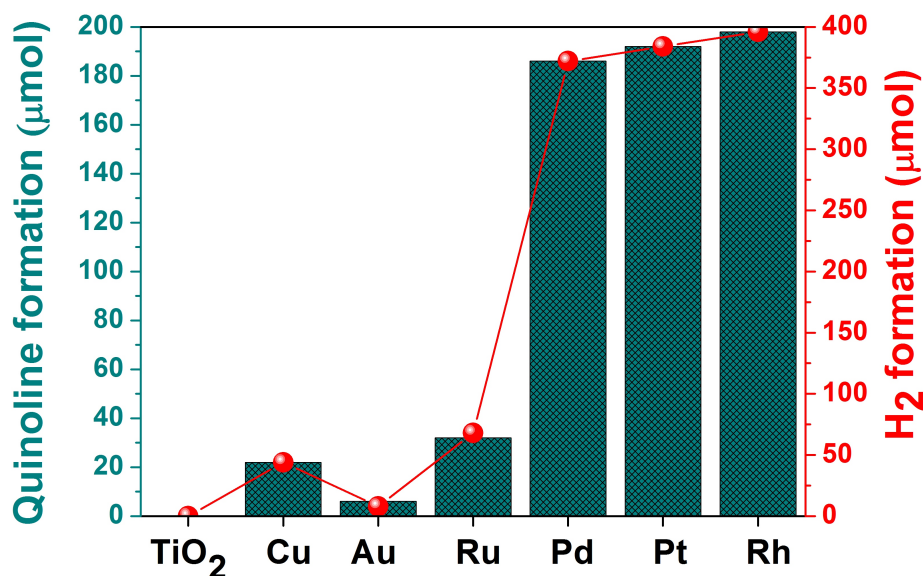


Figure 3.18.: Effect of different co-catalysts photodeposited TiO<sub>2</sub> on ADH reaction of THQ. <sup>a</sup> Reaction conditions: catalyst (5 mg), i-PrOH (2 mL), blue LED light ( $\lambda_{max}=453$  nm), Argon atmosphere, 24 h. The yields were determined by GC-FID using benzyl alcohol (50 mol%) as internal standard. The amount of produced molecular hydrogen were determined by GC-TCD.

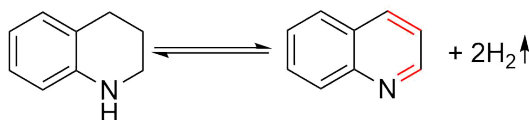
Pd/C and other transition metals ions, i.e., iron, nickel, niobium grafted TiO<sub>2</sub> (not shown in Table 3.7) did not show any photocatalytic activity for the ADH reaction of THQ. 1 wt% Cu (II) grafted TiO<sub>2</sub> (Figure 3.18) as well as Au, and Ru photodeposited TiO<sub>2</sub> revealed photocatalytic performance which was significantly low in comparison with the active noble metal nanoparticles. The results show that Pd, Pt, and Rh have comparable reactivity in the ADH reaction of THQ. Since Rh as a co-catalyst showed slightly higher efficiency, most of the experiments were carried out in the presence of rhodium photodeposited TiO<sub>2</sub>.

### 3.4.3. Solvent effect and control experiments

The experimental runs were performed with 1 wt% Rh/TiO<sub>2</sub> as the photocatalyst and THQ as the probe reactant in various solvents, i.e., methanol, ethanol, and acetonitrile. The results are

shown in Table 3.7, entries 2-4. The ADH of THQ in acetonitrile resulted in product formation with a moderate yield of quinoline (31 %) (Table 3.7, entry 2).

Table 3.7.: Control reactions for the ADH of THQ in an inert atmosphere.<sup>a</sup>



Entry	Catalysts	Solvent	Quinoline ( $\mu\text{mol}$ , %)	H <sub>2</sub> ( $\mu\text{mol}$ , (%))
1	1 wt% Rh/TiO <sub>2</sub>	i-PrOH	198 (99)	396 (99)
2	1 wt% Rh/TiO <sub>2</sub>	CH <sub>3</sub> CN	62 (31)	131 (32)
3	1 wt% Rh/TiO <sub>2</sub>	CH <sub>3</sub> OH	14 (7)	40 (9)
4	1 wt% Rh/TiO <sub>2</sub>	C <sub>2</sub> H <sub>5</sub> OH	30 (15)	90 (22)
5	TiO <sub>2</sub>	i-PrOH	n.d.	n.d.
6 <sup>b</sup>	1 wt% Rh/TiO <sub>2</sub>	i-PrOH	n.d.	n.d.
7 <sup>c</sup>	1 wt% Rh/TiO <sub>2</sub>	i-PrOH	n.d.	n.d.
8	Rh <sub>2</sub> (OOCCH <sub>3</sub> ) <sub>4</sub>	i-PrOH	n.d.	n.d.
9	H <sub>2</sub> PtCl <sub>6</sub> · 6H <sub>2</sub> O	i-PrOH	n.d.	n.d.
10	Pd/C	i-PrOH	n.d.	n.d.
11	No catalyst	i-PrOH	n.d.	n.d.

<sup>a</sup> Reaction conditions: catalyst (5 mg), THQ (0.2 mmol) (except entry 6), i-PrOH (2 mL), blue LED light ( $\lambda_{max}=453$  nm) (except entry 7), Argon atmosphere, 24 h. <sup>b</sup> no substrate. <sup>c</sup> in dark. n.d.-not detected. The yields were determined by GC-FID using benzyl alcohol (50 mol%) as the internal standard. The amount of produced hydrogen molecules were determined by GC-TCD.

In methanol and ethanol, only small amounts of the desired product (7 % and 15 %, respectively) were formed. Some control experiments were performed to verify the importance of light and photocatalyst in the ADH reactions. During shaking of THQ in 2-propanol in the presence of Rh-loaded TiO<sub>2</sub> in the dark, no reaction was observed (Table 3.7 entry 11). Visible-light illumination of the solution of THQ in i-PrOH containing no photocatalyst showed no dehydrogenation of the reactant (Table 3.7 entry 7). On the other hand, visible-light illumination of Rh-loaded TiO<sub>2</sub>

in 2-propanol, containing no THQ, showed no formation of  $H_2$ , thus evincing that the alcohol is not oxidized upon visible light illumination (Table 3.7, entry 6).

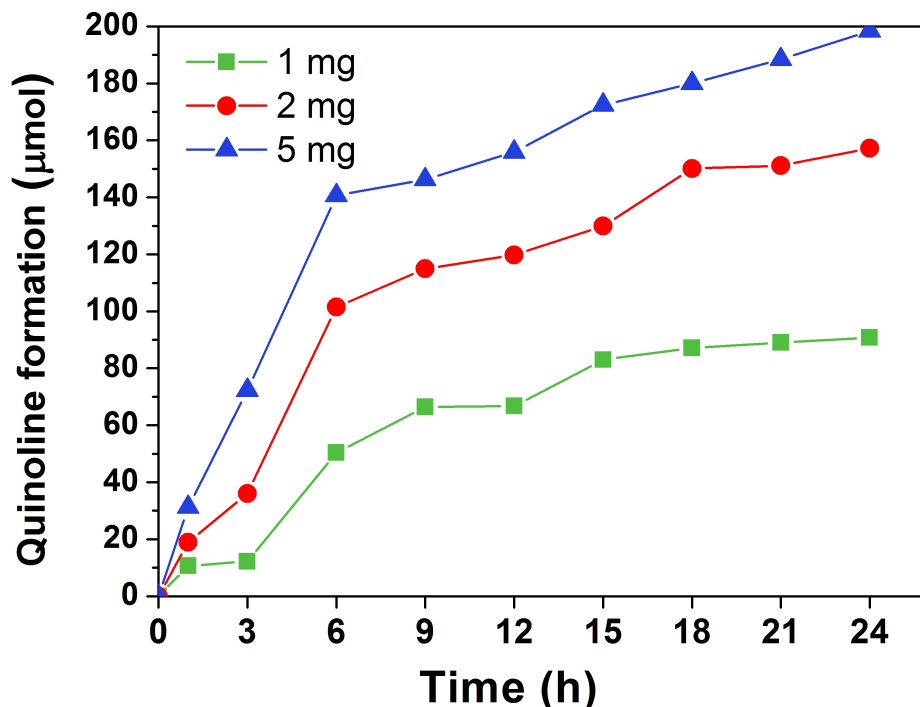


Figure 3.19.: Influence of the photocatalyst amount on the kinetics of the ADH of THQ. Reaction conditions: catalyst (1 wt% Rh/TiO<sub>2</sub>), THQ (0.2 mmol), i-PrOH (2 mL), blue LED light ( $\lambda_{max}=453$  nm), Argon atmosphere. The quinoline amount were determined by GC-FID using benzyl alcohol (50 mol%) as the internal standard.

#### 3.4.4. Effect of the photocatalyst loading

Decreasing the amount of the 1 wt% Rh/TiO<sub>2</sub> photocatalyst in suspension resulted in a significant decrease in the yield (Figure 3.19). Also, the time-dependent experiments with varying the amount of the photocatalyst in a reaction system were performed, revealing that at the initial step, the reaction kinetics is faster, independent from the catalyst loading amount. An increasing amount of photocatalyst shows higher reactivity within a shorter reaction time. The appropriate amount of the catalyst and the reaction time was found to be 5 mg (2.5 g/L) and 24 h for the ADH of 0.2 mmol THQ, respectively. Therefore, all the following experiments have been performed in i-PrOH with 5 mg Rh/TiO<sub>2</sub>. Moreover, a variation of the Rh nanoparticle content was also investigated (Figure 3.20). It was observed that an Rh<sup>0</sup> loading between 0.5 wt% and 1 wt%

gave an excellent yield within 18 h reaction time. However, 5 wt% Rh<sup>0</sup> co-catalyst deposited on TiO<sub>2</sub> showed significantly poor photocatalytic performance.

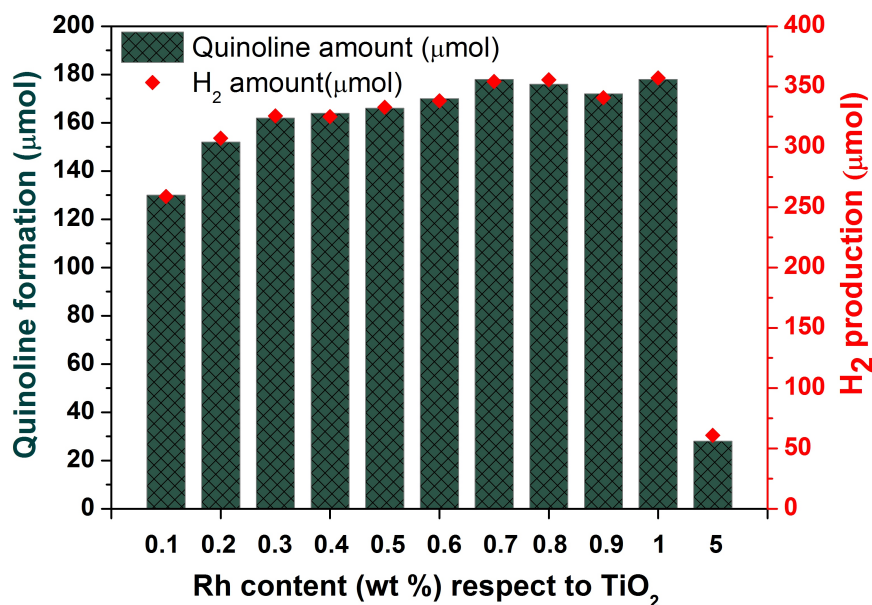


Figure 3.20.: The influence of the loading amount of Rh on TiO<sub>2</sub> on ADH of THQ. Reaction conditions: Rh/TiO<sub>2</sub> photocatalyst (5 mg), THQ (0.2 mmol), i-C<sub>3</sub>H<sub>7</sub>OH (2 mL), blue LED light ( $\lambda_{max}$ =453 nm), Argon atmosphere, 18 h. The quinoline amount were determined by GC-FID using benzyl alcohol (50 mol%) as the internal standard. The amount of producing hydrogen molecules were determined by GC-TCD.

### 3.4.5. Recycling of the 1 wt% Rh/TiO<sub>2</sub> in ADH reactions

Furthermore, the reusability of 1 wt% Rh/TiO<sub>2</sub> was examined by carrying out six successive experimental cycles to demonstrate the advantage of using a heterogeneous photocatalyst. The catalyst was collected by simple centrifugation and was reused without further treatment until the 4<sup>th</sup> cycle (Figure 3.21). Although the selectivity of the ADH reaction of THQ was found to be stable (>96 %), the yield of the product gradually decreased in the course of four experimental runs (Figure 3.21). BET and ICP-OES measurements were carried out to measure the photocatalyst's surface area and the content of the metal nanoparticles on TiO<sub>2</sub> before and after four cycles of the ADH reaction, respectively. No leaching of Rh was detected by ICP-OES measurements, showing the same amount of Rh nanoparticles (0.99 wt% with respect to TiO<sub>2</sub>) before and after four experimental runs. However, the surface area of the catalyst was found to decrease from 316 m<sup>2</sup>/g to 272 m<sup>2</sup>/g after the 4<sup>th</sup> cycle. Therefore, the post-treatment of the catalyst was required

to recover the specific surface area. For this purpose, the water suspended photocatalyst was illuminated at ambient temperature for one hour with a 500 W solar simulator lamp in an oxygen atmosphere. Thus, the surface area recovered up to 312 m<sup>2</sup>/g, and the product yield also reverted to 96 % in the 5<sup>th</sup> cycle. Moreover, the subsequent experimental run showed similar yields to those obtained in the second run, which is clear evidence of the catalyst's excellent reusability.

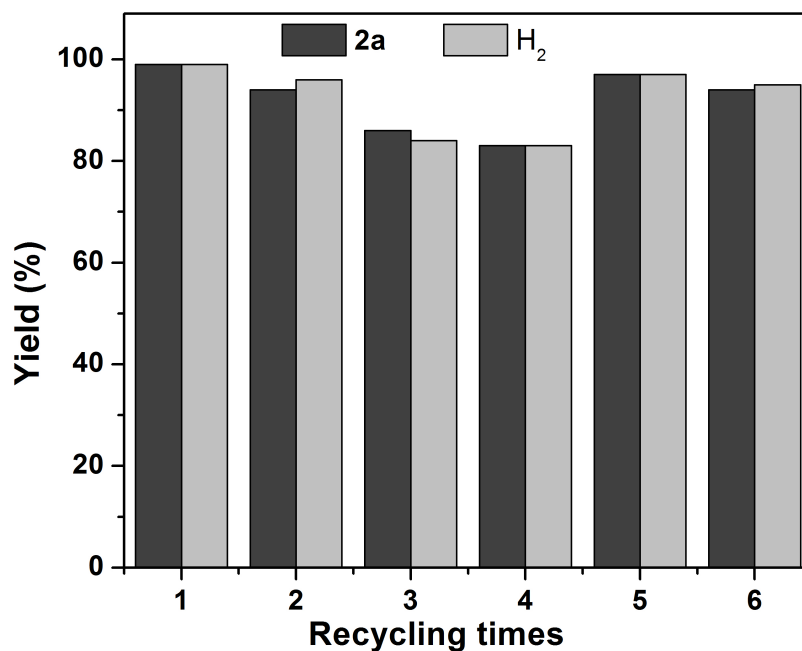


Figure 3.21.: Acceptorless dehydrogenation of 1,2,3,4-tetrahydroquinoline: recycling of 1 wt% Rh/TiO<sub>2</sub>. Reaction conditions: 5mg recovered catalyst (1 wt% Rh/UV100), THQ (0.2 mmol), i-C<sub>3</sub>H<sub>7</sub>OH (2 mL), blue LED light ( $\lambda_{max}$ =453 nm), Argon atmosphere. The quinoline amount were determined by GC-FID using benzyl alcohol (50 mol%) as the internal standard. The amount of producing hydrogen molecules were determined by GC-TCD. 5<sup>th</sup> and 6<sup>th</sup> experimental runs were performed after recovering the surface of the photocatalyst.

A similar trend regarding the photocatalytic performance was also observed even when a washing procedure with acetone was applied after each successive run. Despite washing with acetone, it was observed that the surface area was still reduced. Additionally, leaching of Rh metal nanoparticles down to 0.72 wt% with respect to TiO<sub>2</sub> was proved. However, the reaction yield was still almost the same as the yield obtained with a photocatalyst subjected to the non-washing procedure and could be increased up to 96% after light treatment. These results surely support the significant role of the surface porosity for the catalytic performance as well as the importance of



the surface recovery process.

### 3.4.6. Acceptorless dehydrogenation of tetrahydroquinolines

The ADH results of the broad substrate scope of the THQs will be presented in this section. The yield of the products was measured quantitatively after the isolation of the product by column chromatography. The purity of the compounds was confirmed by <sup>1</sup>H and <sup>13</sup>C NMR spectroscopy. The NMR characterization data of the product are provided in the Appendix. The range of substrates for different N-heterocyclic amines (0.2 mmol) was explored at room temperature in an inert argon atmosphere after optimization of the reaction conditions using 5 mg 1 wt% of Rh photodeposited TiO<sub>2</sub> as the photocatalyst and 2 mL of i-PrOH as the solvent (Table 3.8). Nine different THQs substituted with electron-withdrawing, electron-donating, and alkyl groups in different positions of the benzo-fused N-heterocycles were investigated (Table 3.8). The substrate bearing a strong electron-donating group, 6-methoxy-THQ, afforded a good yield of 68% after 24 h illumination ((**2b**)). Increasing the reaction time up to 36 h increased the yield for the 6-Me-THQ substrate up to 89% ((**2h**)). However, the significant improvement was not observed for the substrate (**1c**) bearing the methyl group at the C2 position, presumably because of the steric effect caused by the methyl group (**2c**). However, substrate ((**1d**)) bearing the 7-hydroxyl group poorly reacted, thus affording ((**2d**)) in only 7% yield along with unreactive starting material despite its strong electron-donating nature. This phenomenon was also observed in aerobic conditions, where the results suggested that the hydroxyl group and the amino group likely competed for the surface complexation with titania (Chapter 3.3.8). Protecting the hydroxyl group as a TBS ether removed its complexation with TiO<sub>2</sub>, and indeed, the oxidative dehydrogenation of 7-TBSO-THQ was afforded in high yield (Table 3.5, (**1e**)). Compounds bearing two substituents such as 4-methylthio-2-phenyl-THQ (**1j**) and 8-carboxyl-2-methyl-THQ (**1i**) demonstrated good to excellent yields. It seemed that a large phenyl group in the substrate (**1j**) rather hindered the binding of the amine group on the TiO<sub>2</sub> surface and thus slightly affected the reaction performance. Interestingly, unlike the hydroxyl group, the carboxyl group had no detrimental effects on the dehydrogenation reaction ((**2i**)).

The chlorine group at C6 position was found to be compatible with the reaction conditions, and 6-chloro-quinoline (**2g**) was obtained in a 90% yield. However, the substrate (**1f**), bearing a

strong electron-withdrawing 7-NO<sub>2</sub> group, failed to participate in the dehydrogenation with the substrate recovered.

Table 3.8.: Acceptorless dehydrogenation of tetrahydroquinolines over 1 wt% Rh photodeposited TiO<sub>2</sub><sup>a</sup>

Entry	Substrates	Products and Yields (μmol, (%)) <sup>b</sup>	H <sub>2</sub> (μmol, (%)) <sup>c</sup>
1		 <b>2a</b> 192 (96)	397 (99)
2		 <b>2b</b> 136 (68)	275 (67)
3		 <b>2c</b> 108 (54)	226 (56)
4		 <b>2d</b> 14 (7) <sup>(d)</sup>	26 (7)
5		 <b>2f</b> N.D.	N.D.
6		 <b>2g</b> 180 (90)	362 (91)
7		 <b>2h</b> 178 (89)	356 (89)
8		 <b>2i</b> 186 (93)	382 (96)
9		 <b>2j</b> 122 (61)	245(61)

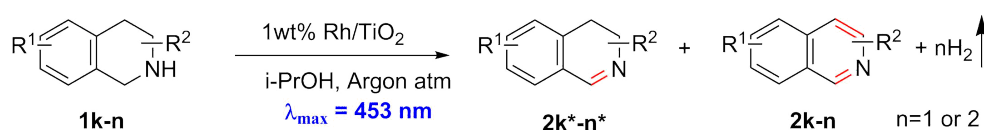
<sup>a</sup> Reaction conditions: 1 wt% Rh/TiO<sub>2</sub> (5mg), 0.2 mmol substrate,  $\lambda_{max}$ =453 nm, 1 atm Ar, 24 h (2a - 2e), 36 h (2f - 2i), 2 mL i-C<sub>3</sub>H<sub>7</sub>OH as the solvent. <sup>b</sup> Yield is that of the isolated product.<sup>c</sup>

The amount of evolved hydrogen molecules was determined by GC-TCD.

## 3.4.7. Acceptorless dehydrogenation of tetrahydroisoquinolines

The ADH results of the broad substrate scope of the THisoQs will be presented in this section. The yield of the products was measured quantitatively after the isolation of the product by column chromatography. Moreover, the purity of the compounds was confirmed by <sup>1</sup>H and <sup>13</sup>C NMR spectroscopy. The NMR characterization data of the product are provided in the Appendix.

Table 3.9.: Acceptorless dehydrogenation of tetrahydroisoquinolines over 1 wt% Rh photodeposited TiO<sub>2</sub><sup>a</sup>



Entry	Substrates	Products and Yields (μmol, (%)) <sup>b</sup>	H <sub>2</sub> (μmol, (%)) <sup>c</sup>
1		 96 (48) 78 (39)	272 (88)
2		 176 (88) [d]	357(89)
3		 96 (46) 68 (34)	228 (81)
4		 112 (56) 64 (32)	242 (88)

<sup>a</sup> Reaction conditions: 1 wt% Rh/TiO<sub>2</sub> (5mg), 0.2 mmol substrate,  $\lambda_{max}$ =453 nm, 1 atm Ar, 48 h, 2 mL i-PrOH as the solvent. <sup>b</sup>Yield is that of the isolated product. <sup>c</sup>The amount of evolved hydrogen molecules was determined by GC-TCD according to the calibration curve. <sup>d</sup> 1/1 CH<sub>2</sub>Cl<sub>2</sub>/i-PrOH was used as the solvent.

Acceptorless dehydrogenation of tetrahydroisoquinolines was also explored at ambient temperature in an inert argon atmosphere with optimized reaction conditions using 5 mg 1 wt% of Rh photodeposited TiO<sub>2</sub> as the photocatalyst and 2 mL of i-PrOH as the solvent upon visible light illumination for 48h (Table 3.9). Four different tetrahydroisoquinoline substrates with electron-donating and electron-withdrawing substituents ((**1k**) – (**1n**)) were targeted in the ADH reactions. It was observed that the tetrahydroisoquinolines in ADH reaction behaved differently compared to tetrahydroquinolines, where partial dehydrogenation products (3,4-dihydroisoquinolines) were obtained along with complete dehydrogenation products (isoquinolines) after 48 h visible-light illumination (Table 3.9). Thus, 1,2,3,4-THisoQ without any substituent group afforded the complete dehydrogenation product, isoquinoline (**2k**), in 48% yield with the partial dehydrogenation product, 3,4-dihydro-quinoline (**2k\***), in 39% yield. THisoQ was bearing a 1-methyl (**1m**) or 1-phenyl (**1n**) group afforded mainly the partial dehydrogenation product with the complete dehydrogenation product as the minor product. However, THisoQ bearing two methoxy groups at C6 and C7 position (**1l**) underwent complete dehydrogenation in excellent yield ((**2l**), 88 %). The high reactivity was likely due to the strong electron-donating methoxy groups that facilitate the oxidation reaction. The optimized reaction conditions were also applied to several indolines using 5 mg 1 wt% of Rh photodeposited TiO<sub>2</sub> as the photocatalyst and 2 mL of i-PrOH as the solvent at room temperature in an inert argon atmosphere upon visible light illumination for 48h (Table 3.10). The unsubstituted indoline (**1o**) and 2-methylindoline (**1p**) were converted to the indoles in 73 % and 49 % yield, respectively (Table 3.10).

## 3.4.8. Acceptorless dehydrogenation of indolines

Table 3.10.: Acceptorless dehydrogenation of indolines over 1 wt% Rh photodeposited TiO<sub>2</sub><sup>a</sup>

$$\text{1o-1t} \xrightarrow[\text{i-PrOH, Argon atm, } \lambda_{\text{max}}=453 \text{ nm}}{\text{1 wt\% Rh/TiO}_2} \text{2o-2t} + \text{H}_2 \uparrow$$

Entry	Substrates	Products and Yields ( $\mu\text{mol}$ , (%)) <sup>b</sup>	H <sub>2</sub> ( $\mu\text{mol}$ , (%)) <sup>c</sup>
1		146 (73)	148 (74)
2		49%	101 (50)
3		172 (86)	175 (87)
4		156 (78)	162 (81)
5		146 (73)	149 (74)
6		150 (75)	158 (79)

<sup>a</sup> Reaction conditions: 1 wt % Rh/ Rh/TiO<sub>2</sub> (5mg), 0.2 mmol substrate,  $\lambda_{\text{max}}=453 \text{ nm}$ , 1 atm Ar, 48 h, 2 mL i-PrOH as the solvent. <sup>b</sup> Yield is that of the isolated product. <sup>c</sup> The amount of evolved hydrogen molecules were determined by GC-TCD according to the calibration curve.

The ADH results of the broad substrate scope of the indolines will be presented in this section. The yield of the products was measured quantitatively by an isolated compound with column chromatography. Moreover, the purity of the compounds was confirmed by <sup>1</sup>H and <sup>13</sup>C NMR

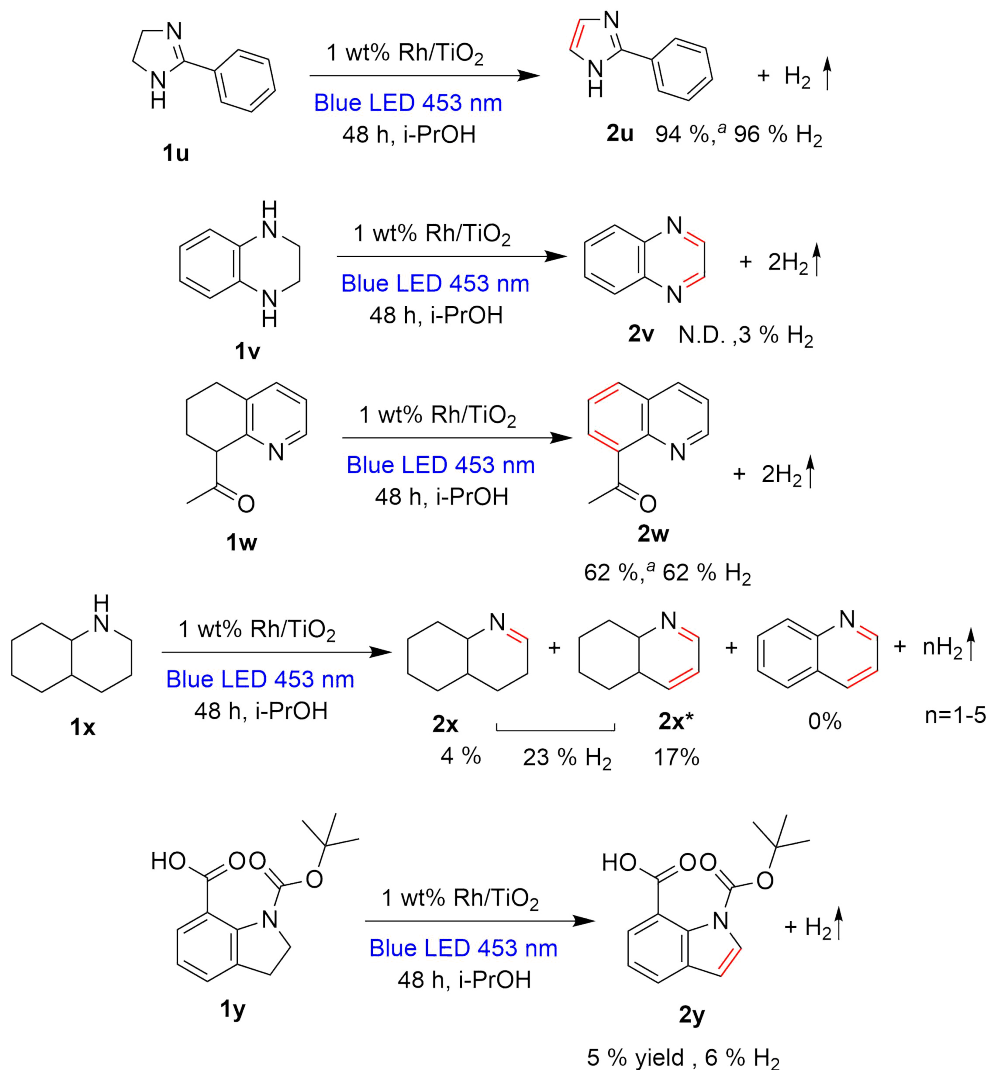
spectroscopy. The NMR characterization data of the product are provided in the Appendix. Interestingly, the strong electron-withdrawing group attached to the indoline moiety did not seem to hinder the ADH of 6-(trifluoromethyl) indoline, which gave the product in excellent yield ((**2q**), 86 %). Decarboxylation was observed with the indoline substrates bearing a carboxyl group in the C2 position ((**1r**) and (**1s**)). In both examples, indole was isolated in good yield, i.e., 78 % of (**2r**) and 73 % of (**2s**). However, when the carboxyl group was protected as a methyl ester, the decarboxylation was prevented entirely, and methyl 1H-indole-2-carboxylate was obtained (**2t**) in 75 % yield.

### 3.4.9. Acceptorless dehydrogenation of other N-heterocycles

The ADH results of other N-heterocycles will be presented in this section. Moreover, the yield of the products was determined either by isolated mass or by NMR crude analysis using dibromomethane ( $\text{CH}_2\text{Br}_2$ ) as an internal standard. The purity of the compounds was confirmed by  $^1\text{H}$  and  $^{13}\text{C}$  NMR spectroscopy. The NMR characterization data of the product are provided in the Appendix. Besides, the same optimized reaction conditions employed for the ADH of THQs was applied for the ADH of N-heterocycles containing two nitrogen atoms (Scheme 3.2). 2-Phenyl-1H-imidazoline (**1u**), belonging to a different class of N-heterocycles bearing two nitrogen atoms, underwent the ADH reaction uneventfully, producing the product (**2u**) in excellent yield (94 %). However, 1,2,3,4-tetrahydroquinoxaline (**1v**) failed to participate in the ADH, although it underwent the oxidative dehydrogenation with molecular oxygen in an oxygen atmosphere (Table 3.8). Surprisingly, the substrate 8-acetyl-5,6,7,8-tetrahydroquinoline (**1w**), which does not have an NH group, furnished the completely aromatized product (**2w**) in 62 % yield. After establishing the substrates' scope, the requirement of the minimal structure for the ADH is investigated (Scheme 3.2). Initially, optimal reaction conditions were subjected to completely saturated perhydroquinoline. This substrate is also attractive from the viewpoint of  $\text{H}_2$  storage materials, as it could theoretically release five molecules of hydrogen. However, only  $96 \mu\text{mol H}_2$  was released along with a poor conversion yielding 5,6,7,8-tetrahydroquinoline (**2x\***). This result indicates that having an aromatic ring fused to the saturated N-heterocycle is essential for the complete dehydrogenation. When the amine group was protected by a Boc group as shown in (**1y**), the surface complexation with titania seems to be inhibited entirely, since the targeted product (**2y**)

### 3.4. ADH OF N-HETEROCYCLIC AMINES ON SURFACE MODIFIED TiO<sub>2</sub>

was obtained in only 5% yield with H<sub>2</sub> in 6% yield. This data also supported that formation of the surface complex between the carboxyl group and titania is not responsible for the visible-light absorption. These studies suggested that having a Lewis basic nitrogen atom in conjunction with a fused arene or N-heteroarene was critical for a successful acceptorless dehydrogenation reaction.



Scheme 3.2: Acceptorless dehydrogenation of other N-heterocycles over 1 wt% Rh photodeposited TiO<sub>2</sub>. Reaction conditions: 1 wt% Rh/UV100 photocatalyst (5 mg), substrate (0.2 mmol) in i-PrOH (2 mL), blue LED light ( $\lambda_{max}$ =453 nm), Argon atmosphere, 48 h. Yield calculated according to the NMR signals. The amount of evolved hydrogen molecules was determined by GC-TCD according to the calibration curve. <sup>a</sup> Yield is that of the isolated product.





# Chapter 4

## Discussion

This chapter covers a comprehensive discussion of the obtained results presented in the previous chapters. The origin of visible light activation and the mechanisms of reactions to understand the role of different reaction factors will be investigated in detail by the results of optical spectroscopy. Moreover, the impact of reactants on reaction yield will be discussed. In the next part, the impact of the different reaction factors on the acceptorless dehydrogenation of N-heterocycles will be discussed in more detail. Reasonable mechanistic models explaining ongoing reactions will be presented and discussed in detail in the final section.

### 4.1. Overview

This work aimed to develop a synthetic method using heterogeneous photocatalysts based on 100% anatase TiO<sub>2</sub> for the dehydrogenation of N-heterocyclic amines upon visible light illumination at room temperature. The dehydrogenation reactions have been performed in the presence and absence of molecular oxygen.

- Dehydrogenation of N-heterocyclic amines in the presence of O<sub>2</sub>

Initial studies demonstrated that aerobic dehydrogenation of 1,2,3,4-tetrahydroquinoline over bare TiO<sub>2</sub> was practical at room temperature upon visible light illumination. The UV-vis and

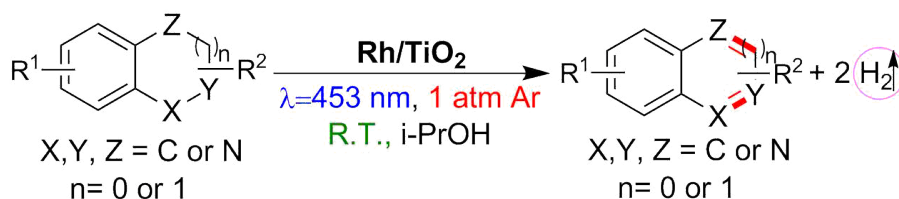
Scheme 4.1: Dehydrogenation reaction conditions of N-heterocycles in O<sub>2</sub> atmosphere.

FTIR spectroscopy results revealed a visible-light-responsive surface complex formation between the amine and TiO<sub>2</sub>. The detailed discussion is presented in Section 4.3. It was observed that the surface-grafting of TiO<sub>2</sub> with various transition metals and metal ions improves the reaction yield and the selectivity. The effect of transition metals in ODH of the N-heterocycles is discussed in detail in the Sections 4.3.3 and 4.3.4. By calculating photonic efficiency ( $\zeta$ ), the reaction performance of different grafted metal ions was compared. The photogenerated species during aerobic dehydrogenation reactions were detected by EPR spectroscopy and elucidated in the following Section 4.3.1. It was observed that the presence of TEMPO derivatives could improve the selectivity of these dehydrogenation reactions. Notably, the combination of surface grafted TiO<sub>2</sub> photocatalyst with TEMPO derivatives significantly enhanced the reaction yield. 4-amino-TEMPO was found to be the most efficient redox mediator in comparison with the other several TEMPO derivatives.

Therefore, the effect of 4-amino-TEMPO in oxidative dehydrogenation reactions is discussed in detail in the following Section 4.3.2. Dehydrogenation of nine examples of tetrahydroquinolines, four examples of tetrahydroisoquinolines, two examples of indolines, and quinoxaline 2-phenylimidazoline were investigated in this study under optimized reaction conditions (Scheme 4.1). All of these substrate scopes will be discussed in depth in the following Section 4.3.6, in order to correlate the influence of the different functional groups attached to the N-heterocycles on reaction yields.

- Acceptorless dehydrogenation of N-heterocyclic amines in an inert atmosphere

When the dehydrogenation reaction of the THQ was performed in an inert atmosphere over TiO<sub>2</sub> photocatalyst, it was found that the reaction was completely inhibited. However, the dehydrogenation reaction of N-heterocycles in an inert atmosphere became possible by using TiO<sub>2</sub> photocatalyst, the surface of which was photodeposited with various noble metal nanoparticles



Scheme 4.2: Dehydrogenation reaction conditions of N-heterocycles in Ar atmosphere.

such as Au, RuO<sub>2</sub>, Pd, Pt, and Rh. As shown in the results (Section 3.4.2), the presence of different noble metal co-catalysts significantly affected the efficiency of the reaction. The results showed that the following order co-catalysts could significantly enhance the formation of quinoline and the concomitant evolution of hydrogen from THQ: Rh > Pt > Pd > Ru > Au. Thus, the origin of these noble metals' effect has been discussed in more detail, taking into account several intrinsic parameters (Section 4.4.1). In addition, the ADH reactions of amines were observed to increase while varying the dispersant in the reaction system in the following order: CH<sub>3</sub>OH < C<sub>2</sub>H<sub>5</sub>OH < CH<sub>3</sub>CN < i-C<sub>3</sub>H<sub>7</sub>OH (7%, 15%, 31%, and 99%, respectively). Additionally, the time course of the photocatalytic dehydrogenation of THQ as a function of the catalysts' loading amount was investigated. Accordingly, the effect of the loading amounts of Rh co-catalyst content on TiO<sub>2</sub> is discussed in Section 3.4.4. Control reactions confirm the importance of visible light and photocatalyst since the reaction did not proceed in the dark. Moreover, the use of metal precursors alone showed the unreacted reaction results in this process. Following the optimized reaction conditions presented in Scheme 4.2, acceptorless dehydrogenation of the range of substrates, such as nine tetrahydroquinolines, four tetrahydroisoquinolines, six indolines, and five examples of the different classes of N-heterocycles was studied. The influences of the nature of functional groups (electron-deficient or electron-rich) attached to the N-heterocycles are discussed in detail in Chapter 4.4.2.

## 4.2. Formation of surface complexes

In photocatalytic reactions, the absorption of light by a photocatalyst is a prerequisite for initiating a chemical reaction. Excitation with photon energy equal to or greater than the bandgap energy of the semiconductor is required to generate electron-hole pairs inside the semiconductor. Since it is well known that TiO<sub>2</sub> has a 3.2 eV bandgap energy, which can only be activated by high-

energy UV light, it was not expected its activation by lower-energy visible light. Similarly, most N-heterocycles display absorption only in the UV region.

However, in this study, it became obvious that the physical mixture of  $\text{TiO}_2$  and THQ suspended in acetonitrile exhibits a broad absorption band in the visible region (450-500 nm) (Figure 3.6). The optical properties of the as-prepared semiconductor and amine mixtures such as  $\text{TiO}_2$ -THQ, 0.1 wt% Ni(II)/ $\text{TiO}_2$ -THQ, and 1 wt% Rh<sup>0</sup>/ $\text{TiO}_2$ -THQ were compared with each other and with bare  $\text{TiO}_2$  UV100. Figure 4.1 represents the subtracted UV-vis spectra of these mixtures from the UV-vis spectrum of THQ. Thus, bare  $\text{TiO}_2$ -THQ mixture showed a significant redshift in the absorption spectrum up to  $\sim 460$  nm as compared with bare  $\text{TiO}_2$ . The dramatic enhancement in light absorption and shift towards visible region was observed with 0.1 wt% Ni(II)/ $\text{TiO}_2$ -THQ mixture. It should be noted that 0.1 wt% Ni(II)/ $\text{TiO}_2$  alone exhibit only UV light absorption similar to bare  $\text{TiO}_2$  (see Figure 3.7 a). Moreover, 1 wt% Rh photodeposited  $\text{TiO}_2$  nanoparticles mixed with THQ indicated a typical redshift up to  $\sim 475$  nm, which was slightly more than the optical shift of the THQ- $\text{TiO}_2$  mixture.

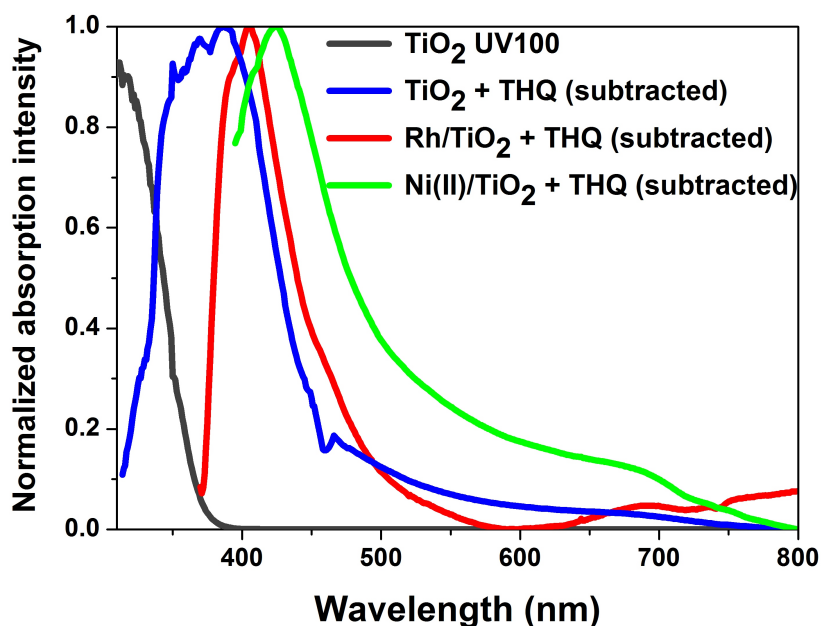


Figure 4.1.: UV-vis absorption spectra of bare  $\text{TiO}_2$  and THQ spectrum subtracted from  $\text{TiO}_2$ /THQ, Ni(II)- $\text{TiO}_2$ /THQ, Rh- $\text{TiO}_2$ /THQ. The concentration of the catalysts and THQ was used as same as the conditions of the reaction.

These results suggested the formation of a visible-light-responsive surface complex between the

amine and the  $\text{TiO}_2$ . As a result, this surface complex induced a new absorption band in the visible range. As a result of this, the non-semiconducting  $\text{SiO}_2$  with a high surface area was used as a catalyst in order to verify the importance of the  $\text{TiO}_2$ . No red-shift was observed in the absorption spectrum of  $\text{SiO}_2$ -THQ mixture. The absorption edge was observed at  $\sim 350$  nm, and the weak absorption edge up to  $\sim 450$  nm was consistent with the THQ UV-vis spectrum (Figure 3.6). As expected, the experimental result shows that there was no practical oxidative dehydrogenation of THQ at  $\text{SiO}_2$  surface upon visible light illumination. Therefore, after 24 h illumination, only unreacted starting material could be detected by GC (see Section 3.3.2). This is in agreement with the UV-vis absorption spectroscopy results. These results strongly suggest the importance of the semiconductor  $\text{TiO}_2$  for interaction with amine molecules (Figure 3.6). Additionally, as discussed above, 0.1 wt% of transition metal nanoclusters significantly affect the optical properties of bare  $\text{TiO}_2$  (Figure 3.7), which also shows the better photocatalytic performance in comparison with bare  $\text{TiO}_2$ . Since electrostatic interaction was assumed to occur only between an amine and  $\text{TiO}_2$  surface, it was not expected that the grafting of  $\text{TiO}_2$  would also affect the absorption properties. However,  $\text{Ni(II)/TiO}_2$ -THQ mixture exhibited more shift in the absorption spectrum towards the visible region than the mixture of bare  $\text{TiO}_2$ -THQ. This observation may be explained in different aspects. Thus, the grafting of the  $\text{TiO}_2$  surface with different transition metal ions might influence the surface acidity, leading to better interaction. Furthermore, the redox potential of the surface grafted transition metal ions have less negative potential ( $E^0(\text{Ni}) = -0.26$  V) than the to bare  $\text{TiO}_2$ . Moreover, it could also be taken into account that the surface grafted metal ions from metal oxides or metal hydroxides island (nanoclusters), which could act as a narrow bandgap material. [166] Therefore, electrons require lower energy to migrate from the conduction band of  $\text{TiO}_2$  to these nanoclusters. Above all, the results of UV-vis absorption spectroscopy revealed that the surface complex of  $\text{TiO}_2$ -THQ is responsible for visible light activation. This photosensitization of  $\text{TiO}_2$  nanoparticles with cyclic amines possibly occurs through a ligand-to-metal charge transfer (LMCT) process, where neither  $\text{TiO}_2$  nor amine absorbs visible light separately. As mentioned in the introduction, this method has been investigated in many applications for activating  $\text{TiO}_2$  upon visible light illumination (Section 1.4.2). In general, ligands such as salicylic acid, catechol, phenol, EDTA, etc. are used as adsorbates on  $\text{TiO}_2$  for oxidation or decomposition of organic compounds by the LMCT. Additional donors are always needed to regenerate these ligands that are

employed as adsorbates. Nevertheless, in this study, N-heterocyclic amines act as an adsorbate (ligand) on the surface of TiO<sub>2</sub>. During photocatalytic reactions, these amines are self-oxidized after visible light illumination, ensuring that no additional donors have been used. With this, the use of visible light as a reaction initiator provides better selectivity than UV light. The photosensitization of the most abundant, non-toxic, and stable TiO<sub>2</sub> leads to selective dehydrogenation of amines upon visible light illumination. Indeed, mild reaction conditions, including visible light and room temperature, are advantages over the use of narrow bandgap semiconductors that are less accessible or toxic. Besides, the dehydrogenation of N-heterocyclic amine upon visible light is an environmentally friendly method. This approach is an excellent alternative to replacing conventional methods where the stoichiometric amount of toxic oxidants, corrosive solvents, and high reaction temperatures are required.

Table 4.1.: Peak frequencies and assignments of the FTIR bands (cm<sup>-1</sup>) obtained from acetonitrile suspension of TiO<sub>2</sub> UV100 mixed with THQ and measured in the dark. \*

THQ peak (cm <sup>-1</sup> )	THQ+TiO <sub>2</sub> peak (cm <sup>-1</sup> )	Observation	Assignment
1606	1606	decreased	(s) NH out of plane
1585	1585	decreased	(w) Ar C-C stretching
1500	1500	decreased	(m) Ar C-C stretching
1309	1309	decreased	(m) Ar C-H in plane bend
1268	1268	decreased	Ar C-H in plane bend
1239	1239	decreased	δ(CH <sub>3</sub> )
3407	3407	vanished	(w) NH stretching

\* Absorption spectroscopy measurements were performed at the same concentration of the catalyst and substrate as appropriate to the organic reaction conditions in a CH<sub>3</sub>CN solvent.

(s)-strong; (w)-weak; (m)-medium

ATR-FTIR spectroscopy measurements were performed to support the surface complexation hypothesis demonstrated by the UV-vis results. Generally, amines are known to be Lewis base, so they can donate their lone pair of electrons to the TiO<sub>2</sub>, which is known to have Lewis acid sites on the surface. Initially, it is predicted that the electrostatic interaction of the Lewis acid side of

the semiconductor surface with the Lewis base site of the amine generates a surface complex that allows visible light absorption. Therefore, the surface acidity of  $\text{TiO}_2$  is one of the critical factors that may affect the surface complex formation with amines. Typically, metal semiconductors have acidic centers on their surface which are either proton-donors or electron-pair-acceptors, respectively called Brønsted acidic and Lewis acidic centers. [179] Adsorbed water molecules and OH-groups on the surface of  $\text{TiO}_2$ , can be proton-donor centers. OH-groups are known for their capacity to create H-bonds and can be used as centers for the physical adsorption of molecules, which are acceptors of protons. It has been reported that the rutile surface has only Lewis acidic centers, thus even exposed to water molecules, new Brønsted acidic centers are not generated. [180] However, anatase surface  $\text{TiO}_2$  has a surface with a Lewis and Brønsted acid sites which has been extensively studied by in situ FTIR spectroscopy in the presence of pyridine. [181–183] With this, the interaction of Lewis acidic site of  $\text{TiO}_2$  with the Lewis base site of amine was investigated by ATR-FTIR spectroscopy.

ATR-FTIR spectra of  $\text{CH}_3\text{CN}$ ,  $\text{CH}_3\text{CN} / \text{THQ}$ ,  $\text{CH}_3\text{CN}/\text{TiO}_2$ , and  $\text{TiO}_2/\text{THQ}$  were recorded in order to identify the type of surface complex formation between  $\text{TiO}_2$  and THQ. As shown in Figure 3.8, intensive bands at 3404, 1606, 1585, 1500, 1309, as well as 1268  $\text{cm}^{-1}$  frequencies are assigned to heteroatom-containing stretching vibration modes in THQ. [184] The signals observed in Figure 3.8 are summarized in Table 4.1. When a solution contained THQ and  $\text{TiO}_2$  mixture, the intensity of these bands diminished. The interaction of the amine and  $\text{TiO}_2$  explicitly identified by the decrease in the intensity of the peaks, i.e., 1606 and 3404  $\text{cm}^{-1}$  strongly suggest NH group and  $\text{Ti}^+$  interaction. Thus, the electron acceptor centers on  $\text{TiO}_2$  form a coordination bond with an adsorbate containing NH groups. Coordination vacant orbitals in the valence electron shell of nitrogen with unsaturated  $\text{Ti}^{n+}$  ions may be the centers of such strong adsorption on  $\text{TiO}_2$ . These vacant orbitals are filled with a free pair of electrons of the nitrogen atom in THQ when the donor-acceptor bond is formed. [185] These observations are consistent with the results reported by Parfitt et al., that spectral bands at 1605, 1575, 1487, and 1225  $\text{cm}^{-1}$  corresponding to surface adsorbed pyridine molecules at the surface of  $\text{TiO}_2$  at the Lewis acidic centers. [186] However, Bezrodna et al. reported that the interaction of pyridine at the Lewis acidic site of the rutile  $\text{TiO}_2$  did not occur at the 1605  $\text{cm}^{-1}$  band. Instead, a strong band was detected at 1581  $\text{cm}^{-1}$ , which characterize that pyridine is hydrogen-bonded with  $\text{TiO}_2$  surface OH groups. [179] These

results suggest that the surface interaction of  $\text{TiO}_2$  with nitrogen-bearing compounds is strongly dependent on the crystal phase of the semiconductor. The ATR-FTIR experimental results indicate that the anatase surface has the Lewis acid side, so the strong band at  $1605\text{ cm}^{-1}$  is allocated to the N-H group in amine. Thus, the interaction of the lone pair electron at the Lewis base of the amine with the Lewis acid site of  $\text{Ti}^+$  results in the loss of the observed peak. Figure 4.2 demonstrates the possible surface interaction of amine and  $\text{TiO}_2$ .

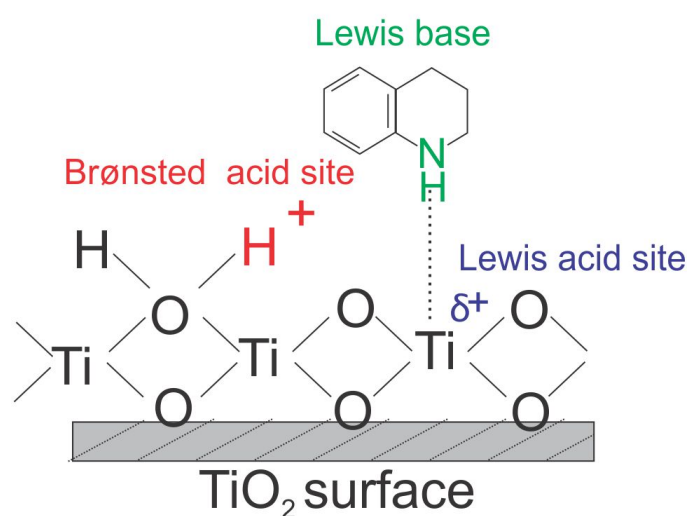


Figure 4.2.: Scheme of proposed electrostatic Lewis acid-base interaction between  $\text{TiO}_2$  and N-heterocyclic amine.

Although benzo-fused cyclic amines and  $\text{TiO}_2$  interaction was not investigated by theoretical and experimental methods, a similar surface complexation of tertiary or benzylic amines with  $\text{TiO}_2$  was investigated by various research groups. Researchers also reported the adsorption of the organic molecules bearing an amine group on different wide bandgap semiconductors. [113, 116, 187] For example, Chen et al. investigated the interaction of tertiary amine trimethylamine (TMA) with different surface sites and crystal phases of  $\text{TiO}_2$  by using commercial Aeroxide Evonik P25  $\text{TiO}_2$ . [112] They have reported a visible-light-harvesting surface complex formation between TMA and  $\text{TiO}_2$  resulting in a red-shift absorption spectrum of about 10 nm. The surface complex formation between  $\text{TiO}_2$  and tertiary amine was also investigated with DFT calculations and demonstrated by theoretical modeling. It was found that the adsorption energy of TMA onto the Ti-5c site of the rutile (110) surface was  $-0.43\text{ eV}$ , and anatase (101) surface



was -0.28 eV. This was indicating that the TMA adsorption of onto rutile (110) is preferable to that onto the anatase (101) surface. The distances from the N atom to the nearest Ti atom was calculated to be 2.79 Å for the rutile (110) surface and 2.44 Å for the anatase (101) surface, indicating that TMA is physically adsorbed onto these two surfaces. They concluded that the binding force between TMA and  $\text{TiO}_2$  is a Lewis base and acid interaction. Spectroscopic studied of the adsorption of ammonia, dimethylamine, and ethylamine on stoichiometric and slightly defective  $\text{TiO}_2$ -(110) surfaces were investigated by Madix et al., where adsorption was explained by the binding of the amine nitrogen atom to the  $\text{Ti}^{4+}$  cation at the Lewis acid sites. [188]

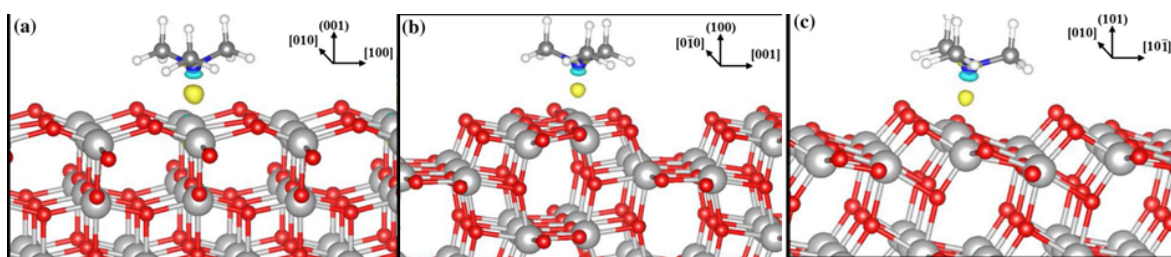


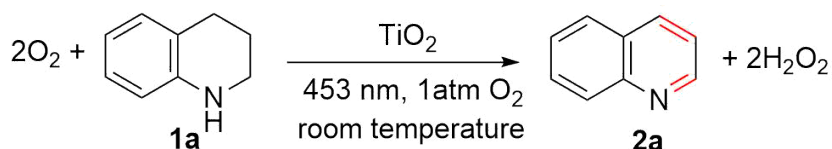
Figure 4.3.: Slice representation of the three surfaces of anatase after adsorption of a TMA molecule. Images refer to the (001) (a), (100) (b) and (101) (c) surfaces. Atom color code: red = oxygen, gray = titanium, blue = nitrogen, dark gray = carbon, white = hydrogen. The charge density difference plots (see text) are reported too: Yellow and cyan areas indicate an increase and a decrease in electronic charge density after adsorption, respectively. Reproduced from the ref. [189] (Copyright Springer, 2015)

DFT calculations have shown that amine groups form strong interactions with the 101 site of anatase  $\text{TiO}_2$  due to the Lewis acidic feature. Pavone et al. studied trimethylamine (TMA) adsorption on anatase  $\text{TiO}_2$  (100), (001) and (101) surfaces. [189] By comparing adsorption energies of (100), (001), and (101) site of anatase  $\text{TiO}_2$ , they reported that there is no preferred surface for the interaction of TMA molecules. Interestingly, it was found that when TMA adsorbed on the (100) surface site, the states at the top edge of the valence band were populated by these adsorbates. The calculated model for the adsorption of TMA molecules at the three different (001) (100) and (101) anatase surfaces is demonstrated in Figure 4.3. The interaction of N-heterocyclic amines with  $\text{TiO}_2$  has not been determined theoretically since yet. Therefore it is not possible to predict the actually preferred interaction sites of both anatase  $\text{TiO}_2$  and cyclic amine.

### 4.3. Dehydrogenation in the presence of molecular oxygen

Photocatalytic dehydrogenation of N-heterocyclic amines involves the N-H and C-H bond cleavage and yields aromatized compounds with and without the presence of molecular oxygen during the reaction. Bare TiO<sub>2</sub> as a semiconductor was employed for the conversion of amines upon visible light illumination. Hence, UV-vis spectroscopy results confirmed that the amine interaction with TiO<sub>2</sub> expands absorption band up to 470 nm, which allows us to perform dehydrogenation reaction with a LED visible light source energy at the wavelength up to  $\lambda_{max}$  = 453 nm.

Table 4.2.: Dehydrogenation of THQ over TiO<sub>2</sub><sup>a</sup>.



Entry	Catalysts	C (%) <sup>b</sup>	Y (%) <sup>b</sup>	S (%) <sup>c</sup>	ζ (%)
1	TiO <sub>2</sub> UV100	81	35	43	2.67
2	P25 TiO <sub>2</sub>	24	10	42	0.76
3 <sup>d</sup>	TiO <sub>2</sub> UV100	-	-	-	-
4 <sup>e</sup>	No catalyst	3	<2	67	0.15
5 <sup>f</sup>	No light	-	-	-	-
6	Ni(II)/UV100	93	57	61	4.36

<sup>a</sup> Reactions conditions: 10 mg photocatalyst TiO<sub>2</sub> (UV100 or P25) or Ni(II)/UV100, 24 h visible light illumination (LED lamp,  $\lambda_{max}$ =453 nm, 4 mW/cm<sup>2</sup>), 1 atm O<sub>2</sub>, 0.4 mmol THQ, 4 mL CH<sub>3</sub>CN. <sup>b</sup> conversion and yield are calculated according to the GC-FID calibration using benzyl alcohol as an internal standard. <sup>c</sup> selectivity is calculated with the ratio of yield over conversion.

<sup>d</sup> Argon atmosphere. <sup>e</sup> no TiO<sub>2</sub>, <sup>f</sup> in dark.

According to the obtained data shown in Table 4.2, the conversion, yield, and selectivity were calculated using the Eqs. 2.3-2.5 presented in Section 2.6.1. Photonic efficiencies were also calculated using Equation 2.9. The photocatalytic performance of three different photocatalysts, as well as control experiments, are presented in Table 4.2. It became obvious that TiO<sub>2</sub> UV100 with a surface area of 320 m<sup>2</sup>/g shows three times better photocatalytic performance than commercial

TiO<sub>2</sub> P25 (Evonik, Aeroxide, powder with 20% rutile and 80% anatase crystal phase and 50 m<sup>2</sup>/g specific surface area). Thus, the quinoline formation during 24 h photocatalytic reactions was observed to be 34% with UV100 (Table 4.2 entry 1) and only 10% with P25. Although TiO<sub>2</sub> P25 usually shows the highest efficiency for photocatalytic reactions upon UV light irradiation, in this study, it exhibits dramatically low activity, which correlates well with the surface area (Table 4.2 entry 2). Indeed, it is likely that having a high surface area increases the adsorption of reactant molecules on TiO<sub>2</sub> surface that acts as active catalytic sites.

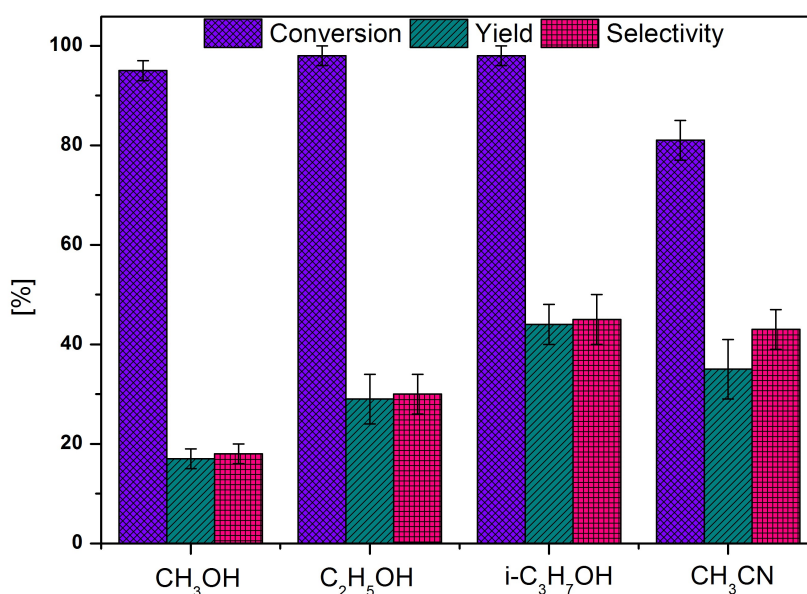


Figure 4.4.: The photocatalytic dehydrogenation of THQ in the presence of different solvents. Reaction conditions: 10 mg photocatalyst TiO<sub>2</sub> (UV100), 24 h visible light illumination (LED lamp,  $\lambda_{max}$ =453 nm, 4 mW/cm<sup>2</sup>), 1 atm O<sub>2</sub>, 0.4 mmol THQ (50.2  $\mu$ L), 4 mL of solvent. Conversion, yield, and selectivity are calculated according to the GC calibration using benzyl alcohol as an internal standard.

Hence, P25 has six times lower surface area, which is not sufficient for the formation of the surface complex with all molecules of amine introduced to the reaction system. Surface modification of TiO<sub>2</sub> is known to improve the lifetime of charge carriers. Therefore, the surface grafted TiO<sub>2</sub> with Ni ions was employed for the dehydrogenation reaction of 1,2,3,4-THQ (Table 4.2 entry 6). It was observed that the surface grafted TiO<sub>2</sub> UV100 with 0.1 wt% Ni(II) ions demonstrates almost two times better photocatalytic performance in comparison with TiO<sub>2</sub> UV100 although their surface areas were similar (Table 4.2 entry 6). [165] Thus, the yield and selectivity increased up

to 57% and 61%, respectively. These results are significantly higher than the yield and selectivity obtained while employing bare  $\text{TiO}_2$  as the photocatalyst. The calculation of the surface coverage is useful in an attempt to gain a better insight into the interaction of the reactant on the surface of  $\text{TiO}_2$ . Since the  $\text{TiO}_2$  UV100 has a surface area of  $320 \text{ m}^2/\text{g}$  and 10 mg photocatalyst is used in the dehydrogenation process, the total surface area of nanoparticles would be  $3.2 \text{ m}^2$  in this system. The theoretically calculated bond lengths and bond angles were taken from the literature to calculate the surface coverage of  $\text{TiO}_2$  by THQ molecules [190]. The surface area of one molecule of THQ was found to be  $33.8 \text{ \AA}^2$  mathematically. The overall molecules number of 0.4 mmol THQ in this system would be  $2.4 \times 10^{20}$ . Theoretically, in the  $3.2 \text{ m}^2$  area of  $\text{TiO}_2$ ,  $10^{20}$  number of THQ molecules can be adsorbed in order to generate one monolayer. Based on the number of THQ molecules in the system, it is assumed to be two and a half monolayers. Since the surface area of P25 is more than six times smaller than UV100, it was found that  $\sim 15.3 \text{ ML}$  of THQ was present on the surface of P25. The total molecules number of the THQ in the reaction system could be calculated with the following Equation 4.1:

$$N_{THQ} = n \times N_A \quad (4.1)$$

The theoretical number of the one monolayer THQ on  $\text{TiO}_2$  is calculated with the Equation 4.2:

$$N_{ML} = \frac{A_{\text{TiO}_2} \times m_{\text{TiO}_2}}{A_{THQ}} \quad (4.2)$$

where,  $N_{THQ}$  is a total molecules number of THQ introduced to the system,  $N_A$  is the Avogadro constant,  $N_{ML}$  is molecules number in one monolayer,  $A_{THQ}$  is the area of one molecule of THQ,  $A_{\text{TiO}_2}$  is the specific surface area of the  $\text{TiO}_2$  UV100 particles which are  $320 \text{ m}^2/\text{g}$ ,  $m_{\text{TiO}_2}$  is the amount of  $\text{TiO}_2$  particles in the reaction condition. In order to convert all THQ on the surface of P25, the reaction time might be increased seven times.

When other solvents, i.e., methanol and ethanol, were employed instead of acetonitrile, the conversion of THQ was increased, whereas the yield and selectivity decreased drastically (Figure 4.4). However, the yield and selectivity were detected to be higher while using 2-propanol instead of acetonitrile. Thus, the maximum yield and selectivity were 41% and 43%, respectively, while using 2-propanol as the solvent.

The calculated photonic efficiencies of different catalytic systems are shown in Table 4.4. A

comparison of all grafted materials' photonic efficiency results shows no significant difference, and high photonic efficiency of about 7.1% was achieved. However, a considerable difference in photonic efficiency is observed with noble metal photodeposited TiO<sub>2</sub> UV100, which was found to be below 4 %.

According to the obtained data from the spectroscopy results, the oxidation process of N-heterocyclic amine on TiO<sub>2</sub> surface is proposed in Figure 4.5. As discussed in Section 4.3, initially amine-TiO<sub>2</sub> surface complex is formed. Electron-rich adsorbate on the TiO<sub>2</sub> poses suitable HOMO level and injects one electron into the conduction band of TiO<sub>2</sub>. Subsequently, after visible light excitation, the electron is transferred from the conduction band of TiO<sub>2</sub> to the surface adsorbed molecular oxygen and thus reduces oxygen molecules to the superoxide radicals. The amine cation radical is oxidized by superoxide radical yielding an imine intermediate and hydrogen peroxide. Further oxidation of the imine intermediates being adsorbed on TiO<sub>2</sub> surface yields the aromatic product. This approach inhibits UV-driven side reactions, such as overoxidation of the reaction product, which results in increased selectivity. Moreover, holes are not generated in the VB band of TiO<sub>2</sub> upon visible light illumination, which results in the formation of oxidative species only from the reduction of oxygen molecules.

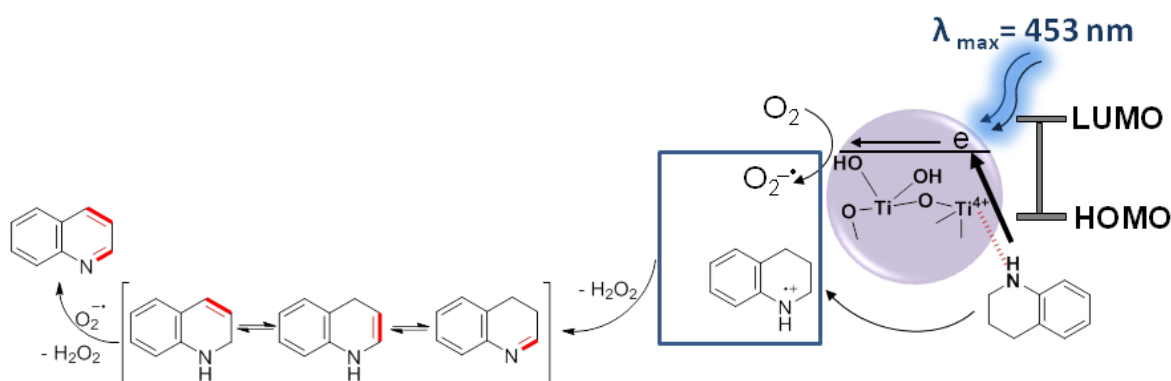
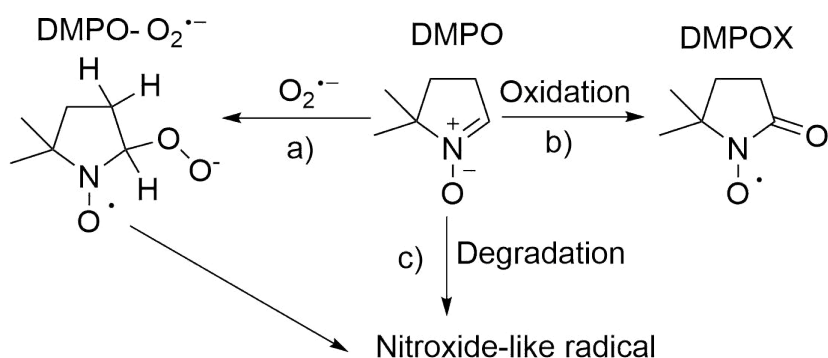


Figure 4.5.: Proposed mechanism for the aerobic oxidation of THQ on the bare TiO<sub>2</sub> surface upon visible light illumination

### 4.3.1. Formation of radicals during oxidative dehydrogenation

EPR spectroscopy measurements were performed in order to screen the generation of superoxide radical anion  $O_2^{\bullet-}$  upon visible light illumination. Experiments were carried out under the same conditions of reaction applied to oxidative dehydrogenation reactions of THQ. 5,5-dimethyl-1-pyrroline-N-oxide (DMPO) was used as a spin trap. The results presented in Section 3.3.4 demonstrate that upon visible light illumination, superoxide radical anions were detected by EPR spectroscopy using an aprotic solvent (Figure 3.11). Interestingly, as a result of this, hydroxyl radicals' formation was not detected either upon UV-vis light or visible light irradiation. Generally, the DMPO/superoxide adduct is unstable, decaying by a first-order process with a half-life of about 60s at pH 7. [191] However, with this, the high stability of DMPO- $O_2^{\bullet-}$  even under UV light irradiation was due to the use of acetonitrile as an aprotic solvent instead of 2-propanol or water. Hence, it is well known that upon UV or full-range light irradiation, the reactivity of the photoinduced holes ( $h^+$ ) and electrons ( $e^-$ ) on the titanium dioxide surface are different in aqueous and non-aqueous solvents. [192] Thus, in aqueous ambient, highly reactive superoxide radical anions ( $O_2^{\bullet-}$ ) formed by the trapped electrons, are eager to undergo further reactions with protons to form hydrogen peroxide and eventually  $OH^{\bullet}$  free radicals. Besides, the high population of  $OH^{\bullet}$  free radicals is more likely to be due to oxidation of water molecules with photoinduced holes. Therefore, the superoxide radicals are more stable in the aprotic solvent. DMPO is a trapping agent that reacts with superoxide or hydroxyl free radicals to form DMPO- $O_2^{\bullet-}$  and DMPO-OH, respectively. Scheme 4.3 demonstrates the formation of DMPO- $O_2^{\bullet-}$  adduct as well as possible degradation and oxidation pathways of DMPO. Since the dehydrogenation reaction was performed upon visible light irradiation, the generation of holes in the valence band of  $TiO_2$  and hydrogen peroxide from solvent oxidation was not expected in non-aqueous media. As a result, only three-line signals corresponding to the DMPO- $O_2^{\bullet-}$  radical adduct were detected, rather than four (three strong and one weak) hyperfine split paramagnetic signals, which typically correspond to trapped hydroxyl free radicals by trapping agent (DMPO). Moreover, with this, it was observed that upon visible light illumination, the photogenerated  $O_2^{\bullet-}$  radicals are more stable than the experiments performed upon UV-light irradiation (Figure 3.11 c and d).

Thus, during the irradiation of the sample with UV-vis light, the radicals  $O_2^{\bullet-}$  are initially formed, and after 20 minutes of irradiation, the peaks correspond to the  $O_2^{\bullet-}$  radicals gradually



Scheme 4.3: (a) Reaction of superoxide radical anion  $O_2^{\bullet-}$  with 5,5-dimethyl-1-pyrroline-N-oxide (DMPO) yielding a paramagnetic adduct DMPO- $O_2^{\bullet-}$ . (b) 5,5-dimethyl-1-pyrroline-N-oxide-N-oxyl (DMPOX) radical formation through oxidation of DMPO. (c) Degradation of DMPO to nitroxide-like radical. [193]

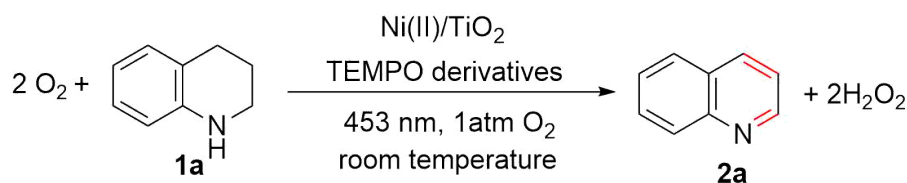
decreased. As can be seen in Figure 3.11 (d) upon UV-vis irradiation, a new peak emerged between two hyperfine peaks corresponding to DEMPO- $O_2^{\bullet-}$ . This could potentially be associated with the degradation of DMPO- $O_2^{\bullet-}$  (Scheme 4.3 path (c)). Nevertheless, the population of  $O_2^{\bullet-}$  increases with an extended time scale under visible light illumination. It can thus be described that DEMPO oxidation occurs only in direction (a) (Scheme 4.3) under visible light illumination. The photogeneration of DMPO- $O_2^{\bullet-}$  (Figure 3.11 a, b, and e) was not observed in the absence of THQ. These results prove that the visible light activation of  $TiO_2$  is initiated by the surface complex formation between THQ- $TiO_2$ .

#### 4.3.2. The role of 4-amino-TEMPO

Section 3.3.1 represents the effect of redox mediators such as TEMPO and 4-amino-TEMPO in the ODH reactions. Thus, although in the presence of TEMPO, a small impact on the conversion of the reactant was observed, the desired yield and the overall selectivity increased significantly (Table 4.3). It was observed that 4-amino-TEMPO shows better improvement in the reaction yield and selectivity in comparison with unsubstituted TEMPO for oxidative dehydrogenation of THQ (Table 4.3 of entries 1 and 2). The substantial effect of 4-amino-TEMPO has been investigated to understand its role in the dehydrogenation reaction process. TEMPO has been previously reported as an organic catalyst in  $TiO_2$ -catalyzed photochemistry by Zhao [101] and Chen [100]. Similarly, the use of TEMPO was reported by other groups as an organo-electrocatalyst in the

electrochemical dehydrogenation of N-heterocycles in N<sub>2</sub> atmosphere.

Table 4.3.: Photocatalytic dehydrogenation of THQ in the presence of different redox mediators<sup>a</sup>.



Entry	Catalysts	Redox mediator	C (%) <sup>b</sup>	Y (%) <sup>b</sup>	S (%) <sup>c</sup>	ζ (%)
1	UV100	TEMPO	86	71	81	5.43
2	UV100	4-amino-TEMPO	98	79	81	6.04
3	Ni(II)/UV100	TEMPO	80	58	73	4.44
4	Ni(II)/UV100	4-hydroxy-TEMPO	69	58	88	4.44
5	Ni(II)/UV100	4-oxo-TEMPO	93	77	83	5.89
6	Ni(II)/UV100	4-amino-TEMPO	100	92 (91 <sup>d</sup> )	91	7.03

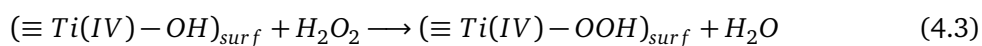
<sup>a</sup> Reaction conditions: 10 mg photocatalyst Ni/TiO<sub>2</sub> (UV100), 24 h visible light illumination (LED lamp,  $\lambda_{max}=453$  nm, 4 mW/cm<sup>2</sup>), 1 atm O<sub>2</sub>, 400 μmol THQ (50.2 μL), 4 mL i-PrOH, 20 mol% redox mediators with respect to the reactant. <sup>b</sup> conversion and yield are calculated according to the GC calibration using benzyl alcohol as an internal standard. <sup>c</sup> selectivity is calculated with the ratio of yield over conversion. <sup>d</sup> isolated yield.

Wu et al. have reported the oxidation of N-heterocycles and subsequent dehydrogenation of N-heterocycles in the presence of TEMPO. [149] Lang et al. have also used TEMPO as a redox mediator in alcohol [194], sulfide [110] and amine [106, 107, 109] oxidation reactions with dye-sensitized TiO<sub>2</sub> upon visible light illumination. They have reported that the dye radical cation activates the oxidation of TEMPO to TEMPO<sup>+</sup>, which undergoes nucleophilic attack by alcohol to produce aldehydes and TEMPOH. TEMPOH could regenerate back to TEMPO by a reaction with the superoxide radicals (O<sub>2</sub><sup>-•</sup>). However, as a result of this, it was observed that 4-amino-TEMPO plays a different role. The hypothesis about the role of the TEMPO was built upon a noticeable phenomenon which was observed during screening studies. Thus, without any redox mediator in the suspension, the initially light yellow suspension became dark brown during the light-induced reaction (Figure 3.12 A1) in addition to the accompanied low selectivity and yield (Table 4.2,

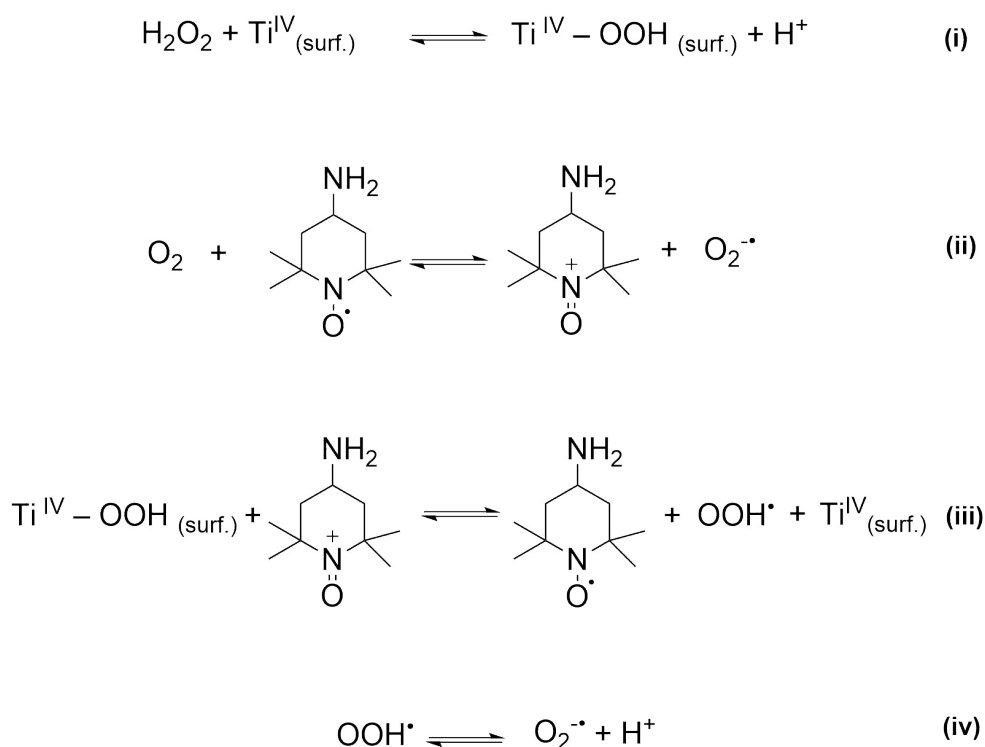


entry 1). In contrast, in the presence of 4-amino-TEMPO, the reaction mixture's color maintained light yellow throughout the reaction (Figure 3.12 B1). The color change during the photocatalytic reaction observed in the absence of 4-amino-TEMPO could be due to the formation of  $\text{TiO}_2\text{-H}_2\text{O}_2$  surface complexes. Thus, during the dehydrogenation reaction of THQ, two equivalent amount of hydrogen peroxide is producing as a side product. It is well known that  $\text{H}_2\text{O}_2$  can form a surface complex with  $\text{TiO}_2$  through a condensation reaction and form  $\text{Ti-OOH}$  surface radical. This complex has a yellow color and absorbs visible light at the wavelength up to 550 nm (Figure 4.7).

Therefore, the low selectivity could be attributed to the saturation of the  $\text{TiO}_2$  surface with  $\text{H}_2\text{O}_2$ . That prevents the formation of the N-heterocycle- $\text{TiO}_2$  surface complex necessary for an efficient electron transfer from the excited organic moiety to the conduction band of the  $\text{TiO}_2$ . As mentioned in Section 3.3.5 after 24 h photocatalytic dehydrogenation process of THQ to quinoline, the amount of photogenerated hydrogen peroxide  $\text{H}_2\text{O}_2$  could be analyzed by starch and iodate solution. Since TEMPO was found to increase the reaction selectivity, it was expected to play a beneficial role in the degradation of  $\text{H}_2\text{O}_2$ . To test the hypothesis mentioned above, the concentration of  $\text{H}_2\text{O}_2$  formed during the dehydrogenation reaction in the absence (Table 4.2, entry 1) and the presence of 4-amino-TEMPO (Table 4.3, entry 2) were measured. Indeed, the concentration of  $\text{H}_2\text{O}_2$  is observed to be significantly higher in the absence of 4-amino-TEMPO (Section 3.3.5, Figure 3.12). The lower concentration of  $\text{H}_2\text{O}_2$ , which is a strong oxidizing agent, observed in the presence of the 4-amino-TEMPO, resulted in minimizing possible side reactions improving the selectivity of the desired reaction. [165] Therefore, in the oxidative dehydrogenation reaction in the absence of 4-amino-TEMPO, the selectivity of the reaction was significantly low, likely due to overoxidation of the reaction product with these reactive oxygen species. In contrast, the selectivity was significantly improved with the introduction of 20 mol% of 4-amino-TEMPO with respect to the reactant to the reaction media. On the other hand, it is supposed that not only the reactive oxygen species could have an impact on the reaction selectivity that could subsequently reduce the yield of the desired product, but also the surface complex of  $\text{TiO}_2\text{-H}_2\text{O}_2$  can play as a competing surface complex with the amine- $\text{TiO}_2$ . Thus since the photon is absorbed by  $\text{TiO}_2\text{-H}_2\text{O}_2$  surface complex, the absorption of photon flux by amine- $\text{TiO}_2$  complex is retarded.



TEMPO and its derivatives are known to be stable radicals and bear one-electron reversible oxidation to form oxoammonium salts ( $\text{TEMPO}^+$ ). [195] These compounds have been investigated as redox mediators for electrochemically oxidizing primary and secondary alcohols. [196, 197] Sen and his group have introduced the oxidation of hydrogen peroxide molecules over 4-hydroxy TEMPO. [198] Lately, it has been reported the electrocatalytic anodic oxidation of  $\text{H}_2\text{O}_2$  by nitroxyl radicals and revealed that among the TEMPO series, 4-amino-TEMPO shows the highest catalytic efficiency due to the strong electron-withdrawing effect of an amino substituent. [199] This evidence is in agreement with the results obtained in this study. Considering developed insights over nitroxyl radicals, the ongoing reaction pathways in this system have been proposed. (Scheme 4.4 (i)-(iv)).



Scheme 4.4: Proposed ongoing reactions pathway with 4-amino-TEMPO.

Thus, the generation of hydrogen peroxide molecules as a byproduct during the dehydrogenation process of N-heterocycles initiates the formation of a surface complex with titania (Scheme 4.4, (i)). 4-amino-TEMPO shows weak absorption at the visible light region of 470 nm (Figure 4.7). Thus, the oxidation of TEMPO to the  $\text{TEMPO}^+$  and one-electron reduction of the oxygen molecule

to the superoxide radical anion were expected to occur. (Scheme 4.4, (ii)) A further understanding of the role of the 4-amino-TEMPO liquid EPR study was performed. Since TEMPO<sup>+</sup> is not paramagnetic and TEMPO is paramagnetic, EPR experiments of the 4-amino-TEMPO were performed with and without exposure to visible light ( $\lambda_{max} = 453$  nm) in an oxygen atmosphere in order to observe the change of paramagnetic species upon illumination (Figure 4.6). It was observed that the intensity of EPR signals corresponding to the 4-amino-TEMPO slightly decreased upon visible light illumination, which was consistent with the formation of 4-amino-TEMPO<sup>+</sup>.

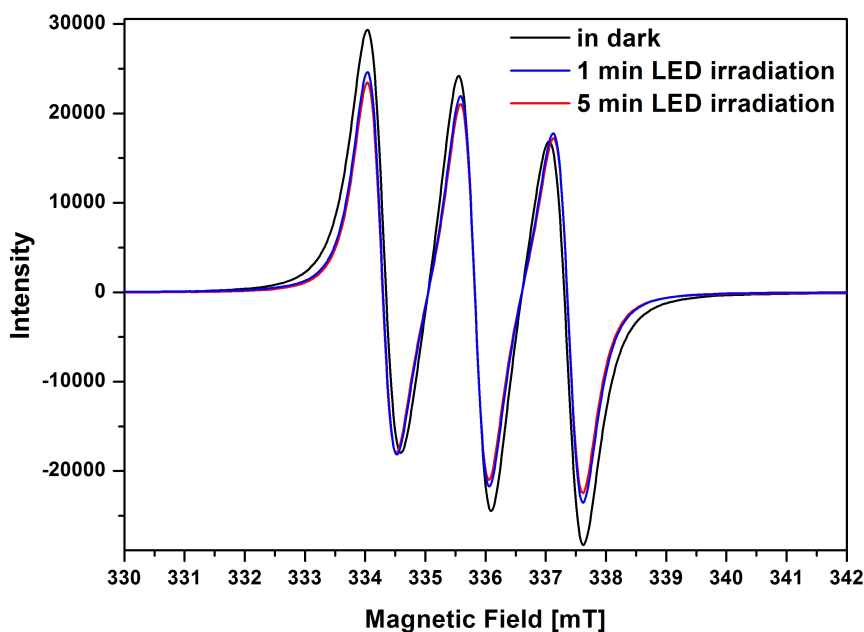


Figure 4.6.: EPR spectra of 4-amino TEMPO in dark and upon visible light illumination. Experiments were performed at room temperature.

That is consistent with the proposed mechanism in Scheme 4.4, (ii) where oxygen molecules oxidized by TEMPO to the superoxide radical anion. Hence, the generated oxoammonium cation leads to the decomposition of the surface titanium (IV) hydrogen peroxide complex and subsequent generation of a superoxide radical (Scheme 4.4, (iii and iv)). Zhao et al. reported the mechanistic studies of the photocatalytic decomposition of H<sub>2</sub>O<sub>2</sub> on TiO<sub>2</sub> surfaces upon visible light irradiation [200]. They carried out the degradation of salicylic acid in the presence of TiO<sub>2</sub> and H<sub>2</sub>O<sub>2</sub> upon visible irradiation, although neither H<sub>2</sub>O<sub>2</sub> nor TiO<sub>2</sub> alone can absorb visible light. The visible light photoreactivity was explained with the surface complex formation between H<sub>2</sub>O<sub>2</sub> and TiO<sub>2</sub> (Eq. 4.3).

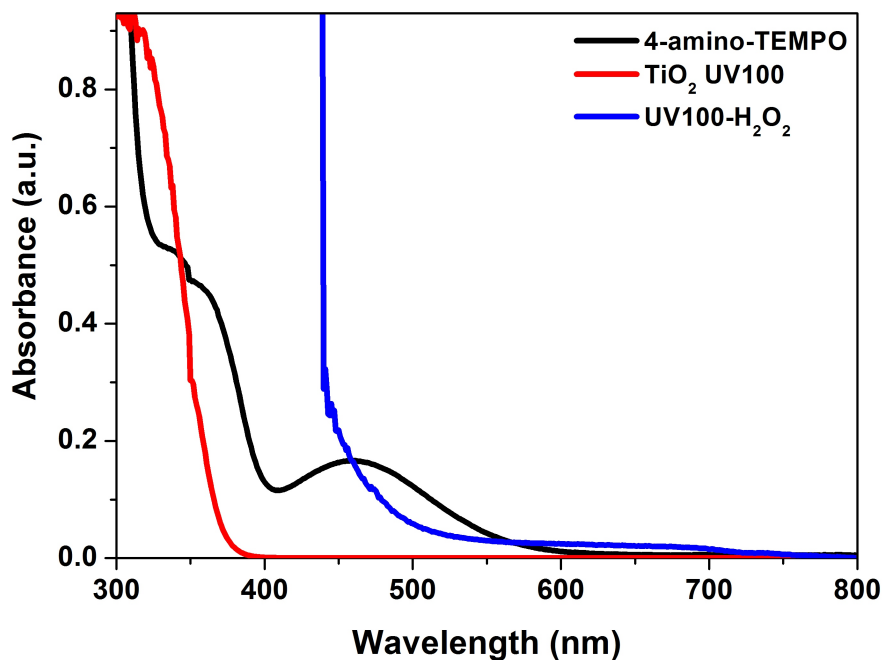
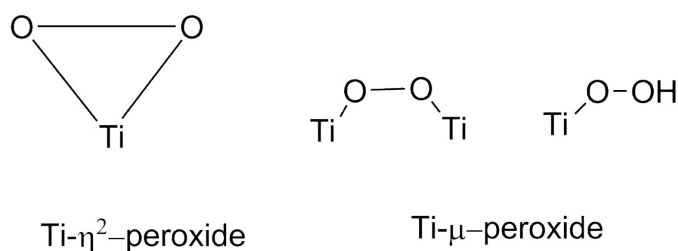


Figure 4.7.: UV-vis absorption spectrum of  $\text{TiO}_2$ , 4-amin-TEMPO, and  $\text{TiO}_2\text{-H}_2\text{O}_2$ .

Thus, depending on the crystal phase of the  $\text{TiO}_2$ , the  $\text{TiO}_2\text{-H}_2\text{O}_2$  complex is reported to present in two configurations:  $\text{Ti-}\eta\text{-peroxide}$  and  $\text{Ti-}\mu\text{-peroxide}$  which was confirmed by FTIR spectroscopy (Scheme 4.5). [201–203]



Scheme 4.5: The possible coordination structure of  $\text{H}_2\text{O}_2$ -adsorbed on the  $\text{TiO}_2$  surface. [187]

$\text{TiO}_2\text{-H}_2\text{O}_2$  surface complex are reported to be of yellowish color that can absorb visible light up to 550 nm. [201] This is in consistent with our UV-vis spectroscopy results where yellowish surface complex show extended absorption up to 550 nm (Figure 4.7). Indeed, concentration of the  $\text{H}_2\text{O}_2$  significantly affects the absorption spectra.

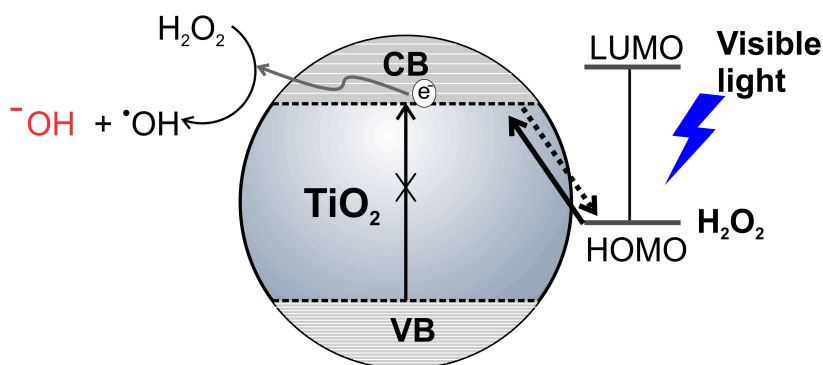


Figure 4.8.: TiO<sub>2</sub>-H<sub>2</sub>O<sub>2</sub> surface complex and a possible hydroxyl radical generation mechanism under visible light.

Moreover, H<sub>2</sub>O<sub>2</sub> is reported to be among those compounds that form the surface complex with TiO<sub>2</sub> through LMCT. LMCT process on TiO<sub>2</sub>-H<sub>2</sub>O<sub>2</sub> complex and a possible hydroxyl radical generation mechanism upon visible light illumination via degradation of H<sub>2</sub>O<sub>2</sub> is shown in Figure 4.8. As mentioned above, the single components are only UV-light responsive. However, the TiO<sub>2</sub>-H<sub>2</sub>O<sub>2</sub> complexation transfers an electron from the HOMO energy level of H<sub>2</sub>O<sub>2</sub> to the conduction band of TiO<sub>2</sub>. This electron can subsequently be injected to another H<sub>2</sub>O<sub>2</sub> molecule adsorbed on the TiO<sub>2</sub> surface to form highly reactive hydroxyl radicals and anions. Several small organic molecules such as cyclohexane, methyl orange, phenyl-urea degradation were studied on TiO<sub>2</sub>-H<sub>2</sub>O<sub>2</sub> surface complex upon visible light illumination. [204–206]

#### 4.3.3. Effect of grafting metal ions in photocatalytic performance

The results presented in Table 3.4 exhibit improved photocatalytic performance of the surface grafted TiO<sub>2</sub> with transition metal ions. These results suggest that the surface modification of TiO<sub>2</sub> improve the lifetime and the mobility of charge carrier. As shown in Figure 3.7, although the amount of grafted metal ions on TiO<sub>2</sub> was significantly low, the absorption spectra of surface grafted TiO<sub>2</sub> and THQ mixture indicate an increased absorption in the visible region in comparison with bare TiO<sub>2</sub>. [165] It has been observed that the grafted Ni ions on TiO<sub>2</sub> promoted yields approximately 20% higher than the yield obtained over the bare TiO<sub>2</sub> (Table 3.2 entry 6). Significant improvement was observed in selectivity when employing 4-amino-TEMPO as a redox mediator. Thus, all grafted metal ions exhibit excellent yield (above 90%) and selectivity (above

91%) in oxidative dehydrogenation of THQ. However, as described in Section 3.3.2, the overall efficiency of oxidative dehydrogenation of THQ with 0.1 wt% Pd, Ru, or Rh noble metals photodeposited TiO<sub>2</sub> are significantly lower in comparison with (60%, 49%, and 30%, respectively) bare TiO<sub>2</sub>. Nevertheless, the selectivity remained still high (97%, 100%, and 88%) (Table 3.4). The negative influence of noble metals could be explained by their strong electron scavenging capacity that retards the reaction momentum, eventually causing low activity. Ni ions grafting on the TiO<sub>2</sub> have been studied extensively for many applications. In this work, due to the low concentration of nickel ions, the actual structure could not be determined. Hence, Kudo et al., reported that Ni(II) grafting on the surface of TiO<sub>2</sub> by an impregnation method usually results in heterogeneous dispersion of nickel species with varying atomic characteristics, i.e., isolated nickel cations, as well as nickel-oxide nanoclusters or nanoparticles. [207]

Table 4.4.: Effect of the employed transition metals modified on TiO<sub>2</sub> UV100 surface in aerobic oxidative dehydrogenation of THQ compared with the photonic efficiency. <sup>a</sup>

Entry	Catalysts	C (%)	Y (%) <sup>b</sup>	S (%) <sup>c</sup>	ζ (%)
1	UV100	98	79	81	6.04
2	Cu(II)/UV100	100	91	91	6.96
3	Ni(II)/UV100	100	91	91	6.96
4	Nb(V)/UV100	95	90	91	6.88
5	Fe(III)/UV100	100	90	90	6.88
6	Co(II)/UV100	100	93	93	7.11
7	Pd(0)/UV100	62	60	97	4.59
8	RuO <sub>2</sub> /UV100	49	49	100	3.74
9	Rh(0)/UV100	34	30	88	2.29

<sup>a</sup> Reaction conditions: 10 mg photocatalyst, 24 h visible light illumination (LED lamp,  $\lambda_{max}=453$  nm, 4 mW/cm<sup>2</sup>), 1 atm O<sub>2</sub>, 0.4 mmol THQ (50.2 μL), 4 mL CH<sub>3</sub>CN, 20 mol% 4-amino-TEMPO (0.08 mmol) as a redox mediator with respect to the reactant. <sup>b</sup> calculated according to the GC calibration using benzyl alcohol as an internal standard. <sup>c</sup> ratio of yield over conversion.

Tada et al. have studied the origin at an electronic level by the density functional simulation

of NiO clusters adsorbed on TiO<sub>2</sub> anatase (001) and rutile (110) surfaces. [208] They found that the bandgap narrowed up to 0.8 eV by NiO modification of TiO<sub>2</sub> surfaces compared with pristine TiO<sub>2</sub>. Ni(II) modified TiO<sub>2</sub> has been reported to be a visible light active photocatalyst due to the excitation from the Ni 3d surface sub-band to the TiO<sub>2</sub> conduction band. Thereby, the NiO species act as a mediator for the electron transfer from the TiO<sub>2</sub> conduction band to O<sub>2</sub> resulting in a better charge separation. [209] Moreover, Venugopal et al. studied the role of the Brønsted and Lewis acid sites on the Ni impregnated TiO<sub>2</sub> in the hydrogenation of Levulinic acid. They reported that increasing the content of Ni ions from 5 wt% to 20 wt% with respect to TiO<sub>2</sub> significantly increases the Lewis acid catalysis sites. [183] This finding may be correlated with our observation that Ni ions significantly increase the dehydrogenation reaction yield of THQ, and are most likely to increase the surface acid site and the lifetime of the photogenerated charge carrier. Therefore, *In-situ* EPR spectroscopy studies were conducted to test the photogenerated paramagnetic species in bare TiO<sub>2</sub> and in Ni(II)/TiO<sub>2</sub> nanoparticles.

#### 4.3.4. *In-situ* EPR spectroscopy studies of Ni(II)/TiO<sub>2</sub>

In order to understand the charge separation and transfer behavior of the Ni(II)/TiO<sub>2</sub>, the *in-situ* EPR spectroscopy was performed in an argon atmosphere. As shown in Figure 4.9, new paramagnetic species are formed within the bare and 0.1 wt% Ni grafted TiO<sub>2</sub> photocatalysts upon UV-vis light irradiation. The signals arising upon UV-vis irradiation are summarized in Table 4.5. Moreover, the comparison spectra of bare and 0.1 wt% Ni grafted TiO<sub>2</sub> are presented in Figure 4.9.

Table 4.5.: EPR parameters of the detected signals on 0.1 wt% Ni/UV100 upon UV-vis illumination and their assignment.

Assignment	g <sub>1</sub>	g <sub>2</sub>	g <sub>3</sub>
Ti <sup>4+</sup> -O <sub>2</sub> <sup>-•</sup>	2.027	2.009	2.005
Ti <sup>3+</sup> anatase	1.990	1.990	1.96
Ti <sup>4+</sup> -O <sup>•-</sup> - Ti <sup>4+</sup> -OH <sup>-</sup>	2.018	2.014	2.005

As it can be seen in Figure 4.9, the intensity of the peak belonging to the trapped electrons at TiO<sub>2</sub> oxygen vacancies at g value 2.004 (Ti<sup>4+</sup>-O<sub>2</sub><sup>-•</sup>), significantly decreases in 0.1 wt% Ni grafted TiO<sub>2</sub> samples. That is clear evidence of the trapping electrons at the nickel ions site and

their consumption efficiently by reducing oxygen molecule instead of trapping at oxygen vacancies when the surface of the  $\text{TiO}_2$  is grafted 0.1 wt% Ni. The photogenerated electrons on  $\text{TiO}_2$  are more populated than those on the Ni grafted  $\text{TiO}_2$ , suggesting that the Ni ions can trap part of the electrons, thus efficiently suppressing the recombination of electron-hole pairs. Consequently, the intensity of the signals B (Figure 3.5) at g values 1.90 and 1.96 of the Ni/UV100 photocatalyst is drastically decreased in comparison with bare  $\text{TiO}_2$ . This observation is consistent with a previous report, [210], which proved that the grafted Ni(II) ions located on the surface and surface defects of  $\text{TiO}_2$ , reduce the amount of  $\text{Ti}^{3+}$  species by trapping photogenerated electrons. The broad weak signal at around  $g = 2.06$  (Signal C) (Figure 3.5) observed in bare  $\text{TiO}_2$  is more intense than in 0.1 wt% Ni/UV100 which corresponds to the surface-adsorbed  $\text{O}_2$  molecules, that act as electron acceptors. [211] As a result of this, EPR results could be assured that Ni ions are located on the surface of  $\text{TiO}_2$  rather than in the crystal cell. These metal ions centers play an essential role in transferring the trapped electrons to the surface adsorbed oxygen molecules, which further oxidize the THQ into the quinoline.

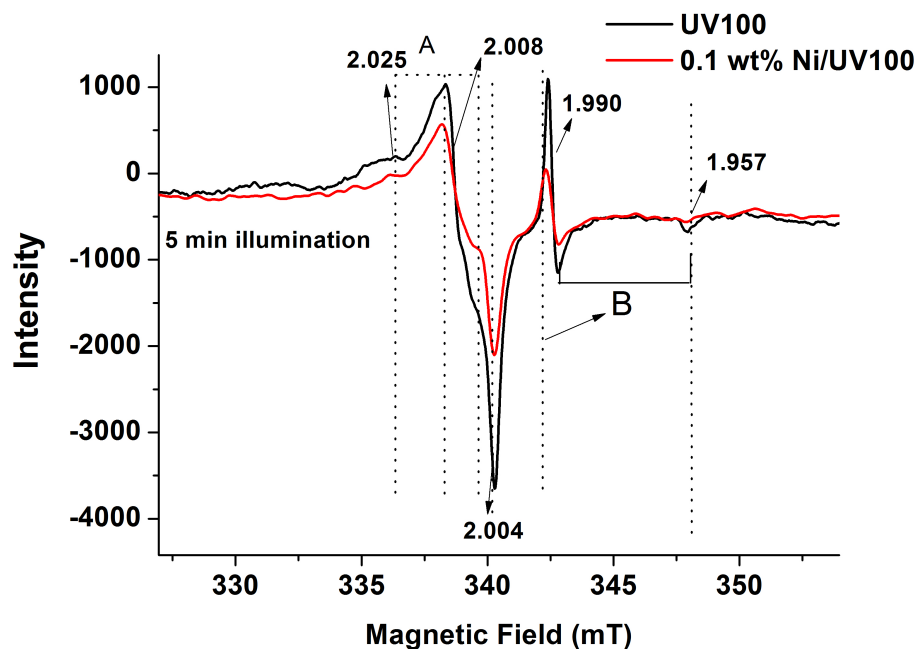
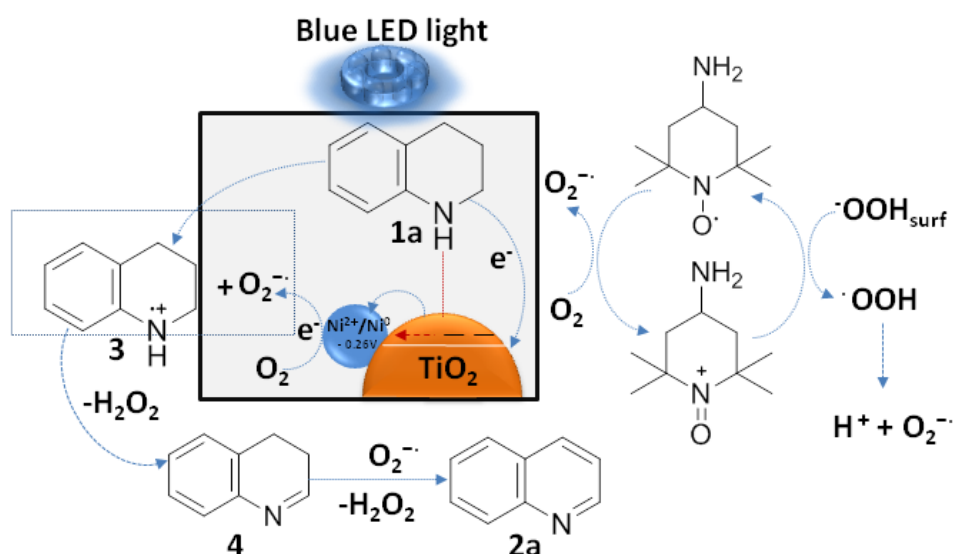


Figure 4.9.: EPR spectra of bare  $\text{TiO}_2$  and 0.1 wt% Ni/ $\text{TiO}_2$  UV100 upon UV-vis light irradiation at 77 K.



### 4.3.5. Proposed reaction mechanism

Based on the obtained results, a tentative mechanism for the dehydrogenation reaction of tetrahydroquinolines in the presence of Ni(II) grafted  $\text{TiO}_2$  is proposed in Scheme 4.6. Initially, due to the Lewis acid-base interaction, tetrahydroquinoline binds to the surface of UV100 to form a surface complex. This surface complex absorbs visible light, and the process LMCT occurs whereby electron leaps directly from the HOMO level of an amine into the conduction band of  $\text{TiO}_2$  and amine radical cation forms. Subsequently, the excited electron transfers from the conduction band of the semiconductor into the Ni ions. After being temporarily stored on the surface grafted Ni ion, the photogenerated electron reduces  $\text{O}_2$  yielding the superoxide radical anion  $\text{O}_2^{\cdot-}$ . This radical anion abstracts two protons and one electron from the tetrahydroquinoline radical cation, forming the C=N bond. [165] This sequence of reaction steps is repeated with the partially dehydrogenated product as the reactant to complete the aromatization to the quinoline, and two hydrogen peroxide molecules are formed as a side product.



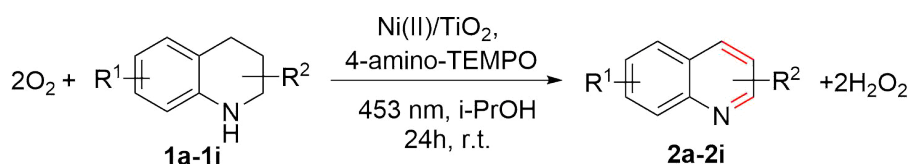
Scheme 4.6: Proposed mechanism of the ongoing reaction in the presence of 4-amino-TEMPO and surface-grafted 0.1 wt% Ni/ $\text{TiO}_2$  photocatalyst.

Hydrogen peroxide can further be oxidized furnishing hydroxyl radicals. These radicals are highly oxidizing agents that can affect the selectivity of the reaction yield. However, the employed 4-amino-TEMPO act as a selective redox mediator to oxidize hydrogen peroxide into superoxide

radical and a proton. Moreover, as illustrated in Scheme 4.6, 4-amino-TEMPO reduces molecular oxygen yielding the superoxide radical. The grafted Ni ion ( $E^0(\text{Ni}^{2+}/\text{Ni}^0) = -0.26\text{V}$  vs. NHE) likely plays the role of an electron shuttle which not only hinders the fast decay of the photogenerated electrons but also promotes the reduction of  $\text{O}_2$  by conduction band electrons, thus enhancing the overall photo-activity of UV-100. However, noble metal co-catalysts demonstrate relatively low reaction yield, which can be explained by their electron scavenging capacity that retards the reaction momentum, eventually causing low activity. Thus electrons are stored by noble metal sites rather than oxygen side. Therefore fewer superoxide radicals are formed.

#### 4.3.6. Oxidative dehydrogenation of N-heterocycles

As it can be seen in results Section (Table 3.5 (2a)), unsubstituted THQ reacted excellently under optimized reaction conditions presented in Scheme 4.1. Quinoline was isolated, giving a yield of 91% in oxygen atmosphere (Table 4.6 entry 1). Although dehydrogenation of THQ over  $\text{TiO}_2$  based photocatalyst was not reported before,  $\text{Nb}_2\text{O}_5$  has been reported to be efficient for the dehydrogenation of THisoQ as a heterogeneous semiconductor. Similar to  $\text{TiO}_2$ ,  $\text{Nb}_2\text{O}_5$  cannot absorb visible light due to its large bandgap energy. However, aerobic dehydrogenation of THQ at the wavelength  $\lambda > 390$  nm was possible, due to the interaction between  $\text{Nb}_2\text{O}_5$  and amines. [116] The photocatalytic performance of the  $\text{TiO}_2$  photocatalyst in aerobic dehydrogenation reactions was observed to be affected by the NH group's position and electron-donating and electron-withdrawing substituent groups in N-heterocycles. In general, tetrahydroquinolines underwent complete dehydrogenation reactions in oxygen atmospheres (Table 4.6). The reactivity drastically dropped when hydroxyl and nitro-group bearing substrates are applied to the oxidative dehydrogenation reactions. The inactivity of the former substrate was likely due to the poor oxidation of the aniline moiety caused by the strongly electron-withdrawing nitro group (Table 4.6 entry 6). The inertness of the hydroxylated compound is probably due to a competitive complex formation on the  $\text{TiO}_2$  surface via the hydroxyl group (Table 4.6 entry 4). To test this hypothesis, the OH group was protected as TBDMS (tert-butyldimethylsilyl) ether and then subjected to the optimized reaction conditions. When OH group was protected as TBDMS (tert-butyldimethylsilyl) ether, the TBSO group reacted efficiently to obtain the corresponding dehydrogenation product with excellent yield with the optimized conditions (2e), 83% (Table 4.6 entry 5).

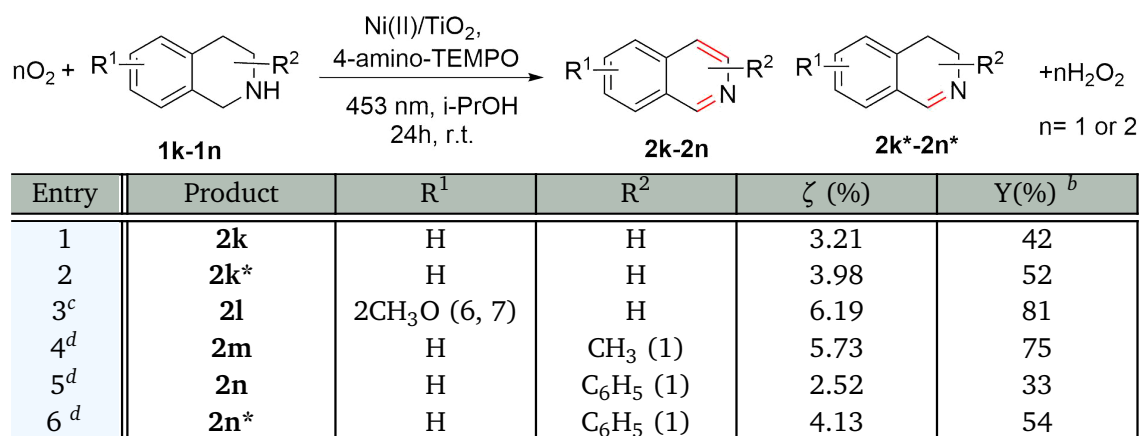
Table 4.6.: Dehydrogenation of the tetrahydroquinolines in oxygen <sup>a</sup>.

Entry	Product	R <sup>1</sup>	R <sup>2</sup>	ζ (%)	Y(%) <sup>b</sup>
1	<b>2a</b>	H	H	6.96	91
2	<b>2b</b>	CH <sub>3</sub> O (6)	H	7.19	94
3	<b>2c</b>	H	CH <sub>3</sub> (2)	6.96	91
4	<b>2d</b>	OH (7)	H	-	0
5	<b>2e</b>	TBSO (7)	H	6.34	83
6	<b>2f</b>	NO <sub>2</sub> (7)	H	-	-
7	<b>2g</b>	Cl (6)	H	7.03	92
8	<b>2h</b>	CH <sub>3</sub> (6)	H	5.66	72
9	<b>2i</b>	COOH (8)	CH <sub>3</sub> (2)	7.11	93

<sup>a</sup> Reaction conditions: 10 mg photocatalyst, 24 h visible light illumination (LED lamp,  $\lambda_{max}=453$  nm, 4 mW/cm<sup>2</sup>), 1 atm O<sub>2</sub>, 0.4 mmol THQs (50.2  $\mu$ L), 4 mL i-C<sub>3</sub>H<sub>7</sub>OH, 20 mol% 4-amino-TEMPO (0.08 mmol) as a redox mediator with respect to the reactant. <sup>b</sup> The yields are those of the isolated product. The numbers in the parenthesis correspond to the position of the functional groups.

Photonic efficiency was found to be similar in most reactive substrates. The electron-donating, methoxy group bearing substrate demonstrated the highest photonic efficiency (7.19 %). Furthermore, the substrate bearing two contradicting groups, electron-withdrawing (COOH) and electron-donating groups (CH<sub>3</sub>) (Table 4.6 entry 9) showed excellent yield (above 90 %). That could be attributed to the fact that the carboxylic acid group at C-8 position interacts with TiO<sub>2</sub>, forming another type of surface complex. The dehydrogenation of tetrahydroquinolines is summarized in Table 4.6. The dehydrogenation of unsubstituted tetrahydroisoquinolines was realized in this study under oxygen atmospheres in optimized reaction conditions. Unsubstituted THisoQ reacted excellently under optimized reaction conditions, and the isolated yield was mainly the partial dehydrogenation product of 3,4-dihydroisoquinoline (**1k\***) (Table 4.7 entry 2) and com-

plete dehydrogenation product of isoquinoline was isolated as the minor product (Table 4.7 entry 2 (**1k**)). These results are consistent with previously reported studies showing that in oxygen atmosphere the dehydrogenation of THisoQ afforded 68% and 47% of 3,4-dihydroisoquinoline over bare  $\text{TiO}_2$  [113] and  $\text{Nb}_2\text{O}_5$  [116] surface upon visible light illumination, respectively. Like the unsubstituted tetrahydroisoquinoline, the substrate bearing phenyl group exhibited a mainly partial dehydrogenation product, and a less complete dehydrogenation product is optimized reaction conditions in oxygenated atmospheres. THisoQ bearing methyl group in the C2 position gave complete aromatized product in (75%) oxygen atmosphere when the reaction temperature was increased up to  $47^\circ\text{C}$  (Table 4.7 entry 4). Notably, the substrate bearing two strong electron-donating methoxy groups showed excellent reactivity in complete dehydrogenation reactions (Table 4.7 entry 3). The enhanced reactivity of this compound is presumably due to the presence of the two electron-donating methoxy groups. The dehydrogenation of tetrahydroisoquinolines is summarized in Table 4.7. Thus, the overall photonic efficiency of the reactants was comparable to that of the photonics efficiency obtained from tetrahydroquinoline substrates (Table 4.7). The highest photonic efficiency was 7.19 %, which corresponds to the sum of photonic efficiencies obtained from complete and partial dehydrogenation of THisoQ. Not surprisingly, the substrate bearing two electron-donating methoxy groups showed higher photonic efficiency (6.18 %) than other substituted tetrahydroisoquinoline substrates (Table 4.7 entry 3). Dehydrogenation of unsubstituted indoline tolerated differently in oxygen atmospheres while using optimized reaction conditions. Thus, it was found that due to its electron-rich nature, photogenerated product (indole) was easily oxidized and degraded during the reaction time in 1 atm  $\text{O}_2$ . However, the excellent yield was obtained while using only air as an oxidant (Table 3.6 (**2o**)). Interestingly, indolines underwent a smooth dehydrogenation reaction in oxygen and air conditions yielding excellent products after 24 h. The substrates bearing electron donating group such as methyl or methoxy underwent to the complete aromatization in oxygen atmosphere (Table 3.5, **1b**, **1c**, **1h**, **1i**). Despite the moderate electron withdrawing nature, substrate bearing chlorine group afforded excellent yield (Table 3.5, **1g**).

Table 4.7.: Dehydrogenation of the tetrahydroisoquinolines in oxygen <sup>a</sup>.

<sup>a</sup> Reaction conditions: 10 mg photocatalyst, 24 h visible light illumination (LED lamp,  $\lambda_{max}=453 \text{ nm}$ ,  $4 \text{ mW/cm}^2$ ), 1 atm O<sub>2</sub>, 0.4 mmol THQs (50.2  $\mu\text{L}$ ), 4 mL i-C<sub>3</sub>H<sub>7</sub>OH, 20 mol% 4-amino-TEMPO (0.08 mmol) as a redox mediator with respect to the reactant. <sup>b</sup> The yields are those of the isolated product. <sup>c</sup> CH<sub>2</sub>Cl<sub>2</sub>: i-C<sub>3</sub>H<sub>7</sub>OH. <sup>d</sup> 47°C. The numbers in the parenthesis correspond to the position of the functional groups.

#### 4.4. ADH of THQ - effect of different reaction parameters

In an attempt to increase the formation of quinoline in ADH reactions, several solvents were employed. The poor to moderate yields were observed in methanol, ethanol, and acetonitrile solvents (7%, 15%, and 31%, respectively). A significant improvement, almost quantitative yields were observed when 2-propanol was used as a solvent (99%). These results have several possible explanations. The results were compared with the dielectric constant and the polarity of the solvents. Comparing the photocatalytic efficiencies in different solvents exhibits an inverse correlation between the dielectric constant and the product formation. As became obvious from the results presented in Table 4.8, 2-propanol has a lower polarity and a lower dielectric constant compared to other solvents, which shows the highest photocatalytic performance compared to all other solvents. Thus, the low dielectric constant of 2-propanol could be associated with the high mobility of the photogenerated charge carrier. Shiraishi et al. reported the selective reduction of 4-nitrophenol in various alcohols (methanol, ethanol, 1-propanol, 2-propanol, 1-butanol, and 2-butanol) with TiO<sub>2</sub> (Degussa P25) under UV irradiation. [212] They have revealed that polarity plays a critical role in the reaction rate. Thus the increase of the polarity parameter leads

to better stabilization of the charged intermediate and therefore accelerates the reduction of the photocatalysis. Brezova et al. also reported the selective reduction of 4-nitrophenol and carefully analyzed the influence of solvent polarity, viscosity, refractive index, and relative permittivity on the reaction rate. [213]

Table 4.8.: Correlation between dielectric constant of solvents and photonic efficiencies in ADH reactions of THQ <sup>a</sup>.

Entry	Solvents	$\zeta$ (%)	Solvent Polarity Index (P)	Dielectric constant ( $\epsilon$ )
1	CH <sub>3</sub> OH	0.54	5.1	32.6
2	C <sub>2</sub> H <sub>5</sub> OH	1.15	5.2	22.4
3	C <sub>3</sub> H <sub>7</sub> OH	7.57	3.92	18.0
4	CH <sub>3</sub> CN	2.37	5.8	37.5

<sup>a</sup> Reaction conditions: 5 mg 1 wt% Rh/TiO<sub>2</sub>, 24 h visible light illumination (LED lamp,  $\lambda_{max}=453$  nm, 4 mW/cm<sup>2</sup>), Argon atmosphere, 0.2 mmol THQ (25.1  $\mu$ L), 2 mL solvent, photonic efficiencies  $\zeta$  (%) are calculated from the results presented in Table 3.7.

Similar to the results mentioned above, they have also observed that high polarity plays an essential role in improving the stabilization of the produced charged intermediate and ultimately achieving a high reaction rate. However, the reverse effect of the solvent polarity was observed in this study. The increased polarity of the solvent has been shown to reduce the reaction yield dramatically. Wang et al. also reported the same acceptorless dehydrogenation reactions of N-heterocycles over g-BCN and observed that the highest reaction yield was achieved using 2-propanol. [160] These results are in agreement with the method established in the present work. However, interestingly, they also achieved a high yield while using water as a solvent. However, in the present work, the reaction's yield was meager, while using water as solvent (results are not presented).

#### 4.4.1. Effect of noble metals on the reaction yield

The ADH reactions of N-heterocycles could only be facilitated by the presence of co-catalysts on  $\text{TiO}_2$ . Noble metals are known to be a strong electron scavenger and thus improve the separation of the photogenerated charge-carriers as well as enhance the reaction rate. The photocatalytic performance of different noble metal nanoparticles photodeposited on  $\text{TiO}_2$  was compared in the ADH reaction of THQ under optimized reaction conditions (Scheme 4.2). As it was shown in Section 3.4.2, the yields increased with the order of  $\text{Au} < \text{RuO}_2 < \text{Pd} < \text{Pt} < \text{Rh}$ . To specify the critical feature of noble metals that affect the reaction yield different intrinsic factors of noble metals were examined. Interestingly, UV-vis diffuse reflectance spectra (Figure 3.2) show that only ruthenium oxide and gold nanoparticles photodeposited  $\text{TiO}_2$  has a strong plasmonic absorption peak at around 400-630 nm. It is well known that Au nanoparticles have localized surface plasmon resonance (LSPR), which can directly be excited upon visible light illumination. [214] On the other hand, Jeon et al. demonstrated the LSPR effect of  $\text{RuO}_2$  decorated on ZnO nanorods, which allow visible light absorption. [215]

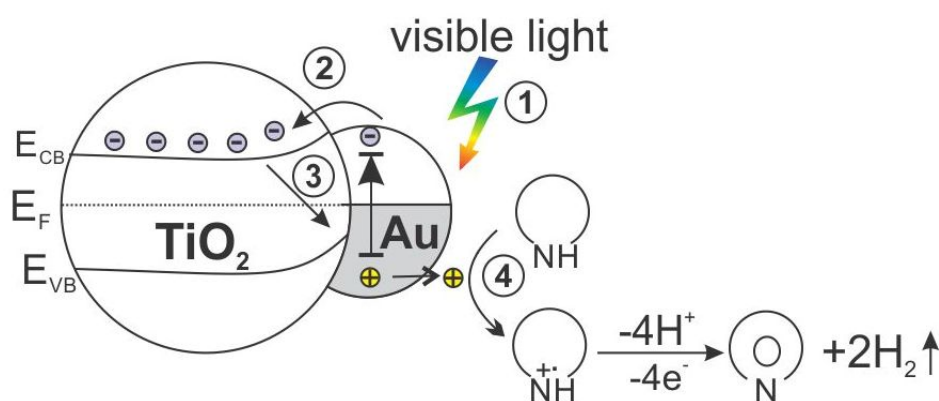


Figure 4.10.: Schematic illustration of proposed mechanism of anaerobic amine dehydrogenation over Au/ $\text{TiO}_2$  nanoparticles upon visible light illumination. path 1 is the excitation of Au nanoparticles with visible light, path 2 is the electron transfer from Au nanoparticles to the conduction band of  $\text{TiO}_2$ , path 3 is the recombination of the photogenerated charge carriers, path 4 is the oxidative dehydrogenation of N-heterocyclic amines by photogenerated holes.

Although Pt and Pd photodeposited  $\text{TiO}_2$  exhibit the weak absorption edge at around 600-800 nm, the Rh photodeposited  $\text{TiO}_2$  only has an absorption in the UV region (Figure 3.2). The visible-

light absorption of RuO<sub>2</sub> and Au co-catalysts possibly hinder the dehydrogenation reaction due to other competitive visible-light-induced reaction pathways. These results were consistent with the suggestion that the dehydrogenation was initialized by visible-light excitation of the amine-TiO<sub>2</sub> complex. Several effects can have an impact on the photocatalytic performance of noble metal nanoparticles. It should be considered all of the employed noble metals have low hydrogen overpotential that can easily accept photogenerated electrons from the conduction band of TiO<sub>2</sub>. [164] Another most common factor is usually applied to correlate the photocatalytic activity of noble metal co-catalysts with their work function ((Figure 4.11, left)). Since TiO<sub>2</sub> has work function (4.2 eV) lower than all employed noble metals such as Pt, Pd, Au, Rh, and Ru ( 5.65, 5.55, 5.1, 4.98, and 4.71 eV, respectively) a Schottky barrier can be formed at the metal-TiO<sub>2</sub> interface. [216] Thus, having a bigger work function on the noble-metals introduces a more substantial Schottky barrier, which subsequently results in better charge separation. The ADH results obtained in this study in the assistance of various noble metals photodeposited on TiO<sub>2</sub> are correlated with noble metals' work function. Interestingly, the results are supported by the fact that the photoactivity of THQ dehydrogenation decreases with decreasing work function value of noble metals. However, it was observed that although Au nanoparticles have a 5.1 eV work function value, they demonstrated poor photocatalytic performance. That could be correlated with their plasmonic effect. Generally, Rh, Pd, and Pt showed better photocatalytic performance, whereas the work function of Au is higher than the work function of Rh (Figure 4.11, right). These results actively support the adverse plasmonic effect of Au nanoparticles on the ADH reaction, restricting the absorption of visible light by the surface complex. Golovko et al. the reported LSPR effect of RuO<sub>2</sub> supported on TiO<sub>2</sub> in visible-light-driven aerobic oxidation of amines to nitriles. [217] They have demonstrated that visible light absorption is initiated by RuO<sub>2</sub> nanoparticles, where surface adsorbed molecular oxygen act as the electron acceptor from RuO<sub>2</sub> nanoparticles via conduction band of TiO<sub>2</sub>. Their mechanistic investigations indicated the involvement of singlet oxygen in the photocatalytic amine oxidation was significantly important. Besides, Figure 4.10 shows the example of the LSPR effect of Au nanoparticles under visible light illumination by presenting the reaction conditions used for the acceptorless dehydrogenation of N-heterocycles. Initially, upon visible light illumination, gold nanoparticles are excited (path 1) and transfer its electron into the conduction band of TiO<sub>2</sub> (path 2). Since the system is free of oxygen in an acceptorless dehy-



drogenation reaction, the recombination rate of the photogenerated charges are high (path 3). The absorption of visible light by surface plasmonic nanoparticle such as Au and RuO<sub>2</sub> restricts the formation of the surface complex between TiO<sub>2</sub> and amine. The holes generated inside the Au nanoparticles could potentially oxidize the amines. However, the results show that the yield is quite poor. Therefore, the surface complexation between the amine and TiO<sub>2</sub> is preferable for visible light activation. [164]

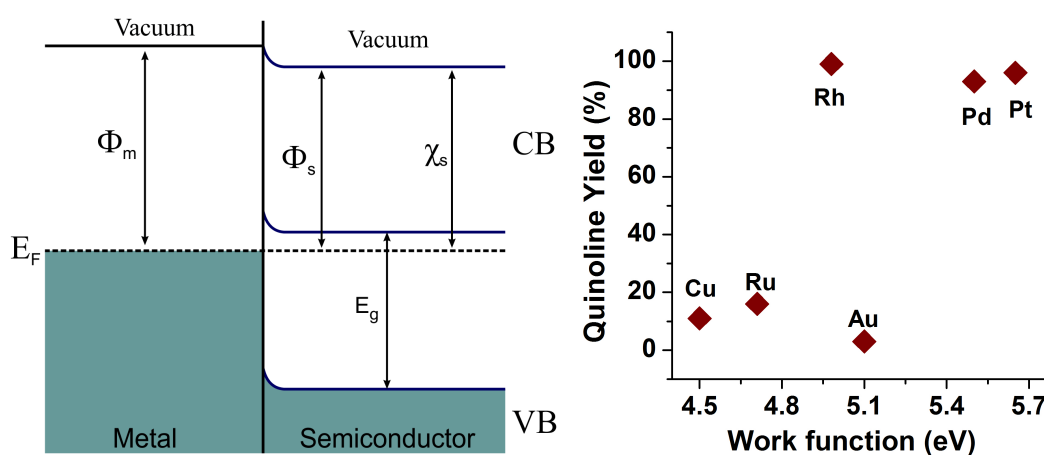


Figure 4.11.: Schematic illustration when metal and semiconductor bring into the contact (left), dependence of the photocatalytic performance of 1 wt% of the noble metal photodeposited on TiO<sub>2</sub> from the work function of the noble metals (right).

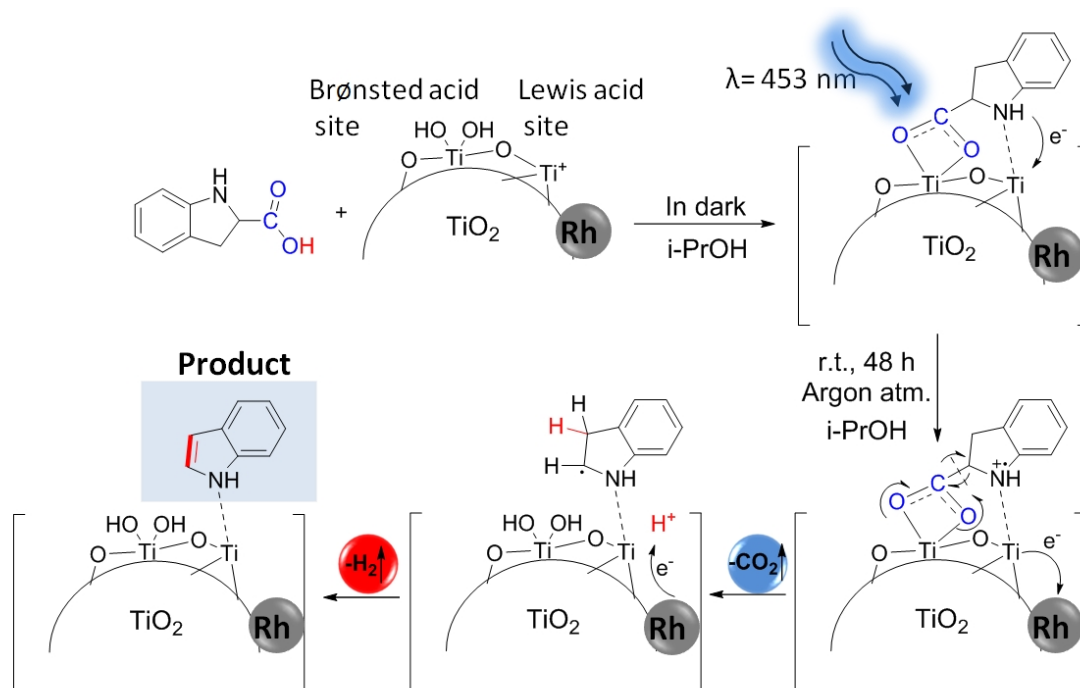
Likewise, as it could be observed from UV-vis spectroscopy results that the absorption coefficients of these Au/TiO<sub>2</sub> and RuO<sub>2</sub>/TiO<sub>2</sub> are three times less than the absorption coefficient of amine-TiO<sub>2</sub> surface complex which therefore shows drastically low photocatalytic performance in comparison with other noble metal photodeposited TiO<sub>2</sub> nanoparticles.

Moromi et al. also observed the similar order of catalytic performance of noble metals in thermal dehydrogenation of tetrahydroquinolines supported on carbon. They have compared the dehydrogenation rate as a function of the d-band center ( $\epsilon d$ ) relative to the Fermi energy ( $E_F$ ) for the clean metal surface. [218]

#### 4.4.2. General overview of ADH of N-heterocycles

ADH of N-heterocyclic amines, i.e., tetrahydroquinolines, tetrahydroisoquinolines, indolines, and other cyclic class amines with surface photodeposited TiO<sub>2</sub> was investigated in this study. The reactions took place under argon atmosphere at room temperature upon illumination with 34W LED blue visible light ( $\lambda_{max} = 453$  nm). [164] As it can be seen in the results section, unsubstituted THQ reacted excellently under in optimized reaction conditions and 96% yield in argon (Table 3.8 (2a)) atmosphere were isolated. The dehydrogenation of unsubstituted THisoQ was realized in this study under argon atmospheres in optimized reaction conditions where, as the main product, the isolated yield was mainly the partial dehydrogenation product of 3,4-dihydroisoquinoline (See Table 3.9 (1k)). Dehydrogenation of unsubstituted indoline is tolerated differently in argon atmospheres compared with the ADH of other N-heterocycles using optimized reaction conditions. The photocatalytic performance of TiO<sub>2</sub>, in anaerobic dehydrogenation reactions, was observed to be affected by the position of the NH group as well as electron-donating and electron-withdrawing substituent groups in N-heterocycles. Generally, tetrahydroquinolines underwent complete dehydrogenation reactions in anaerobic atmospheres (Table 3.8). Similar to the unsubstituted THisoQ, tetrahydroisoquinolines exhibited a mainly partial dehydrogenation product and a less complete dehydrogenation product in the optimized reaction conditions in inert atmospheres. However, indolines underwent dehydrogenation reaction in inert atmospheres within 48 h reaction time obtaining good yield. The substrates bearing electron-donating group such as methyl or methoxy underwent to the complete aromatization product (Table 3.8, 1b, 1c, 1h 1i). Despite the moderate electron-withdrawing nature, the substrate bearing chlorine group afforded excellent yield in an inert condition (Table 3.8, 1g). The reactivity drastically dropped when hydroxyl and nitro-group bearing substrates are applied to the dehydrogenation process in acceptorless reactions similar to the oxidative dehydrogenation process. Thus, these substrates were almost inactive in both atmospheres. THisoQ bearing methyl group in C2 position gave the complete aromatized product in acceptorless catalytic conditions gave the product (2m\*) in 34% and product (2m) in 46% isolated yield after 48 h. Notably, substrate bearing two electron-donating methoxy groups showed excellent reactivity in complete dehydrogenation reactions yielding 88%. The enhanced reactivity of this compound is presumably due to the presence of the two electron-donating methoxy groups. Substrates bearing electron-deficient groups such as -C(O)Me and

CF<sub>3</sub> underwent ADH reaction smoothly and gave the desired products in good to excellent yield. Indolines having a carboxylic acid group, underwent dehydrogenation and decarboxylation reactions. It was observed that the substrates bearing carboxylic acid group at C2 position of indoline (See Table 3.10 (**1r**) and (**1s**)) undergoes decarboxylation and dehydrogenation reaction in the optimized reaction condition. The possible ongoing reaction pathways were investigated in order to propose the reaction mechanism. It has been reported that a chemical bond is formed between the carboxylic group and the TiO<sub>2</sub> surface Brønsted acid site (Ti-OH). [219]



Scheme 4.7: Acceptorless decarboxylation and dehydrogenation mechanism of 2-carboxyl-indoline upon visible-light illumination. Reaction conditions: 1 wt% Rh/TiO<sub>2</sub> photocatalyst (5 mg), 2-carboxyl-indoline (0.2 mmol) i-C<sub>3</sub>H<sub>7</sub>OH (2 mL), blue LED light ( $\lambda = 453$  nm), Argon atmosphere, 48 h.

FTIR study revealed that the interaction of the carboxyl group with the TiO<sub>2</sub> surface is more favorable than the interaction of the amine group with the oxide surface. [220] On the other hand, it is well-established that Photo-Kolbe decarboxylation occurred when acetic acid adsorbed on the surface of TiO<sub>2</sub>, which has been irradiated with UV light. [10] Although visible light is employed in our system, the reaction exhibited that decarboxylation was still favorable in the C2 position of indoline before the dehydrogenation reaction. Recently, visible-light decarboxylation of the same

substrate (**1r**) was studied on metal-halide perovskite in  $N_2$  atmosphere. However, both decarboxylation and dehydrogenation occurred in an  $O_2$  atmosphere. [221] According to the previous works, a decarboxylation and dehydrogenation reaction mechanism of indoline-2-carboxylic acid on the Rh/TiO<sub>2</sub> surface (Scheme 4.7) was proposed. It is supposed that while the carboxyl group interacts with the Ti-OH Brønsted acid site, and amine group forms a surface complex with Ti<sup>+</sup> Lewis acid site of TiO<sub>2</sub>. The latter complex, as the visible-light-absorbing species, initiates the photon absorption and amine cation radical formation by transferring a single electron to the conduction band of TiO<sub>2</sub>. Subsequently, the substrate undergoes the decarboxylation through C-C bond cleavage, and an alpha-amino radical is generated. The radical cation loses a proton to form a double bond. [164] Since it has been discussed that an amine group adsorbed onto TiO<sub>2</sub> surface initiates the visible-light absorption and electron-transfer reactions, it was unexpected to be observed the ADH of the (**1w**) substrate which is not bearing an amine group.

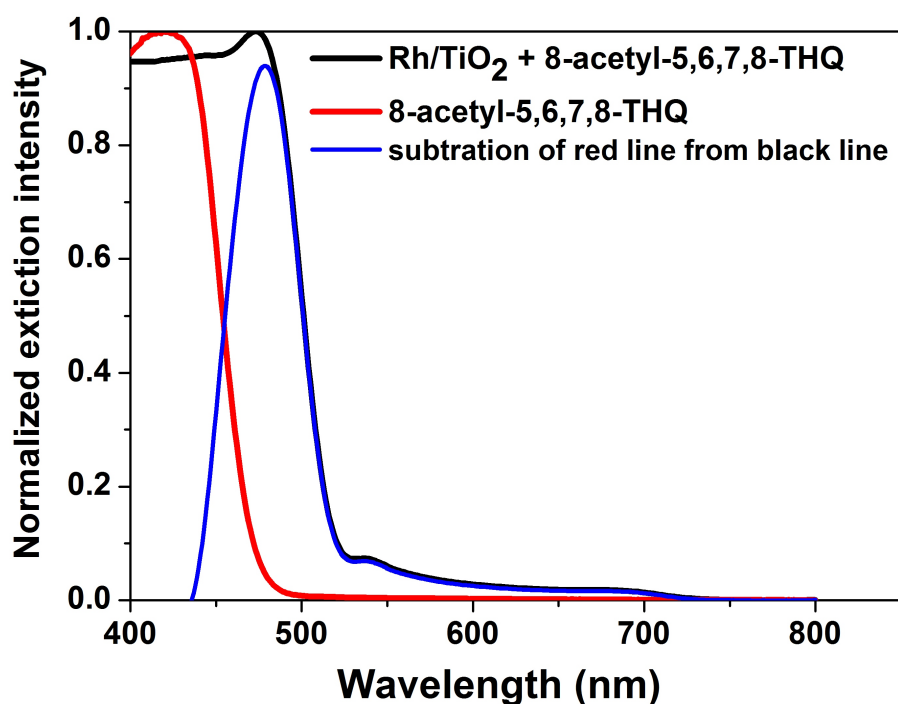
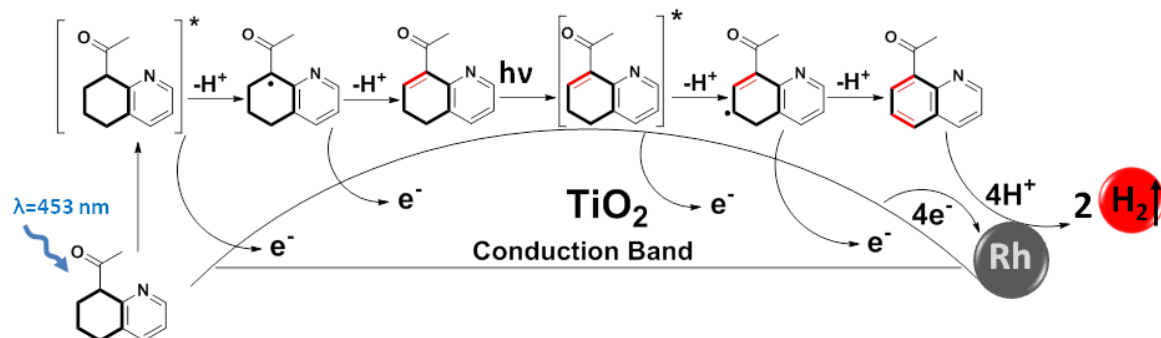


Figure 4.12.: Normalized optical absorption spectrum and extinction spectrum of 8-Acetyl-5,6,7,8-THQ and 1 wt% Rh/TiO<sub>2</sub> (UV100) suspension containing 8-Acetyl-5,6,7,8-THQ in 2 mL  $i-C_3H_7OH$ , respectively and blue line spectrum is extraction of the optical absorption spectrum of 8-Acetyl-5,6,7,8-THQ from the extinction spectrum of 8-Acetyl-5,6,7,8-THQ/ 1 wt% Rh/TiO<sub>2</sub>.

Therefore, the origin of the light-absorbing-species was further investigated by UV-vis spec-

trosopy. The bright yellow substrate (8-acetyl-5,6,7,8-tetrahydroquinoline) showed the absorption up to 475 nm (Figure 4.12). Moreover, adding 1 wt% Rh/UV100 catalyst into 8-acetyl-5,6,7,8-tetrahydroquinoline and *i*-PrOH solution, demonstrated extended optical absorption up to 525 nm (Figure 4.12). These spectroscopic analyses evince that a prerequisite for the visible-light-mediated photocatalytic ADH is either substrate, which absorbs visible-light or a surface complex due to surface interaction between 8-acetyl-5,6,7,8-tetrahydroquinoline and TiO<sub>2</sub>. Therefore, the ongoing photocatalytic reaction mechanism was proposed in Scheme 4.8 to assume that 8-acetyl-5,6,7,8-tetrahydroquinoline acts as the antenna molecule and initiate a visible-light ADH reaction. Hence, initially, upon visible-light illumination, the substrate excited from HOMO to the LUMO energy level. In the next step, the excited substrate transfers its electron to the conduction band of the semiconducting TiO<sub>2</sub>. The electron is consecutively transferred to the noble metal attached to the TiO<sub>2</sub> surface, where it becomes temporarily stored. The formed cation of the substrate generated by electron transfer is a strong Brønsted acid, which undergoes the first deprotonation and subsequently forms the partial dehydrogenation product. Since the partial dehydrogenation product was not observed after the photocatalytic experiment, it is assumed that the second dehydrogenation occurs as the same subsequent pathway to give the 8-acetyl-quinoline (Scheme 3.2, (**1w**)). Control studies showed the importance of photocatalyst and visible light where no transformation of 8-acetyl-5,6,7,8-THQ was achieved either in the absence of 1 wt% Rh/TiO<sub>2</sub> or visible-light. This result underlines the aromatization of cyclohexane-fused pyridine bearing acetyl group in the presence of 1 wt% Rh/TiO<sub>2</sub> in an inert atmosphere upon visible-light illumination could be realized. [164] However, the conclusion requires an in-depth investigation of the broad range of substrates, which opens a new pathway in the visible-light-mediated ADH of cyclohexane-fused pyridines involving TiO<sub>2</sub> photocatalyst. A better understanding of the underlying reaction mechanism and optimization of the reaction conditions might improve the moderate yield up to excellent yield.



Scheme 4.8: The ongoing reaction mechanism of photocatalytic acceptorless dehydrogenation of 8-Acetyl-5,6,7,8-THQ over 1 wt% Rh/UV100

#### 4.4.3. Proposed mechanism of the ADH reaction

Based on the experimental results, a reaction mechanism of acceptorless dehydrogenation is proposed in Figure 4.13. As it became evident from the results of UV-vis spectroscopy, although both the amines and 1 wt% Rh/TiO<sub>2</sub> separately absorb light only in the UV region, their physical mixture exhibited a broad absorption band in the visible region up to ~500 nm, suggesting the formation of a visible-light-responsive surface complex.

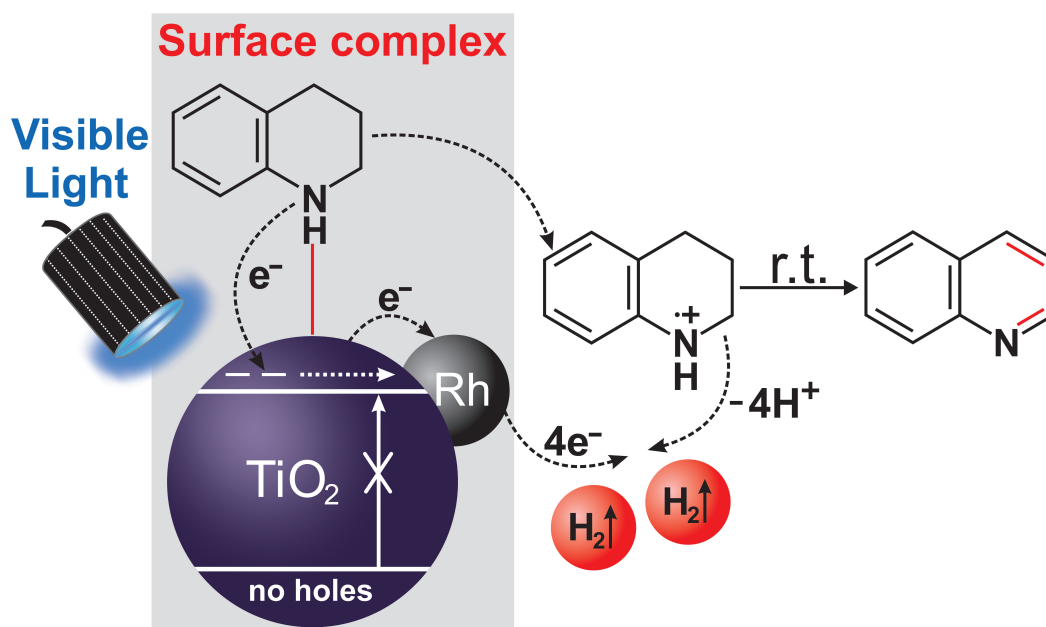


Figure 4.13.: A plausible mechanism of the acceptorless dehydrogenation reaction of the 1,2,3,4-tetrahydroquinoline in the presence of 1 wt% Rh/TiO<sub>2</sub> photocatalyst.

The visible light photosensitization of TiO<sub>2</sub> nanoparticles with N-heterocycles is assumed to occur through the LMCT method due to their Lewis acid-base interaction. Upon visible light excitation of the surface complex, the electron from the amine's ground state is injected directly into the conduction band of the TiO<sub>2</sub> UV-100. Subsequently, noble metal co-catalysts temporarily store injected electrons from the conduction band of TiO<sub>2</sub>. Two proton abstraction from the amine radical and reduction by two electrons forms the C=N bond and one molecular hydrogen. The repeating process drives the formation of another molecular hydrogen and the complete aromatization, yielding quinoline.





# Chapter 5

## Conclusions and outlook

Choosing the appropriate reaction conditions for the selective dehydrogenation process is crucial for the synthesis of aromatic N-heterocycles. For the first time in this work, the visible-light-induced dehydrogenation of N-heterocyclic amines over surface-modified TiO<sub>2</sub> nanoparticles was successfully performed in the presence of oxygen as well as in inert atmospheres. The developed method showed that TiO<sub>2</sub> nanoparticles are promising photocatalysts for the dehydrogenation of a broad range of N-heterocyclic arenes bearing electron-rich and electron-deficient functional groups. All photocatalytic reactions were carried out upon visible light illumination, despite the known fact that TiO<sub>2</sub> nanoparticles only absorb high energy UV light due to their large bandgap energy. This study showed that the optical absorption spectrum of TiO<sub>2</sub> shifts toward the visible region by about 60 nm when cyclic amines are adsorbed on the titania surface. The ATR-FTIR results showed the possible Lewis acid-base interaction between Ti<sup>+</sup> sites of TiO<sub>2</sub> and the NH group of N-heterocyclic amine. These surface complexes act as photosensitizers driving the visible light oxidation of the N-heterocycles. Scheme 5.1 represents the general ongoing reaction mechanism of photocatalytic dehydrogenation of THQ in aerobic and anaerobic atmospheres.

Initially, upon visible light illumination, a single electron transfer occurs from the unexcited state (HOMO) of the N-heterocycle (**2a**) to the conduction band of TiO<sub>2</sub> (Scheme 5.1, path 1). Indeed, the oxidation potentials of these amines required to be well-matched with the redox po-

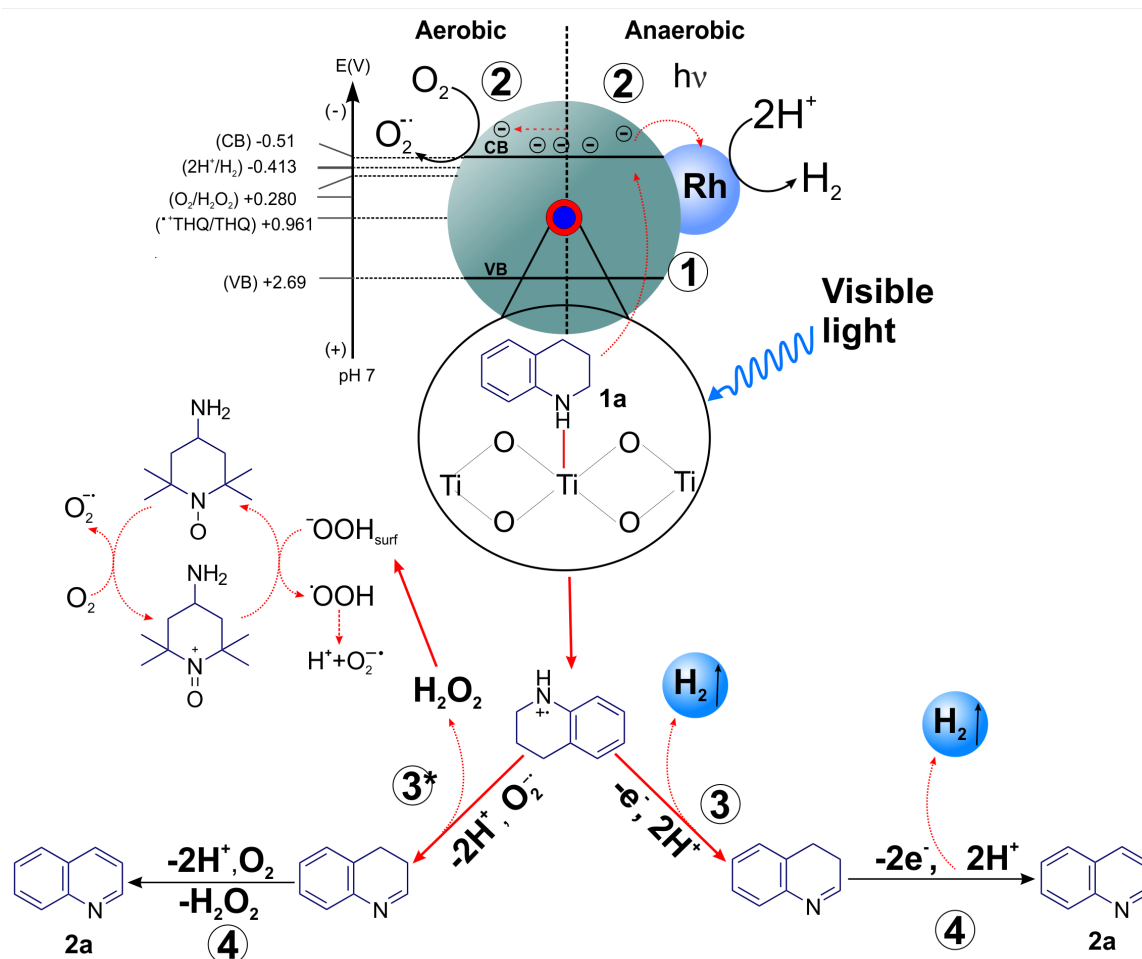
tential of TiO<sub>2</sub> (2.7 V vs. NHE for anatase) to ensure smooth electron transfer process. In the next step, the excited electron will be transferred from the conduction band of TiO<sub>2</sub> to the electron acceptor, which can be either surface-adsorbed O<sub>2</sub> or a suitable co-catalyst (Scheme 5.1, path 2). Under aerobic conditions, the subsequent reduction of oxygen molecules forms superoxide radicals (O<sub>2</sub><sup>•-</sup>) which further oxidize the amine radical cation to imine through the hydrogen-atom transfer (HAT) mechanism with a concomitant generation of H<sub>2</sub>O<sub>2</sub> (Scheme 5.1, path 3\*). On the other hand, in an argon atmosphere, the important electron acceptor on the surface of TiO<sub>2</sub>, such as noble metals, is reduced by the injected electrons. Thereby, the radical amine cation undergoes further one-electron oxidation with subsequent release of two protons. Eventually, the proton reduction by noble metal nanoparticles leads to the generation of a H<sub>2</sub> molecule (Scheme 5.1, path 3). Finally, in both reaction conditions the repetition of above photocatalytic cycles give the complete dehydrogenated product (**2a**) (Scheme 5.1, path 4).

This strategy avoids the photogeneration of holes in the valence band, which often causes the oxidation of protic solvents and the degradation of the reaction products, leading to low selectivities. The optimal reaction conditions for the dehydrogenation of N-heterocyclic amines for both aerobic and anaerobic atmospheres were successfully established.

The results exhibited that, independent from the reaction environment either oxygenated or inert, the specific surface area of the TiO<sub>2</sub> photocatalyst plays an important role that affects the photocatalytic efficiency. Although TiO<sub>2</sub> P25 is usually reported to demonstrate higher photocatalytic performance than anatase TiO<sub>2</sub> UV100 under UV irradiation, here it was found that TiO<sub>2</sub> UV100 showed significantly better photocatalytic efficiencies. That is associated with the high specific surface area of TiO<sub>2</sub> UV100. The surface coverage of probe molecules (THQ) of anatase UV100 TiO<sub>2</sub> was theoretically calculated to be 2.4 ML (monolayer), while 14.6 ML for P25 (rutile-anatase) TiO<sub>2</sub> in an optimized reaction condition. This evinces that the UV100 surface has larger adsorption sites as compared with P25 that exhibits saturation of all active sites. Therefore, to achieve the complete conversion of all amine molecules on P25 TiO<sub>2</sub> nanoparticles, longer reaction time is required.

In this study, the photocatalytic efficiency of the Hombikat UV100 TiO<sub>2</sub> nanoparticles was further improved by surface grafting and photodepositing with transition metal ion and metals. The as-synthesized nanoparticles were characterized by different analytical techniques such as UV-vis,

TEM, ICP-OES, FTIR, XRD, EPR, and BET. The dehydrogenation results under aerobic conditions revealed that transition metal ions grafted on TiO<sub>2</sub> serve as electron shuttles for transferring the excited electrons to molecular O<sub>2</sub>, thus retarding the fast decay of the photogenerated charge carriers. Moreover, these metal ions could act as electron-acceptor centers upon visible light illumination through interfacial charge transfer processes. The Ni(II) grafted TiO<sub>2</sub> nanoparticles showed improved yields (from 35% to 57%) and selectivity (from 43% to 61%) for the dehydrogenation of THQ, but further improvement was targeted in order to obtain yields and selectivities above 90%. The moderate yield and poor selectivity are presumed to be due to the competitive surface complexation of the H<sub>2</sub>O<sub>2</sub> (byproduct) with TiO<sub>2</sub> and the high oxidation behavior of the hydroperoxyl radicals (<sup>•</sup>OOH).



Scheme 5.1: The general ongoing reaction mechanism of photocatalytic dehydrogenation of THQ in aerobic and anaerobic atmosphere

Therefore, 20 mol% of TEMPO derivatives were used with respect to the substrate in order to increase the yield and the chemoselectivity of the dehydrogenation reaction. Significantly higher efficiency was achieved when 4-amino-TEMPO was used to investigate the role of TEMPO derivatives in the dehydrogenation reaction. It was revealed that 4-amino-TEMPO primarily acts as a radical trap for the decomposition of the surface adsorbed hydroperoxyl radicals ( $\bullet\text{OOH}$ ) resulting in the minimization of possible side reactions and thus the improvement of the reaction selectivity (Scheme 5.1, path 5). Under optimized reaction conditions inspired by the high photocatalyst activity of 0.1 wt% Ni/UV-100 and 20 mol% 4-amino-TEMPO in *i*-PrOH and an  $\text{O}_2$  atmosphere (1 atm) at room temperature, the range of substrates was explored resulting in good to excellent yields.

Although TEMPO redox mediators were required to increase the aerobic system's overall chemoselectivity, the anaerobic dehydrogenation of N-heterocycles was carried out in a single heterogeneous photocatalytic system with high selectivity. For comparing their photocatalytic activity, different noble metals such as Pt, Rh, Ru, Pd, and Au photodeposited on the surface of  $\text{TiO}_2$  have been investigated for the visible-light-induced dehydrogenation reaction in an argon atmosphere. As a result of this, it was observed that Au and  $\text{RuO}_2$  photodeposited  $\text{TiO}_2$  demonstrated dramatically poor photocatalytic performance (3% and 16%, respectively), whereas Rh, Pt, and Pd nanoparticles photodeposited on  $\text{TiO}_2$  showed similar comparable efficiencies (99%, 96 %, and 93%, respectively) in acceptorless dehydrogenation reactions. The formation of quinoline and simultaneous release of hydrogen molecules were noted to boost in the following order while varying the solvent in the reaction system:  $\text{CH}_3\text{OH} < \text{C}_2\text{H}_5\text{OH} < \text{CH}_3\text{CN} < i\text{-C}_3\text{H}_7\text{OH}$  (7%, 15%, 31%, and 99%, respectively). It was observed that increasing the deposition amount of noble metals higher than that 1 wt% affecting inferiorly to the photocatalytic performance of  $\text{TiO}_2$ .

It was also found that changing the photocatalysts amount in the system affects the formation rate of yields. For the complete anaerobic dehydrogenation, the appropriate catalyst amount and reaction time was 2.5 g/L and 24 h. Following the optimization of the reaction condition, dehydrogenation of several substrates such as tetrahydroquinolines (THQ), tetrahydroisoquinolines (THisoQs) and indolines in argon atmosphere were studied using 1 wt% Rh/ $\text{TiO}_2$  as a photocatalyst and isopropanol as a dispersant, which yielded good to excellent yield based on the nature of bearing reactive functional groups (electron-deficient or electron-rich). The results show that the

---

perhydroquinoline substrate lacking aromatic ring attached to the piperidine scaffold failed full aromatization, proving the essential role of the benzene ring in the dehydrogenation reaction. Sixfold subsequent experimental runs confirmed the robustness of the developed acceptorless dehydrogenation method. With this, the visible-light-mediated ADH reactions of the industrially significant organic compounds were successfully synthesized with the concomitant formation of hydrogen molecules.

In summary, selective oxidative and an acceptorless, base-free dehydrogenation of heterocyclic nitrogen-containing compounds using commercially available  $\text{TiO}_2$  has been developed. This new synthetic methodology could be applied to the various large bandgap semiconductors using visible light. Besides, further photocatalytic dehydrogenation and dehydrogenative coupling reactions of small organic molecules under visible light illumination could be investigated over  $\text{TiO}_2$  photocatalyst.



# Appendix

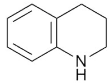
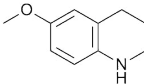
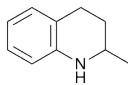
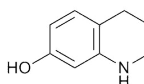
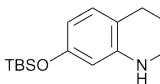
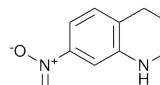
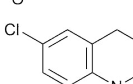
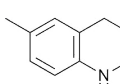
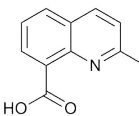
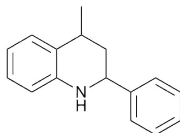
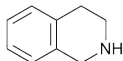
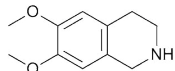
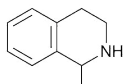
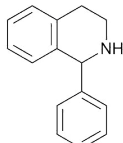


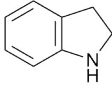
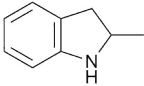
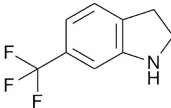
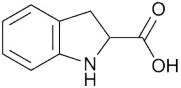
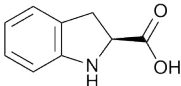
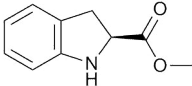
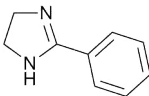
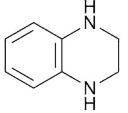
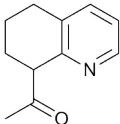
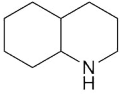
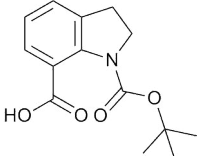


# Chapter A

## List of chemicals

Table A.1.: List of compounds name, chemicals structure, and symbols that employed in this study

Compounds name	Chemicals structure	Symbols
1,2,3,4-tetrahydroquinoline		<b>1a</b>
6-methoxy-1,2,3,4-tetrahydroquinoline		<b>1b</b>
2-methyl-1,2,3,4-tetrahydroquinoline		<b>1c</b>
1,2,3,4-tetrahydroquinolin-7-ol		<b>1d</b>
7-(( <i>tert</i> -butyldimethylsilyl)oxy)-1,2,3,4-tetrahydroquinoline		<b>1e</b>
7-nitro-1,2,3,4-tetrahydroquinoline		<b>1f</b>
6-chloro-1,2,3,4-tetrahydroquinoline		<b>1g</b>
6-methyl-1,2,3,4-tetrahydroquinoline		<b>1h</b>
2-methylquinoline-8-carboxylic acid		<b>1i</b>
4-methyl-2-phenyl-1,2,3,4-tetrahydroquinoline		<b>1j</b>
1,2,3,4-tetrahydroisoquinoline		<b>1k</b>
6,7-dimethoxy-1,2,3,4-tetrahydroisoquinoline		<b>1l</b>
1-methyl-1,2,3,4-tetrahydroisoquinoline		<b>1m</b>
1-phenyl-1,2,3,4-tetrahydroisoquinoline		<b>1n</b>

Compounds name	Chemicals structure	Symbols
indoline		<b>1o</b>
2-methyl indoline		<b>1p</b>
6-(trifluoromethyl)indoline		<b>1q</b>
indoline-2-carboxylic acid		<b>1r</b>
(S)-indoline-2-carboxylic acid		<b>1s</b>
methyl (S)-indoline-2-carboxylate		<b>1t</b>
2-phenyl-4,5-dihydro-1H-imidazole		<b>1u</b>
1,2,3,4-tetrahydroquinoxaline		<b>1v</b>
8-Acetyl-5,6,7,8-tetrahydroquinoline		<b>1w</b>
perhydroquinoline		<b>1x</b>
N-Boc-indoline-7-carboxylic acid		<b>1y</b>



# Chapter B

## NMR characterization of the products from aerobic dehydrogenation

**(2a)** Following the representative procedure, quinoline was synthesized from 0.4 mmol 1,2,3,4-tetrahydroquinoline upon 24 h LED blue light illumination, at room temperature, in a solvent of 4 mL of 2-propanol in 1 atm O<sub>2</sub> (balloon) condition. The transparent (colorless) product was isolated with flash column using silica gel (3:2 Hex/EtOAc) (43.6 mg, 91%). Characterization data matched with those reported by Sigma Aldrich. <sup>1</sup>H NMR (400 MHz, Chloroform-d) δ 8.93 (dd, J = 4.3, 1.8 Hz, 1H), 8.17 (t, J = 8.7, 8.4 Hz, 1.2 Hz, 2H), 7.83 (dd, J = 8.2, 1.5 Hz, 1H), 7.73 (t, J = 8.4, 6.9, 1.5 Hz, 1H), 7.55 (t, J = 8.1, 6.8, 1.2 Hz, 1H), 7.41 (dd, J = 8.3, 4.2 Hz, 1H). <sup>13</sup>C NMR (101 MHz, Chloroform-d) δ 149.96, 147.86, 135.57, 129.03, 127.83, 127.32, 126.28, 126.07, 120.61.

**(2b)** Following the representative procedure, 6-methoxy-quinoline was synthesized from 0.4 mmol 6-methoxy-1,2,3,4-tetrahydroquinoline (upon 24 h LED blue light illumination, at room temperature, in a solvent of 4 mL of 2-propanol in 1 atm O<sub>2</sub> (balloon) condition. The white-beige product was isolated with flash column using silica gel (2:1 Hex/EtOAc) (60 mg, 94%). Characterization data matched with those reported by Sigma Aldrich. <sup>1</sup>H NMR (400 MHz, Chloroform-d)

$\delta$  8.81 – 8.71 (m, 1H), 8.07 – 7.96 (m, 2H), 7.40 – 7.30 (m, 2H), 7.06 (dd,  $J = 3.0, 1.6$  Hz, 1H), 3.96 – 3.89 (s, 3H).  $^{13}\text{C}$  NMR (101 MHz,  $\text{CDCl}_3$ )  $\delta$  157.71, 147.87, 144.36, 134.81, 131.07, 129.29, 122.28, 121.35, 105.12, 55.51.

**(1e)** The white powder product TBSO-1,2,3,4-tetrahydroquinoline was isolated with flash column using silica gel (5:1 Hex/EtOAc) (368 mg, 70%) of TBSO-THQ was isolated. Characterization data matched with those reported by AIST.  $^1\text{H}$  NMR (400 MHz, Chloroform- $d$ )  $\delta$  6.76 (dt,  $J = 8.1, 1.0$  Hz, 1H), 6.11 (dd,  $J = 8.1, 2.4$  Hz, 1H), 5.98 (d,  $J = 2.4$  Hz, 1H), 3.30 – 3.21 (m, 2H), 2.68 (t,  $J = 6.6$  Hz, 2H), 1.95 – 1.87 (m, 2H), 0.96 (s, 9H), 0.17 (s, 6H).  $^{13}\text{C}$  NMR (101 MHz,  $\text{CDCl}_3$ )  $\delta$  154.03, 144.95, 129.44, 114.15, 108.57, 105.09, 76.87, 76.55, 76.23, 41.43, 25.85, 25.28, 21.99, 17.73, -4.84.

**(2c)** Following the representative procedure, quinaldine was synthesized from 0.4 mmol 1,2,3,4-tetrahydroquinaldine upon 24 h LED blue light illumination, at room temperature, in a solvent of 4 mL of acetonitrile in 1 atm  $\text{O}_2$  (balloon) condition. The colorless product was isolated with flash column using silica gel (3:2 Hex/EtOAc) (55.2 mg, 92%). Characterization data matched with those reported by AIST.  $^1\text{H}$  NMR (400 MHz, Chloroform- $d$ )  $\delta$  8.02 (ddd,  $J = 8.6, 2.6, 0.9$  Hz, 2H), 7.75 (dd,  $J = 8.1, 1.5$  Hz, 1H), 7.67 (ddd,  $J = 8.5, 6.9, 1.5$  Hz, 1H), 7.46 (ddd,  $J = 8.1, 6.9, 1.2$  Hz, 1H), 7.32 – 7.22 (m, 1H), 2.74 (s, 3H).  $^{13}\text{C}$  NMR (101 MHz, Chloroform- $d$ )  $\delta$  158.97, 147.87, 136.13, 129.39, 128.63, 127.47, 126.47, 125.64, 121.97, 25.38.

**(2e)** Following the representative procedure, 7-TBSO-quinoline was synthesized from 0.4 mmol 7-TBSO-1,2,3,4-tetrahydroquinoline upon 24 h LED blue light illumination, at room temperature, in a solvent of 4 mL of 2-propanol in 1 atm  $\text{O}_2$  (balloon) condition. The pale white product was isolated with flash column using silica gel (5:1 Hex/EtOAc) (86 mg, 83%).  $^1\text{H}$  NMR (400 MHz, Chloroform- $d$ )  $\delta$  8.83 (dd,  $J = 4.3, 1.8$  Hz, 1H), 8.06 (ddd,  $J = 8.2, 1.8, 0.8$  Hz, 1H), 7.69 (d,  $J = 8.8$  Hz, 1H), 7.47 (dt,  $J = 2.5, 0.6$  Hz, 1H), 7.30 – 7.20 (m, 1H), 7.15 (dd,  $J = 8.8, 2.4$  Hz, 1H), 1.03 (s, 9H), 0.29 (s, 6H).  $^{13}\text{C}$  NMR (101 MHz,  $\text{CDCl}_3$ )  $\delta$  156.36, 150.13, 149.25, 135.18, 128.37, 123.39, 122.55, 122.52, 118.62, 115.69, 25.27, 25.26, 25.22, 17.83, -4.55, -4.83, -5.12.

---

**(2g)** Following the representative procedure, 6-Chloroquinoline was synthesized from 0.4 mmol 6-chloro - 1,2,3,4-tetrahydroquinoline upon 24 h LED blue light illumination, at room temperature, in a solvent of 4 mL of 2-propanol in 1 atm O<sub>2</sub> (balloon) condition. The product was isolated with flash column using silica gel (3:1 Hex/EtOAc) (62.2 mg, 92%). Characterization data matched with those reported by Sigma Aldrich. <sup>1</sup>H NMR (400 MHz, Chloroform-d)  $\delta$  8.89 (dd, *J* = 4.2, 1.7 Hz, 1H), 8.07 – 7.98 (m, 2H), 7.77 (d, *J* = 2.3 Hz, 1H), 7.62 (dd, *J* = 9.0, 2.3 Hz, 1H), 7.39 (dd, *J* = 8.4, 4.2 Hz, 1H). <sup>13</sup>C NMR (101 MHz, CDCl<sub>3</sub>)  $\delta$  150.59, 146.64, 135.08, 132.27, 131.12, 130.39, 128.82, 126.40, 121.90.

**(2h)** Following the representative procedure, 6-methylquinoline was synthesized from 0.4 mmol 6-methyl - 1,2,3,4-tetrahydroquinoline upon 24 h LED blue light illumination, at room temperature, in a solvent of 4 mL of 2-propanol in 1 atm O<sub>2</sub> (balloon) condition. The product was isolated with flash column using silica gel (3:1 Hex/EtOAc) (33.3 mg, 74%). Characterization data matched with those reported by Sigma Aldrich. <sup>1</sup>H NMR (400 MHz, Chloroform-d)  $\delta$  8.84 (dd, *J* = 4.2, 1.7 Hz, 1H), 8.05 (dd, *J* = 8.3, 1.3 Hz, 1H), 8.00 (d, *J* = 8.6 Hz, 1H), 7.60 – 7.50 (m, 2H), 7.34 (dd, *J* = 8.3, 4.2 Hz, 1H), 2.53 (s, 3H). <sup>13</sup>C NMR (101 MHz, CDCl<sub>3</sub>)  $\delta$  149.54, 146.93, 136.37, 135.29, 131.73, 129.10, 128.32, 126.58, 121.06, 21.54.

**(2i)** Following the representative procedure, 2-methylquinoline-8-carboxylic acid was synthesized from 0.4 mmol 2-methyl-8-carboxylic acid - 1,2,3,4-tetrahydroquinoline upon 24 h LED blue light illumination, at room temperature, in a solvent of 4 mL of 2-propanol in 1 atm O<sub>2</sub> (balloon) condition. The product was isolated with flash column using silica gel (1:2 Hex/EtOAc) (69.7 mg, 93%). Characterization data matched with those reported by Sigma Aldrich. <sup>1</sup>H NMR (400 MHz, Chloroform-d)  $\delta$  8.69 (dd, *J* = 7.4, 1.5 Hz, 1H), 8.26 (d, *J* = 8.5 Hz, 1H), 8.02 (dd, *J* = 8.1, 1.5 Hz, 1H), 7.69 – 7.61 (m, 1H), 7.44 (d, *J* = 8.5 Hz, 1H), 2.80 (s, 3H). <sup>13</sup>C NMR (101 MHz, CDCl<sub>3</sub>)  $\delta$  167.36, 158.52, 144.53, 138.47, 134.62, 132.63, 126.18, 126.10, 123.59, 122.64, 24.59.

**(2k)** Following the representative procedure, isoquinoline was synthesized from 0.4 mmol 1,2,3,4-tetrahydroisoquinoline upon 24 h LED blue light illumination, at room temperature, in a solvent of 4 mL of 2-propanol in 1 atm O<sub>2</sub> (balloon) condition. The colorless product was iso-

lated with flash column using alumina gel (3:1 Hex/EtOAc) (22.1 mg, 43%). Characterization data matched with those reported by Sigma Aldrich.  $^1\text{H}$  NMR (400 MHz, Chloroform- $d$ )  $\delta$  9.26 (t,  $J = 1.0$  Hz, 1H), 8.53 (d,  $J = 5.7$  Hz, 1H), 7.97 (dd,  $J = 8.2, 1.1$  Hz, 1H), 7.82 (dd,  $J = 8.3, 1.0$  Hz, 1H), 7.73 – 7.57 (m, 3H).  $^{13}\text{C}$  NMR (101 MHz, Chloroform- $d$ )  $\delta$  152.18, 142.67, 135.41, 129.94, 128.32, 127.24, 126.85, 126.09, 120.05.

**(2k\*)** Following the representative procedure, 3,4-dihydroisoquinoline was synthesized from 0.4 mmol 1,2,3,4-tetrahydroisoquinoline upon 24 h LED blue light illumination, at room temperature, in a solvent of 4 mL of 2-propanol in 1 atm  $\text{O}_2$  (balloon) condition as a second main product. The pale yellow product was isolated with flash column using alumina gel (3:1 Hex/EtOAc) (27.2 mg, 52%).  $^1\text{H}$  NMR (400 MHz, Chloroform- $d$ )  $\delta$  8.35 (s, 1H), 7.37 (td,  $J = 7.1, 2.1$  Hz, 1H), 7.35 – 7.21 (m, 2H), 7.24 – 7.11 (m, 1H), 3.79 (ddd,  $J = 9.9, 6.2, 2.2$  Hz, 2H), 2.83 – 2.70 (m, 2H).  $^{13}\text{C}$  NMR (101 MHz,  $\text{CDCl}_3$ )  $\delta$  159.99, 135.98, 131.81, 130.69, 127.06, 126.85, 126.72, 47.02, 24.68.

**(2m)** Following the representative procedure, 1-methyl isoquinoline was synthesized from 0.4 mmol 1-methyl-1,2,3,4-tetrahydroisoquinoline upon 24 h LED blue light illumination, at 47°C temperature, in a solvent of 4 mL of 2-propanol in 1 atm  $\text{O}_2$  (balloon) condition. The pale yellow product was isolated with flash column using silica gel (2:1 Hex/EtOAc) (43.1 mg, 75%). Characterization data matched with those reported by Sigma Aldrich.  $^1\text{H}$  NMR (400 MHz, Chloroform- $d$ )  $\delta$  8.39 (d,  $J = 5.8$  Hz, 1H), 8.12 (dq,  $J = 8.3, 1.0$  Hz, 1H), 7.80 (dt,  $J = 8.3, 0.9$  Hz, 1H), 7.67 (ddd,  $J = 8.2, 6.9, 1.2$  Hz, 1H), 7.59 (ddd,  $J = 8.3, 6.9, 1.3$  Hz, 1H), 7.50 (d,  $J = 5.8$  Hz, 1H), 2.97 (s, 3H).  $^{13}\text{C}$  NMR (101 MHz,  $\text{CDCl}_3$ )  $\delta$  158.13, 141.37, 135.44, 129.45, 127.06, 126.74, 126.55, 125.16, 118.79, 21.96.

**(2l)** Following the representative procedure, 6,7-dimethoxy-isoquinoline was synthesized from 0.4 mmol 6,7-dimethoxy-1,2,3,4-tetrahydroisoquinoline upon 24 h LED blue light illumination, at room temperature, in a solvent of 2 mL of  $\text{CH}_2\text{Cl}_2$  (dichloromethane) and 2 mL of 2-propanol in 1 atm  $\text{O}_2$  (balloon) condition. The pale yellow product was isolated with flash column using silica gel (10:1 DCM/acetone) (61.5 mg, 81%). Characterization data matched with those re-



---

ported by Sigma Aldrich. <sup>1</sup>H NMR (400 MHz, Chloroform-d)  $\delta$  9.05 (s, 1H), 8.39 (d, *J* = 5.7 Hz, 1H), 7.51 (d, *J* = 4.8 Hz, 1H), 7.21 (s, 1H), 7.07 (s, 1H), 4.04 (s, 6H). <sup>13</sup>C NMR (101 MHz, CDCl<sub>3</sub>)  $\delta$  152.64, 149.95, 149.54, 141.58, 132.15, 124.38, 118.85, 104.93, 104.17, 55.70, 55.66.

**(2n)** Following the representative procedure, 1-phenyl isoquinoline was synthesized from 0.4 mmol 1-phenyl-1,2,3,4-tetrahydroisoquinoline upon 24 h LED blue light illumination, at 47°C temperature, in a solvent of 4 mL of 2-propanol in 1 atm O<sub>2</sub> (balloon) condition. The white powder product was isolated with flash column using silica gel (3:1 Hex/EtOAc) (27.0 mg, 33%). Characterization data matched with those reported by Sigma Aldrich. NMR (400 MHz, Chloroform-d)  $\delta$  8.62 (d, *J* = 5.7 Hz, 1H), 8.11 (dq, *J* = 8.6, 1.0 Hz, 1H), 7.89 (dt, *J* = 8.3, 1.0 Hz, 1H), 7.73 – 7.67 (m, 3H), 7.65 (dd, *J* = 5.7, 0.9 Hz, 1H), 7.57 – 7.47 (m, 4H). <sup>13</sup>C NMR (101 MHz, CDCl<sub>3</sub>)  $\delta$  160.41, 141.89, 139.26, 136.51, 129.64, 129.56, 128.22, 127.99, 127.24, 126.80, 126.63, 126.38.

**(2n\*)** Following the representative procedure, 1-phenyl-3,4-dihydroisoquinoline was synthesized from 0.4 mmol 1-phenyl-1,2,3,4-tetrahydroisoquinoline upon 24 h LED blue light illumination, at 47°C temperature, in a solvent of 4 mL of 2-propanol in 1 atm O<sub>2</sub> (balloon) condition as a second main product. The product was isolated with flash column using silica gel (3:1 Hex/EtOAc) (43.9 mg, 54%). Characterization data matched with those reported by Sigma Aldrich. <sup>1</sup>H NMR (400 MHz, Chloroform-d)  $\delta$  7.65 – 7.54 (m, 2H), 7.49 – 7.33 (m, 4H), 7.31 – 7.21 (m, 3H), 3.89 – 3.83 (m, 2H), 2.84 – 2.78 (m, 2H). <sup>13</sup>C NMR (101 MHz, CDCl<sub>3</sub>)  $\delta$  167.22, 138.98, 138.80, 130.61, 129.24, 128.79, 128.74, 128.09, 127.87, 127.35, 126.51, 47.62, 26.28.

**(2v)** Following the representative procedure, quinoxaline was synthesized from 0.4 mmol 1,2,3,4-tetrahydroquinoxaline (upon 24 h LED blue light illumination, at room temperature, 4 mL of 2-propanol in 1 atm O<sub>2</sub> (O<sub>2</sub> purging) condition. The white crystal product was isolated with flash column using alumina gel (5:1 Hex/EtOAc) (43.3 mg, 83%). Characterization data matched with those reported by Sigma Aldrich. <sup>1</sup>H NMR (400 MHz, Chloroform-d)  $\delta$  8.86 (d, *J* = 6.7 Hz, 2H), 8.12 (dd, *J* = 6.4, 3.5 Hz, 2H), 7.79 (dd, *J* = 6.5, 3.5 Hz, 2H). <sup>13</sup>C NMR (101 MHz, CDCl<sub>3</sub>)  $\delta$  144.52, 142.61, 129.61, 129.08.

**(2u)** Following the representative procedure, 2-phenylimidazole was synthesized from 0.4 mmol 2-phenyl-2-imidazoline upon 24 h LED blue light illumination, at room temperature, in a solvent of 4 mL of 2-propanol in 1 atm O<sub>2</sub> (balloon) condition. The product was isolated with flash column using silica gel (5:1 Hex/EtOAc) (53.2 mg, 93%). Characterization data matched with those reported by Sigma Aldrich. <sup>1</sup>H NMR (400 MHz, Chloroform-d)  $\delta$  7.93 – 7.86 (m, 2H), 7.38 – 7.28 (m, 3H), 7.14 (s, 2H). <sup>13</sup>C NMR (101 MHz, CDCl<sub>3</sub>)  $\delta$  147.16, 130.37, 128.87, 128.59, 125.52, 123.06.

**(2o)** Following the representative procedure, indole was synthesized from 0.4 mmol indoline upon 24 h LED blue light illumination, at room temperature, in a solvent of 4 mL of 2-propanol in air (needle poked through septum). The colorless product was isolated with flash column using silica gel (12:1 Hex/EtOAc) (39.4 mg, 84%). Characterization data matched with those reported by Sigma Aldrich. <sup>1</sup>H NMR (400 MHz, Chloroform-d)  $\delta$  8.12 (s, 1H), 7.69 (dd, J = 7.9, 1.2 Hz, 1H), 7.42 (dd, J = 8.1, 1.2 Hz, 1H), 7.27 – 7.19 (m, 2H), 7.16 (ddd, J = 8.1, 7.1, 1.1 Hz, 1H), 6.59 (ddd, J = 3.1, 2.1, 1.0 Hz, 1H). <sup>13</sup>C NMR (101 MHz, Chloroform-d)  $\delta$  135.33, 127.41, 123.66, 121.54, 120.29, 119.37, 110.56, 102.19.

**(2p)** Following the representative procedure, 2-methyl indole was synthesized from 0.4 mmol 2-methyl indoline upon 24 h LED blue light illumination, at room temperature, in a solvent of 4ml of 2-propanol in 1atm O<sub>2</sub> (O<sub>2</sub> purging) condition. The colorless product was isolated with flash column using silica gel (13:1 Hex/EtOAc) (43.2 mg, a mixture of 7% starting material and 76% product). Notably, because the starting material and the product had the same R<sub>f</sub> value, the unconverted starting material could not be separated from the product. Characterization data matched with those reported by AIST. <sup>1</sup>H NMR (400 MHz, Chloroform-d)  $\delta$  7.79 (s, 1H), 7.55 (dq, J = 7.5, 0.9 Hz, 1H), 7.28 (dq, J = 8.1, 0.9 Hz, 1H), 7.18 – 7.06 (m, 2H), 6.24 (dp, J = 2.0, 1.0 Hz, 1H), 2.44 (s, J = 1.0 Hz, 3H). <sup>13</sup>C NMR (101 MHz, CDCl<sub>3</sub>)  $\delta$  135.61, 134.60, 128.63, 124.31, 120.48, 119.18, 109.77, 99.95, 13.25.

# Bibliography

- [1] C. RENZ, *Lichtreaktionen der oxyde des titans, cers und der erdsäuren*, Helvetica Chimica Acta **4**, 1:961, 1921.
- [2] C. GOODEVE, J. KITCHENER, *Photosensitisation by titanium dioxide*, Transactions of the Faraday Society **34**:570, 1938.
- [3] S. KATO, F. MASHIO, *Autooxidation by TiO<sub>2</sub> as a photocatalyst*, Abtr. Book Annu. Meet Chemical Society of Japan **223**, 1956.
- [4] S. KATO, *TiO<sub>2</sub> Photocatalyzed Oxidation of Tetraline in Liquid Phase*, Kogyo Kagaku Zasshi **67**:1136, 1964.
- [5] I. S. McLINTOCK, M. RITCHIE, *Reactions on titanium dioxide; photo-adsorption and oxidation of ethylene and propylene*, Transactions of the Faraday Society **61**:1007, 1965, doi:10.1039/TF9656101007.
- [6] A. FUJISHIMA, K. HONDA, *Electrochemical photolysis of water at a semiconductor electrode*, nature **238**, 5358:37, 1972.
- [7] S. N. FRANK, A. J. BARD, *Heterogeneous photocatalytic oxidation of cyanide and sulfite in aqueous solutions at semiconductor powders*, The journal of physical chemistry **81**, 15:1484, 1977.
- [8] S. N. FRANK, A. J. BARD, *Heterogeneous photocatalytic oxidation of cyanide ion in aqueous*

- solutions at titanium dioxide powder*, Journal of the American Chemical Society **99**, 1:303, 1977.
- [9] B. KRAEUTLER, A. J. BARD, *Photoelectrosynthesis of ethane from acetate ion at an n-type titanium dioxide electrode. The photo-Kolbe reaction*, Journal of the American Chemical Society **99**, 23:7729, 1977.
- [10] B. KRAEUTLER, A. J. BARD, *Heterogeneous photocatalytic synthesis of methane from acetic acid-new Kolbe reaction pathway*, Journal of the American Chemical Society **100**, 7:2239, 1978.
- [11] R. WANG, K. HASHIMOTO, A. FUJISHIMA, M. CHIKUNI, E. KOJIMA, A. KITAMURA, M. SHIMOHIGOSHI, T. WATANABE, *Light-induced amphiphilic surfaces*, Nature **388**, 6641:431, 1997.
- [12] B. O'REGAN, M. GRÄTZEL, *A low-cost, high-efficiency solar cell based on dye-sensitized colloidal TiO<sub>2</sub> films*, nature **353**, 6346:737, 1991.
- [13] H. REICHE, A. J. BARD, *Heterogeneous photosynthetic production of amino acids from methane-ammonia-water at platinum/titanium dioxide. Implications in chemical evolution*, Journal of the American Chemical Society **101**, 11:3127, 1979.
- [14] M. FUJIHIRA, Y. SATOH, T. OSA, *Heterogeneous photocatalytic oxidation of aromatic compounds on TiO<sub>2</sub>*, Nature **293**, 5829:206, 1981.
- [15] M. A. FOX, C.-C. CHEN, *Mechanistic features of the semiconductor photocatalyzed olefin-to-carbonyl oxidative cleavage*, Journal of the American Chemical Society **103**, 22:6757, 1981, doi:10.1021/ja00412a044.
- [16] V. ETACHERI, C. DI VALENTIN, J. SCHNEIDER, D. BAHNEMANN, S. C. PILLAI, *Visible-light activation of TiO<sub>2</sub> photocatalysts: Advances in theory and experiments*, Journal of Photochemistry and Photobiology C: Photochemistry Reviews **25**:1, 2015.
- [17] A. BELTRAN, L. GRACIA, J. ANDRES, *Density functional theory study of the brookite surfaces and phase transitions between natural titania polymorphs*, The Journal of Physical Chemistry B **110**, 46:23417, 2006.

- 
- [18] M. RAMAMOORTHY, D. VANDERBILT, R. KING-SMITH, *First-principles calculations of the energetics of stoichiometric TiO<sub>2</sub> surfaces*, Physical Review B **49**, 23:16721, 1994.
- [19] A. FUJISHIMA, X. ZHANG, D. A. TRYK, *TiO<sub>2</sub> photocatalysis and related surface phenomena*, Surface science reports **63**, 12:515, 2008.
- [20] D. A. HANAOR, C. C. SORRELL, *Review of the anatase to rutile phase transformation*, Journal of Materials science **46**, 4:855, 2011.
- [21] V. SHKLOVER, M. K. NAZEERUDDIN, S. SAKEERUDDIN, C. BARBÉ, a. Kay, T. Haibach, W. Steurer, R. Hermann, H.-U. Nissen, M. Grätzel, Chem. Mater **9**:430, 1997.
- [22] A. FURUBE, T. ASAHI, H. MASUHARA, H. YAMASHITA, M. ANPO, *Charge carrier dynamics of standard TiO<sub>2</sub> catalysts revealed by femtosecond diffuse reflectance spectroscopy*, The Journal of Physical Chemistry B **103**, 16:3120, 1999.
- [23] V. SHKLOVER, M.-K. NAZEERUDDIN, S. ZAKEERUDDIN, C. BARBE, A. KAY, T. HAIBACH, W. STEURER, R. HERMANN, H.-U. NISSEN, M. GRÄTZEL, *Structure of nanocrystalline TiO<sub>2</sub> powders and precursor to their highly efficient photosensitizer*, Chemistry of materials **9**, 2:430, 1997.
- [24] A. AMTOUT, R. LEONELLI, *Optical properties of rutile near its fundamental band gap*, Physical Review B **51**, 11:6842, 1995.
- [25] J. PASCUAL, J. CAMASSEL, H. MATHIEU, *Fine structure in the intrinsic absorption edge of TiO<sub>2</sub>*, Physical Review B **18**, 10:5606, 1978.
- [26] H. TANG, F. LEVY, H. BERGER, P. SCHMID, *Urbach tail of anatase TiO<sub>2</sub>*, Physical Review B **52**, 11:7771, 1995.
- [27] A. MATTSSON, L. OSTERLUND, *Adsorption and photoinduced decomposition of acetone and acetic acid on anatase, brookite, and rutile TiO<sub>2</sub> nanoparticles*, The Journal of Physical Chemistry C **114**, 33:14121, 2010.
- [28] E. A. IRENE, *Electronic materials science*, John Wiley & Sons, 2005.
-

- [29] Z. ZHANG, J. T. YATES JR, *Band bending in semiconductors: chemical and physical consequences at surfaces and interfaces*, Chemical reviews **112**, 10:5520, 2012.
- [30] M. D. EARLE, *The electrical conductivity of titanium dioxide*, Physical Review **61**, 1-2:56, 1942.
- [31] H. PARK, Y. PARK, W. KIM, W. CHOI, *Surface modification of TiO<sub>2</sub> photocatalyst for environmental applications*, Journal of Photochemistry and Photobiology C: Photochemistry Reviews **15**:1, 2013.
- [32] W. VIELSTICH, *BE Conway, J. O'M. Bockris, E. Yeager, SUM Khan, RE White: Kinetics and Mechanisms of Electrode Processes, Vol. 7 aus der Reihe: Comprehensive Treatise of Electrochemistry, Plenum Press New York and London 1983. 788 Seiten, Preis: 95,-(+ 20% ausserhalb der USA).*, Berichte der Bunsengesellschaft für physikalische Chemie **88**, 8:777, 1984.
- [33] K. E. KARAKITSOU, X. E. VERYKIOS, *Effects of altermvalent cation doping of titania on its performance as a photocatalyst for water cleavage*, The Journal of Physical Chemistry **97**, 6:1184, 1993.
- [34] S. YAN, Z. LI, Z. ZOU, *Photodegradation of rhodamine B and methyl orange over boron-doped g-C<sub>3</sub>N<sub>4</sub> under visible light irradiation*, Langmuir **26**, 6:3894, 2010.
- [35] L. GE, C. HAN, J. LIU, *Novel visible light-induced g-C<sub>3</sub>N<sub>4</sub>/Bi<sub>2</sub>WO<sub>6</sub> composite photocatalysts for efficient degradation of methyl orange*, Applied Catalysis B: Environmental **108**:100, 2011.
- [36] W. CHOI, A. TERMIN, M. R. HOFFMANN, *Effects of metal-ion dopants on the photocatalytic reactivity of quantum-sized TiO<sub>2</sub> particles*, Angewandte Chemie International Edition in English **33**, 10:1091, 1994.
- [37] A. ZALESKA, *Doped-TiO<sub>2</sub>: a review*, Recent patents on engineering **2**, 3:157, 2008.
- [38] D. MITORAJ, H. KISCH, *the nature of nitrogen-modified titanium dioxide photocatalysts active in visible light*, Angewandte Chemie International Edition **47**, 51:9975, 2008.

- [39] X. WANG, K. MAEDA, A. THOMAS, K. TAKANABE, G. XIN, J. M. CARLSSON, K. DOMEN, M. ANTONIETTI, *A metal-free polymeric photocatalyst for hydrogen production from water under visible light*, *Nature materials* **8**, 1:76, 2009.
- [40] F. SU, T. WANG, R. LY, J. ZHANG, P. ZHANG, J. LU, J. GONG, *Dendritic Au/TiO<sub>2</sub> nanorod arrays for visible-light driven photoelectrochemical water splitting*, *Nanoscale* **5**, 19:9001, 2013.
- [41] R. DAGHRIR, P. DROGUI, D. ROBERT, *Modified TiO<sub>2</sub> for environmental photocatalytic applications: a review*, *Industrial & Engineering Chemistry Research* **52**, 10:3581, 2013.
- [42] L.-C. JIANG, W.-D. ZHANG, *Charge transfer properties and photoelectrocatalytic activity of TiO<sub>2</sub>/MWCNT hybrid*, *Electrochimica Acta* **56**, 1:406, 2010.
- [43] W. CHOI, A. TERMIN, M. R. HOFFMANN, *The role of metal ion dopants in quantum-sized TiO<sub>2</sub>: correlation between photoreactivity and charge carrier recombination dynamics*, *The Journal of Physical Chemistry* **98**, 51:13669, 2002.
- [44] W. LI, *Influence of electronic structures of doped TiO<sub>2</sub> on their photocatalysis*, *physica status solidi (RRL)–Rapid Research Letters* **9**, 1:10, 2015.
- [45] E. BORGARELLO, J. KIWI, M. GRAETZEL, E. PELIZZETTI, M. VISCA, *Visible light induced water cleavage in colloidal solutions of chromium-doped titanium dioxide particles*, *Journal of the American Chemical Society* **104**, 11:2996, 1982.
- [46] S. SATO, *Photocatalytic activity of NO<sub>x</sub>-doped TiO<sub>2</sub> in the visible light region*, *Chemical Physics Letters* **123**, 1-2:126, 1986.
- [47] M. MROWETZ, W. BALCERSKI, A. COLUSSI, M. R. HOFFMANN, *Oxidative power of nitrogen-doped TiO<sub>2</sub> photocatalysts under visible illumination*, *The Journal of Physical Chemistry B* **108**, 45:17269, 2004.
- [48] R. ASAHI, T. MORIKAWA, T. OHWAKI, K. AOKI, Y. TAGA, *Visible-light photocatalysis in nitrogen-doped titanium oxides*, *science* **293**, 5528:269, 2001.
- [49] T. UMEBAYASHI, T. YAMAKI, H. ITOH, K. ASAI, *Band gap narrowing of titanium dioxide by sulfur doping*, *Applied Physics Letters* **81**, 3:454, 2002.

- [50] X. WANG, S. MENG, X. ZHANG, H. WANG, W. ZHONG, Q. DU, *Multi-type carbon doping of TiO<sub>2</sub> photocatalyst*, Chemical Physics Letters **444**, 4-6:292, 2007.
- [51] J. VARLEY, A. JANOTTI, C. VAN DE WALLE, *Mechanism of visible-light photocatalysis in nitrogen-doped TiO<sub>2</sub>*, Advanced Materials **23**, 20:2343, 2011.
- [52] R. NAKAMURA, T. TANAKA, Y. NAKATO, *Mechanism for visible light responses in anodic photocurrents at N-doped TiO<sub>2</sub> film electrodes*, The Journal of Physical Chemistry B **108**, 30:10617, 2004.
- [53] A. A. ISMAIL, D. W. BAHNEMANN, S. A. AL-SAYARI, *Synthesis and photocatalytic properties of nanocrystalline Au, Pd and Pt photodeposited onto mesoporous RuO<sub>2</sub>-TiO<sub>2</sub> nanocomposites*, Applied Catalysis A: General **431**:62, 2012.
- [54] M. PELAEZ, N. T. NOLAN, S. C. PILLAI, M. K. SEERY, P. FALARAS, A. G. KONTOS, P. S. DUNLOP, J. W. HAMILTON, J. A. BYRNE, K. O'SHEA ET AL., *A review on the visible light active titanium dioxide photocatalysts for environmental applications*, Applied Catalysis B: Environmental **125**:331, 2012.
- [55] D. EASTMAN, *Photoelectric work functions of transition, rare-earth, and noble metals*, Physical Review B **2**, 1:1, 1970.
- [56] Y. NOSAKA, K. NORIMATSU, H. MIYAMA, *The function of metals in metal-compounded semiconductor photocatalysts*, Chemical physics letters **106**, 1-2:128, 1984.
- [57] G. L. CHIARELLO, M. H. AGUIRRE, E. SELLI, *Hydrogen production by photocatalytic steam reforming of methanol on noble metal-modified TiO<sub>2</sub>*, Journal of Catalysis **273**, 2:182, 2010.
- [58] M. K. SEERY, R. GEORGE, P. FLORIS, S. C. PILLAI, *Silver doped titanium dioxide nanomaterials for enhanced visible light photocatalysis*, Journal of photochemistry and Photobiology A: Chemistry **189**, 2-3:258, 2007.
- [59] C. GUNAWAN, W. Y. TEOH, C. P. MARQUIS, J. LIFIA, R. AMAL, *Reversible antimicrobial photo-switching in nanosilver*, Small **5**, 3:341, 2009.



- [60] P. A. DESARIO, J. J. PIETRON, D. E. DEVANTIER, T. H. BRINTLINGER, R. M. STROUD, D. R. ROLISON, *Plasmonic enhancement of visible-light water splitting with Au–TiO<sub>2</sub> composite aerogels*, *Nanoscale* **5**, 17:8073, 2013.
- [61] U. SCHARE, M. SCHRAML-MARTH, A. WOKAUN, A. BAIKER, *Comparison of grafted vanadia species on ZrO<sub>2</sub>, TiO<sub>2</sub>, SiO<sub>2</sub> and TiO<sub>2</sub>/SiO<sub>2</sub> mixed oxides*, *Journal of the Chemical Society, Faraday Transactions* **87**, 19:3299, 1991.
- [62] Y. NOSAKA, S. TAKAHASHI, H. SAKAMOTO, A. Y. NOSAKA, *Reaction mechanism of Cu (II)-grafted visible-light responsive TiO<sub>2</sub> and WO<sub>3</sub> photocatalysts studied by means of ESR spectroscopy and chemiluminescence photometry*, *The Journal of Physical Chemistry C* **115**, 43:21283, 2011.
- [63] N. NISHIYAMA, K. KOZASA, S. YAMAZAKI, *Photocatalytic degradation of 4-chlorophenol on titanium dioxide modified with Cu (II) or Cr (III) ion under visible light irradiation*, *Applied Catalysis A: General* **527**:109, 2016.
- [64] M. NISHIKAWA, Y. MITANI, Y. NOSAKA, *Photocatalytic reaction mechanism of Fe (III)-grafted TiO<sub>2</sub> studied by means of ESR spectroscopy and chemiluminescence photometry*, *The Journal of Physical Chemistry C* **116**, 28:14900, 2012.
- [65] M. LIU, X. QIU, K. HASHIMOTO, M. MIYAUCHI, *Cu (II) nanocluster-grafted, Nb-doped TiO<sub>2</sub> as an efficient visible-light-sensitive photocatalyst based on energy-level matching between surface and bulk states*, *Journal of Materials Chemistry A* **2**, 33:13571, 2014.
- [66] M. LIU, X. QIU, M. MIYAUCHI, K. HASHIMOTO, *Cu (II) oxide amorphous nanoclusters grafted Ti<sup>3+</sup> self-doped TiO<sub>2</sub>: an efficient visible light photocatalyst*, *Chemistry of Materials* **23**, 23:5282, 2011.
- [67] M. LIU, X. QIU, M. MIYAUCHI, K. HASHIMOTO, *Energy-level matching of Fe (III) ions grafted at surface and doped in bulk for efficient visible-light photocatalysts*, *Journal of the American Chemical Society* **135**, 27:10064, 2013.
- [68] N. O. BALAYEVA, M. FLEISCH, D. W. BAHNEMANN, *Surface-grafted WO<sub>3</sub>/TiO<sub>2</sub> photocatalysts: Enhanced visible-light activity towards indoor air purification*, *Catalysis Today* **313**:63, 2018.

- [69] K. DHANALAKSHMI, S. LATHA, S. ANANDAN, P. MARUTHAMUTHU, *Dye sensitized hydrogen evolution from water*, International Journal of Hydrogen Energy **26**, 7:669, 2001.
- [70] A. S. POLO, M. K. ITOKAZU, N. Y. M. IHA, *Metal complex sensitizers in dye-sensitized solar cells*, Coordination Chemistry Reviews **248**, 13-14:1343, 2004.
- [71] I. MARTINI, J. H. HODAK, G. V. HARTLAND, *Effect of water on the electron transfer dynamics of 9-anthracenecarboxylic acid bound to TiO<sub>2</sub> nanoparticles: demonstration of the Marcus inverted region*, The Journal of Physical Chemistry B **102**, 3:607, 1998.
- [72] B. BURFEINDT, T. HANNAPPEL, W. STORCK, F. WILLIG, *Measurement of temperature-independent femtosecond interfacial electron transfer from an anchored molecular electron donor to a semiconductor as acceptor*, The Journal of Physical Chemistry **100**, 41:16463, 1996.
- [73] J. M. REHM, G. L. MCLENDON, Y. NAGASAWA, K. YOSHIHARA, J. MOSER, M. GRÄTZEL, *Femtosecond electron-transfer Dynamics at a sensitizing dye- semiconductor (TiO<sub>2</sub>) interface*, The Journal of Physical Chemistry **100**, 23:9577, 1996.
- [74] J. R. SWIERK, T. E. MALLOUK, *Design and development of photoanodes for water-splitting dye-sensitized photoelectrochemical cells*, Chemical Society Reviews **42**, 6:2357, 2013.
- [75] R. A. SHELDON, *Green solvents for sustainable organic synthesis: state of the art*, Green Chemistry **7**, 5:267, 2005.
- [76] B. KÖNIG, *Photocatalysis in organic synthesis—past, present, and future*, European Journal of Organic Chemistry **2017**, 15:1979, 2017.
- [77] N. HOFFMANN, *Photochemical reactions as key steps in organic synthesis*, Chemical Reviews **108**, 3:1052, 2008.
- [78] G. CIAMICIAN, P. SILVER, *Chemical Light Effects*, Reports of the German Chemical Society **34**, 2:2040, 1901.
- [79] K. VINODGOPAL, X. HUA, R. L. DAHLGREN, A. LAPPIN, L. PATTERSON, P. V. KAMAT, *Photochemistry of Ru (bpy) <sub>2</sub> (dcbpy) <sub>2+</sub> on Al<sub>2</sub>O<sub>3</sub> and TiO<sub>2</sub> surfaces. An insight into the mechanism of photosensitization*, The Journal of Physical Chemistry **99**, 27:10883, 1995.

- [80] N. DJEGHRI, M. FORMENTI, F. JUILLET, S. TEICHNER, *Photointeraction on the surface of titanium dioxide between oxygen and alkanes*, Faraday Discussions of the Chemical Society **58**:185, 1974.
- [81] M. A. FOX, *Organic heterogeneous photocatalysis: chemical conversions sensitized by irradiated semiconductors*, Accounts of Chemical Research **16**, 9:314, 1983.
- [82] M. R. HOFFMANN, S. T. MARTIN, W. CHOI, D. W. BAHNEMANN, *Environmental applications of semiconductor photocatalysis*, Chemical reviews **95**, 1:69, 1995.
- [83] S. YAMAGATA, S. NAKABAYASHI, K. M. SANCIER, A. FUJISHIMA, *Photocatalytic oxidation of alcohols on TiO<sub>2</sub>*, Bulletin of the Chemical Society of Japan **61**, 10:3429, 1988.
- [84] M. A. FOX, J. N. YOUNATHAN, *Radical cation intermediates in the formation of Schiff bases on irradiated semiconductor powders*, Tetrahedron **42**, 22:6285, 1986.
- [85] P. BOARINI, V. CARASSITI, A. MALDOTTI, R. AMADELLI, *Photocatalytic oxygenation of cyclohexane on titanium dioxide suspensions: Effect of the solvent and of oxygen*, Langmuir **14**, 8:2080, 1998.
- [86] F. MAHDAVI, T. C. BRUTON, Y. LI, *Photoinduced reduction of nitro compounds on semiconductor particles*, The Journal of Organic Chemistry **58**, 3:744, 1993.
- [87] S. FLORES, O. RIOS-BERNIJ, M. VALENZUELA, I. CORDOVA, R. GOMEZ, R. GUTIERREZ, *Photocatalytic reduction of nitrobenzene over titanium dioxide: by-product identification and possible pathways.*, Topics in Catalysis **44**, 4, 2007.
- [88] A. HAKKI, R. DILLERT, D. BAHNEMANN, *Photocatalytic conversion of nitroaromatic compounds in the presence of TiO<sub>2</sub>*, Catalysis Today **144**, 1-2:154, 2009.
- [89] A. MALDOTTI, A. MOLINARI, R. AMADELLI, *Photocatalysis with organized systems for the oxofunctionalization of hydrocarbons by O<sub>2</sub>*, Chemical Reviews **102**, 10:3811, 2002.
- [90] A. MILLS, S. LE HUNTE, *An overview of semiconductor photocatalysis*, Journal of photochemistry and photobiology A: Chemistry **108**, 1:1, 1997.

- [91] Y. NOSAKA, A. Y. NOSAKA, *Generation and detection of reactive oxygen species in photocatalysis*, *Chemical reviews* **117**, 17:11302, 2017.
- [92] D. M. SCHULTZ, T. P. YOON, *Solar synthesis: prospects in visible light photocatalysis*, *Science* **343**, 6174:1239176, 2014.
- [93] D. WORSLEY, A. MILLS, K. SMITH, M. G. HUTCHINGS, *Acid enhancement effect in the clean oxidation of toluenes photocatalysed by TiO<sub>2</sub>*, *Journal of the Chemical Society, Chemical Communications*, 11:1119, 1995.
- [94] S. YURDAKAL, B. S. TEK, O. ALAGOZ, V. AUGUGLIARO, V. LODDO, G. PALMISANO, L. PALMISANO, *Photocatalytic selective oxidation of 5-(hydroxymethyl)-2-furaldehyde to 2, 5-furandicarbaldehyde in water by using anatase, rutile, and brookite TiO<sub>2</sub> nanoparticles*, *ACS Sustainable Chemistry and Engineering* **1**, 5:456, 2013.
- [95] O. S. MOHAMED, A. E.-A. M. GABER, A. ABDEL-WAHAB, *Photocatalytic oxidation of selected aryl alcohols in acetonitrile*, *Journal of Photochemistry and Photobiology A: Chemistry* **148**, 1-3:205, 2002.
- [96] S. HIGASHIDA, A. HARADA, R. KAWAKATSU, N. FUJIWARA, M. MATSUMURA, *Synthesis of a coumarin compound from phenanthrene by a TiO<sub>2</sub>-photocatalyzed reaction*, *Chemical Communications*, 26:2804, 2006.
- [97] C. JOYCE-PRUDEN, J. K. PROSS, Y. LI, *Photoinduced reduction of aldehydes on titanium dioxide*, *The Journal of Organic Chemistry* **57**, 19:5087, 1992.
- [98] H. WANG, R. E. PARTCH, Y. LI, *Synthesis of 2-alkylbenzimidazoles via TiO<sub>2</sub>-mediated photocatalysis*, *The Journal of Organic Chemistry* **62**, 15:5222, 1997.
- [99] K. H. PARK, H. S. JOO, K. I. AHN, K. JUN, *One step synthesis of 4-ethoxy-1, 2, 3, 4-tetrahydroquinoline from nitroarene and ethanol: A TiO<sub>2</sub> mediated photocatalytic reaction*, *Tetrahedron letters* **36**, 33:5943, 1995.
- [100] X. LANG, J. ZHAO, X. CHEN, *Visible-Light-Induced Photoredox Catalysis of Dye-Sensitized Titanium Dioxide: Selective Aerobic Oxidation of Organic Sulfides*, *Angewandte Chemie International Edition* **55**, 15:4697, 2016.

- [101] M. ZHANG, C. CHEN, W. MA, J. ZHAO, *Visible-light-induced aerobic oxidation of alcohols in a coupled photocatalytic system of dye-sensitized TiO<sub>2</sub> and TEMPO*, *Angewandte Chemie International Edition* **47**, 50:9730, 2008.
- [102] V. HOULDING, M. GRATZEL, *Photochemical hydrogen generation by visible light. Sensitization of titanium dioxide particles by surface complexation with 8-hydroxyquinoline*, *Journal of the American Chemical Society* **105**, 17:5695, 1983.
- [103] G. KIM, W. CHOI, *Charge-transfer surface complex of EDTA-TiO<sub>2</sub> and its effect on photocatalysis under visible light*, *Applied Catalysis B: Environmental* **100**, 1-2:77, 2010.
- [104] S. IKEDA, C. ABE, T. TORIMOTO, B. OHTANI, *Photochemical hydrogen evolution from aqueous triethanolamine solutions sensitized by binaphthol-modified titanium (IV) oxide under visible-light irradiation*, *Journal of Photochemistry and Photobiology A: Chemistry* **160**, 1-2:61, 2003.
- [105] Y. PARK, N. J. SINGH, K. S. KIM, T. TACHIKAWA, T. MAJIMA, W. CHOI, *Fullerol–titania charge-transfer-mediated photocatalysis working under visible light*, *Chemistry—A European Journal* **15**, 41:10843, 2009.
- [106] J.-L. SHI, H. HAO, X. LANG, *Phenol–TiO<sub>2</sub> complex photocatalysis: visible light-driven selective oxidation of amines into imines in air*, *Sustainable Energy & Fuels* **3**, 2:488, 2019.
- [107] J.-L. SHI, H. HAO, X. LI, X. LANG, *Merging the catechol–TiO<sub>2</sub> complex photocatalyst with TEMPO for selective aerobic oxidation of amines into imines*, *Catalysis Science & Technology* **8**, 15:3910, 2018.
- [108] H. HAO, J.-L. SHI, H. XU, X. LI, X. LANG, *N-hydroxyphthalimide-TiO<sub>2</sub> complex visible light photocatalysis*, *Applied Catalysis B: Environmental* **246**:149, 2019.
- [109] X. LI, H. XU, J.-L. SHI, H. HAO, H. YUAN, X. LANG, *Salicylic acid complexed with TiO<sub>2</sub> for visible light-driven selective oxidation of amines into imines with air*, *Applied Catalysis B: Environmental* **244**:758, 2019.
- [110] J.-L. SHI, X. LANG, *Assembling Polydopamine on TiO<sub>2</sub> for Photocatalytic Selective Oxidation of Sulfides with Aerial O<sub>2</sub>*, *Chemical Engineering Journal* 123632, 2019.

- [111] X. LANG, W. R. LEOW, J. ZHAO, X. CHEN, *Synergistic photocatalytic aerobic oxidation of sulfides and amines on TiO<sub>2</sub> under visible-light irradiation*, *Chemical science* **6**, 2:1075, 2015.
- [112] X. LANG, W. HAO, W. R. LEOW, S. LI, J. ZHAO, X. CHEN, *Tertiary amine mediated aerobic oxidation of sulfides into sulfoxides by visible-light photoredox catalysis on TiO<sub>2</sub>*, *Chemical science* **6**, 8:5000, 2015.
- [113] X. LANG, W. MA, Y. ZHAO, C. CHEN, H. JI, J. ZHAO, *Visible-Light-Induced Selective Photocatalytic Aerobic Oxidation of Amines into Imines on TiO<sub>2</sub>*, *Chemistry—A European Journal* **18**, 9:2624, 2012.
- [114] X. LANG, X. CHEN, J. ZHAO, *Heterogeneous visible light photocatalysis for selective organic transformations*, *Chemical Society Reviews* **43**, 1:473, 2014.
- [115] N. LI, X. LANG, W. MA, H. JI, C. CHEN, J. ZHAO, *Selective aerobic oxidation of amines to imines by TiO<sub>2</sub> photocatalysis in water*, *Chemical Communications* **49**, 44:5034, 2013.
- [116] S. FURUKAWA, Y. OHNO, T. SHISHIDO, K. TERAMURA, T. TANAKA, *Selective amine oxidation using Nb<sub>2</sub>O<sub>5</sub> photocatalyst and O<sub>2</sub>*, *ACS Catalysis* **1**, 10:1150, 2011.
- [117] D. WALKER, J. D. HIEBERT, *2, 3-Dichloro-5, 6-dicyanobenzoquinone and its reactions*, *Chemical reviews* **67**, 2:153, 1967.
- [118] M. KITAMURA, M. YOSHIDA, T. KIKUCHI, K. NARASAKA, *Synthesis of quinolines and 2H-dihydropyrroles by nucleophilic substitution at the nitrogen atom of oxime derivatives*, *Synthesis* **2003**, 15:2415, 2003.
- [119] P. P. FU, R. G. HARVEY, *Dehydrogenation of polycyclic hydroaromatic compounds*, *Chemical Reviews* **78**, 4:317, 1978.
- [120] D. JUNG, M. H. KIM, J. KIM, *Cu-catalyzed aerobic oxidation of di-tert-butyl hydrazodicarboxylate to di-tert-butyl azodicarboxylate and its application on dehydrogenation of 1, 2, 3, 4-tetrahydroquinolines under mild conditions*, *Organic letters* **18**, 24:6300, 2016.
- [121] Y. SHANG, X. JIE, K. JONNADA, S. N. ZAFAR, W. SU, *Dehydrogenative desaturation-relay via formation of multicenter-stabilized radical intermediates*, *Nature communications* **8**, 1:2273, 2017.

- 
- [122] N. ZUMBRÄGEL, M. SAKO, S. TAKIZAWA, H. SASAI, H. GRÖGER, *Vanadium-Catalyzed Dehydrogenation of N-Heterocycles in Water*, *Organic letters* **20**, 16:4723, 2018.
- [123] J. LI, G. LIU, X. LONG, G. GAO, J. WU, F. LI, *Different active sites in a bifunctional Co@N-doped graphene shells based catalyst for the oxidative dehydrogenation and hydrogenation reactions*, *Journal of catalysis* **355**:53, 2017.
- [124] A. V. IOSUB, S. S. STAHL, *Catalytic aerobic dehydrogenation of nitrogen heterocycles using heterogeneous cobalt oxide supported on nitrogen-doped carbon*, *Organic letters* **17**, 18:4404, 2015.
- [125] X. CUI, Y. LI, S. BACHMANN, M. SCALONE, A.-E. SURKUS, K. JUNGE, C. TOPF, M. BELLER, *Synthesis and characterization of iron–nitrogen-doped graphene/core–shell catalysts: Efficient oxidative dehydrogenation of N-heterocycles*, *Journal of the American Chemical Society* **137**, 33:10652, 2015.
- [126] C. DERAEDT, R. YE, W. T. RALSTON, F. D. TOSTE, G. A. SOMORJAI, *Dendrimer-stabilized metal nanoparticles as efficient catalysts for reversible dehydrogenation/hydrogenation of N-heterocycles*, *Journal of the American Chemical Society* **139**, 49:18084, 2017.
- [127] M.-H. SO, Y. LIU, C.-M. HO, C.-M. CHE, *Graphite-Supported Gold Nanoparticles as Efficient Catalyst for Aerobic Oxidation of Benzylic Amines to Imines and N-Substituted 1, 2, 3, 4-Tetrahydroisoquinolines to Amides: Synthetic Applications and Mechanistic Study*, *Chemistry–An Asian Journal* **4**, 10:1551, 2009.
- [128] E. KUMARAN, W. K. LEONG, *Gold (0) catalyzed dehydrogenation of N-heterocycles*, *Tetrahedron Letters* **59**, 44:3958, 2018.
- [129] W. R. LEOW, W. K. H. NG, T. PENG, X. LIU, B. LI, W. SHI, Y. LUM, X. WANG, X. LANG, S. LI ET AL., *Al<sub>2</sub>O<sub>3</sub> surface complexation for photocatalytic organic transformations*, *Journal of the American Chemical Society* **139**, 1:269, 2016.
- [130] D. V. JAWALE, E. GRAVEL, N. SHAH, V. DAUVOIS, H. LI, I. N. NAMBOOTHIRI, E. DORIS, *Cooperative Dehydrogenation of N-Heterocycles Using a Carbon Nanotube–Rhodium Nanohybrid*, *Chemistry–A European Journal* **21**, 19:7039, 2015.
-

- [131] Y. ZHANG, S. PANG, Z. WEI, H. JIAO, X. DAI, H. WANG, F. SHI, *Synthesis of a molecularly defined single-active site heterogeneous catalyst for selective oxidation of N-heterocycles*, *Nature communications* **9**, 1:1465, 2018.
- [132] S. CHEN, Q. WAN, A. K. BADU-TAWIAH, *Picomole-scale real-time photoreaction screening: discovery of the visible-light-promoted dehydrogenation of tetrahydroquinolines under ambient conditions*, *Angewandte Chemie* **128**, 32:9491, 2016.
- [133] M. KOJIMA, M. KANAI, *Tris (pentafluorophenyl) borane-catalyzed acceptorless dehydrogenation of N-heterocycles*, *Angewandte Chemie International Edition* **55**, 40:12224, 2016.
- [134] M. K. SAHOO, G. JAISWAL, J. RANA, E. BALARAMAN, *Organo-Photoredox Catalyzed Oxidative Dehydrogenation of N-Heterocycles*, *Chemistry–A European Journal* **23**, 57:14167, 2017.
- [135] S. CHAKRABORTY, W. W. BRENNESSEL, W. D. JONES, *A molecular iron catalyst for the acceptorless dehydrogenation and hydrogenation of N-heterocycles*, *Journal of the American Chemical Society* **136**, 24:8564, 2014.
- [136] R. YAMAGUCHI, C. IKEDA, Y. TAKAHASHI, K.-I. FUJITA, *Homogeneous catalytic system for reversible dehydrogenation- hydrogenation reactions of nitrogen heterocycles with reversible interconversion of catalytic species*, *Journal of the American Chemical Society* **131**, 24:8410, 2009.
- [137] S. MUTHAIAH, S. H. HONG, *Acceptorless and base-free dehydrogenation of alcohols and amines using ruthenium-hydride complexes*, *Advanced Synthesis & Catalysis* **354**, 16:3045, 2012.
- [138] M. L. BUIL, M. A. ESTERUELAS, M. P. GAY, M. GOMEZ-GALLEGO, A. I. NICASIO, E. ONATE, A. SANTIAGO, M. A. SIERRA, *Osmium Catalysts for Acceptorless and Base-Free Dehydrogenation of Alcohols and Amines: Unusual Coordination Modes of a BPI Anion*, *Organometallics* **37**, 4:603, 2018.
- [139] D. TALWAR, A. GONZALEZ-DE CASTRO, H. Y. LI, J. XIAO, *Regioselective Acceptorless Dehydrogenative Coupling of N-Heterocycles toward Functionalized Quinolines, Phenanthrolines, and Indoles*, *Angewandte Chemie International Edition* **54**, 17:5223, 2015.



- [140] K.-I. FUJITA, Y. TANAKA, M. KOBAYASHI, R. YAMAGUCHI, *Homogeneous perdehydrogenation and perhydrogenation of fused bicyclic N-heterocycles catalyzed by iridium complexes bearing a functional bipyridonate ligand*, *Journal of the American Chemical Society* **136**, 13:4829, 2014.
- [141] M. G. MANAS, L. S. SHARNINGHAUSEN, E. LIN, R. H. CRABTREE, *Iridium catalyzed reversible dehydrogenation–Hydrogenation of quinoline derivatives under mild conditions*, *Journal of Organometallic Chemistry* **792**:184, 2015.
- [142] J. WU, D. TALWAR, S. JOHNSTON, M. YAN, J. XIAO, *Acceptorless dehydrogenation of nitrogen heterocycles with a versatile iridium catalyst*, *Angewandte Chemie International Edition* **52**, 27:6983, 2013.
- [143] S. WANG, H. HUANG, C. BRUNEAU, C. FISCHMEISTER, *Iridium-Catalyzed Hydrogenation and Dehydrogenation of N-Heterocycles in Water under Mild Conditions*, *ChemSusChem* 2019.
- [144] R. XU, S. CHAKRABORTY, H. YUAN, W. D. JONES, *Acceptorless, reversible dehydrogenation and hydrogenation of N-heterocycles with a cobalt pincer catalyst*, *ACS Catalysis* **5**, 11:6350, 2015.
- [145] O. R. LUCA, D. L. HUANG, M. K. TAKASE, R. H. CRABTREE, *Redox-active cyclopentadienyl Ni complexes with quinoid N-heterocyclic carbene ligands for the electrocatalytic hydrogen release from chemical fuels*, *New Journal of Chemistry* **37**, 11:3402, 2013.
- [146] P. RYABCHUK, A. AGAPOVA, C. KREYENSCHULTE, H. LUND, H. JUNGE, K. JUNGE, M. BELLER, *Heterogeneous nickel-catalysed reversible, acceptorless dehydrogenation of N-heterocycles for hydrogen storage*, *Chemical Communications* **55**, 34:4969, 2019.
- [147] T. LIU, K. WU, L. WANG, Z. YU, *Potassium tert-Butoxide-Promoted Acceptorless Dehydrogenation of N-Heterocycles*, *Advanced Synthesis & Catalysis* .
- [148] A. F. MAIER, S. TUSSING, T. SCHNEIDER, U. FLOERKE, Z.-W. QU, S. GRIMME, J. PARADIES, *Frustrated lewis pair catalyzed dehydrogenative oxidation of indolines and other heterocycles*, *Angewandte Chemie International Edition* **55**, 40:12219, 2016.

- [149] Y. WU, H. YI, A. LEI, *Electrochemical acceptorless dehydrogenation of N-heterocycles utilizing TEMPO as organo-electrocatalyst*, ACS Catalysis **8**, 2:1192, 2018.
- [150] D. AINEMBABAZI, N. AN, J. C. MANAYIL, K. WILSON, A. F. LEE, A. M. VOUTCHKOVA-KOSTAL, *Acceptorless amine dehydrogenation and transamination using Pd-doped hydrotalcites*, ACS Catalysis **9**, 2:1055, 2018.
- [151] Y. HAN, Z. WANG, R. XU, W. ZHANG, W. CHEN, L. ZHENG, J. ZHANG, J. LUO, K. WU, Y. ZHU ET AL., *Ordered Porous Nitrogen-Doped Carbon Matrix with Atomically Dispersed Cobalt Sites as an Efficient Catalyst for Dehydrogenation and Transfer Hydrogenation of N-Heterocycles*, Angewandte Chemie International Edition **57**, 35:11262, 2018.
- [152] G. JAISWAL, M. SUBARAMANIAN, M. K. SAHOO, E. BALARAMAN, *A Reusable Cobalt Catalyst for Reversible Acceptorless Dehydrogenation and Hydrogenation of N-Heterocycles*, Chem-CatChem **11**, 10:2449, 2019.
- [153] G. JAISWAL, V. G. LANDGE, D. JAGADEESAN, E. BALARAMAN, *Iron-based nanocatalyst for the acceptorless dehydrogenation reactions*, Nature communications **8**, 1:2147, 2017.
- [154] K.-H. HE, F.-F. TAN, C.-Z. ZHOU, G.-J. ZHOU, X.-L. YANG, Y. LI, *Acceptorless dehydrogenation of n-heterocycles by merging visible-light photoredox catalysis and cobalt catalysis*, Angewandte Chemie International Edition **56**, 11:3080, 2017.
- [155] Z. JIA, Q. YANG, L. ZHANG, S. LUO, *Photoredox Mediated Acceptorless Dehydrogenative Coupling of Saturated N-Heterocycles*, ACS Catalysis **9**, 4:3589, 2019.
- [156] M. K. SAHOO, E. BALARAMAN, *Room temperature catalytic dehydrogenation of cyclic amines with the liberation of H<sub>2</sub> using water as a solvent*, Green Chemistry **21**, 8:2119, 2019.
- [157] S. KATO, Y. SAGA, M. KOJIMA, H. FUSE, S. MATSUNAGA, A. FUKATSU, M. KONDO, S. MASAOKA, M. KANAI, *Hybrid catalysis enabling room-temperature hydrogen gas release from N-heterocycles and tetrahydronaphthalenes*, Journal of the American Chemical Society **139**, 6:2204, 2017.
- [158] J.-J. ZHONG, W.-P. TO, Y. LIU, W. LU, C.-M. CHE, *Efficient acceptorless photo-dehydrogenation*

- 
- of alcohols and N-heterocycles with binuclear platinum (ii) diphosphite complexes*, Chemical science **10**, 18:4883, 2019.
- [159] D. CHAO, M. ZHAO, *A supramolecular assembly bearing an organic TADF chromophore: synthesis, characterization and light-driven cooperative acceptorless dehydrogenation of secondary amines*, Dalton Transactions **48**, 16:5444, 2019.
- [160] M. ZHENG, J. SHI, T. YUAN, X. WANG, *Metal-Free Dehydrogenation of N-Heterocycles by Ternary h-BCN Nanosheets with Visible Light*, Angewandte Chemie **130**, 19:5585, 2018.
- [161] M. HAO, X. DENG, L. XU, Z. LI, *Noble metal Free MoS<sub>2</sub>/ZnIn<sub>2</sub>S<sub>4</sub> nanocomposite for acceptorless photocatalytic semi-dehydrogenation of 1, 2, 3, 4-tetrahydroisoquinoline to produce 3, 4-dihydroisoquinoline*, Applied Catalysis B: Environmental **252**:18, 2019.
- [162] G. E. DOBEREINER, R. H. CRABTREE, *Dehydrogenation as a Substrate-Activating Strategy in Homogeneous Transition-Metal Catalysis*, Chemical Reviews **110**, 2:681, 2010, doi:10.1021/cr900202j, PMID: 19938813.
- [163] J. CHOI, A. H. R. MACARTHUR, M. BROOKHART, A. S. GOLDMAN, *Dehydrogenation and related reactions catalyzed by iridium pincer complexes*, Chemical Reviews **111**, 3:1761, 2011.
- [164] N. O. BALAYEVA, Z. MAMIYEV, R. DILLERT, N. ZHENG, D. W. BAHNEMANN, *Rh/TiO<sub>2</sub>-Photocatalyzed Acceptorless Dehydrogenation of N-Heterocycles upon Visible-Light Illumination*, ACS Catalysis **10**, 10:5542, 2020.
- [165] N. O. BALAYEVA, N. ZHENG, R. DILLERT, D. W. BAHNEMANN, *Visible-Light-Mediated Photocatalytic Aerobic Dehydrogenation of N-heterocycles by Surface-Grafted TiO<sub>2</sub> and 4-amino-TEMPO*, ACS Catalysis **9**, 12:10694, 2019.
- [166] H. IRIE, K. KAMIYA, T. SHIBANUMA, S. MIURA, D. A. TRYK, T. YOKOYAMA, K. HASHIMOTO, *Visible light-sensitive Cu (II)-grafted TiO<sub>2</sub> photocatalysts: activities and X-ray absorption fine structure analyses*, The Journal of Physical Chemistry C **113**, 24:10761, 2009.
- [167] S. M. PAUFF, S. C. MILLER, *Synthesis of Near-IR Fluorescent Oxazine Dyes with Esterase-Labile Sulfonate Esters*, Organic letters **13**, 23:6196, 2011.
-

- [168] K. L. BILLINGSLEY, K. W. ANDERSON, S. L. BUCHWALD, *A Highly Active Catalyst for Suzuki–Miyaura Cross-Coupling Reactions of Heteroaryl Compounds*, *Angewandte Chemie International Edition* **45**, 21:3484, 2006.
- [169] N. SERPONE, *Relative photonic efficiencies and quantum yields in heterogeneous photocatalysis*, *Journal of Photochemistry and Photobiology A: Chemistry* **104**, 1-3:1, 1997.
- [170] Y. V. LARICHEV, O. NETSKINA, O. KOMOVA, V. SIMAGINA, *Comparative XPS study of Rh/Al<sub>2</sub>O<sub>3</sub> and Rh/TiO<sub>2</sub> as catalysts for NaBH<sub>4</sub> hydrolysis*, *international journal of hydrogen energy* **35**, 13:6501, 2010.
- [171] Y. SONG, C. WEI, X. ZHANG, X. WEI, X. SONG, Z. SUN, *Nanoporous Pd/TiO<sub>2</sub> composites prepared by one-step dealloying and their electrocatalytic performance for methanol/ethanol oxidation*, *Materials Chemistry and Physics* **161**:153, 2015.
- [172] R. A. RATHER, S. SINGH, B. PAL, *A C<sub>3</sub>N<sub>4</sub> surface passivated highly photoactive Au-TiO<sub>2</sub> tubular nanostructure for the efficient H<sub>2</sub> production from water under sunlight irradiation*, *Applied Catalysis B: Environmental* **213**:9, 2017.
- [173] F. LI, X. LI, *The enhancement of photodegradation efficiency using Pt–TiO<sub>2</sub> catalyst*, *Chemosphere* **48**, 10:1103, 2002.
- [174] R. F. HOWE, M. GRATZEL, *EPR study of hydrated anatase under UV irradiation*, *Journal of Physical Chemistry* **91**, 14:3906, 1987.
- [175] O. I. MICIC, Y. ZHANG, K. R. CROMACK, A. D. TRIFUNAC, M. C. THURNAUER, *Trapped holes on titania colloids studied by electron paramagnetic resonance*, *The Journal of Physical Chemistry* **97**, 28:7277, 1993.
- [176] J. B. PRIEBE, M. KARNAHL, H. JUNGE, M. BELLER, D. HOLLMANN, A. BRÜCKNER, *Water Reduction with Visible Light: Synergy between Optical Transitions and Electron Transfer in Au-TiO<sub>2</sub> Catalysts Visualized by In situ EPR Spectroscopy*, *Angewandte Chemie International Edition* **52**, 43:11420, 2013.
- [177] T. HIRAKAWA, H. KOMINAMI, B. OHTANI, Y. NOSAKA, *Mechanism of photocatalytic production*

- 
- of active oxygens on highly crystalline TiO<sub>2</sub> particles by means of chemiluminescent probing and ESR spectroscopy*, The Journal of Physical Chemistry B **105**, 29:6993, 2001.
- [178] T. BARZETTI, E. SELLI, D. MOSCOTTI, L. FORNI, *Pyridine and ammonia as probes for FTIR analysis of solid acid catalysts*, Journal of the Chemical Society, Faraday Transactions **92**, 8:1401, 1996.
- [179] T. BEZRODNA, G. PUCHKOVSKA, V. SHIMANOVSKA, I. CHASHECHNIKOVA, T. KHALYAVKA, J. BARAN, *Pyridine-TiO<sub>2</sub> surface interaction as a probe for surface active centers analysis*, Applied surface science **214**, 1-4:222, 2003.
- [180] P. JONES, J. HOCKEY, *Infra-red studies of rutile surfaces. Part 1*, Transactions of the Faraday Society **67**:2669, 1971.
- [181] G. MARTRA, *Lewis acid and base sites at the surface of microcrystalline TiO<sub>2</sub> anatase: relationships between surface morphology and chemical behaviour*, Applied Catalysis A: General **200**, 1-2:275, 2000.
- [182] L. SAVARY, J. SAUSSEY, G. COSTENTIN, M. BETTAHAR, M. GUBELMANN-BONNEAU, J. LAVALLEY, *Propane oxydehydrogenation reaction on a VPO/TiO<sub>2</sub> catalyst. Role of the nature of acid sites determined by dynamic in-situ IR studies*, Catalysis today **32**, 1-4:57, 1996.
- [183] V. V. KUMAR, G. NARESH, M. SUDHAKAR, J. TARDIO, S. K. BHARGAVA, A. VENUGOPAL, *Role of Brønsted and Lewis acid sites on Ni/TiO<sub>2</sub> catalyst for vapour phase hydrogenation of levulinic acid: Kinetic and mechanistic study*, Applied Catalysis A: General **505**:217, 2015.
- [184] E. SCHMIDT, D. FERRI, A. BAIKER, *Surface processes occurring on Rh/alumina during chiral modification by cinchonidine: An ATR-IR spectroscopy study*, Langmuir **23**, 15:8087, 2007.
- [185] M. R. BASILA, T. R. KANTNER, K. H. RHEE, *The Nature of the Acidic Sites on a Silica-Alumina. Characterization by Infrared Spectroscopic Studies of Trimethylamine and Pyridine Chemisorption1*, The Journal of Physical Chemistry **68**, 11:3197, 1964.
- [186] G. PARFITT, J. RAMSBOTHAM, C. ROCHESTER, *An infra-red study of pyridine adsorption on rutile surfaces*, Transactions of the Faraday Society **67**:1500, 1971.
-

- [187] G. ZHANG, G. KIM, W. CHOI, *Visible light driven photocatalysis mediated via ligand-to-metal charge transfer (LMCT): an alternative approach to solar activation of titania*, *Energy & Environmental Science* **7**, 3:954, 2014.
- [188] E. FARFAN-ARRIBAS, R. J. MADIX, *Characterization of the acid- base properties of the TiO<sub>2</sub> (110) surface by adsorption of amines*, *The Journal of Physical Chemistry B* **107**, 14:3225, 2003.
- [189] L. TRIGGIANI, A. B. MUNOZ-GARCIA, A. AGOSTIANO, M. PAVONE, *First-principles study of trimethylamine adsorption on anatase TiO<sub>2</sub> nanorod surfaces*, *Theoretical Chemistry Accounts* **134**, 10:119, 2015.
- [190] Y. ZALAOGLU, A. T. ULGEN, C. TERZIOGLU, G. YILDIRIM, *Theoretical study on the characterization of 6-methyl 1, 2, 3, 4-tetrahydroquinoline using quantum mechanical calculation methods*, *Fen Bilimleri Dergisi* **14**:66, 2010.
- [191] E. FINKELSTEIN, G. M. ROSEN, E. J. RAUCKMAN, *Production of hydroxyl radical by decomposition of superoxide spin-trapped adducts.*, *Molecular pharmacology* **21**, 2:262, 1982.
- [192] F. A. VILLAMENA, J. K. MERLE, C. M. HADAD, J. L. ZWEIER, *Superoxide radical anion adduct of 5, 5-dimethyl-1-pyrroline N-oxide (DMPO). 2. The thermodynamics of decay and EPR spectral properties*, *The Journal of Physical Chemistry A* **109**, 27:6089, 2005.
- [193] C. E. DIAZ-URIBE, M. C. DAZA, F. MARTINEZ, E. A. PAEZ-MOZO, C. L. GUEDES, E. DI MAURO, *Visible light superoxide radical anion generation by tetra (4-carboxyphenyl) porphyrin/TiO<sub>2</sub>: EPR characterization*, *Journal of Photochemistry and Photobiology A: Chemistry* **215**, 2-3:172, 2010.
- [194] Y. ZHANG, Z. WANG, X. LANG, *Merging visible light photocatalysis of dye-sensitized TiO<sub>2</sub> with TEMPO: the selective aerobic oxidation of alcohols*, *Catalysis Science & Technology* **7**, 21:4955, 2017.
- [195] J. M. BOBBITT, M. C. L. FLORES, *Organic nitrosonium salts as oxidants in organic chemistry*, *Heterocycles* **27**, 2:509, 1988.

- [196] B. CHMIELEWSKA, P. KRZYCZMONIK, H. SCHOLL, *Electrode reactions of nitroxyl radicals. XI: Coulometric experiments on the oxidation of aliphatic alcohols by oxoammonium cations*, Journal of Electroanalytical Chemistry **395**, 1-2:167, 1995.
- [197] M. F. SEMMELHACK, C. S. CHOU, D. A. CORTES, *Nitroxyl-mediated electrooxidation of alcohols to aldehydes and ketones*, Journal of the American Chemical Society **105**, 13:4492, 1983.
- [198] L. B. VOLODARSKY, V. A. REZNIKOV, V. I. OVCHARENKO, *Synthetic chemistry of stable nitroxides*, CRC Press, 2017.
- [199] B. LIMOGES, C. DEGRAND, *Electrocatalytic oxidation of hydrogen peroxide by nitroxyl radicals*, Journal of Electroanalytical Chemistry **422**, 1-2:7, 1997.
- [200] X. LI, C. CHEN, J. ZHAO, *Mechanism of photodecomposition of H<sub>2</sub>O<sub>2</sub> on TiO<sub>2</sub> surfaces under visible light irradiation*, Langmuir **17**, 13:4118, 2001.
- [201] T. OHNO, Y. MASAKI, S. HIRAYAMA, M. MATSUMURA, *TiO<sub>2</sub>-photocatalyzed epoxidation of 1-decene by H<sub>2</sub>O<sub>2</sub> under visible light*, Journal of Catalysis **204**, 1:163, 2001.
- [202] R. D. JONES, D. A. SUMMERVILLE, F. BASOLO, *Synthetic oxygen carriers related to biological systems*, Chemical Reviews **79**, 2:139, 1979.
- [203] J. EVANS, *The peroxide-ion fundamental frequency*, Journal of the Chemical Society D: Chemical Communications , 12:682, 1969.
- [204] Y. RAO, W. CHU, *Reaction mechanism of linuron degradation in TiO<sub>2</sub> suspension under visible light irradiation with the assistance of H<sub>2</sub>O<sub>2</sub>*, Environmental science & technology **43**, 16:6183, 2009.
- [205] Y. K. TAKAHARA, Y. HANADA, T. OHNO, S. USHIRODA, S. IKEDA, M. MATSUMURA, *Photooxidation of organic compounds in a solution containing hydrogen peroxide and TiO<sub>2</sub> particles under visible light*, Journal of applied electrochemistry **35**, 7-8:793, 2005.
- [206] J. ZOU, J. GAO, F. XIE, *An amorphous TiO<sub>2</sub> sol sensitized with H<sub>2</sub>O<sub>2</sub> with the enhancement of photocatalytic activity*, Journal of Alloys and Compounds **497**, 1-2:420, 2010.

- [207] A. KUDO, Y. MISEKI, *Heterogeneous photocatalyst materials for water splitting*, Chemical Society Reviews **38**, 1:253, 2009.
- [208] A. IWASZUK, M. NOLAN, Q. JIN, M. FUJISHIMA, H. TADA, *Origin of the visible-light response of nickel (II) oxide cluster surface modified titanium (IV) dioxide*, The Journal of Physical Chemistry C **117**, 6:2709, 2013.
- [209] J. RAN, J. ZHANG, J. YU, M. JARONIEC, S. Z. QIAO, *Earth-abundant cocatalysts for semiconductor-based photocatalytic water splitting*, Chemical Society Reviews **43**, 22:7787, 2014.
- [210] L. FAN, J. LONG, Q. GU, H. HUANG, H. LIN, X. WANG, *Single-site nickel-grafted anatase TiO<sub>2</sub> for hydrogen production: Toward understanding the nature of visible-light photocatalysis*, Journal of catalysis **320**:147, 2014.
- [211] Y. NAKAOKA, Y. NOSAKA, *ESR investigation into the effects of heat treatment and crystal structure on radicals produced over irradiated TiO<sub>2</sub> powder*, Journal of Photochemistry and Photobiology A: Chemistry **110**, 3:299, 1997.
- [212] Y. SHIRAIISHI, T. HIRAI, *Selective organic transformations on titanium oxide-based photocatalysts*, Journal of Photochemistry and Photobiology C: Photochemistry Reviews **9**, 4:157, 2008.
- [213] V. BREZOVA, A. BLAKOVA, I. SURINA, B. HAVLINOVA, *Solvent effect on the photocatalytic reduction of 4-nitrophenol in titanium dioxide suspensions*, Journal of Photochemistry and Photobiology A: Chemistry **107**, 1-3:233, 1997.
- [214] A. TAKAI, P.V. KAMAT, *Capture, store, and discharge. Shuttling photogenerated electrons across TiO<sub>2</sub>-silver interface*, Acs Nano **5**, 9:7369, 2011.
- [215] S. BANG, S. LEE, T. PARK, Y. KO, S. SHIN, S.-Y. YIM, H. SEO, H. JEON, *Dual optical functionality of local surface plasmon resonance for RuO<sub>2</sub> nanoparticle-ZnO nanorod hybrids grown by atomic layer deposition*, Journal of Materials Chemistry **22**, 28:14141, 2012.
- [216] S. TRASATTI, *Work function, electronegativity, and electrochemical behaviour of metals: III*.



- Electrolytic hydrogen evolution in acid solutions*, Journal of Electroanalytical Chemistry and Interfacial Electrochemistry **39**, 1:163, 1972.
- [217] D. S. OVOSHCHNIKOV, B. G. DONOEVA, V. B. GOLOVKO, *Visible-light-driven aerobic oxidation of amines to nitriles over hydrous ruthenium oxide supported on TiO<sub>2</sub>*, ACS Catalysis **5**, 1:34, 2015.
- [218] S. K. MOROMI, S. SIDDIKI, K. KON, T. TOYAO, K.-I. SHIMIZU, *Acceptorless dehydrogenation of N-heterocycles by supported Pt catalysts*, Catalysis today **281**:507, 2017.
- [219] N. NAKAYAMA, T. HAYASHI, *Preparation and characterization of poly (L-lactic acid)/TiO<sub>2</sub> nanoparticle nanocomposite films with high transparency and efficient photodegradability*, Polymer degradation and stability **92**, 7:1255, 2007.
- [220] M. F. ATITAR, R. DILLERT, D. W. BAHNEMANN, *Surface interactions between imazapyr and the TiO<sub>2</sub> surface: an in situ ATR-FTIR study*, The Journal of Physical Chemistry C **121**, 8:4293, 2017.
- [221] Z. HONG, W. K. CHONG, A. Y. R. NG, M. LI, R. GANGULY, T. C. SUM, H. S. SOO, *Hydrophobic Metal Halide Perovskites for Visible-Light Photoredox C- C Bond Cleavage and Dehydrogenation Catalysis*, Angewandte Chemie International Edition **58**, 11:3456, 2019.



## List of Publications

- [1] NARMINA O. BALAYEVA, ZAMIN MAMIYEV, RALF DILLERT, NAN ZHENG, DETLEF W. BAHNEMANN, *Rh/TiO<sub>2</sub>-photocatalyzed acceptorless dehydrogenation of N-heterocycles upon visible-light illumination*, ACS Catalysis **10** (10), 5542-5553 (2020). doi.org/10.1021/acscatal.0c00556
- [2] BIANCA-MARIA BRESOLIN, NARMINA O. BALAYEVA, LUIS I. GRANONE, RALF DILLERT, DETLEF W. BAHNEMANN, *Anchoring lead-free halide Cs<sub>3</sub>Bi<sub>2</sub>I<sub>9</sub> perovskite on UV100–TiO<sub>2</sub> for enhanced photocatalytic performance*, Solar Energy Materials and Solar Cells **204**, 110214 (2020). doi:10.1016/j.solmat.2019.110214
- [3] NARMINA O. BALAYEVA, RALF DILLERT, NAN ZHENG, DETLEF W. BAHNEMANN, *Visible-Light-Mediated Photocatalytic Aerobic Dehydrogenation of N-heterocycles by Surface-Grafted TiO<sub>2</sub> and 4-amino-TEMPO*, ACS Catalysis **9**, (12), 10694-10704 (2019) doi.org/10.1021/acscatal.9b03322
- [4] SOUKAINA AKEL, RALF DILLERT, NARMINA O. BALAYEVA, REDOUAN BOUGHALED, MOHAMMED EL AZZOUZI, DETLEF W. BAHNEMANN, *Ag/Ag<sub>2</sub>O as a Co-catalyst in TiO<sub>2</sub> photocatalysis: Effect of the Co-catalyst/photocatalyst mass ratio*, Catalysts **8** (12), 647, (2018). doi:10.3390/catal8120647
- [5] NARMINA O. BALAYEVA, MANUEL FLEISCH, DETLEF W. BAHNEMANN, *Surface-grafted WO<sub>3</sub>/TiO<sub>2</sub> photocatalysts: Enhanced visible-light activity towards indoor air purification*, Catalysis Today **313**, 63-71, (2018). doi.org/10.1016/j.cattod.2017.12.008
- [6] NARMINA O. BALAYEVA, RALF DILLERT, DETLEF W. BAHNEMANN, *Cu(II) Grafted WO<sub>3</sub>/TiO<sub>2</sub>*

*Nanocomposites for Selective and Efficient Photoconversion of NO<sub>x</sub> and Acetaldehyde Gases upon UV and Visible Illumination*, In preparation

[7] VIJAY KHANAL, **NARMINA O. BALAYEVA**, VAIDYANATHAN (RAVI) SUBRAMANIAN, CARSTEN GUENNEMANN AND DETLEF W. BAHNEMANN, *Photocatalytic Gas Phase photoconversion of NO<sub>x</sub> with Tantalum Oxide Nanoparticles*, ready for submission

[8] VIJAY KHANAL, DHANESH CHANDRA, **NARMINA O. BALAYEVA**, VAIDYANATHAN SUBRAMANIAN, DETLEF W. BAHNEMANN, *Examining the Activity of Tantalum Oxide and Tantalum Nitride towards Methylene Blue Photodegradation*, ready for submission

### **Oral Presentations:**

**Narmina O. Balayeva**, “Acceptorless Dehydrogenation of N-heterocycles upon Visible Light Illumination over Rh/TiO<sub>2</sub> Photocatalyst”, Russian-German Workshop, 27 November - 02 December, 2019. Sankt- Petersburg, Russia.

**Narmina O. Balayeva**, Manuel Fleisch, Detlef W. Bahnemann, “Enhanced Visible-Light Activity of Surface Grafted WO<sub>3</sub>-TiO<sub>2</sub> Photocatalysts”, International conference of Photochemistry 28, 16-21 Juli, 2017. Strasburg, France.

**Narmina O. Balayeva**, Manuel Fleisch, Detlef W. Bahnemann, “WO<sub>3</sub>-TiO<sub>2</sub> based photocatalysis: Toward indoor air purification under visible-light illumination”, EAAOP-5, 25-29 June, 2017. **Awarded Best student oral presentation (SPC)**. Prague, Czech Republic.

**Narmina O. Balayeva**, Nan Zheng, Ralf Dillert, Manuel Fleisch, Detlef W. Bahnemann, “Dehydrogenation of 1,2,3,4-Tetrahydroquinoline to Quinoline by Surface Grafted TiO<sub>2</sub> under Visible Light Illumination”, SPASEC-22, 13-16 November, 2017. Clearwater beach, Florida, USA.

**Narmina O. Balayeva**, Nan Zheng, Ralf Dillert, Manuel Fleisch, Detlef W. Bahnemann, “Photocatalytic Dehydrogenation of 1,2,3,4-Tetrahydroquinoline to Quinoline by Surface

Grafted TiO<sub>2</sub> under Visible Light Illumination”, SP-6, 11-14 September, 2017. Oldenburg, Germany,

**Narmina O. Balayeva**, Manuel Fleisch, Detlef W. Bahnemann, “Fe(III)/Cu(II) Grafted WO<sub>3</sub>-TiO<sub>2</sub> Composites as Photocatalysts with Improved Visible-Light Activity”, German-Russian Workshop, 28 November-02 December, 2016, Hannover, Germany.

### **Poster Presentations:**

**Narmina O. Balayeva**, Zamin Mamiyev, Nan Zheng, Ralf Dillert, Detlef W. Bahnemann, “Acceptorless Dehydrogenation of N-heterocyclic amines and Simultaneous Hydrogen Production by Rh/TiO<sub>2</sub> photocatalyst under visible light illumination” Nanoday, 10 October, 2019. Hannover, Germany (**Best Poster Prize**).

**Narmina O. Balayeva**, Manuel Fleisch, Detlef W. Bahnemann, “WO<sub>3</sub>-TiO<sub>2</sub> based photocatalysis: Toward indoor air purification under visible-light illumination”, EAAOP-5, 25-29 June, 2017. Prague, Czech Republic.

**Narmina O. Balayeva**, Manuel Fleisch, Detlef W. Bahnemann, “Photocatalytic Degradation of Nitric Oxide (NO<sub>x</sub>) and Acetaldehyde Over Visible-Light-Sensitive Fe(III)-Grafted WO<sub>3</sub>-TiO<sub>2</sub> Photocatalysts”, Nanoday, 29 September, 2016. Hannover, Germany.

**Narmina O. Balayeva**, Manuel Fleisch, Detlef W. Bahnemann, “Synergistic Effect Studies of Surface Fe<sup>3+</sup> Doped and Grafted (Fe(III), Cu(II)) TiO<sub>2</sub> Composites for Evaluation of Their Photocatalytic Activity Under Visible Light Illumination”, NPM-1, 7-11 June, 2015. Göttingen, Germany.



# Curriculum Vitae

## ***Personal Information***

Name, Surname      Narmina, Balayeva  
Date of Birth        27.04.1990  
Place of Birth       Sumgayit, Azerbaijan

## ***Education:***

11.2015 – 06.2020    Doctoral studies, Gottfried Wilhelm Leibniz Universität Hannover. Thesis title: *Visible-Light-Driven Photocatalytic Organic Synthesis with Surface Modified TiO<sub>2</sub>-Composites*  
09.2011 – 06.2013    Magistr Diploma in Physical Chemistry of Nanomaterials (with Honors), Baku State University. Thesis title: *Synthesis and investigation of polymer nanocomposites on the basis of chlorophosphonated nitrile butadiene rubber/polyethylene matrix*  
09.2007 – 06.2011    Bachelor Diploma in Chemistry, Baku State University. Thesis title: *Synthesis and investigation of various substituted thiiranes and their amino-derivatives*  
1996 – 2007          16<sup>th</sup> Middle School, Sumgayit, Azerbaijan

## ***Working experiences:***

02.2016 – 06.2018    Research Assistant at the Institut für Technische Chemie, Gottfried Wilhelm Leibniz Universität Hannover  
01.2014 – 05.2015    Scientific Researcher at the Institute of Physics, Azerbaijan National Academy of Science